Title
Mechanics of Confined Microbial Populations

Author
Gniewek, Pawel

Publication Date
2018

Peer reviewed|Thesis/dissertation

Mechanics of Confined Microbial Populations

by

Pawel Gniewek

A dissertation submitted in partial satisfaction of the

requirements for the degree of

Doctor of Philosophy

in

Biophysics

in the

Graduate Division

of the

University of California, Berkeley

Committee in charge:

Professor Oskar Hallatschek, Chair
Professor Mohammad R. K. Mofrad
Professor Hernan G. Garcia
Professor Sanjay Govindjee

Fall 2018

Abstract

Mechanics of Confined Microbial Populations

by

Pawel Gniewek

Doctor of Philosophy in Biophysics

University of California, Berkeley

Professor Oskar Hallatschek, Chair

Living systems offer a richness of behaviors that are of broad interest to many fields of science. For instance, cells that are dwelling in their natural environment are mostly subject not only to the scarcity of energy resources, but also the space in which they can grow and live. This space limitation eventually leads to the emergence of contact forces (mechanical stress) between neighboring cells or the cells and their confining environment. These emergent forces may further have a crucial impact on the cells' biology, the dynamics of the whole population, or even the integrity of confinement (resulting in the remodeling of the environment). Even though the general importance of these forces has been widely recognized, technical difficulties and the complexity of the emergent phenomena prevented much progress in this direction. In this thesis, using mostly computer simulations, I make steps towards overcoming these barriers. In the first part of this thesis, I describe, on the coarse level, how the geometric properties of micro-confinement entails clogging of the microbial populations of *Saccharomyces cerevisiae*. These clogged populations are found to be quite disordered, with intermittent growth dynamics and heterogeneous mechanical stresses — properties much more like those of granular materials than a continuum. Thus, granular materials are an appealing framework to describe dense microbial populations. However, using a simple 2D model, I numerically show that the coupling between cellular growth rate and mechanical stress gives rise to deviation from the expected behavior of inanimate granular materials, and it increases the complexity of the emergent phenomena. The simple and coarse model used in the first part of the thesis is sufficient for relatively low density systems, but it is not adequate for strongly compacted systems. Thus, in the second part of this thesis, I employ the Finite Element Method to study in detail the structure and mechanics of the disordered packings of elastic shells — our proxy model for dense cellular packings. Therein, I discuss how deformations resulting from large compressive forces couple the structural and mechanical properties of the compact packings. Finally, using Lattice-Boltzmann simulations, I investigate the fluid transport in such compacted packings of deformable shells. I show that a relatively simple model proposed by Kozeny & Carman, combined with a percolation theory, can capture the fluid transport in porous materials. This result is of interest not only in dense biological systems, but also in a broader class of granular porous materials.

To my parents.

Contents

Citations to previously published works

Chapter 2 appears in its entirety as

> Morgan Delarue, Jörn Hartung, Carl Schreck, Pawel Gniewek, Lucy Hu, Stephan Herminghaus, Oskar Hallatschek (2016). "Self-driven jamming in growing microbial populations", *Nature Physics*, 12, 762–766. https://www.nature.com/articles/nphys3741

Chapter 3 appears in its entirety as

> Pawel Gniewek, Carl Schreck, Oskar Hallatschek (2018). "Jamming by growth",
> https://arxiv.org/abs/1810.01999

Chapter 5 appears in its entirety as

> Pawel Gniewek, Oskar Hallatschek (2018) "Liquid transport through packings of elastic shells",
> https://arxiv.org/abs/1807.00249

Acknowledgments

I have the great pleasure to thank all of the members of our informal "Jamming Group" in Hallatschek Lab that helped me during my time in grad school: Morgan Delarue, Carl Schreck, and Marie-Cecilia Duvernoy. In particular, I had the pleasure of working quite closely with Carl Schreck, who taught me many things about the physics of jamming and about computer simulations, and was also a great companion and officemate. I am also especially grateful to Morgan and Marie-Cecilia, whose healthy skepticism and understanding of experiments prevented me from making embarrassing mistakes and helped me focus on the relevant questions.

It is also my privilege to thank the other members of Hallatschek Lab: Ben, Daniel, Diana, Jayson, Joao, Jona, Jörn, Lucas, Matti, Qinqin, Stephen, Tom, Wolfram, and Yuya, to whom I owe a great time while at UC Berkeley. Our countless talks over coffee, (sometimes too long) lunches, Tahoe trips, and spontaneous pints of beer in nearby pubs will stay with me for a long time.

I also thank my advisor, Oskar Hallatchek, for his help, advice, and financial support during my PhD studies. Alongside, I am really thankful to the members of my thesis committee: Mohammad Mofrad, Hernan Garcia, and Sanjay Govindjee. Your continuous encouragement and enthusiasm are much appreciated.

And finally, I want to thank Sylvia Do. It was Sylvia who helped me remain sane and grounded in the reality of the non-academic world. This thesis is partially also her achievement.

1
Introduction

In order to proliferate within a crowded environment, cells must exert mechanical forces onto their surroundings. These forces are necessary to create the space needed to accommodate new cellular material. To that end, cells act against extracellular material, steric constraints due to confinement, and other cells. Hence, cell proliferation leads to the generation of compressive forces, which in turn influence the movement of the cells and the self-organization of the cellular assembly. The importance of forces induced by growth and their feedback onto growth has been recognized over the last 10 years[1,2]. Namely, these forces turned out to be crucial for morphophonemics[2–4], tumor[5] and tissue[3,6] growth, collective cell migration[7], and bacterial colonies and biofilms development[8–10].

Except for some studies on biofilms, physical stresses that arise due to the growth of the microbial population and their feedback on genes expression are much less investigated than the influences of other cues such as chemical or starvation[11,12]. This is largely due to the fact that the classical method of culturing microbes is in liquid media, and the cells are allowed to grow and divide in the absence of any physical constraints. Yet, most microbes live in the form of solid biofilms attached to surfaces and restricted by an extracellular matrix (a polymeric network of peculiar physical and chemical properties). Thus, these studies do not capture the effects of cellular crowding and emergent mechanical stresses, and as such there have been very few quantitative studies on the impact of confinement on growth[13,14].

Furthermore, most microbes that inhabit soil, rocks, and other solid surfaces dwell in pores less than 10 μm in diameter[15]. Upon cellular growth, due to the lack of space, the cells may leave the confinement in a fluid-like or plug-like manner. However, for certain geometries of the habitats, the microbial populations may become clogged inside micro-pores[16,17]. When microbes become clogged, further growth leads to internal pressure buildup. For example, dense populations of budding yeast generate pressure large enough (up to 1.0 MPa) to affect growth and motility[18,19] or even impact the integrity of the cells' environment[20]; thus this mechanism may be crucial for microbial pathogenicity[9,21–23].

Despite the ubiquitous nature of mechanical forces during the growth of confined cellular populations, the nature of these forces is largely unknown. Experimentally, a few studies address this aspect and reliably measure growth forces on the cells' population level[18,24–27]. However, the mathematical description of biofilm formation and development is still incomplete. On one hand, continuum models[28–32] can cap-

ture large-scale and long-time behaviors but lack the proper descriptions of the stress and density fluctuations and cellular granularity that are responsible for clogging in micro-cavities[33,34]. On the other hand, individual-based cells simulations can capture these effects; however, a simplified description of intercellular forces with a lack of deformations provides only a tentative description of the structure and mechanics of a strongly compacted microbial population[34–38].

Henceforth, in this thesis, I develop a computational framework and numerically study the mechanics and structure of *Saccharomyces cerevisiae* cells in confined spaces. For relatively diluted cellular packings, I use single-cell based simulations that properly account for cellular granularity, contact forces, and density fluctuations[18,39–42]. As the cellular population becomes dense, the emergent forces deform cells to the extent that they can no longer be approximated by idealized shapes, and the pair-wise contact forces approximation is no longer valid. Thus, I study the structure of highly compacted packings using a continuum mechanics model of deformable cells[43–46]. As the cellular packings get very compacted and dense, the limitation of nutrients, on top of the compressive stress, become an additional obstacle in population development. Thus, I numerically study a liquid transport, close to the percolation transition, in 3D disordered packings representing budding yeast cells.

1.1 Structure of this thesis

Chapters in this thesis are, to a large extent, independent projects ranging from the physics of granular materials to elastic shells mechanics to porous materials to fluid mechanics. Thus, in this introductory chapter, I only briefly mention the physics background and numerical approach used in the thesis. Details are left to the corresponding chapters where they are discussed more comprehensively and relevant references are given.

The following thesis is organized as follow: In Chapter 2, I present a joint experimental and numerical effort where we found that confinement of growing yeast cells result in the clogging of the population inside fabricated microchambers. Microfluidics experiments, done by Morgan Delarue and Jorn Hartung, show that the clogged yeast population can develop a significant internal pressure which severely impacts the growth of the cells and the dynamics of the entire population. Using computational models and image analysis techniques, together with Carl Schreck, we link this behavior to the granularity of the cells and supposed jamming transition that occurs as the population gets clogged.

In Chapter 3, I extend the numerical model developed in Chapter 2. I discuss how the coupling between compressive stresses and growth rate impacts the mechanical properties of confined cellular populations and how they relate to inanimate granular and amorphous materials.

In Chapter 4, I analyze the structure and mechanics of highly compacted elastic shells using Finite El-

ements simulations. Therein, I discuss compression mechanics of a pressurized elastic shell, including a buckling condition for a pressurized shell. Furthermore, I speculate about the minimum energy structure of disordered packings, and I discuss an "anomalous" shell coordination number upon the approach of a full compaction. I explain this in terms of the emergent rotational degrees of freedom that need to be stabilized upon the shells' deformation. Finally, I address one of the puzzling results from Chapter 2 — presumably a turgor pressure adaptation as the cellular packings get more compact.

In Chapter 5, using Lattice-Boltzmann simulations and percolation theory, I study the liquid transport in the packings of elastic shells. I confirm that the classical model for porous materials developed by Kozeny & Carman, extended by the parameters grounded in percolation theory, provides a good description of liquid permeability in a broad range of packing densities.

This thesis is shortly summarized in Chapter 6. In Appendices A and B, I provide computational details of the software that I developed during my PhD studies. In Appendix A, I describe a Monte-Carlo algorithm and an open-source library `rndmesh` that I used to generate disordered meshes on spheres, which is necessary for Finite Element simulations. In Appendix B, I review computational models of elastic shells with their foundations in elasticity theory. Then, I describe in detail the implementation of the `elasticshells` software and its benchmarking against known solutions.

References

[1] T. Mammoto and D. E. Ingber. Mechanical control of tissue and organ development. *Development*, 137(9):1407–1420, 2010.

[2] C.-P. Heisenberg and Y. Bellaiche. Forces in tissue morphogenesis and patterning. *Cell*, 153:948, 2013.

[3] B. Shraiman. Mechanical feedback as a possible regulator of tissue growth. *Proceedings of the National Academy of Sciences of the United States of America*, 102:3318, 2005.

[4] E. Farge. Mechanical induction of twist in the drosophila foregut/stomodeal primordium. *Current Biology*, 13(6):1365–77, 2003.

[5] F. Montel, M. Delarue, J. Elgeti, L. Malaquin, M. Basan, T. Risler, B. Cabane, D. Vignjevic, J. Prost, G. Cappello, and J.-F. Joanny. Stress Clamp Experiments on multicellular Tumor Spheroids. *Physical Review Letters*, 107:188102, 2011.

[6] J. Lange and B. Fabry. Cell and tissue mechanics in cell migration. *Experimental Cell Research*, 319 (16):2418–2423, 2013.

[7] S. Monirosadat, N. Qazvini, R. Krishnan, C. Park, and J. Fredberg. Collective migration and cell jamming. *Differentiation*, 86(3):121–125, 2013.

[8] P. Watnick and R. Kolter. Biofilm, city of microbes. *Journal of Bacteriology*, 182(10):2576–9, 2000.

[9] L. Hall-Stoodley, J. Costerton, and P. Stoodley. Bacterial biofilms: from the natural environment to infectious diseases. *Nature Reviews Microbiology*, 2(2):95–108, 2004.

[10] P. Stoodley, K. Sauer, D. Davies, and J. Costerton. Biofilms as complex differentiated communities. *Annual Review of Microbiology*, 56:187–209, 2002.

[11] Y.-S. Bahn, C. Xue, A. Idnurm, J. Rutherford, J. Heitman, and M. Cardenas. Sensing the environment: lessons from fungi. *Nature Reviews Microbiology*, 5(1):57–69, 2007.

[12] M. Asally, A. Robinsonb, H. Lu, M. Kittisopikul, P. Rue, Y. Du, Z. Hu, T. Cagatay, J. Garcia-Ojalvo, and G. Suel. Localized cell death focuses mechanical forces during 3d patterning in a biofilm. *Proceedings of the National Academy of Sciences of the United States of America*, 109(46):18891–18896, 2012.

[13] N. Minc, A. Boudadoud, and F. Chang. Mechanical forces of fission yeast growth. *Current Biology*, 19(13):1096–1101, 2009.

[14] H. Tuson, G. Auer, L. Renner, M. Hasebe, C. Tropini, M. Salick, W. Crone, A. Gopinathan, K. Huang, and D. Weibel. Measuring the stiffness of bacterial cells from growth rates in hydrogels of tunable elasticity. *Current Biology*, 84(5):874–91, 2012.

[15] I. M. Young and J. Crawford. Interactions and self-organization in the soil-microbe complex. *Science*, 304(5677):1634–1637, 2004.

[16] I. Zuriguel, D. R. Parisi, R. C. Hidalgo, C. Lozano, A. Janda, P. A. Gago, J. P. Peralta, L. M. Ferrer, L. A. Pugnaloni, E. Clément, D. Maza, I. Pagonabarraga, and A. Garcimartín. Clogging transition of many-particle systems flowing through bottlenecks. *Scientific Reports*, 4:7324, 2014.

[17] E. Dressaire and A. Sauret. Clogging of microfluidic systems. *Soft Matter*, 13:37–48, 2017.

[18] M. Delarue, J. Hartung, C. Schreck, P. Gniewek, L. Hu, S. Herminghaus, and O. Hallatschek. Self-driven jamming in growing microbial populations. *Nature Physics*, 12(8):762, 2016.

[19] J. Hartung. *Forces in Cellular Growth and Division*. Georg-August-Universitat, Gottingen, 2015.

[20] T. Warscheid and J. Braams. Biodeterioration of stone: a review. *International Biodeterioration & Biodegradation*, 46:343–368, 2000.

[21] J. Costerton, P. Stewart, and E. Greenberg. Bacterial biofilms: a common cause of persistent infections. *Science*, 284(5418):1318–22, 1999.

[22] J. Costerton, L. Montanaro, and C. Arciola. Biofilm in implant infections: its production and regulation. *The International Journal of Artificial Organs*, 28(11):1062–8, 2005.

[23] C. do Nascimento, Barbosa, R.E., Issa, J.P., E. Watanabe, I. Ito, and R. J. Albuquerque. Bacterial leakage along the implant-abutment interface of premachined or cast components. *International Journal of Oral and Maxillofacial Surgery*, 37(2):177–80, 2007.

[24] K. Alessandri, B. R. Sarangi, V. V. Gurchenkov, B. Sinha, T. R. Kießling, L. Fetler, F. Rico, S. Scheuring, C. Lamaze, A. Simon, S. Geraldo, D. Vignjević, H. Doméjean, L. Rolland, A. Funfak, J. Bibette, N. Bremond, and P. Nassoy. Cellular capsules as a tool for multicellular spheroid production and for investigating the mechanics of tumor progression in vitro. *Proceedings of the National Academy of Sciences of the United States of America*, 110(37):14843–14848, 2013.

[25] M. Delarue, F. Montel, D. Vignjevic, J. Prost, J. J.-F., and G. Cappello. Compressive stress inhibits proliferation in tumor spheroids through a volume limitation. *Biophysical Journal*, 107:1821–1828, 2014.

[26] O. Campas, T. Mammoto, S. Hasso, R. Sperling, D. O'Connell, A. Bischof, R. Maas, D. Weitz, L. Mahadevan, , and D. Ingber. Quantifying cell-generated mechanical forces within living embryonic tissues. *Nature Methods*, 11:183–189, 2014.

[27] K. Sugimura, P.-F. Lenne, and F. Graner. Measuring forces and stresses in situ in living tissues. *Development*, 143(2):186–196, 2016. doi: 10.1242/dev.119776.

[28] H. Eberl, D. Parker, and M. Vanloosdrecht. A new deterministic spatio-temporal continuum model for biofilm development. *Journal of Theoretical Medicine*, 3:161–175, 2007.

[29] R. Duddu, D. Chopp, and B. Moran. A two-dimensional continuum model of biofilm growth incorporating fluid flow and shear stress based detachment. *Biotechnology and Bioengineering*, 103: 92–104, 2009.

[30] M. Basan, T. Risler, J.-F. Joanny, X. Sastre-Garau, and J. Prost. Homeostatic competition drives tumor growth and metastasis nucleation. *HFSP Journal*, 3:265–272, 2009.

[31] C. Vulin, J.-M. Di Meglio, A. Lindner, A. Daerr, A. Murray, and P. Hersen. Growing yeast into cylindrical colonies. *Biophysical Journal*, 106:2214–2221, 2014.

[32] M. Mattei, L. Frunzo, B. D'Acunto, Y. Pechaud, F. Pirozzi, and G. Esposito. Continuum and discrete approach in modeling biofilm development and structure: a review. *Journal of Mathematical Biology*, 76:945–1003, 2018.

[33] H. Zhang, A. Beer, E.-L. Florin, and H. Swinney. Collective motion and density fluctuations in bacterial colonies. *Proceedings of the National Academy of Sciences of the United States of America*, 107:13626–13630, 2010.

[34] P. Ghosh, J. Mondal, E. Ben-Jacob, and H. Levine. Mechanically-driven phase separation in a growing bacterial colony. *Proceedings of the National Academy of Sciences of the United States of America*, 112(17):E2166–E2173, 2015. doi: 10.1073/pnas.1504948112.

[35] D. Drasdo, S. Hoehme, and M. Block. On the role of physics in the growth and pattern formation of multi-cellular systems: What can we learn from individual-cell based models? *Journal of Statistical Physics*, 128:287–345, 2007.

[36] M. Basan, J. Prost, J.-F. Joanny, and J. Elgeti. Dissipative particle dynamics simulations for biological tissues: rheology and competition. *Physical Biology*, 8(2):026014, 2011.

[37] D. Drasdo and S. Hoehme. Modeling the impact of granular embedding media, and pulling versus pushing cells on growing cell clones. *New Journal of Physics*, 14(5):055025, 2012.

[38] Z. Xu, P. Meakin, A. Tartakovsky, and T. D. Scheibe. Dissipative-particle-dynamics model of biofilm growth. *Physical Review E*, 83:066702, 2011.

[39] C. F. Schreck, N. Xu, and C. S. O'Hern. A comparison of jamming behavior in systems composed of dimer- and ellipse-shaped particles. *Soft Matter*, 6:2960–2969, 2010.

[40] F. D. C. Farrell, O. Hallatschek, D. Marenduzzo, and B. Waclaw. Mechanically driven growth of quasi-two-dimensional microbial colonies. *Physical Review Letters*, 111:168101, Oct 2013. doi: 10.1103/PhysRevLett.111.168101.

[41] M. A. A. Grant, B. Wacław, R. J. Allen, and P. Cicuta. The role of mechanical forces in the planar-to-bulk transition in growing escherichia coli microcolonies. *Journal of The Royal Society Interface*, 11(97), 2014.

[42] J. Kayser, C. Schreck, M. Gralka, D. Fusco, and O. Hallatschek. Collective motion conceals fitness differences in crowded cellular populations. *bioRxiv*, 2018. doi: 10.1101/267286.

[43] S. Sandersius and T. Newman. Modeling cell rheology with the subcellular element model. *Physical Biology*, 5(1):015002, 2008.

[44] A. M. M. M. Jamali, . Y. A sub-cellular viscoelastic model for cell population mechanics. *PLoS ONE*, 5(8):e12097, 2010.

[45] F. Milde, G. Tauriello, H. Haberkern, and P. Koumoutsakos. Sem++: A particle model of cellular growth, signaling and migration. *Computational Particle Mechanics*, 1(2):211–227, Jun 2014.

[46] P. Van Liedekerke, A. Buttenschön, and D. Drasdo. Chapter 14 - off-lattice agent-based models for cell and tumor growth: Numerical methods, implementation, and applications. In M. Cerrolaza, S. J. Shefelbine, and D. Garzón-Alvarado, editors, *Numerical Methods and Advanced Simulation in Biomechanics and Biological Processes*, pages 245 – 267. Academic Press, 2018.

2

Self-Driven Jamming in Growing Microbial Populations

2.1 Introduction

In natural settings, microbes tend to grow in dense populations[1–4] where they need to push against their surroundings to accommodate space for new cells. The associated contact forces play a critical role in a variety of population-level processes, including biofilm formation[5–7], the colonization of porous media[8,9], and the invasion of biological tissues[10–12]. Although mechanical forces have been characterized at the single cell level[13–16], it remains elusive how collective pushing forces result from the combination of single cell forces. Here, we reveal a collective mechanism of confinement, which we call self-driven jamming, that promotes the build-up of large mechanical pressures in microbial populations. Microfluidic experiments on budding yeast populations in space-limited environments show that self-driven jamming arises from the gradual formation and sudden collapse of force chains driven by microbial proliferation, extending the framework of driven granular matter[17–20]. The resulting contact pressures can become large enough to slow down cell growth, to delay the cell cycle in the G1 phase, and to strain or even destroy the microenvironment through crack propagation. Our results suggest that self-driven jamming and build-up of large mechanical pressures is a natural tendency of microbes growing in confined spaces, contributing to microbial pathogenesis and biofouling[21–26].

2.2 Results

The simultaneous measurement of the physiology and mechanics of microbes is enabled by a microfluidic bioreactor[27–30] that we have designed to culture microbes under tightly controlled chemical and mechanical conditions. The setup, shown in Fig. 2.1a, is optimized for budding yeast

(*S. cerevisiae*). We use this device to measure mechanical forces generated by partially-confined growing populations and the impact of those forces on both the population itself and its micro-environment.

At the beginning of each experiment, we trap a single yeast cell in the growth chamber of the device, which can hold up to about 100 cells. The cells are fed by a continuous flow of culture medium, provided by a narrow set of channels that are impassable for cells.

While cells first proliferate exponentially as in liquid culture, their growth dynamics is dramatically altered once the chamber is filled. At high density, cells move in a stop-and-go manner and increasingly push against the chamber walls. The population develops a contact pressure that increases over time until it reaches a steady state, subject to large fluctuations. Note that this contact pressure is conceptually very different from the hydrostatic pressure because water can flow in and out of cells. Depending on the geometry of the outlet (Fig. 2.1b and c), the mean steady-state pressure can reach up to 0.7 ± 0.1 MPa. This pressure is larger than the osmotic pressure difference, ≈ 0.2 MPa (stationary phase[31]), between the interior of a budding yeast cell and the surrounding medium, and much larger than the ≈ 1 mPa needed for the cells to overcome viscous friction (see Appendix).

Although the initial pressure build-up is similar in different devices, we find a sensitive dependence on the device geometry. The steady state pressure can be finely tuned by the shape of the outlet gate (shown in Fig. 2.1b and c) or the width of the outlet channel (Fig. S2.13).

Both the intermittent flow and pressure build-up are counter-intuitive because, in all cases, the outlet channel is wide enough for cells to pass. In principle, excess cells could flow like a liquid out of the chamber. Time lapse movies (**Movie S1**) reveal that blockages in the device stabilize the cell packing and prevent flow. Cells proliferate until a sudden avalanche flushes them through the outlet (Fig. 2.1d and e). Another jamming event occurs, and the process repeats. These dynamics generate characteristic slow pressure increases followed by sudden pressure drops (Fig. 2.1c).

Jamming, intermittency and avalanches are familiar aspects of flowing sand, grains or even jelly beans[24]. To test whether the interplay of growth, collective rearrangement, and outflow of cells from the chamber can be explained by the mechanics of granular materials, we set up coarse-grained computer simulations with cells represented as elastic particles that grow exponentially and reproduce by budding. In our simulations, cells move via frictionless over-damped dynamics with repulsive contact interactions between neighbors.

Our simulations indeed reproduce the intermittent dynamics observed in the experiments (Fig. 2.2a–

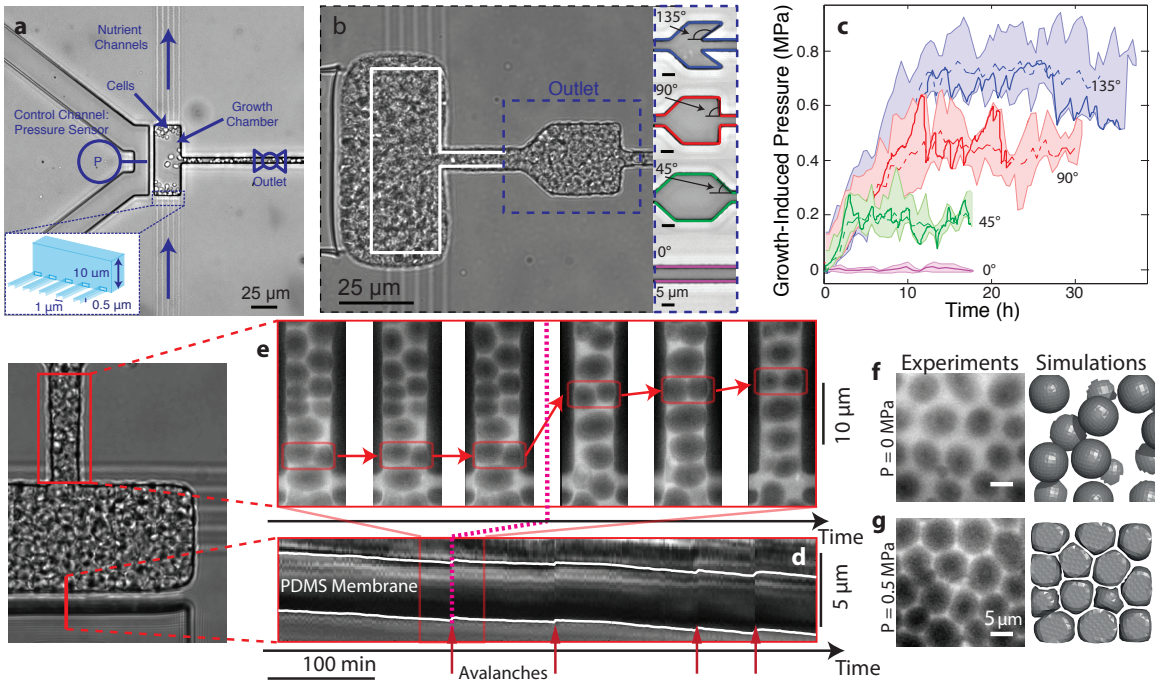

Figure 2.1: Self-driven jamming of microbes enables collective pressure build-up in microfluidic environments. (a) Budding yeast cells are grown in a growth chamber threaded by narrow nutrient channels (inset). (b) The jamming of excess microbes produced by proliferation in the device leads to a partial confinement of the population and a gradual build-up of a contact pressure of up to 0.65 ± 0.1 MPa (in the shown experiment), which strongly deforms the device (white line represents the undeformed layout). The steady-state pressure generated in a given device depends on the geometry of the outlets (b, right), which effectively act as leaky one-way valves. The resulting time-dependent pressure curves are shown in (c) for different outlets. The pressure measurements were enabled by an automatic feedback system that actively controls the deformation of a thin membrane separating the growth chamber and a control channel (see a and Appendix). The bold curves correspond to one realization of the experiment, which is characterized by large pressure fluctuations due to gradual jamming and sudden unjamming. The shaded region represents the envelope of the replicates: all replicates are binned together, and within each bin, the minimum and the maximum define the shading. The dashed line corresponds to the mean of all realizations. The cellular flows exhibits collective features known from physics of jamming in granular media: The outflow of cells is not steady but consists of periods of stasis, accompanied by pressure-build up, and sudden cell avalanches and pressure drops. This can be seen in time lapse movies (**`Movie S1`**) as well as Kimographs: (d) shows the random zig-zag motion of the chamber membrane and (e) shows the flow through the outlet before, during and after an avalanche with one snapshot every 20 minutes. Note that, depending on the local stresses, cells assume shapes from nearly spherical (f, low stress) to nearly polyhedral (g, high stress). (f, g, left) Micrographs taken close to the coverslip at the bottom of the chamber. (f, g, right) Mass-spring simulations, in which cell walls are represented as (at vanishing contact pressure) spherical meshworks of springs (see Appendix). For better visualization, the simulations only show the first layer of cells. The depths of this layer are 5.25 μm and 1.7 μm for low and high pressure respectively.

c). We find that the distribution of pressure drops have an exponential tail in both experiments and simulations (Fig. 2.2d) for $P > \langle P \rangle$, similar to avalanche size distributions in hopper flows[32].

Highly intermittent cell flows might reflect spatially heterogeneous mechanical stresses, a hallmark of driven granular materials[17–20]. Assuming that cell shape deformation is indicative of the forces between cells, we developed a non-invasive method to infer these forces (Fig. 2.2f, Appendix, and Fig. S2.1). Using this approach, we analyzed microscopy images to determine stress distributions of crowded populations. Both *S. cerevisiae* experiments and our coarse-grained simulations exhibit disordered cell packings that are stabilized by heterogeneous force networks (Fig. 2.2f and g). Stress is highly localized along branching "force chains"[17,18] while adjacent "spectator cells"[33] experience very little mechanical stress.

We find that jamming-induced contact forces can become so large that they feed back on the cell physiology. Indeed, a feedback on both cell shape and the dynamics of cell growth is evident in experiments where we place two devices of different steady state pressures next to one another, as seen in the time lapse movie (**Movie S2**). These devices only differ by the width of their outlet channels (5μm vs. 7.5μm). We find that an increased outlet channel width leads to an increased mean avalanche size, and correspondingly, a smaller mean pressure (Fig. S2.13). To quantify the feedback on growth, we estimate the net growth rate, which is the difference between birth and death rate, in our microfluidic bioreactors by measuring mean cell outflow rate at steady state (see Appendix). We find that the growth rate decays roughly exponentially with pressure until growth is undetectable at a stalling pressure of about 1 MPa (Fig. 2.3c). The stalling pressure, or homeostatic pressure[34], is obtained by using a special device with a "self-closing valve", in which yeast populations fully confine themselves by the pressure they build up, as seen in Fig. 2.3a. In this device, the rate of pressure increase gradually decays with pressure until saturation (Fig. 2.3b). This diminishing return is due to smaller growth rates at higher pressures, and serves as another, dynamical measure for the feedback between contact pressure and growth rate.

Control experiments supported by finite element simulations show that cells are well-fed and viable even at the highest densities suggesting a mechanobiological origin for the reduced growth rates (Appendix and Figs. S2.3 and S2.4). As a first step to uncover the mechanistic basis for the force-growth feedback, we have explored the impact of contact forces on the pace of cell cycle progression. In budding yeasts, the late G1 checkpoint Start, homolog to the mammalian Restriction point, controls the irreversible cell commitment to division[35]. Passing of the checkpoint requires multiple phosphorylations of the repressor Whi5, upon which Whi5 is exported out of the nucleus

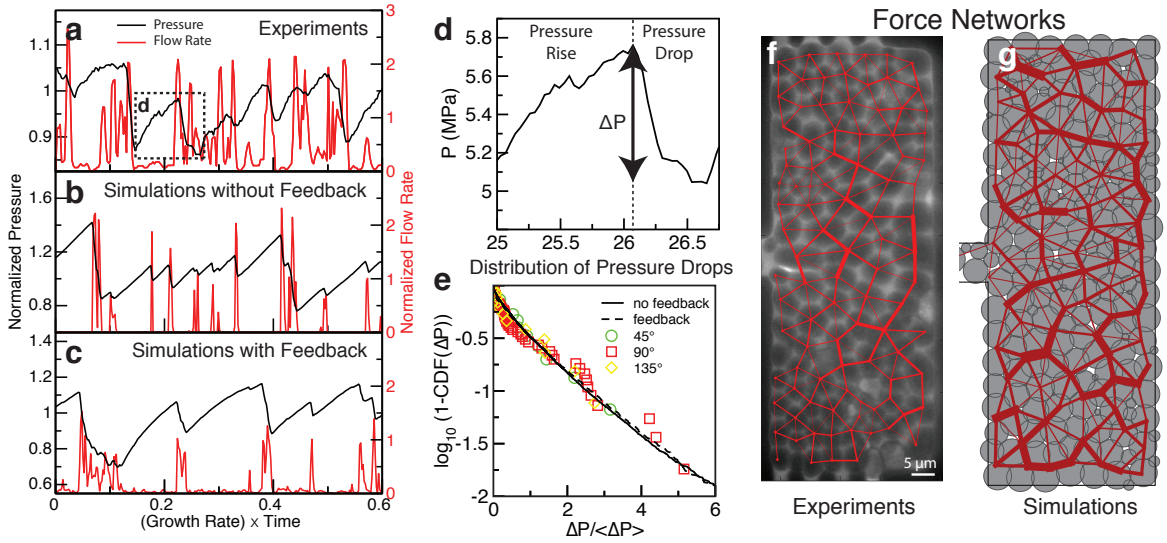

Figure 2.2: Pressure fluctuations and intermittent flows of partially confined budding yeast populations can be reproduced in simulations of proliferating elastic particles. (a) Experimental pressure time series are characterized by periods of gradual pressure build-up and sudden pressure drops. (b) Simulations show that such time series are the generic outcome of jammed elastic particles proliferating in confined spaces. (c) A feedback of pressure onto growth, reported in Fig. 2.3c below, further improves our simulations. The gradual pressure increases prior to avalanche events show diminishing return similar to the experimental time series in (a). Pressure drops during avalanche events, defined as the pressure change from the peak pressure prior to an outflow event to the base pressure just after the event (d), are nearly exponentially distributed for drops larger than the mean pressure drop, $\langle \Delta P \rangle$, in both experiments (e: symbols) and coarse-grained simulations (e: lines). We can estimate inter-cell contact forces in our experiments by measuring the area of contact between two cells through image analysis. (f) The resulting network of contact forces in packings of budding yeast cells shows a heterogeneous distribution of mechanical stresses (pressure on the membrane: 0.5 MPa). (g) Force networks obtained from simulations of exponentially growing budding cells. In both (f) and (g), large forces are clustered into chain-like structures. A movie illustrating the dynamics of force networks in our experiments can be seen **Movie S3**, and a coarse-grained simulation movie can be seen **Movie S4**. For our simulations, we used box and outlet sizes that match the microfludic chamber and parameterized the over-damped dynamics using the experimental flow rate and pressure fluctuation data (see Appendix).

until the cell cycle is completed. As a consequence, Whi5 is localized in the nucleus in the G1 phase prior to Start, and cytosolic otherwise (Fig. 2.3d, top). Using a mutant that express fluorescently labeled Whi5 thus enabled us to probe the cellular commitment to cell division. We found that an increased contact pressure is accompanied by an increase in the fraction of cells with nuclear Whi5 signal (Fig. 2.3d), suggesting a force-induced slowdown of the cell cycle in G1. This finding is

consistent with the view of the late G1 checkpoint as an integrator of numerous stresses, including osmotic, chemical and heat shock stresses[36–38]. Force-induced cell cycle arrest has been observed in mammalian cells[39,40], but the associated mechanical stresses are two to three orders lower than the stalling pressure measured in our experiments.

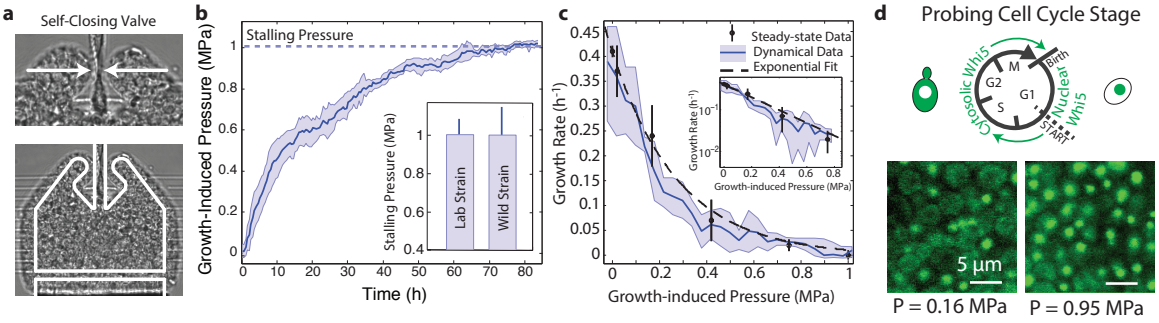

Figure 2.3: Pressure-induced slow down of growth. (a) Budding yeast populations can be fully confined using a "self-closing" device that takes advantage of the contact pressure developed by the population to close the inlet/outlet channel. The cells are fed through narrow nutrient channels, as in 2.1a. The layout of the undeformed device is shown in white. (b) The time-dependent pressure curve in the self-closing devices shows a diminishing return: The rate of increase of the growth-induced pressure in the fully confined region gradually slows until it stops at the stalling pressure of 1 ± 0.1 MPa (5 replicates, mean $\pm$ standard deviation). Inset: stalling pressure measured for the lab strain and the wild strain. (c) Growth rate as a function of growth-induced pressure, estimated in two ways (Appendix): The black points represent net growth rates determined from the cell flow out of our leaky devices in the steady-state (black points; ≥ 5 replicates, mean $\pm$ standard deviation). The continuous blue line, on the other hand, has been inferred from the diminishing return in the dynamical data of (b) under a quasi-steady state assumption (Appendix; shading indicates $\pm$ standard deviation). The dashed curves represents an exponential fit to the steady-state data (k = 0.41 (h^{-1}) exp(-P/0.28 (MPa))). (d) We probed the cell cycle progression using mutants that express fluorescently labeled Whi5 repressor proteins. In the G1 phase of the cell cycle prior to the checkpoint Start, Whi5 is localized in the nucleus yielding a subcellular fluorescent focus (see scheme). We find that at high contact pressures of 0.95 MPa almost four times as many cells exhibiting a nuclear Whi5 signal than at low pressures of P = 0.16 MPa (Fig. S2.5).

Perhaps the most salient consequence of growth-induced pressure is cell shape deformations. While budding yeast cells grown in the absence of mechanical stresses are nearly spherical, we observe that they tend to morph into convex polyhedra as the population pressure becomes growth-limiting (Fig. 2.1f and g). Close to the stalling pressure, the packing resembles the structure of a dry foam[41], consisting of cells with nearly flat faces and sharp edges in between, shown in Fig. 2.2f. The pressure-induced cell shape deformation can be best visualized at the interface between coverslip and cell population: the cell-coverslip contact area increases as the growth-induced pressure

increases (Fig. S2.6). Our simulations further suggest that, in our experiments, the osmotic pressure inside the cells may increase as a function of the growth-induced pressure (Fig. S2.6).

Most microbial cells are sticky[42,43]. Indeed, while our lab strains of budding yeast have been domesticated to become non-sticky, wild strains can have strong, velcro-like intercellular fiber connections[44]. We find that while sticky yeasts develop in our microfluidic devices a very similar maximal pressure as the lab strains do (Fig. 2.3b), they develop substantial contact pressures under much weaker confinement (Fig. 2.4a). Our coarse-grained simulations likewise suggest that attractive interactions promote jamming: The measured build up of pressure is much larger than expected under a non-granular model of a liquid droplet with surface tension, in which jamming is impossible (Fig. 2.4c and d).

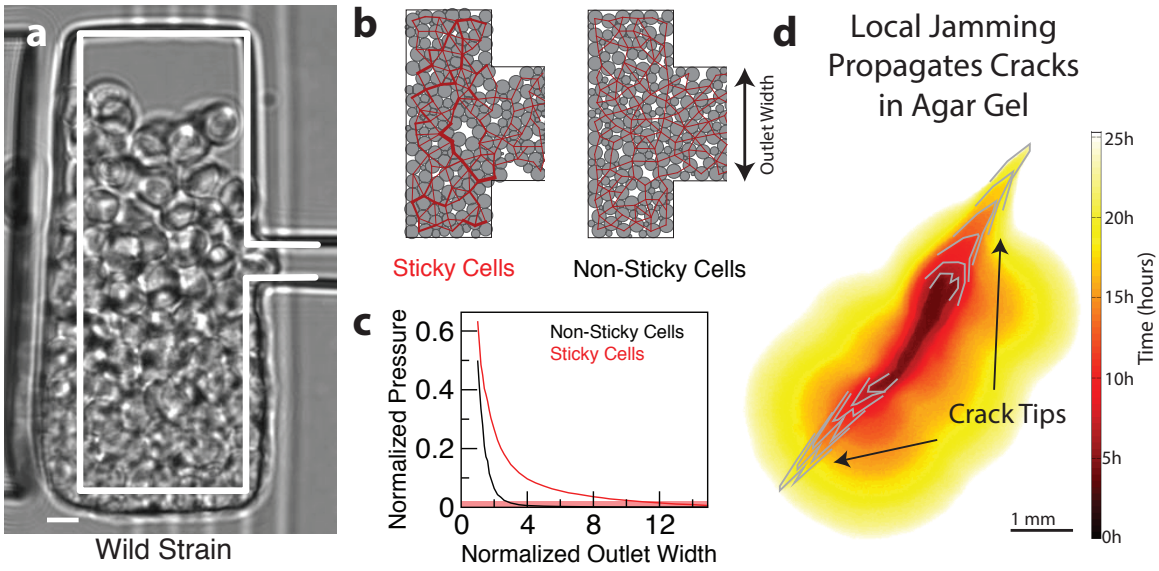

Figure 2.4: Self-driven jamming is promoted by stickiness and can remodel the microenvironment. (a) Wild strains of yeast stick together via strong velcro-like connections between cells[44]. This stabilizes the spherical growth of the population against shear stresses. (b, c) Simulations show that even weak attractive forces between cells can strongly promote jamming. (b) Packing of slightly sticky cells (right, see Appendix) exhibit a force network with pronounced force chains in contrast to the non-sticky case for the shown device. (c) The increase in growth-induced pressure (steady-state) with stickiness is much larger than expected from the continuum limit (red base line) over a broad range of outlet sizes (see Appendix). (d) Gradual propagation of agar gel cracks by growing populations of budding yeast (lab strain). Cells grow out of a pre-existing agar crack and, at the same time, propagate the crack tips inside the agar. A time-lapse movie of the crack propagation is available **Movie S5**.

Bacteria and fungi have the ability to colonize a wide range of porous media, including tiny cavities barely larger than their cell size[3,4]. Our work suggests that self-driven jamming of growing microbes can emerge in these microenvironments as it does in our microfluidic devices if chemical resources are sufficiently abundant.

The resulting growth-induced forces endow biofilms with the potential to remodel, or even destroy, their micro-environment. This could aid microbes in penetrating the soft tissues of host organisms[10–12], or to invade soil, where most microbes grow in pores of several micro-meter in diameters[3,4]. At this length scale, it is possible that the growth-induced pressures measured here contribute to straining of even stiff materials. Indeed, when we grow budding yeast populations inside agar gels, we observe the formation and propagation of cracks (Fig. 2.4d, Fig. S2.8 and time lapse movie **Movie S5**). Thus, just like jamming of granular media can threaten the mechanical integrity of their confinements, which can lead to the bursting of grain silos[32,45], it could also be an important mechanical aspect of host invasion[10–12] and biofouling[21].

2.3 Conclusions

We argue that the mechanism underlying self-driven jamming, cell proliferation, extends the notion of driven granular materials, which are usually jammed by external forces, such as shear, compression, or gravity[17–20]. On a fundamental level, cell proliferation and death are unique driving forces because they alter the number of macroscopic degrees of freedom, and thus directly affect Maxwellian rigidity criteria for jammed materials[46,47]. New granular physics may also result from biological features that have no analog in traditionally-driven granular materials. For instance, the pressure-growth feedback, that we have described above, could homogenize force networks and enhance pressure buildup, as our simulations indicate (Fig. S2.11). Intermittent flows may be influenced by the shape of cells, as rod-like cells tend to align spontaneously, thus increasing the packing fraction[48] (Fig. S2.12). We also expect cell motility[49] and viscoelastic extracellular substances[6], expressed by many microbes to promote biofilm formation, to engage in a rich mechanical interplay with the packing of growing cells in confined spaces.

References

[1] P. Watnick and R. Kolter. Biofilm, city of microbes. *Journal of Bacteriology*, 182:2675–2679, 2000.

[2] S. Fanning and A. P. Mitchell. Fungal biofilms. *PLOS Pathogens*, 8:e1002585, 2012.

[3] V. Torsvik and L. Øvreås. Microbial diversity and function in soil: from genes to ecosystems. *Current Opinion in Microbiology*, 5:240–245, 2002.

[4] L. Ranjard and A. Richaume. Quantitative and qualitatice microscale distribution of bacteria in soil. *Research in Microbiology*, 152:707–716, 2001.

[5] J. N. Wilking. Liquid transport facilitated by channels in bacillus subtilis biofilms. *Proceedings of the National Academy of Sciences of the United States of America*, 110:848–852, 2013.

[6] J. N. Wilking, T. E. Angelini, A. Seminara, M. P. Brenner, and D. A. Weitz. Biofilms as complex fluids. *MRS Bulletin*, 36:385–391, 2011.

[7] M. Asally. Localized cell death focuses mechanical forces during 3d patterning in a biofilm. *Proceedings of the National Academy of Sciences of the United States of America*, 109:18891–18896, 2012.

[8] A. Cunningham, W. Characklis, F. Abedeen, and D. Crawford. Influence of biofilm accumulation on porous media hydrodynamics. *Environmental Science & Technology*, 25: 1305–1311, 1991.

[9] B. Rittman. The significance of biofilms in porous media. *Water Resources Research*, 29: 2195–2202, 1993.

[10] N. Gow, A. Brown, and F. Odds. Fungal morphogenesis and host invasion. *Current Opinion in Microbiology*, 5:366–371, 2002.

[11] N. Money. Turgor pressure and the mechanics of fungal penetration. *Canadian Journal of Botany*, 73:96–102, 2002.

[12] T. Foster, J. Geoghegan, V. Ganesh, and M. Höök. Adhesion, invasion and evasion: the many functions of the surface proteins of staphylococcus aureus. *Nature Reviews Microbiology*, 12:49–62, 2014.

[13] A. Smith, Z. Zhang, C. R. Thomas, K. E. Moxham, and A. P. J. Middelberg. The mechanical properties of saccharomyces cerevisiae. *Proceedings of the National Academy of Sciences of the United States of America*, 97:9871–9874, 2000.

[14] N. Minc, A. Boudaoud, and F. Chang. Mechanical forces of fission yeast growth. *Current Biology*, 19:1096–1101, 2009.

[15] J. D. Stenson, C. R. Thomas, and P. Hartley. Modelling the mechanical properties of yeast cells. *Chemical Engineering Science*, 64:1892–1903, 2009.

[16] H. H. Tuson. Measuring the stiffness of bacterial cells from growth rates in hydrogel of tunable elasticity. *Molecular Microbiology*, 84:874–891, 2012.

[17] F. Radjai, M. Jean, J. J. Moreau, and S. Roux. Force distribution in dense two-dimensional granular systems. *Physical Review Letters*, 77:274–277, 1996.

[18] T. Majmudar and R. Behringer. Contact force measurement and stress-induced anisotropy in granular materials. *Nature*, 435:1079–1082, 2005.

[19] D. Bi, J. Zhang, B. Chakraborty, and R. Behringer. Jamming by shear. *Nature*, 480:335–358, 2011.

[20] C. Heussinger and J. Barrat. Jamming transition as probed by quasistatic shear flow. *Physical Review Letters*, 102:218303, 2009.

[21] T. Warscheid and J. Braams. Biodeterioration of stone: a review. *International Biodeterioration & Biodegradation*, 46:343–368, 2000.

[22] C. Seebacher. Onychomycosis. *Mycosis*, 50:321–327, 2007.

[23] L. J. Douglas. Candida biofilms and their role in infection. *Trends in Microbiology*, 11:30–36, 2003.

[24] G. D. R. MiDi. On dense granular flows. *The European Physical Journal E*, 14:341–365, 2004.

[25] L. Hall-Stoodley, J. Costerton, and P. Stoodley. Bacterial biofilms: from the natural environment to infectious diseases. *Nature Reviews Microbiology*, 2:95–108, 2004.

[26] J. Park. Unjamming and cell shape in the asthmatic airway epithelium. *Nature Materials*, 14:1040–1048, 2015.

[27] A. Rowat, J. Bird, J. Agresti, O. Rando, and D. Weitz. Tracking lineages of single cells in lines using a microfluidic device. *Proceedings of the National Academy of Sciences of the United States of America*, 106:18149–18154, 2009.

[28] H. Cho. Self-organization in high-density bacterial colonies: efficient crowd control. *PLOS Biology*, 5:e302, 2007.

[29] F. Balagaddé, L. You, C. Hansen, F. Arnold, and S. Quake. Long-term monitoring of bacteria undergoing programmed population control in a microchemostat. *Science*, 309:137–140, 2005.

[30] G. Charvin, F. Cross, and E. Siggia. A microfluidic device for temporally controlled gene expresion and long-term fluorescent imaging in unperturbed dividing yeast cells. *PLOS One*, 3:e1468, 2008.

[31] I. Martinez de Maranon, P. Maréchal, and P. Gervais. Passive response of saccharomyces cerevisiae to osmotic shift: cell volume variations depending on the physiological state. *Biochemical and Biophysical Research Communications*, 227:519–523, 1996.

[32] I. Zuriguel, A. Garcimartin, D. Maza, L. Pugnaloni, and J. M. Pastor. Jamming during the discharge of granular matter from a silo. *Physical Review E*, 71:051303, 2005.

[33] M. E. Cates, J. Wittmer, J. Bouchaud, and P. Claudin. Jamming, force chains, and fragile matter. *Physical Review Letters*, 81:1841–1844, 1998.

[34] M. Basan, T. Risler, J.-F. Joanny, X. Sastre-Garau, and J. Prost. Homeostatic competition drives tumor growth and metastatic nucleation. *HFSP Journal*, 3:265–272, 2009.

[35] G. Charvin, C. Oikonomou, E. Siggia, and F. Cross. Origin of irreversibility of cell cycle start in budding yeast. *PLOS Biology*, 8:e1000284, 2010.

[36] X. Escoté, M. Zapater, J. Clotet, and F. Posas. Hog1 mediates cell-cycle arrest in g1 phase by dual targeting of sic1. *Nature Cell Biology*, 6:997–1002, 2004.

[37] G. I. Shapiro and J. W. Harper. Anticancer drug targets: cell cycle and checkpoint control. *Journal of Clinical Investigation*, 104:1645–1653, 1999.

[38] A. Rowley, G. Johnston, B. Butler, M. Werner-Washburne, and R. A. Singer. Heat shock-mediated cell cycle blockage and g1 cyclin expression in the yeast saccharomyces cerevisiae. *Molecular and Cellular Biology*, 13:1034–1041, 1993.

[39] S. Huang, C. Chen, and D. Ingber. Control of cyclin d1, p27kip1, and cell cycle progression in human capillary endothelial cells by cell shape and cytoskeletal tension. *Molecular Biology of the Cell*, 9:3179–3193, 1998.

[40] M. Delarue, F. Montel, D. Vignjevic, J. Prost, J.-F. Joanny, and G. Cappello. Compressive stress inhibits proliferation in tumor spheroids through a volume limitation. *Biophysical Journal*, 107:1821–1828, 2014.

[41] D. Weaire, M. Fortes, and M. A. Fortes. Stress and strain in liquid and solid foam. *Advances in Physics*, 43:685–738, 1994.

[42] Y. F. Dufrêne. Sticky microbes: forces in microbial cell adhesion. *Trends in Microbiology*, 6:376–382, 2015.

[43] D. Soll. Candida biofilms: is adhesion sexy? *Current Biology*, 18:R717–R720, 2008.

[44] L. Váchová. Flo11p, drug efflux pumps, and the extracellular matrix cooperate to form biofilm yeast colonies. *Journal of Cell Biology*, 194:679–687, 2011.

[45] A. Dogangun, Z. Karaca, A. Durmus, and H. Sezen. Cause of damage and failures in silo structures. *Journal of Performance of Constructed Facilities*, 23:65–71, 2009.

[46] J. C. Maxwell. On the calculation of the equilibrium and stiffness of frames. *Philosophical Magazine*, 27:294–299, 1864.

[47] M. Wyart, L. E. Silbert, S. R. Nagel, and T. A. Witten. Effect of compression on the vibrational modes of marginally jammed solids. *Physical Review E*, 72:051306, 2005.

[48] D. Volfson, S. Cookson, J. Hasty, and L. S. Tsimring. Biomechanical ordering of dense cell populations. *Proceedings of the National Academy of Sciences of the United States of America*, 105:15346–15351, 2008.

[49] D. Bi, X. Yang, M. Marchetti, and L. Manning. Motility-driven glass and jamming transitions in biological tissues. *arXiv preprint arXiv:1509.06578*, 2015.

2.4 Appendix

Yeast strains and growth conditions: *S. cerevisiae* cells (S288C background, with a Whi5-GFP construct, courtesy of J. Thorner, UC Berkeley, USA) and wild undomesticated cells (BR-103F strain, courtesy of Palkova lab at Charles University in Czech Republic) are cultured in complete synthetic medium (CSM, 20 g/L glucose) at 30° C. The device is loaded with cells in exponential phase.

Preparation of the micro-fluidic bioreactor ("Mechano-chemostat"): The mold consists of 2 layers of different heights, each layer prepared using a classical soft lithography protocol described in Ref. 1. The first layer is prepared using SU 2000.5 negative photoresist (0.5 μm height), and the second using SU 2010 (10 μm height). Polydimethylsiloxane (PDMS, Sylgard 184, Dow Corning, USA) is mixed with the curing agent (ratio 1:10 in mass), poured onto the mold, and cured overnight at 60° C. PDMS is bound to No. 1 thickness glass slides through an oxygen plasma generated by a reactive ion etcher (RIE) machine (P_{02} = 200 mTorr, exposure time = 20 sec). Prior to loading the device, the surface is treated with Pluronics 127 (VWR, USA) as in Ref. 2 to decrease any non-specific adhesion that could result in cell-PDMS adhesion or friction.

Two methods for measuring the growth-induced pressure: To measure the contact pressure generated by the population, we monitor the position of a 4μm thick membrane separating the growth chamber and a control channel. We adjust the hydrostatic pressure every 30 seconds to keep the membrane at a fixed position. In this way, we ensure that the known hydrostatic pressure mirrors the mechanical contact pressure with a precision of 0.02 MPa.

Finite element simulations (Comsol) show that, in the absence of a hydrostatic control pressure, the deformation of the membrane is proportional to the contact pressure in the growth chamber. This linear relation can be used to convert the deformation of the membrane into the growth-induced pressure, with a precision of 0.05 MPa. However, this second method of measuring a growth-induced pressure first requires a calibration of the Young's modulus of the PDMS device. When necessary, the calibration is done before each experiment. On average, we measure a PDMS Young's modulus of 2 MPa.

Visualizing cell deformations and the contact area between cells and the coverslip: FITC-conjugated Dextran (3kDa, Invitrogen) is added to the culture medium, at a concentration of 0.1 mg/mL. Since Dextran is not internalized by single yeast cells[1], it stains the extracellular space, and enables the imaging of cell deformation. The contact between cells and the coverslip is imaged by reflectom-

etry. Briefly, we shine a 635 nm laser on the sample through a pinhole closed to a minimum, to obtain an optical slice of 0.3 μm. The reflected light is collected without filter, so that local changes in refractive index can be measured at the level of the glass slide. Typical images of cell deformations are shown in the main text of Chapter 2 (Fig. 2.1), and images obtained by reflectometry are shown in Fig. S2.6a.

Dependence of contact surface area on pressure: We measure the cell contact area at the interface between the coverslip and cell population, and compare it to our mass-spring simulations (see below). Reflectometry reveals that the average fraction of the coverslip that is in contact with cells increases as the population pressure increases, shown in Fig. S2.6a. We find that the experimentally measured growth-induced pressure increases super-linearly with surface coverage, contradicting our simple tpressurized-shell model. This may indicate that the yeast cell turgor pressure increases with growth-induced pressure (Fig. S2.6b).

Measuring the steady-state and instantaneous growth rate: Each outlet design, shown in Fig. 2.1b (right), leads to a different steady-state pressure, and a different steady-state cell outflow rate. We measure the cell outflow rate J_{cell} from time lapse movies using a custom-made particle image velocimetry algorithm (Matlab), and infer the growth rate in the chamber as $k = J_{\text{cell}}/\text{V}_{\text{ch}}$, where V_{ch} is the volume of the growth chamber.

Alternatively, we can estimate the instantaneous growth rate from the pressure vs. time relationship measured for the self-closing device. Since the cells are fully trapped in the growth chamber, the time-derivative of the pressure is directly proportional to the growth rate. The proportionality depends on the packing fraction of the cells (ϕ) and on the volume of the chamber (V).

We infer the instantaneous growth rate γ of the cells by

$$\gamma = \frac{\partial_t V_c}{V_c} \tag{S2.1}$$

where V_c is the volume occupied by the cells. By definition, the packing fraction is the fraction of volume occupied by cells divided by the volume of the chamber:

$$\phi = \frac{V_c}{V} \tag{S2.2}$$

Hence,

$$\gamma = \partial_t \log\phi + \partial_t \log V \tag{S2.3}$$

Now we assume that, at any time, the packing fraction and the chamber volume only depend on the pressure: $V(t) = V(P(t))$ and $\phi(t) = \phi(P(t))$. This quasi-steady state assumption is acceptable only if the cells can adapt their growth rates sufficiently fast to the current pressure curve or, conversely, that the pressure changes sufficiently slowly.

This enables us to rewrite the growth rate:

$$\gamma = \partial_t P \left(\partial_P \log\phi + \partial_P \log V\right) \tag{S2.4}$$

In order to plot the growth rate γ as a function of growth-induced pressure, we need three pieces of information: the time-derivative of the pressure, the packing fraction, and the pressure-dependency of the volume of the growth chamber. The packing fraction is measured using exclusion fluorescence technique (see Fig. S2.2a and S2.2c), and the dependency on pressure of the volume of the chamber is calculated through finite element simulations (Comsol) (Fig. S2.2b).

As shown in Fig. S2.2d, the growth-rate vs pressure relationship obtained in this way is in good agreement with the more direct steady-state measurements. This justifies our steady-state assumptions and suggests that the feedback on growth should act as fast or faster than the typical division time.

Inferring force maps: The interface area between cells in contact is used to estimate the contact force between the cells. To this end, we have modeled the mechanical response of budding yeast cells in the simplest possible way by assuming that a cell responds to contact forces like a pressurized elastic shell, as illustrated in Fig. 2.2f. The force between cells in contact is then given by $F = PA \propto Pl^2$, where A is the area of contact, P is the cell turgor pressure, and l is the projection of the contact surface onto the measurement plane. This takes into account the effects of turgor pressure and the near-inextensibility of the cell wall, but assumes that these effects dominate over elastic energies due to bending of the cell wall or cytoskeleton (the turgor pressure of ≈ 0.2 MPa[2] is nearly two orders of magnitude larger than the elastic moduli of cytoskeletal networks). Single-cell studies[3–6] have indeed found that compressed *S. cerevisiae* cells exert forces proportional to the area of contact, in agreement with a model that incorporates only internal pressure and cell wall stretching even for large deformations. We further validate our approach by performing sim-

ulations of deformable cells composed of spring networks, which show similar deformations as *S. cerevisiae* cells at corresponding pressures. The simulations are described in the next paragraph and in Fig. S2.1 and Fig. S2.7.

Description of mass-spring simulation: The mechanics of a budding yeast cell is primarily controlled by the mechanics of the cell wall and the turgor pressure[6]. In our "mass-spring" (MS) simulations, the cell wall is represented as a spherical meshwork of springs, obtained from surface triangulation, and connecting set of vertices. The neighbor vertices, separated by a vector R, are held together via Hookean spring interactions:

$$\mathrm{F(R)} = k_{\mathrm{MS}}\mathrm{R}(1 - R_0/R) \tag{S2.5}$$

where k_{MS} is a spring constant, and R_0 is a length of the relaxed spring. The Hookean spring constants are taken to be the same and related to the Young's modulus by the following equation:

$$k_{\mathrm{MS}} = \frac{2Et}{1-\nu} \cdot \frac{A_0}{\sum_i L_i^2} \tag{S2.6}$$

where E is Young's modulus, ν is cell wall Poisson's ratio, t is the cell wall thickness, A_0 is the initial cell surface area, and L_i is the relaxed length of the i^{th} spring[7].
The overlap between two non-bonded vertices is modeled by Hertzian repulsive force:

$$\mathrm{F(R)} = -\frac{4}{3}h^{3/2}E^*\sqrt{R^*}\hat{\mathrm{R}} \tag{S2.7}$$

where E^* is an effective Young's modulus defined as $1/E^* = (1-\nu_1^2)/E_1 + (1-\nu_2^2)/E_2$, E_i is cell wall Young's modulus of the i^{th} vertex, ν_i is cell wall Poisson's ratio of the i^{th} vertex, $R^* = 0.5 \cdot R_{\mathrm{vert}}$ is an effective radius, R_{vert} is a radius of a vertex, here set to be the same as the cell wall thickness t, $h = 2 \cdot R_{\mathrm{vert}} - R$ is an overlap between two vertices, and $\hat{\mathrm{R}}$ is a unit vector along R.
The overlap between a vertex and box walls is modeled similarly but with an effective radius $R^* = R$, and an effective Young's modulus:

$$\frac{1}{E^*} = \frac{1-\nu_{\mathrm{vert}}^2}{E_{\mathrm{vert}}} + \frac{1-\nu_{\mathrm{box}}^2}{E_{\mathrm{box}}} \tag{S2.8}$$

The force due to the cell volume-dependent turgor pressure $\Pi(V_{\text{cell}})$ on vertex i is calculated as:

$$\mathrm{F}_{\Pi}(\mathrm{r}_i) = \nabla_{\mathrm{r}_i}\big(\Pi(V_{\text{cell}})V_{\text{cell}}\big) \tag{S2.9}$$

where $V_{\text{cell}}(\mathrm{r}_1, ..., \mathrm{r}_{N_{\text{vert}}})$ is a function of the N_{vert} vertices triangulating the cell surface and the volume change for the vertex i is calculated using tetrahedral volume defined by the vertex i, its neighboring vertices in the meshwork, and center of the mass. The equations of motion of over-damped dynamics have been solved using Heun's method (explicit second-order Runge-Kutta method). In the simulations for all vertices (box wall) Young's modulus E_{vert} = 150 MPa (E_{box} = 200 MPa) and Poisson's ratio $\nu_{\text{vert}} = \nu_{\text{box}} = 1/2$ are set the same, turgor pressure is $\Pi = 1.0$ MPa (unless stated otherwise), cell wall thickness is $t = 0.1\mu$m, and the initial cell radius is $R_0 = 2.5\mu m$.

Coarse-grained simulations of proliferating elastic particles: In our 2D coarse-grained simulations, illustrated in Fig. S2.9, cells are modeled as two frictionless rigidly-attached spherical lobes[8] (mother and bud) that grow exponentially at rate γ_i by bud expansion (Eq. S2.10), move according to over-damped dynamics with mobility μ (Eqs. S2.11 and S2.12), and interact via repulsive spring forces with elastic modulus k (Eq. S2.13)

$$\dot{a}_i = \gamma_i a_i \tag{S2.10}$$

$$\dot{\mathrm{r}}_i = \mu \mathrm{F}_{\mathrm{i}} \tag{S2.11}$$

$$\dot{\theta}_i = \frac{m}{I}\mu T_i \tag{S2.12}$$

$$V = \sum_{ikjl} \frac{1}{2} k_{\text{CG}} \delta^2_{ik,jl} \Theta(\delta_{ik,jl}) \tag{S2.13}$$

where $a_i = \frac{\pi}{4}(\sigma^2_{i,\text{mother}} + \sigma^2_{i,\text{bud}})$ is the cell area, $\sigma_{i,\text{mother}}$ ($\sigma_{i,\text{bud}}$) is the diameter of the mother (bud), $\mathrm{r_i}$ (θ_i) is the cell position (orientation), m_i ($I_i = \frac{1}{8}Ma^2\big(\frac{1+\Delta^4}{1+\Delta^2} + 2\big(\frac{(1+\Delta)\Delta}{1+\Delta^2}\big)^2\big)$ with $\Delta_i = \sigma_{i,\text{bud}}/\sigma_{i,\text{mother}}$) is the cell mass (inertia), V is the total potential energy, $\mathrm{F_i} = -\nabla_{\mathrm{r_i}}\mathrm{V}$ ($T_i = -\partial_{\theta_i} V$) is the force (torque) on cell i, and $\delta_{ik,jl} = \frac{1}{2}\big(\sigma_{ik} + \sigma_{jl}\big) - \big|\mathrm{r_{ik}} - \mathrm{r_{jl}}\big|$ is the overlap between lobes k of cell i and l of cell j, and Θ is the Heaviside Step function. This method is similar to studies performed with growing spherocylinders[9,10]. For simulations with attraction, we extend the potential

in Eq. S2.13 beyond its repulsive core to have an attractive range of width Δ [11,12]

$$V = \sum_{ikjl} \left(\frac{1}{2} k_{\mathrm{CG}} \delta_{ik,jl}^2 \Theta(\delta_{im,jn} + \Delta) - \frac{1}{2} k_{\mathrm{CG}} \Delta^2 \right) \tag{S2.14}$$

In this model, the mother lobe has the same size $\sigma_{i,\mathrm{mother}} = \sigma$ for all cells. Equations of motions are integrated using a 3$^{\mathrm{rd}}$ order Gear Predictor-Corrector algorithm. Growth progresses while $\sigma_{i,\mathrm{bud}} < \sigma$ and culminates in division. After division, both new cells retain the orientation of cell i.

Cells grow in a rectangular box of dimensions $L_x \times L_y$ with an outlet of width a. For the simulations in this chapter, we used $L_x = 6\sigma$, $L_y = 16\sigma$, and $a = 1.4\sigma$ to match experiments unless stated otherwise. Cells interact with the wall with the same cell-cell repulsive spring force, $V_{\mathrm{wall}} = \frac{1}{2} k_{\mathrm{CG}} \delta^2 \Theta(\delta)$, where δ is the overlap between the cell and wall.

Without pressure feedback, $\gamma_i = \gamma_i^0$ where γ_i^0 is chosen from a uniform distribution of width 20% around a mean growth rate γ. With pressure feedback, the growth rate depends on pressure as $\gamma_i = \gamma_i^0 e^{-P_i/P_0}$ where P_i is the pressure of cell i.

The free parameters in this model are an effective friction coefficient $\mu/\left(\gamma\sqrt{mk_{\mathrm{CG}}}\right)$ and a characteristic pressure feedback scale P_0/k. In Fig. 2.3 of Chapter 2, we use parameters that best matches the experimental pressure fluctuations in the case of intermittent flow where the pressure slowly builds and then suddenly drops during avalanches. We choose values of $\mu = 8 \times 10^4 \gamma\sqrt{mk_{\mathrm{CG}}}$ and $\mu = 2 \times 10^3 \gamma\sqrt{mk_{\mathrm{CG}}}$ for simulations with (Fig. 2.2b) and without (Fig. 2.2c) feedback that best capture the ratio of pressure increase ($\dot{P}_\uparrow$) and drop ($\dot{P}_\downarrow$) rates in the case as shown in Fig. S2.10. To obtain an experimentally-motivated value of feedback pressure P_0 (Fig. 2.2c), we used a value of P_0 that yields the same ratio of $P_0^{\mathrm{exp}} = 0.28$ MPa (Fig. 2.3c) to $\langle P \rangle^{\mathrm{exp}} = 0.7$ MPa (135° data in Fig. 2.1c), $P_0^{\mathrm{exp}}/\langle P \rangle^{\mathrm{exp}} = 0.4$. Coarse-grained simulations without feedback yield $\langle P \rangle^{\mathrm{sim}} = 0.19 k_{\mathrm{CG}}$, giving $P_0^{\mathrm{sim}} = \langle P \rangle^{\mathrm{sim}} \times P_0^{\mathrm{exp}}/\langle P \rangle^{\mathrm{exp}} = 0.07k$.

Estimation of pressure due to viscous friction: Here we estimate the pressure arising from friction between cells in the outlet and the surrounding medium. In a chamber of dimensions $L_x \times L_y$ with an outlet of dimensions width$\times$length$= a \times d$, the chamber holds $N_{\mathrm{c}} \approx L_x L_y h/\sigma^3$ cells and the outlet holds $N_{\mathrm{o}} \approx adh/\sigma^3$ cells, where σ is a typical cell diameter and h is the height of the device. Assuming that the height h of the system and the width of the outlet a are both $a = h = \sigma$, so that $N_{\mathrm{c}} \approx L_x L_y/\sigma^2$ and $N_{\mathrm{o}} \approx ad/\sigma^2$. If the cells in the outlet are pushed out at velocity v, the total frictional force they experience is $F = fvN_{\mathrm{o}}$, where f is a friction coefficient per cell, and

therefore the pressure at the outlet is

$$P = F/(ah) = fvN_o/\sigma^2 \tag{S2.15}$$

Standard viscous friction of a sphere in a liquid yields $f = 6\pi\eta\sigma/2$. We further estimate the flow velocity by $v = N_c\sigma k$ where k is the growth rate for cells in the chamber, assuming that cells in the outlet are not growing. This gives:

$$P = \big(6\pi\eta\sigma/2\big)\big(N_c\sigma k\big)N_o/\sigma^2 \tag{S2.16}$$

$$= 3\pi k\eta N_o N_c \tag{S2.17}$$

Using $\eta = 10^{-3}$Pa s, $k \approx 0.4\text{h}^{-1} \approx 10^{-4}\text{s}^{-1}$, $N_c \approx 100$, and $N_o \approx 10$, we get

$$P = 3\pi k\eta N_o N_c \tag{S2.18}$$

$$= 3\pi \times 10^{-3}\text{Pa}s \times 10^{-4}s^{-1} \times 100 \times 10 \tag{S2.19}$$

$$= 1 \times 10^{-3}\text{Pa} \tag{S2.20}$$

Thus, viscous friction gives a negligible contribution to the pressure generated in the outlet, which is in the MPa range.

Conversely, we can use the above estimate to define an effective viscosity of the cell packing of 1 MPa s needed to achieve a pressure of 1 MPa. This effective viscosity is much larger than has been measured for mammalian cells[13].

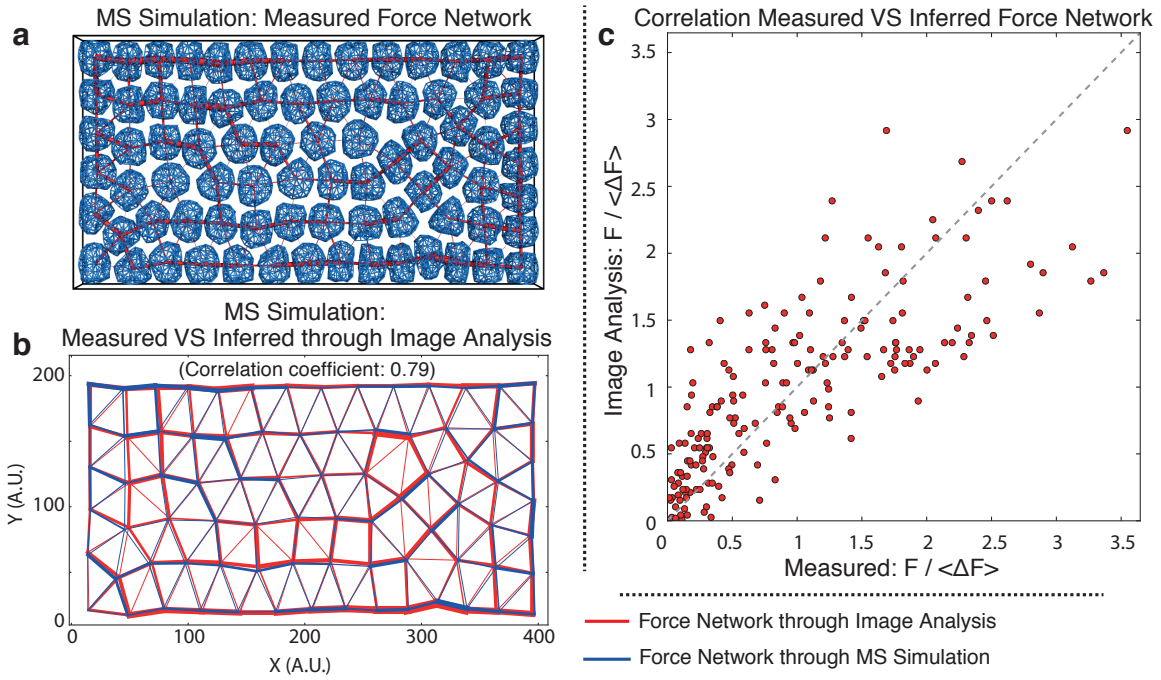

Figure S2.1: Testing our indirect force-inference method on simulated packings. In Chapter 2, we reported mechanical forces in packings of yeast cells that we have inferred from the observed cell shape deformations. Our force-inference method uses use a custom Matlab image analysis code to process the time-lapse movies that we obtained with the fluorescence exclusion method (Fig. S2.2). Each cell is identified with a watershed algorithm and manually refined if necessary. For each identified cell, the contour is defined as a set of spline functions. These splines are further used to calculate the length l of the contact line between each pair of cells. As a first order approximation, we estimate the contact area as $A \propto l^2$, and we assume that the contact force is proportional to the contact area $F \propto A$ (Appendix: See Inferring force maps). Here, we test our force-inference method on packing generated by our mass-spring simulation. To this end, we compare the inferred force network with the actual force network in the simulations. (**a**) 80 cells of the same size ($R_0 = 1.5\mu$m), turgor pressure ($\Pi = 1.0$ MPa), and E=100 MPa are randomly distributed and compressed in a slab geometry. The cells are depicted as a semi-transparent blue meshwork, confined by the rigid box. The contact forces are evaluated numerically and are represented as the red lines between neighbor cells. The thickness of the lines corresponds to the magnitude of the contact forces. (**b**) The final snapshot from the simulation is processed with the in-house Matlab code for image analysis, and contact forces have been inferred. The numerical (in blue) and image analysis (in red) force networks are superimposed on top of each other for visual comparison. The correlation coefficient calculated for these two sets of contact forces is 0.79. (**c**) Scatter plot of each contact force in **b**. Forces have been scaled by the average value. Measured are the forces obtained from the mass-spring simulations, and compared against the one obtained from the image analysis procedure.

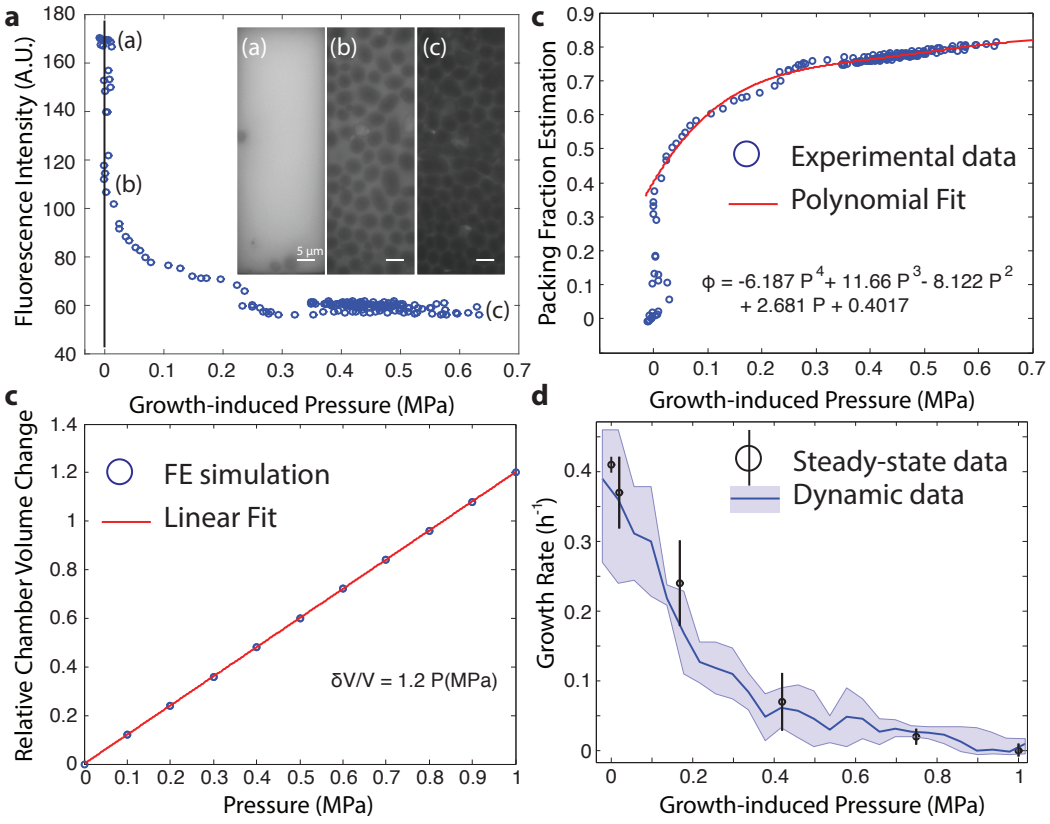

Figure S2.2: Inferring the instantaneous growth rate as a function of pressure using the pressure curve obtained from the self-closing valve. (**a**) A fluorescent dye, FITC-conjugated Dextran, added to the medium allows us to label the space between the cells. FITC-conjugated Dextran does not penetrate inside the cells, such that its fluorescence is excluded from a cell. As a consequence, as the cells are filling the chamber, the fluorescence intensity is, in first order, proportional to the void in between cells, like in the fluorescent exclusion method[14]. Denoting ϕ the packing fraction, and V the volume of the chamber, we assume that the intensity I of fluorophore is $I \propto (1-\phi)V$. (**b**) We use finite element simulations (Comsol) to estimate the change in volume of the growth chamber as a function of the pressure. We define the PDMS as a hyperelastic material as in[15], with an estimated Young's modulus E = 2MPa. We find that the change in volume is to good approximation linear in the pressure. (**c**) We use the excluded fluorescence, as well as the finite element simulation, to estimate the cell packing fraction, ϕ, as a function of the growth-induced pressure. We observe that the growth-induced pressure starts to rise in the chamber for a packing fraction of about 0.4. We fit the resulting relationship by a forth order polynomial function to obtain a continuously differentiable function. (**d**) We use the values extracted from b and c to calculate the instantaneous volumetric growth rate γ, using a quasi-steady state assumption as described in the Appendix (see Measuring the steady-state and instantaneous growth rate). The dark blue line corresponds to the values calculated from the mean pressure, and the envelope corresponds to the values calculated from the envelope of the pressure curve. Note that the inferred continuous relationship between growth rate and contact pressure is in good agreement with the steady-state data obtained independently, from outflow rates in our leaky devices (black points, mean $\pm$ standard deviation).

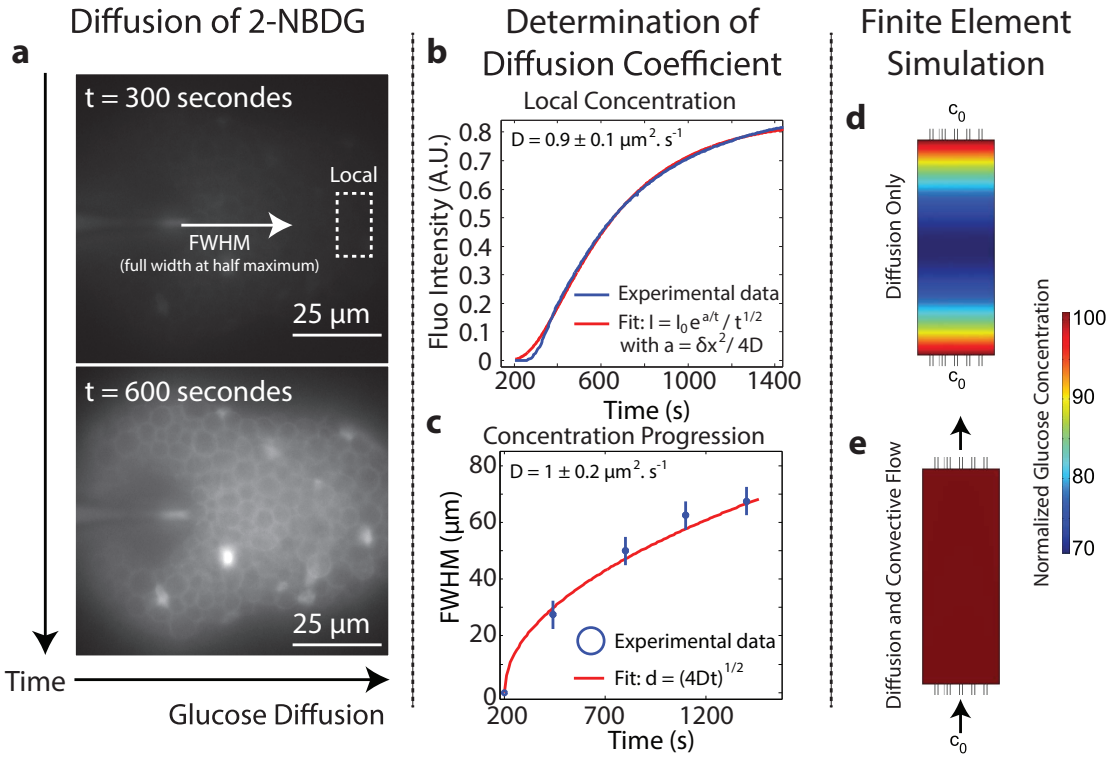

Figure S2.3: The reduction of growth rate is not due to glucose depletion in the growth chamber. To estimate whether glucose depletion could account for the observed reduction of growth rate, we assume that cells would locally consume glucose at the maximum rate. We consider two cases: either glucose merely diffuses inside the growth chamber, or it is also advected by the imposed nutrient flow. In both cases, we find that the reduction of glucose concentration in the chamber is not enough to stall cell growth. (**a**) We first measure the diffusion of 2-NDBG, a fluorescent glucose analog molecule. Here, we observe at the beginning of the experiment that there is almost no glucose in the self closing valve, and that it progressively diffuses in the chamber. Notice the foam-like packing of the cells, which results from the growth-induced pressure nearly balancing the turgor pressure. (**b - c**) We measure the diffusion constant of the glucose analog in 2 different ways. We measure either the local concentration at a fixed position in the chamber (**b**) or the full width at half maximum (FWHM) as a function of time (**c**, mean $\pm$ standard deviation). Fitting of a simple diffusion model agrees well with the experimental data, and enables us to extract values for the diffusion constant of the glucose analog (see figure). (**d - e**) The biomass yield of *S. cerevisiae* cells is 0.45 $\times$ $g_{cells}/g_{glucose}$ [16]. With a minimum doubling time of 2 hours, this yields a glucose consumption rate of 2.2×10^7 molecules/s. We simulate glucose consumption in the fully packed growth chamber using finite element simulations (Comsol) and the measured glucose diffusion constant extracted in **b** and **c**. We consider two cases: either there is only consumption and diffusion (**d**) or consumption, diffusion and convection (**e**). We find that in the case where there is only diffusion, the glucose concentration drops at about 70% of its boundary value c_0, which is about 14 g/L, and still above the concentration where depletion of glucose affects growth [17]. In a finite element simulation set-up where we impose a convective flow of 0.2 nL/s, we observe that there is no glucose gradient in the growth chamber. We conclude that the observed reduction of growth rate in figure 3c is not an effect of glucose depletion in the growth chamber.

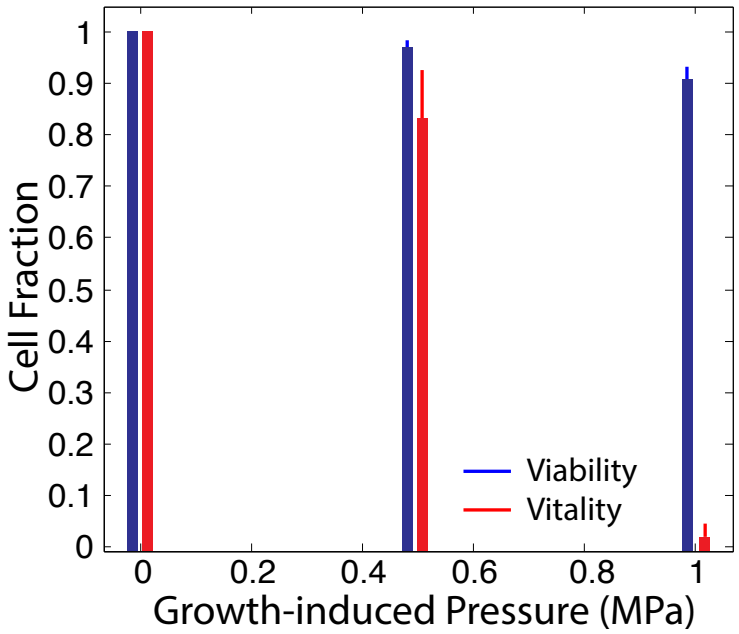

Figure S2.4: Measurement of cell viability and cell vitality. We assess how pressure changes cell viability and metabolic activity. Cell viability is assessed through a viability kit (LIVE/DEAD Yeast Viability Kit, Thermo Fisher Scientific). Briefly, propidium iodide (PI) is added to the culture medium. PI only enters the nucleus of dead cells and binds to DNA. We observe that, even at maximum pressure, most of the cells are alive (more than 90% of the cells). Cell vitality is assessed by adding a cell permeable esterase substrate (FungaLight Yeast CFDA, AM, Thermo Fisher Scientific) that is cleaved by esterases. The cleaved molecule becomes fluorescent, which enables one to assess esterase activity, which is directly linked to the global cell metabolic activity. We observe that, even though cell vitality does not change much at 0.5 MPa (the change is less than 15%), it is almost non existent at the maximum pressure of 1MPa. This suggests that, even though alive, cells are not metabolically active. This could be explained by pressure-induced molecular crowding, as in [18], where all processes in the cell are slowed down to the point of stalling by the very high compression. Note that at the highest pressure, we observe about 5% of the cells bursting. The data represent, for $N \geq 3$ independent replicates, the mean $\pm$ standard deviation.

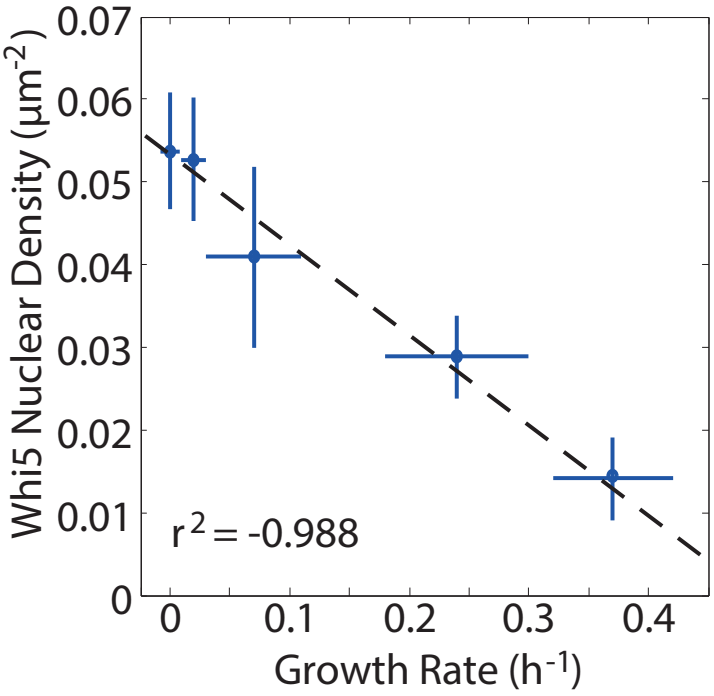

Figure S2.5: The density of nuclear Whi5 is anti-correlated with the growth rate. This plot shows the nuclear Whi5 density for different growth-induced pressures. The Whi5 density was obtained by measuring the number of cells with a nuclear Whi5 normalized by the observed area. Note that the nuclear density of Whi5 is increasing with decreasing growth rate, suggesting that growth rate reduction is accompanied with a cell cycle delay in the G1 phase of the cell cycle. Errors are mean $\pm$ standard deviation for $N \geq 5$ independent replicates.

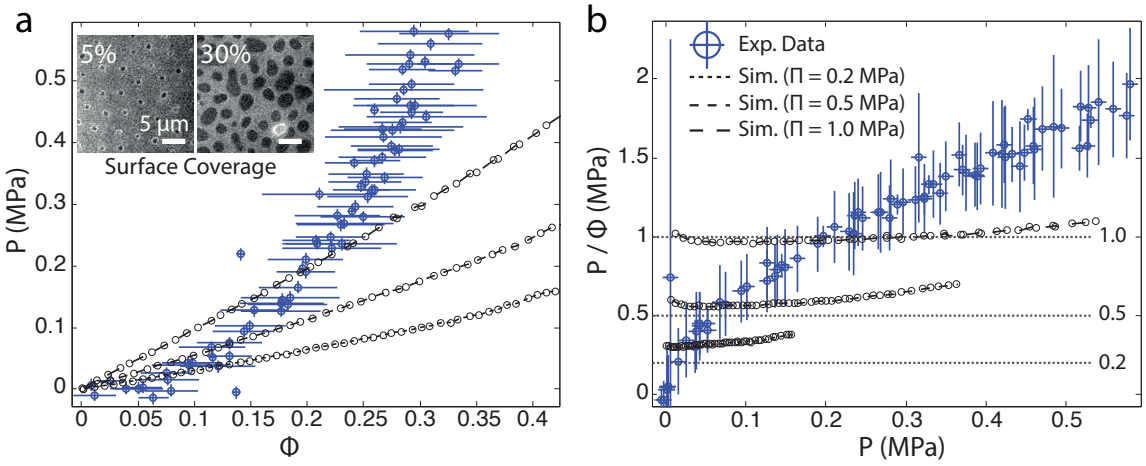

Figure S2.6: Relationship between fraction of surface covered and growth-induced pressure indicates turgor pressure adaptation. (a) The growth-induced pressure increases (circles) faster than linearly with the fraction of surface covered. Typical pictures obtained by reflectometry are presented in the inset for different values of surface coverage. The dashed lines are obtained from our mass-spring simulations, in which yeast cells are modeled as elastic shells subject to a *constant* turgor pressure. The simulations yield a growth-induced pressure that increases linearly with surface coverage. The slope is equal to the turgor pressure Π, for which we chose three different values. The discrepancy between data and simulations suggests that the turgor pressure increases with growth-induced pressure. (b) The growth-induced pressure divided by the fraction of covered surface corresponds to the pressure exerted in the contacts between cells and cover slip. Accordingly, the constant turgor pressure simulations of elastic shells yield nearly horizontal lines. The data, however, clearly shows that the pressure in the cell-coverslip contacts increase with the growth-induced pressure. This may indicate a gradual increase in turgor pressure. Error bars of the simulation data are smaller than the symbols. Error bars for the surface coverage are estimated as followed: We assume that we cannot measure the contact better than the diffraction limit. Hence, assuming a circular contact, we write that the radius of the contact has a typical error of $\pm\delta$, where δ is the radius of the Point Spread Function.

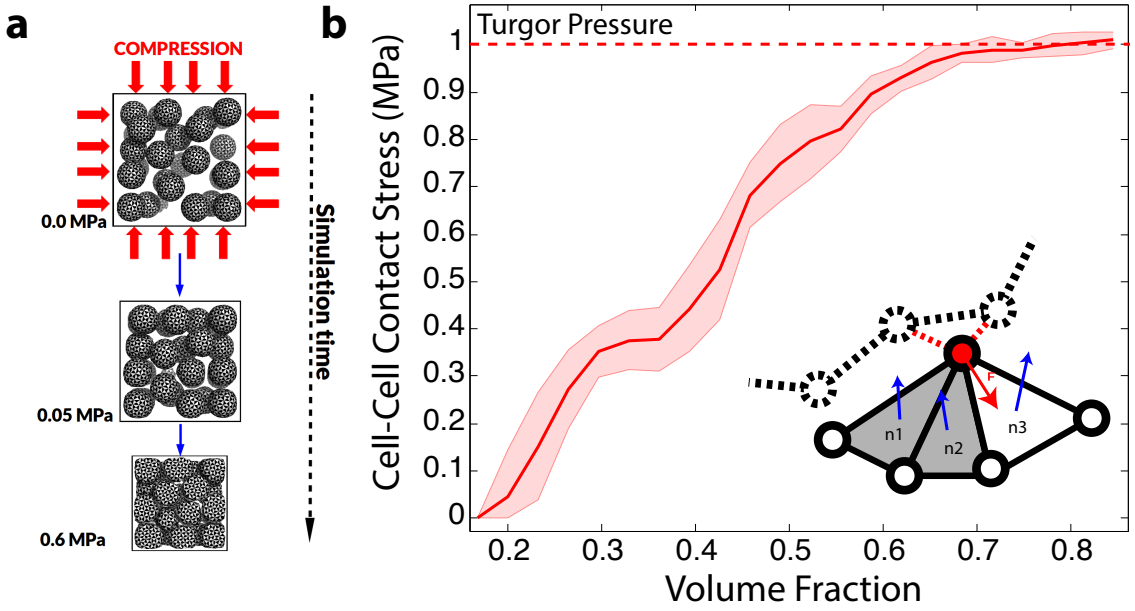

Figure S2.7: The average cell-cell contact stress approaches the cell turgor pressure under high compressive stress. We measure the cell-cell contact stress in mass-spring simulations, and find that for high compression / packing fraction, the stress approaches the internal cell turgor pressure. (**a**) Mass-spring simulations scheme. Identical cells are randomly distributed in a rigid box. The initial concentration is low so the cells do not touch one another. The simulation box is progressively compressed, hence increasing the packing fraction. (**b**) 50 identical cells ($R_0 = 2.5\mu$m, $\Pi = 1.0$ MPa, E = 150 MPa, t = 0.1μm) are compressed. For each pair of cells, the contact stress is calculated and the average contact stress is plotted (red line) versus the fraction of box volume occupied by cells. For high compression ($>$0.7) the value of the average contact stress saturates at the value equal to turgor pressure, 1 MPa. The envelope corresponds to $\pm$ standard deviation and is obtained out of 5 replicates simulations with different random initial cell positions and orientations. **Inset.** The contact stress is calculated as a ratio of the total normal force between two cells F_n and total contact area A_c. The contact area A_c on one cell is a sum of areas of all triangles being in contact with the other cell. A triangle is in contact with another cell if all its vertices are in contact with the neighbor cell (non-zero repulsive forces). The total normal force exerted on one cell is a sum of all normal forces exerted on each vertex by the neighbor cell. To calculate the normal force F (red arrow) acting on a vertex (black-red circle), first the sum of all non-bonded repulsive forces, F_{rep} (red dashed lines), is calculated. Next the normal component of this force is extracted as a dot product with all the triangles (described by the normal vectors n_i) being in contact with the neighboring cell (shaded triangles), $\mathrm{n}_i \cdot \mathrm{F}_{rep}$. In order to avoid double counting of the normal component of the force F_{rep}, each dot product with n_i (here i=1,2) is multiplied by the area of the triangle on which the force F_{rep} is acting, and divided by the total contact area (it is the sum of areas of shaded triangles $A = A_1 + A_2$).

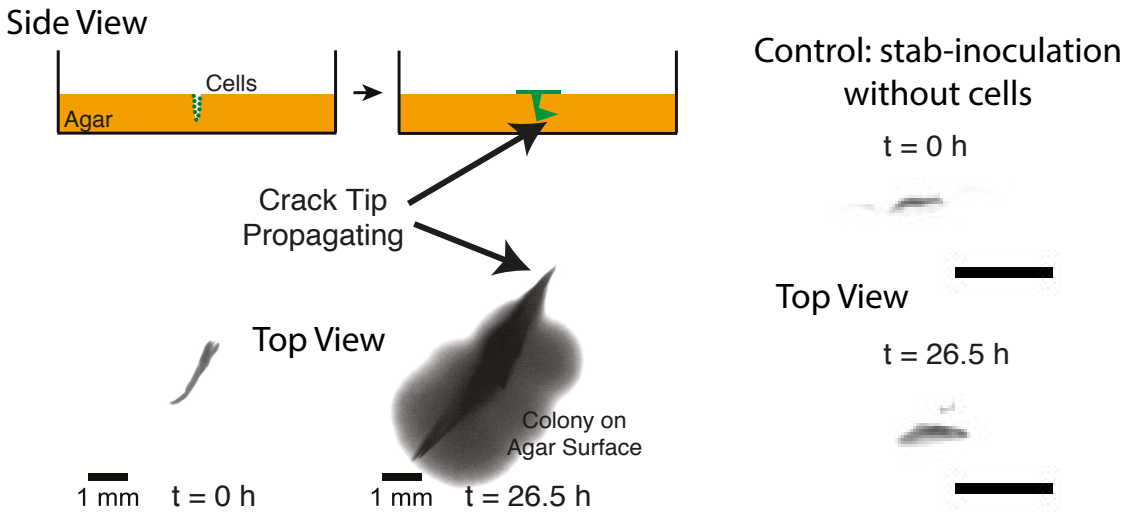

Figure S2.8: Self-driven jamming can propagate cracks in agar gels. We inoculate an agar gel (2%) by plunging in it a 0.45 mm diameter needle, which was first dipped in an overnight culture of budding yeast (strain S288C). The agar dish is then incubated at 30 degree Celsius under humidity control (to avoid drying). As the cartoon illustrates, cells flow out of the crack, and grow on the surface of the agar gel. The cells on top of the dish give rise to the large cloud on the lower image observed at 26.5 h, showing that the cells are not fully trapped in the crack. Nevertheless, the crack tips are propagating as a function of time, presumably due to jamming. As a control, we show images of cracks that were created by stabbing without cells and then incubated for the same amount of time. A time-lapse movie of the crack propagation is available `Movie S5`.

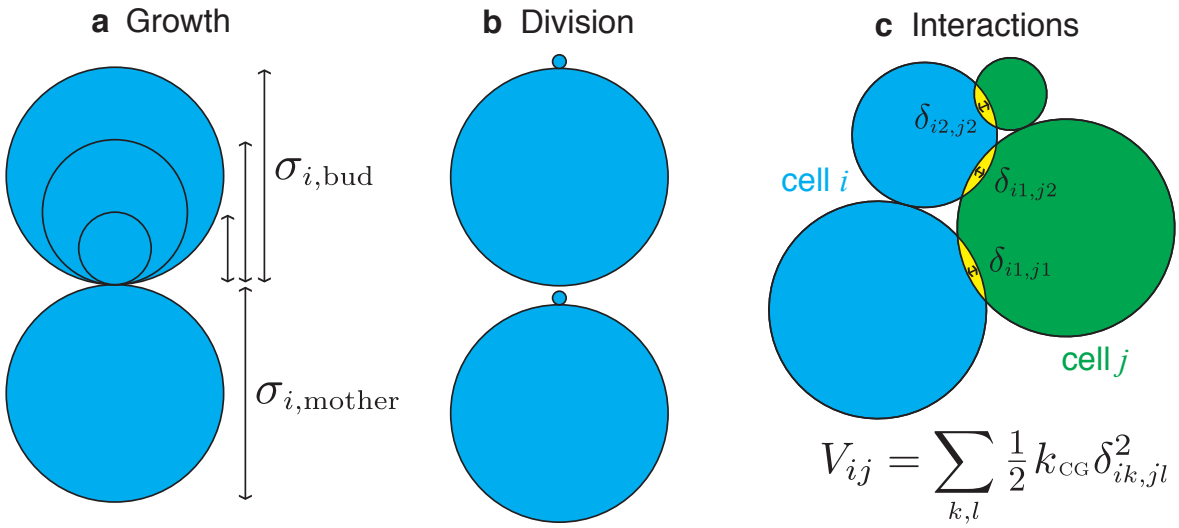

Figure S2.9: How cells grow in our coarse-grain simulation. Schematic of **a** the growth and **b** division processes and **c** inter-cell interactions in our coarse-grained simulations. Each cell is composed to two lobes, the mother and bud. **a** During growth, the mother lobe diameter of cell i stays fixed at $\sigma_{i,\mathrm{mother}} = \sigma$ while the bud grows from $\sigma_{i,\mathrm{bud}} = 0$ to $\sigma_{i,\mathrm{mother}} = \sigma$. **b** Once the bud reaches $\sigma_{i,\mathrm{mother}} = \sigma$, cell i divides into two new daughter cells that retain the orientation of their mother cell. **c** Cells i and j interact via only upon overlap via repulsive linear spring interactions with modulus k.

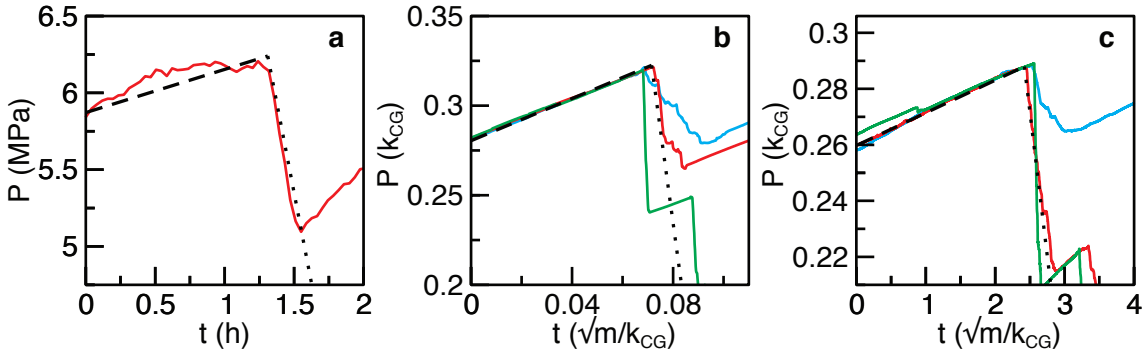

Figure S2.10: How we parameterize our coarse-grain simulation. We use the experimental pressure curves to parameterize our coarse-grain simulations: the pressure rise enables to parameterize the growth, and the pressure drop the damping rate. (**a**) Pressure as function of time during a single pressure drop for experiments. (**b**) Pressure as function of time during a single pressure drop for simulations without feedback. (**c**) Pressure as function of time during a single pressure drop for simulations with feedback ($P_0/k = 0.07$). The red line in **a** corresponds to experiments with an outlet gate with an angle of 135°. The red lines in **b** and **c** corresponds to simulations with best-fit values of μ (**b**: $\mu = 8 \times 10^4 \gamma\sqrt{mk_{\mathrm{CG}}}$ and **c**: $\mu = 2 \times 10^3 \gamma\sqrt{mk_{\mathrm{CG}}}$) used in Fig. 2b and Fig. 2c of the main text, the cyan line corresponds to larger values of μ (**b**: $\mu = 3.2 \times 10^5 \gamma\sqrt{mk_{\mathrm{CG}}}$ and **c**: $\mu = 8 \times 10^4 \gamma\sqrt{mk_{\mathrm{CG}}}$) and the green line corresponds to smaller values of μ (**b**: $\mu = 2 \times 10^4 \gamma\sqrt{mk_{\mathrm{CG}}}$ and **c**: $\mu = 5 \times 10^2 \gamma\sqrt{mk_{\mathrm{CG}}}$). For **a**, the dashed line shows the mean slope during pressure increase $\left(\dot{P}_{\uparrow}^{\mathrm{exp}}\right)$ and the dotted line shows mean slope during avalanche $\left(\dot{P}_{\downarrow}^{\mathrm{exp}}\right)$. For **b** and **c**, the dashed line is the mean slope during increase $\left(\dot{P}_{\uparrow}^{\mathrm{sim}}\right)$ and the dotted line shows the extracted value of $\dot{P}_{\downarrow}^{\mathrm{sim}}$ that yields the same ratio of $\dot{P}_{\downarrow}/\dot{P}_{\uparrow}$ as experiments.

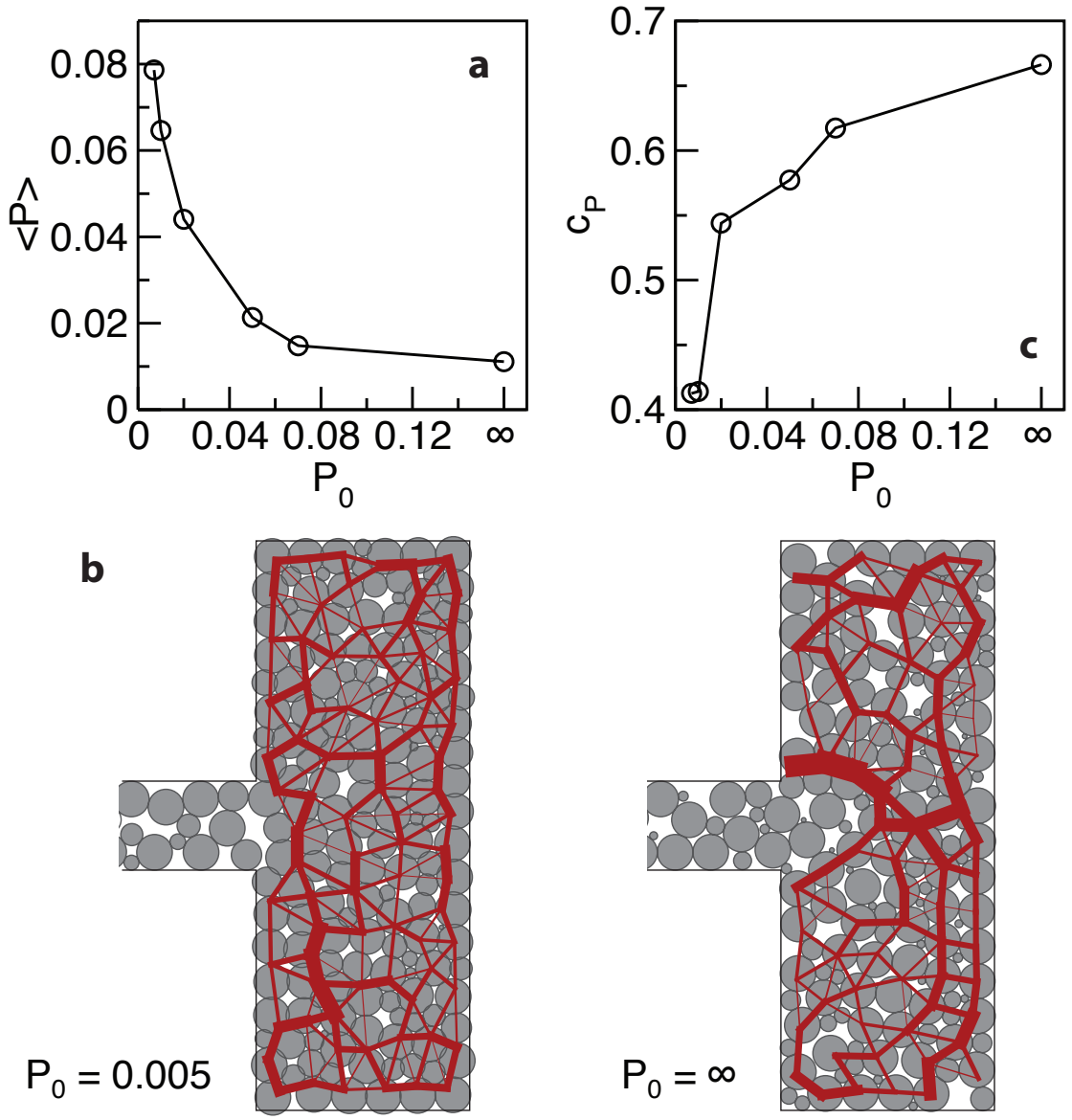

Figure S2.11: Effect of feedback on force networks in coarse-grained simulations. (**a**) In simulations where individual cell growth rates (k_i) decrease exponentially with pressure (P_i), $k_i \propto e^{-P_i/P_0}$, we observe that the time-averaged steady-state population pressure $\langle P \rangle$ increases as the feedback becomes stronger (P_0 decreases). $\langle P \rangle$ increases with decreasing P_0 because cell growth slows for $\langle P \rangle > P_0$, causing the population to spend more time at larger pressures. (**b**) Furthermore, feedback homogenizes force networks as illustrated by representative configurations without feedback and a heterogeneous force network ($P_0 = \infty$) and with strong feedback and a homogeneous force network ($P_0 = 0.005$). The reason for this homogenization is that low-pressure cells grow more quickly than high-pressure cells and fill in gaps in the force network. (**c**). We see that force-network homogenization is a strong effect - the coefficient of variation of individual cell pressures $c_P = \sqrt{\langle P^2 \rangle / \langle P \rangle^2 - 1}$ decreases by 40% with decreasing P_0

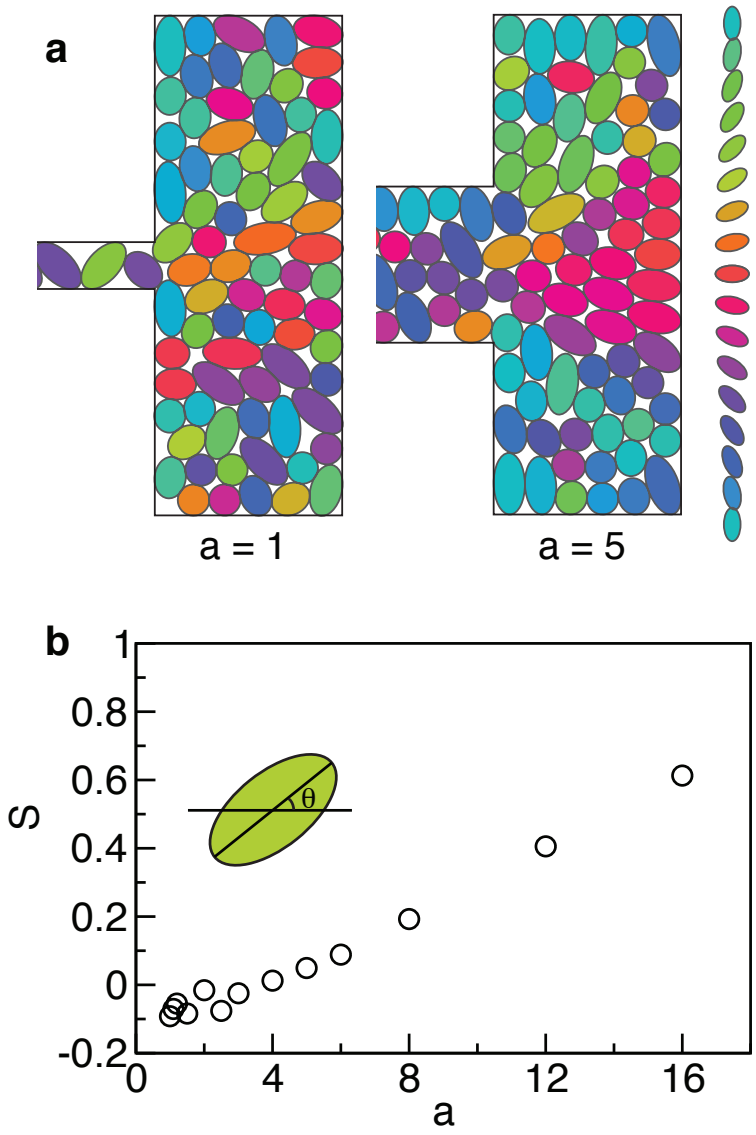

Figure S2.12: Orientational alignment in coarse-grained simulations of elongated cells. Simulations of proliferating ellipsoidal cells show that cells orientationally align in the direction of the outlet. (**a**) This alignment is stronger for wider outlet channels, illustrated for outlets channel widths of $a = 1$ which has very little alignment and $a = 5\sigma$ which has significant alignment. (**b**) We can quantify the degree of alignment via a nematic order parameter $S = \langle cos(2\theta) \rangle$, which measures the mean alignment of cells with the horizontal axis. S shows that orientations are disordered for $a < 4$ and become increasingly aligned with the horizontal axis as a increases.

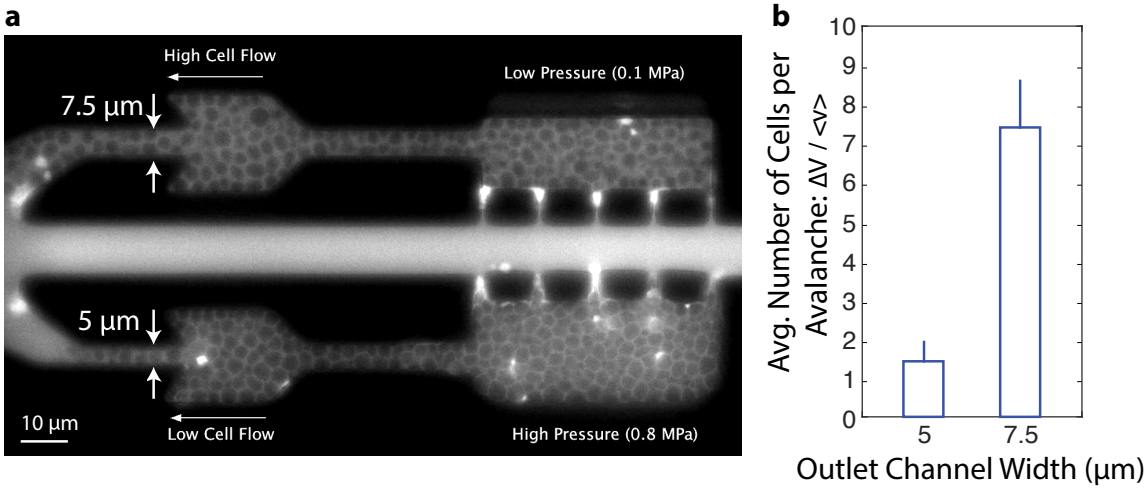

Figure S2.13: Effect of outlet channel width on mean avalanche size. We analyzed the movie (**Movie S2**), which was also referenced in the main text for a direct comparison of growth under different contact pressures. (**a**) Snapshot of the time-lapse movie, showing the two filled growth chambers connected in the same way to a single nutrient channel. The outlets of both chambers are connected to an outlet gate with an angle of 135^o, but the outlets have a different channel width, of 5μm and 7.5μm. We observe in this movie that the cells coming out of the outlet with a channel width of 7.5μm develop less pressure than the cells in the 5μm outlet channel width, and exhibit more avalanche events. (**b**) We measure for each avalanche, defined as the duration from when cells start to move until the next moment of stasis, the displacement l of the cell population in the channel. We then calculate the mean cell volume displacement, $\Delta V = l \times A$, where A is the cross-section of the outlet channel. An estimate of the average number of cells per avalanche is then obtained by dividing ΔV by a typical cell volume of $< v >$ = 65.5 fL. This volume corresponds to a mean cell diameter of 5μm. We note that the average size of an avalanche increases with increased outlet channel width (mean $\pm$ standard deviation for $N \geq 10$ avalanches).

References

[1] R. Preston, R. Murphy, and E. Jones. Apparent endocytosis of fluorescein isothiocyanate-conjugated dextran by saccharomyces cerevisiae reflects uptake of low molecular weight impurities, not dextran. *The Journal of Cell Biology*, 105(5):1981–1987, 1987. doi: 10.1083/jcb.105.5.1981.

[2] I. Martinez de Maranon, P. Maréchal, and P. Gervais. Passive response of saccharomyces cerevisiae to osmotic shift: cell volume variations depending on the physiological state. *Biochemical and Biophysical Research Communications*, 227:519–523, 1996.

[3] J. Stenson, C. Thomas, and P. Hartley. Modelling the mechanical properties of yeast cells. *Chemical Engineering Science*, 64:1892–1903, 2009.

[4] J. Stenson, P. Hartley, C. Wang, and C. Thomas. Determining the mechanical properties of yeast cell walls. *Biotechnology Progress*, 27:505–12, 2011.

[5] W.-H. Yang and W. Feng. On the contact problem of an inflated spherical nonlinear membrane. *Journal of Applied Mechanics*, 40:209–214, 1973.

[6] A. Smith, Z. Zhang, C. Thomas, K. Moxham, and A. Middelberg. The mechanical properties of saccharomyces cerevisiae. *Proceedings of the National Academy of Sciences of the United States of America*, 97(18):9871–9874, 2000.

[7] M. Kot, H. Nagahashi, and P. Szymczak. Elastic moduli of simple mass spring models. *The Visual Computer*, 31:1339–1350, 2015.

[8] C. F. Schreck, N. Xu, and C. S. O'Hern. A comparison of jamming behavior in systems composed of dimer-and ellipse-shaped particles. *Soft Matter*, 6(13):2960–2969, 2010.

[9] F. D. C. Farrell, O. Hallatschek, D. Marenduzzo, and B. Waclaw. Mechanically driven growth of quasi-two-dimensional microbial colonies. *Physical Review Letters*, 111:168101, Oct 2013. doi: 10.1103/PhysRevLett.111.168101.

[10] D. Volfson, S. Cookson, J. Hasty, and L. S. Tsimring. Biomechanical ordering of dense cell populations. *Proceedings of the National Academy of Sciences of the United States of America*, 105(40):15346–15351, 2008. doi: 10.1073/pnas.0706805105.

[11] E. Irani, P. Chaudhuri, and C. Heussinger. Impact of attractive interactions on the rheology of dense athermal particles. *Physical Review Letters*, 112:188303, May 2014. doi: 10.1103/PhysRevLett.112.188303.

[12] G. Lois, J. Blawzdziewicz, and C. S. O'Hern. Jamming transition and new percolation universality classes in particulate systems with attraction. *Physical Review Letters*, 100:028001, Jan 2008. doi: 10.1103/PhysRevLett.100.028001.

[13] K. Guevorkian, M.-J. Colbert, M. Durth, S. Dufour, and F. m. c. Brochard-Wyart. Aspiration of biological viscoelastic drops. *Physical Review Letters*, 104:218101, May 2010. doi: 10.1103/PhysRevLett.104.218101.

[14] C. Bottier, C. Gabella, B. Vianay, S. I. Buscemi, L., J. Meister, and A. Verkhovsky. Dynamic measurement of the height and volume of migrating cells by novel fluorescence microscopy technique. *Lab Chip*, 11:3855–3863, 2011.

[15] B. Hardy, K. Uechi, J. Zhen, and H. Kavehpour. The deformation of flexible pdms microchannels under a pressure driven flow. *Lab Chip*, 9:935–938, 2009.

[16] N. Ertugay, H. Hamaci, and A. Bayindirli. Fed-batch cultivation of bakers yeast: effect of nutrient depletion and heat stress on cell composition. *Folia microbiologica*, 42:214–218, 1997.

[17] H. Youk and A. van Oudenaarden. Growth landscape formed by perception and import of glucose in yeast. *Nature*, 462:875–879, 2009.

[18] P. Hersen, M. McClean, L. Mahadevan, and S. Ramanathan. Signal processing by the hog map kinase pathway. *Proceedings of the National Academy of Sciences of the United States of America*, 105(20):7165–7170, 2008. doi: 10.1073/pnas.0710770105.

3
Jamming by Growth

3.1 Introduction

Granular materials undergo a jamming transition upon compression, at which point the entire system becomes rigid so that further compaction is not possible without pressure build-up[1,2]. Packings obtained in this manner are spatially-disordered similar to liquids but, like solids, do not yield (irreversibly deform) upon application of an external stress[3]. The transition occurs at a well-defined density $\phi = \phi_J$[2], at which the system is marginally stable (*i.e.* removing a single contact causes the system to lose mechanical rigidity)[4]. Compression beyond the jamming point ($\phi > \phi_J$) rigidifies packings, resulting in mechanical properties that exhibit nontrivial power law scalings as a function of $\delta\phi = \phi - \phi_J$[2,4–8]. It has been recently demonstrated that confined microbial populations can similarly drive themselves into a rigid state via cellular growth and division[9]. Cellular populations fundamentally differ from inert granular media in that, whereas granular systems are static unless driven externally[10–15], cellular populations are active systems that are driven internally as cells consume energy from their environments in order to move or grow[9,16–21]. Growth-driven jamming also differs from the recently studied motility-driven jamming transition[18,22], where the system is kept at constant density and is driven by innate cell motility rather than cellular growth. In the case of growth-driven jamming, it is an open question if the cellular packings have the same universal physical properties as conventional granular materials[2,7]. In particular, experiments have shown that cell-cell forces slow down cell growth[9], but it remains unknown whether this mechanical feedback at the single-cell level has consequences for population-level mechanical properties. In this work, we show that budding cells can control the mechanical properties of densely-packed populations by leveraging their shape and the coupling between cellular growth rate and cell-cell forces[9,23].

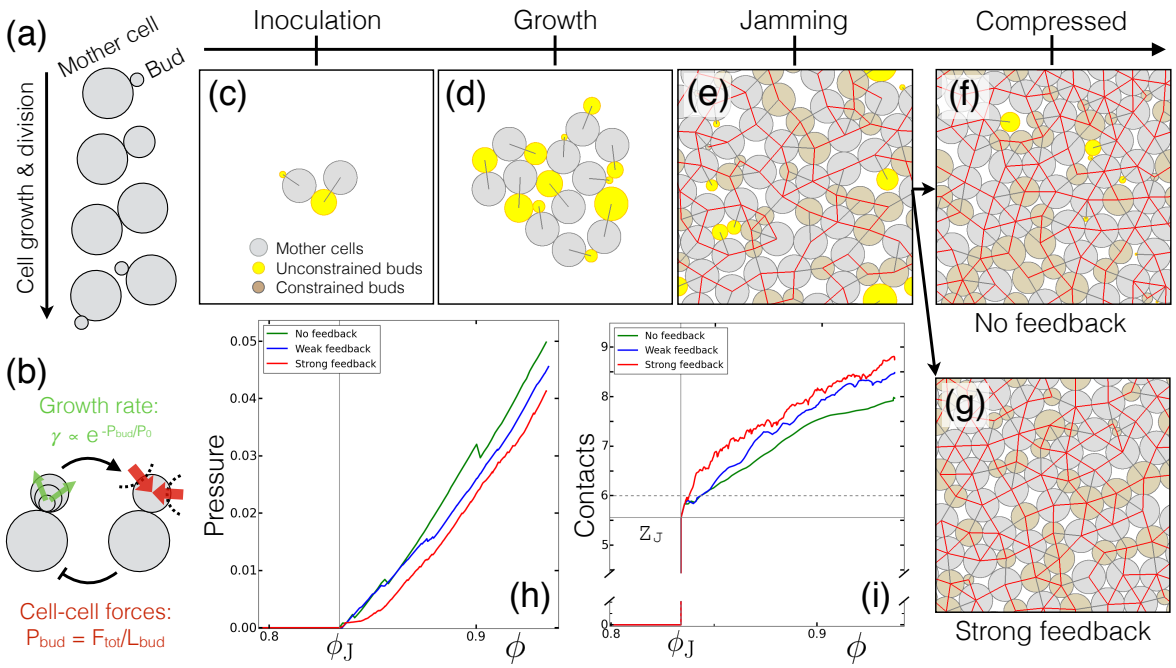

Figure 3.1: (a) Schematic of the growth and division process. Each cell grows by bud expansion. Budding culminates via mother-daughter separation when the daughter reaches the size of a mother cell. (b) Schematic of feedback of cell-cell contact forces onto cell growth. Daughter buds contact their neighbors as they grow (dashed black lines). The associated contact forces generate pressure on the growing bud, defined here as the ratio of total force F_{tot} to the perimeter L_{bud} of the daughter bud (Section 3.4.1): $P_{\text{bud}} = F_{\text{tot}}/L_{\text{bud}}$. This pressure in turn slows its growth as $\gamma \propto e^{-P_{\text{bud}}/P_0}$. (c-g) Snapshots from a typical simulation. (c) Each simulation is inoculated with two cells. (d) Cell growth drives the population to expand outward. During expansion, cells interact with their neighbors via repulsive elastic forces and completely overdamped dynamics. (e) The population undergoes a "jamming transition" at $\phi_J = 0.84$, at which point a system-spanning network of force-bearing intercellular contacts develops (red lines). At jamming, most mother (gray) and daughter (brown) buds are constrained by their neighbors, but $\approx 25\%$ of buds (yellow) are unconstrained (see SI). Above jamming, populations have fewer unconstrained buds when (f) mechanical pressure feeds back onto cell growth ($P_0 = 0.001$) than when (g) cellular growth rates are independent of mechanical pressure (both f and g are at $\phi = 0.89$). (h) The pressure that the entire population exerts on its surroundings P (Section 3.4.3) is zero below jamming ($\phi < \phi_J$) and increases as the cells grow above jamming ($\phi > \phi_J$). With no feedback and weak feedback ($P_0 = 0.005$), P is almost linear in ϕ. For strong feedback ($P_0 = 0.001$), P increases more slowly with ϕ. All pressures are measured in units of the cell-cell modulus k (Section 3.4.1). (i) The number of contacts Z per cell jumps discontinuously from $Z \approx 0$ to $Z = Z_J \approx 5.5$ at jamming at ϕ_J, and increases more quickly for strong feedback than for weak or no feedback. (c)-(g) uses box size $L = 7\sigma$ and (h), (i) use box size $L = 15\sigma$ where σ is a cell diameter. (h) and (i) show data for one typical population.

3.2 Results

We perform 2D numerical simulations of budding yeast populations growing in space-limited environments. Each cell is represented as conjoined mother and daughter lobes that reproduce asexually via expansion of the daughter "bud" (Fig. 3.1a), a modeling approach first developed in[9] alongside microfluidic experiments. In this mode of proliferation, bud expansion progresses until the bud reaches the size of a mother cell, at which point the bud detaches and mother and bud form two new cells. To capture the experimentally-measured diminished growth rate under compressive mechanical stress[9], each cell in our model grows at a rate that decreases exponentially with the pressure exerted on its daughter bud: $\gamma \propto e^{-P_{\text{bud}}/P_0}$ (Fig. 3.1b). The feedback pressure P_0 controls the strength of feedback, with smaller values of P_0 corresponding to "stronger" feedback.

As cells proliferate, repulsive elastic forces between cells (Section 3.4.1, Fig. S3.1) push the population to expand outward via completely over-damped dynamics (Fig. 3.1c-g). In the absence of external confinement (Fig. 3.1c,d), the population remains at zero pressure with no force-bearing contacts between cells. However once the population fills the environment in which it resides, it is driven through a jamming transition (Fig. 3.1e) at volume fraction $\phi_J \approx 0.84$ that is characterized by a sudden increase in the population pressure P (Fig. 3.1h) and a discontinuous jump in the number of contacts Z (Fig. 3.1i). While mechanical feedback does not affect packings below jamming, feedback strength P_0 determines how pressure and contacts build up beyond jamming. To understand how mechanical rigidity emerges beyond jamming we first investigate mechanisms underlying the creation of cell-cell contacts, since contacts are know to control the mechanical properties of non-living granular media[2,7,24].

At the jamming point, the average number of contacts per cell jumps from $Z = 0$ to $Z = Z_J \approx 5.5$ (Fig. 3.1i), a result that is independent of P_0. The value $Z_J \approx 5.5$ is smaller than the naive *isostatic* expectation $Z_{\text{iso}}^{\text{naive}} = 6$, predicted by the Maxwell criterion by equating the number of constraints per cell ($Z_{\text{iso}}^{\text{naive}}/2$) to the number of degrees of freedom per cell (3)[25]. This deviation from naive isostaticity results from the presence of numerous cells whose buds are not in contact with their neighbors (depicted in yellow in Fig. 3.1e). Cells with "unconstrained" buds are free to rotate about their mother, and therefore correspond to degrees of freedom that are not constrained by cell-cell contacts. By subtracting the number of unconstrained buds per cell f_u from the number cellular degrees of freedom, we can derive a modified isostatic criterion $Z_{\text{iso}} = 6 - 2f_u$ (Section 3.4.5) that is satisfied by nearly all simulated populations (Fig. S3.2).

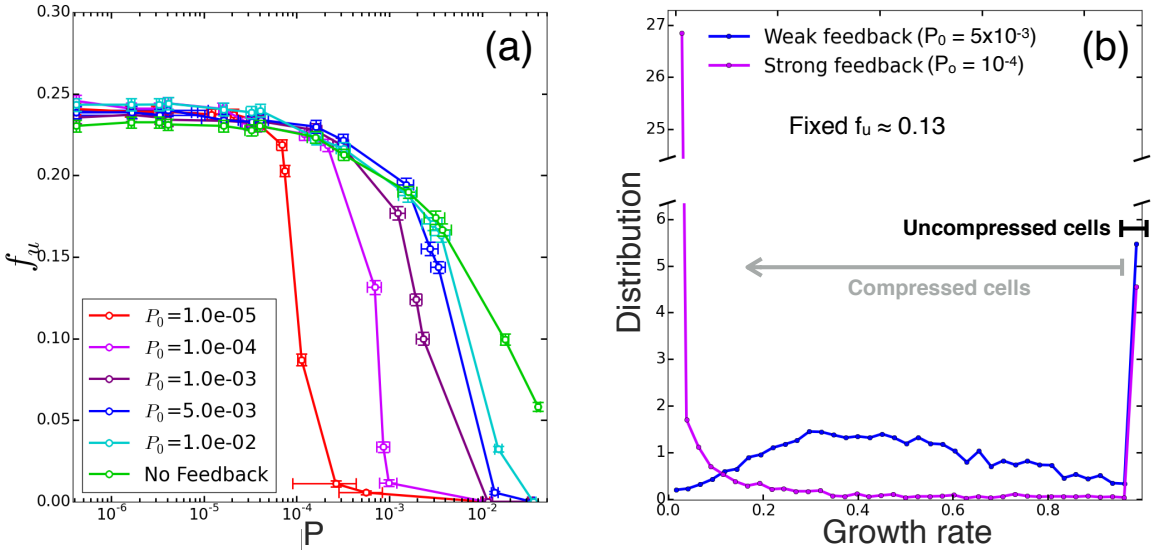

Figure 3.2: (a) Fraction of unconstrained buds f_u as a function of the population pressure generated by growing budding yeast packings above the jamming point. Numerical data is shown for populations with no feedback (bright green line), weak feedback (cyan, blue, purple lines), and strong feedback (magenta and red lines). Populations without feedback have a finite number of unconstrained buds up to $P_{\text{max}} \approx 0.1$ which corresponds to $\phi \approx 1$ (Fig. 3.1h). (b) Distribution of cell growth rates for microbial populations with weak ($P_0 = 5 \times 10^{-3}$) and strong ($P_0 = 10^{-4}$) feedback. In order to measure growth rates as unconstrained buds make contact, both populations have a value of f_u that is $\approx 50\%$ of that measured at jamming ($f_u \approx 0.13$). These values of f_u correspond to $P/P_{\text{max}} \approx 0.12$ ($P/P_{\text{max}} \approx 0.028$) for weak (strong) feedback. The black bar denotes cells under no or very little pressure, thus growing as they would in the absence of feedback. The gray bar denotes cells whose growth rates are reduced by pressure. The growth rate $\gamma(i)$ of each cell is normalized by γ_i^0, the growth rate that a cell would have without feedback (Section 3.4.1). Simulations have box size $L = 15\sigma$. Each data point is averaged over 100 independent inoculations.

We find that a substantial fraction of cells ($f_u \approx 25\%$) have unconstrained buds, which manifests in a strong departure (Fig. S3.2) from naive isostaticity ($Z_{\text{iso}}^{\text{naive}} - Z_J \approx 0.5$). The relationship between unconstrained buds and contacts is also observed in non-growing systems. Packings of asymmetric dumbbell-shaped particles that resemble budding cells yield similar results ($f_u \gtrsim 10\%$ and $Z_{\text{iso}}^{\text{naive}} - Z_J \gtrsim 0.2$)[26], whereas packings of symmetric dumbbells with equal-sized lobes have many fewer unconstrained buds ($f_u \lesssim 2\%$) and are therefore much closer to isostacity ($Z_{\text{iso}}^{\text{naive}} - Z_J \lesssim 0.04$)[27].

As cells grow beyond the jamming point ($\phi > \phi_J$), the population pressure P builds (Fig. 3.1h) and unconstrained buds begin to make contact with their neighbors (Fig. 3.1f,g and Fig. 3.2a). This

increase in population pressure, corresponding to comparable pressure on individual cells $\langle P_{\text{bud}} \rangle \approx P$, triggers mechanical feedback and slows the growth of cells as $P \gtrsim P_0$ (Fig. 3.1b). We observe two distinct behaviors for "strong" ($P_0/P_{\text{max}} \lesssim 0.05$) and "weak" ($P_0/P_{\text{max}} \gtrsim 0.05$) feedback, where $P_{\text{max}} \approx 0.1$ is the pressure felt by populations near confluency $\phi \approx 1$ (see Section 3.4.4 for relation of ϕ and P_{max}). For weak feedback, cell growth rates are not strongly reduced as unconstrained buds make contact with their neighbors (Fig. 3.2b). On the other hand, strong feedback slows the growth of compressed buds by such an extent that it creates two distinct subpopulations: compressed buds that are effectively stalled in their cell cycle and unconstrained (and therefore uncompressed) buds that are actively growing. The threshold between strong and weak feedback corresponds to the pressure ($P/P_{\text{max}} \approx 0.05$) at which the majority of previously unconstrained buds contact their neighbors in the absence of feedback (Fig. 3.2a). Therefore, in contrast to weak feedback where cells are driven into contact by nearly uniform population growth, strong feedback directs growth toward unconstrained buds. This directed drives unconstrained buds to make more contacts under strong feedback (Fig. 3.1f) than in the absence of feedback (Fig. 3.1g), enhancing the number contacts created per added volume fraction (Fig. 3.1i). Correspondingly, the preferential growth of unconstrained buds reduces the amount of pressure build-up near jamming (Fig. 3.1h) because unconstrained buds have free space to grow without incurring cell-cell forces.

By simultaneously driving pressures down and contacts numbers up, strong feedback enables populations to create additional contacts with very little associated pressure build-up compared to growth without feedback (Fig. 3.3a). In the absence of feedback, the excess number of contacts increases roughly as $\Delta Z = Z - Z_J \propto P^{1/2}$, as expected from studies on jamming in non-living systems[2,27]. However, populations growing under strong feedback exhibit abrupt departures from this expectation (Fig. 3.3a) at pressures that vanish for increasing feedback strength ($P \propto P_0$). For strong feedback, additional contacts are generated rapidly as a function of P until all unconstrained buds make contact with their neighbors (Fig. 3.2a), at which point $\Delta Z_{\text{u}} \approx 1$ (Fig 3.3b, see Section 3.4.6 for derivation of Z_u). This excess of contacts is pushed to lower pressures as P_0 decreases, so for $P_0 = 0$ we expect cell packings to have more contacts than required for mechanical stability even at $P = 0$ (i.e., *hyperstaticity*).

How do excess contacts impact the mechanical properties of populations growing under strong feedback? Since prior studies have found that contacts generated by external compression increase the rigidity of granular packings[2], we hypothesize that contacts generated via bud growth likewise rigidify cell packings. To test this hypothesis, we first measure resistance to external compression

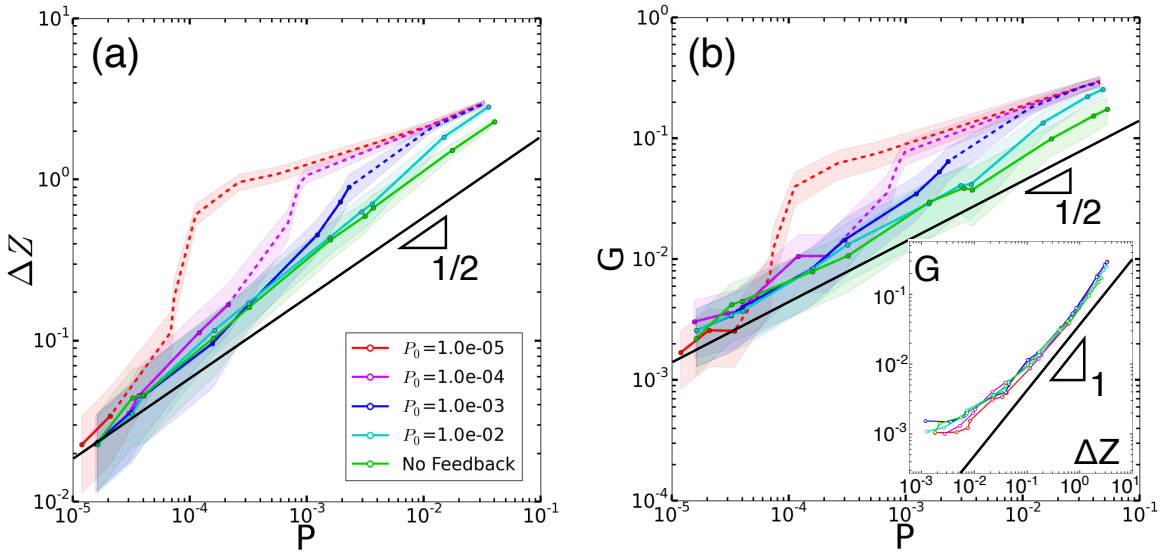

Figure 3.3: (a) Excess number of contacts (Z) beyond that measured at jamming (Z_J), $\Delta Z = Z - Z_J$. Colored lines correspond to growth under a range of feedback values and shaded regions represent one standard deviation. To show where growth has been appreciably slowed by cell-cell forces, dashed colored lines correspond to populations whose average cell growth rate is reduced by a factor of 10 compared to growth without feedback (Fig. S3.5). Solid colored lines correspond to growth rates within a factor of 10 of those without feedback. The dotted black line shows the number of contact resulting from unconstrained bud contacts $\Delta Z_u = 4f_u \approx 1$ (Section 3.4.6). (b) Shear modulus G for cell packings. Inset: Shear modulus in terms of excess contact number ΔZ. Line-types in (b) are the same as shown in (a). Black lines for each panel show known results for disk packings $G \propto \Delta Z \propto P^{1/2}$[2]. Simulations have box size $L = 15\sigma$. Each data point is averaged over 100 independent inoculations.

as quantified by the bulk modulus $B = \phi_e dP/d\phi_e$, where the increase in volume fraction ϕ_e is caused compaction rather than cell growth. We find that B increases with feedback strength (Fig. S3.3), a direct consequence of the formation of the additional contacts (Fig. S3.4). In contrast to the increase in B ($dP/d\phi_e$ increases with P_0), pressure increases more slowly as volume fraction is added via cellular growth ($dP/d\phi$ decreases with P_0 in Fig. 3.1h). Mechanical feedback therefore allows cell populations to disentangle their mechanical response to internal perturbations (cell growth) from their response to external perturbations (external compression).

While the generation of excess contacts only slightly modifies the bulk modulus (B increases by $\lesssim 20\%$), we expect these contacts to substantially impact the shear modulus since non-living packings are known to be fragile with respect to shear[2,24,28]. By measuring the shear stress Σ_{xy} generated under simple shear strain γ_{xy} (Section 3.4.3), we find that the shear modulus $G = d\Sigma_{xy}/d\gamma_{xy}$

scales with pressure as $G \propto P^{1/2}$ in the absence of feedback but increases sharply for strong feedback (Fig 3.3b) as unconstrained buds make contact (Fig 3.2a). The sharp increase in G is indeed controlled by contacts made by unconstrained buds, as we find a one-to-one relationship between contact number and shear modulus (Fig 3.3b inset). The stabilizing role of the added contacts can be understood from constraint counting: both Z and Z_{iso} increase as unconstrained buds make contact, but Z increases faster than Z_{iso} so that packings are pushed above isostaticity as cells grow (Section 3.4.6). The result $G \propto P^{1/2}$ for growth without feedback, also observed for non-living packings[2,27], suggests that populations near jamming fragile with respect to shear and therefore susceptible to fluidization under thermal excitation[28] or cell motility[22]. Populations growing under strong feedback, on the other hand, are stabilized by excess contacts even at very small pressure. Therefore, in contrast to populations without feedback and non-living packings where rigidity comes at a cost of increased cell-cell forces, cell populations growing under strong feedback can rigidify themselves with minimal associated pressure.

3.3 Conclusions

We have shown that budding cell populations undergo a growth-driven jamming transition that has mechanical properties not observed in the jamming of non-living systems. Populations growing under mechanical feedback develop a greater number of cell-cell contacts. These contacts are force-bearing and increase the population's resistance to shear and compressive stresses by an amount expected from studies on non-living granular materials[2]. As the population grows, this creation of excess intercellular contacts is not accompanied by a faster buildup of the internal pressure in contrast to the anticipated behavior of ordinary granular materials. Thus, the aforementioned feedback mechanism is a simple and efficient mean for expanding microbial populations to increase their resistance to mechanical stress without building up growth-limiting compressive mechanical forces. This mechanism may have important biological consequences for growing microbial populations, such as the increased resistance to mechanical stress may prevent unwanted fluidization that can be caused by processes such as division and apoptosis[29–31,31,32] or cell motility[17,22].

References

[1] C. S. O'Hern, S. A. Langer, A. J. Liu, and S. R. Nagel. Random packings of frictionless particles. *Physical Review Letters*, 88:075507, Jan 2002. doi: 10.1103/PhysRevLett.88.075507.

[2] C. O'Hern, L. Silbert, A. Liu, and S. Nagel. Jamming at zero temperature and zero applied stress: The epitome of disorder. *Physical Review E*, 68:011306, 2003.

[3] A. J. Liu and S. R. Nagel. Nonlinear dynamics: Jamming is not just cool any more. *Nature*, 396(6706):21–22, 1998.

[4] M. Wyart, S. R. Nagel, and T. A. Witten. Geometric origin of excess low-frequency vibrational modes in weakly connected amorphous solids. *Europhysics Letters*, 72(3):486, 2005.

[5] L. E. Silbert, A. J. Liu, and S. R. Nagel. Vibrations and diverging length scales near the unjamming transition. *Physical Review Letters*, 95:098301, Aug 2005. doi: 10.1103/PhysRevLett.95.098301.

[6] L. E. Silbert, A. J. Liu, and S. R. Nagel. Structural signatures of the unjamming transition at zero temperature. *Physical Review E*, 73:041304, Apr 2006. doi: 10.1103/PhysRevE.73.041304.

[7] M. Wyart. On the rigidity of amorphous solids. *Annales de Physique*, 30:1–96, 2005.

[8] W. G. Ellenbroek, E. Somfai, M. van Hecke, and W. van Saarloos. Critical scaling in linear response of frictionless granular packings near jamming. *Physical Review Letters*, 97:258001, Dec 2006. doi: 10.1103/PhysRevLett.97.258001.

[9] M. Delarue, J. Hartung, C. Schreck, P. Gniewek, L. Hu, S. Herminghaus, and O. Hallatschek. Self-driven jamming in growing microbial populations. *Nature Physics*, 12(8):762, 2016.

[10] T. S. Majmudar and R. P. Behringer. Contact force measurements and stress-induced anisotropy in granular materials. *Nature*, 435(7045):1079, 2005.

[11] D. Bi, J. Zhang, B. Chakraborty, and R. P. Behringer. Jamming by shear. *Nature*, 480(7377): 355, 2011.

[12] C. Heussinger and J.-L. Barrat. Jamming transition as probed by quasistatic shear flow. *Physical Review Letters*, 102:218303, 2009.

[13] S. Dagois-Bohy, B. Tighe, J. Simon, S. Henkes, and M. van Hecke. Soft-sphere packings at finite pressure but unstable to shear. *Physical Review Letters*, 109:095703, Aug 2012. doi: 10.1103/PhysRevLett.109.095703.

[14] N. Iikawa, M. Bandi, and H. Katsuragi. Sensitivity of granular force chain orientation to disorder-induced metastable relaxation. *Physical Review Letters*, 116:128001, 2016.

[15] T. Bertrand, R. P. Behringer, B. Chakraborty, C. S. O'Hern, and M. D. Shattuck. Protocol dependence of the jamming transition. *Physical Review E*, 93:012901.

[16] S. Ramaswamy. The mechanics and statistics of active matter. *Annual Review of Condensed Matter Physics*, 1(1):323–345, 2010.

[17] D. Bi, J. H. Lopez, J. M. Schwarz, and M. L. Manning. A density-independent rigidity transition in biological tissues. *Nature Physics*, 11:1074–1079, 2015.

[18] D. Bi, X. Yang, M. Marchetti, and M. Manning. Motility-driven glass and jamming transitions in biological tissues. *Physical Review X*, 6:021011, 2016.

[19] D. Barton, S. Henkes, C. Weijer, and R. Sknepnek. Active vertex model for cell-resolution description of epithelial tissue mechanics. *PLoS Computational Biology*, 13:e1005569, 2017.

[20] F. Giavazzi, M. Paoluzzi, M. Macchi, D. Bi, G. Scita, M. Manning, R. Cerbino, and M. Marchetti. Flocking transitions in confluent tissues. *Soft Matter*, 14:3471–3477, 2018.

[21] A. Fodor and M. C. Marchetti. The statistical physics of active matter: From self-catalytic colloids to living cells. *Physica A*, 504:106 – 120, 2018.

[22] S. Henkes, Y. Fily, and M. C. Marchetti. Active jamming: Self-propelled soft particles at high density. *Physical Review E*, 84:040301, 2011.

[23] M. Delarue, G. Poterewicz, O. Hoxha, J. Choi, W. Yoo, J. Kayser, L. Holt, and O. Hallatschek. Scwish network is essential for survival under mechanical pressure. *Proceedings of the National Academy of Sciences of the United States of America*, 114(51):13465–13470, 2017. doi: 10.1073/pnas.1711204114.

[24] C. P. Goodrich, A. J. Liu, and S. R. Nagel. Finite-size scaling at the jamming transition. *Physical Revirew Letters*, 109:095704, 2012.

[25] S. Alexander. Amorphous solids: their structure, lattice dynamics and elasticity. *Physics Reports*, 296(2):65 – 236, 1998.

[26] K. VanderWerf, W. Jin, M. Shattuck, and C. O'Hern. Hypostatic jammed packings of frictionless nonspherical particles. *Physica Review E*, 97:012909, 2018.

[27] C. F. Schreck, N. Xu, and C. S. O'Hern. A comparison of jamming behavior in systems composed of dimer-and ellipse-shaped particles. *Soft Matter*, 6(13):2960–2969, 2010.

[28] P. Olsson and S. Teitel. Critical scaling of shear viscosity at the jamming transition. *Physical Review Letters*, 99:178001, 2007.

[29] J. Ranft, M. Basan, J. Elgeti, J.-F. Joanny, J. Prost, and F. Julicher. Fluidization of tissues by cell division and apoptosis. *Proceedings of the National Academy of Sciences of the United States of America*, 107(49):20863–20868, 2010. doi: 10.1073/pnas.1011086107.

[30] D. A. Matoz-Fernandez, E. Agoritsas, J.-L. Barrat, E. Bertin, and K. Martens. Nonlinear rheology in a model biological tissue. *Physical Review Letters*, 118:158105, Apr 2017. doi: 10.1103/PhysRevLett.118.158105.

[31] S. Jacobeen, J. T. Pentz, E. C. Graba, C. G. Brandys, W. C. Ratcliff, and P. J. Yunker. Cellular packing, mechanical stress?and the evolution of multicellularity. *Nature Physics*, 14(3):286–290, 2018.

[32] S. Jacobeen, E. C. Graba, C. G. Brandys, T. C. Day, W. C. Ratcliff, and P. J. Yunker. Geometry, packing, and evolutionary paths to increased multicellular size. *Physical Review E*, 97: 050401, May 2018. doi: 10.1103/PhysRevE.97.050401.

3.4 Appendix

The source-codes are available on GitHub[1].

3.4.1 Cell-based simulations

In 2D cell-based simulations, illustrated in Fig. S3.1, cells are modeled as two frictionless rigidly-attached spherical lobes[2,3] (mother and bud) that grow exponentially in time at rate γ_i by bud expansion (Eq. S3.1) and interact via repulsive spring forces with elastic modulus k (Eq. S3.2):

$$\dot{a}_i = \gamma_i a_i \tag{S3.1}$$

$$\mathrm{V} = \sum_{i>j} \sum_{k,l} \frac{1}{2} \mathrm{k} \delta_{ik,jl}^2 \Theta(\delta_{ik,jl}) \tag{S3.2}$$

where $a_i = \frac{\pi}{4}(\sigma_{i,\mathrm{mother}}^2 + \sigma_{i,\mathrm{bud}}^2)$ is the cell area, $\sigma_{i,\mathrm{mother}}$ ($\sigma_{i,\mathrm{bud}}$) is the diameter of the mother (bud), V is the total potential energy, $\delta_{ik,jl} = \frac{1}{2}\left(\sigma_{ik} + \sigma_{jl}\right) - \left|\mathrm{r}_{ik} - \mathrm{r}_{jl}\right|$ is the overlap between lobes k of cell i and l of cell j, and Θ is the Heaviside Step function (Fig. S3.1). The potential energy is measured in units of $\mathrm{k}\sigma_{\mathrm{i,mother}}^2$ throughout this chapter.

The system is relaxed with quasistatic dynamics via conjugate gradient energy minimization[4]. Conjugate gradient minimization terminates upon one of the two conditions: (i) two successive steps j and j+1 yield nearly the same energy value $(\mathrm{V_{j+1}} - \mathrm{V_j})/\mathrm{V_j} < \epsilon_{\mathrm{tol}}^2 = 10^{-16}$ or (ii) the potential energy per particle at the current step is $\mathrm{V_j}/(\mathrm{kN}) < \epsilon_{\mathrm{tol}}^2 = 10^{-16}$. The forces ($\mathrm{F}_i$) and torques ($T_i$) acting on each cell are calculated as:

$$\mathrm{F}_i = -\nabla_{\mathrm{r}_i} \mathrm{V} \tag{S3.3}$$

$$T_i = -\partial_{\theta_i} \mathrm{V} \tag{S3.4}$$

where r_i and θ_i are the position and orientation of cell i. For conjugate gradient minimization, we transform these forces to a $3N$-dimensional gradient of the potential energy as:

$\nabla \mathrm{V} = \{F_1^x, F_1^y, M_1/I_1 T_1, ..., F_N^x, F_N^y, M_N/I_N T_N\}$, where the ratio of moment of inertia to mass of each cell is $I_i/M_i = \frac{1}{8}\sigma^2 \left(\frac{1+\Delta^4}{1+\Delta^2} + 2\left(\frac{(1+\Delta)\Delta}{1+\Delta^2}\right)^2 \right)$ with $\Delta_i = \frac{\sigma_{i,\mathrm{bud}}}{\sigma_{i,\mathrm{mother}}}$.

In this model, all mother cells have the same size, $\sigma_{i,\mathrm{mother}} = \sigma$. Cells grow in a square box with

periodic boundary conditions. Cell growth progresses while $\sigma_{i,\text{bud}} < \sigma$ and culminates in division. After division, both new cells acquire a random orientation (see Fig. S3.1).

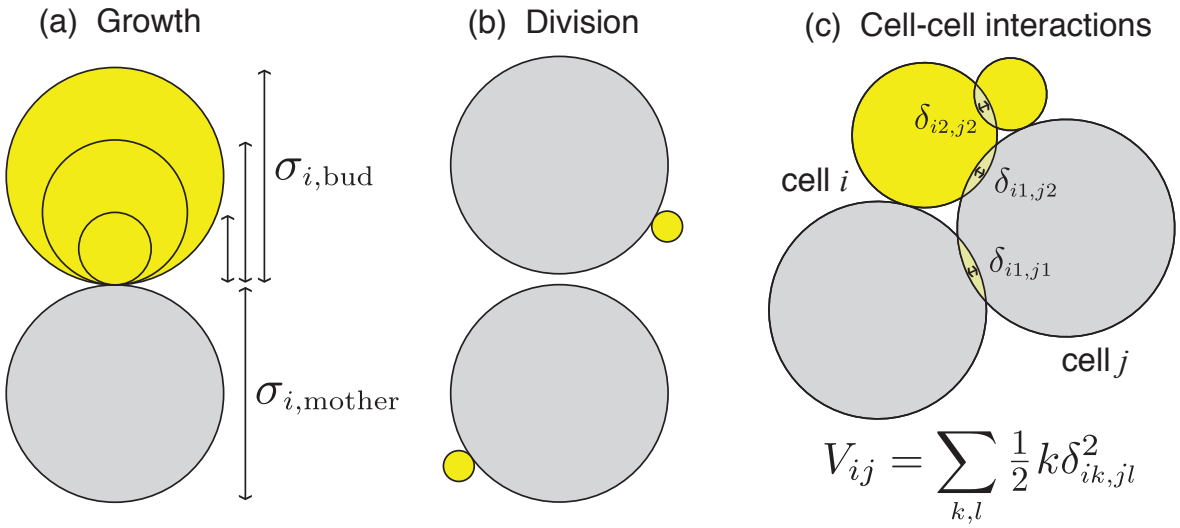

Figure S3.1: Schematic of (a) the growth and (b) division processes and (c) cell-cell interactions in our cell-based simulations. Each cell is composed to two lobes, the mother (gray) and bud (yellow). (a) During growth, the mother lobe diameter of cell i stays fixed at $\sigma_{i,\text{mother}} = \sigma$ while the bud grows from $\sigma_{i,\text{bud}} = 0$ to $\sigma_{i,\text{mother}} = \sigma$. (b) Once the bud reaches $\sigma_{i,\text{mother}} = \sigma$, cell i divides into two new daughter cells that have random orientations. (c) Cells i and j interact only upon overlap ($\delta_{ik,jl}$) via repulsive linear spring interactions with modulus k.

Without pressure feedback, the growth rate for cell i is: $\gamma_i = \gamma_i^0$ where γ_i^0 is chosen from a uniform distribution of width 20% around a mean growth rate γ^0. With pressure feedback, the growth rate is additionally exponentially modulated as $\gamma_i = \gamma_i^0 e^{-P_i/P_0}$ where P_i is the pressure on the bud of the cell i, and P_0 is a strength of the feedback[3]. The pressure $\mathrm{P_i}$ is calculated as $\mathrm{P_i} = \sum_{\mathrm{j(i)}} |\mathrm{F_{ij}}|/\mathrm{L_{i,bud}}$, where $\mathrm{L_{i,bud}} = \pi\sigma_{\mathrm{i,bud}}$ is the perimeter of bud i, $|\mathrm{F_{ij}}|$ is the magnitude of the contact force between a bud i and a particle j, and $\mathrm{j(i)}$ is a set of the particles in contact with i. In Figure S3.5 we show the relation between the strength of feedback P_0, population-averaged growth rate $\Gamma = \frac{1}{A}\sum_i a_i\gamma_i$ ($A = \sum_i a_i$), and growth-induced pressure P (see Section 3.4.3 for details on the calculation of P).

3.4.2 Generating jammed packings

The simulation starts with two randomly oriented yeast cells. Initially the cells grow according to Equation S3.1 with a time-step of $\mathrm{dt_o} = 0.002/\gamma^\circ$, and this continues while $\mathrm{V/(kN)} < \epsilon_{\mathrm{tol}}^2$. If

the population energy per cell at time step j is greater than $V_j/(kN) > 2 \cdot \epsilon_{tol}^2$, the growth step is rejected and the time step is halved ($dt_j \rightarrow \frac{1}{2} \cdot dt_j$), and the growth step (proceeded by energy minimization) is repeated (Equation S3.1). If the average potential drops below $V/(kN) < \epsilon_{tol}^2$, the time step is reset to $dt = dt_0$. The simulation terminates when the the average energy per particles of a static energy is $\epsilon_{tol}^2 < V/kN < 2 \cdot \epsilon_{tol}^2$.

This growth-driven protocol differs from previously-used compression protocols[5]. Whereas compression simulations start with a fixed number of objects and reduce the box size until the systems jams, growth-driven simulations start with few objects and increase the number of objects via growth until the system jams.

Once the population reaches the jamming point at ϕ_J, the colony grows beyond that point—up to the preassigned value $\delta\phi = \phi - \phi_J$. The protocol is similar to the one used to find ϕ_J, however the time-step is halved when the volume fraction exceeds $\delta\phi$ by a margin of $\Delta = 0.5 \cdot 10^{-8}$, i.e. $\phi > \phi_J + \delta\phi + \Delta$. The time-step is reset to $dt = dt_0$ if the volume fraction falls below: $\phi < \phi_J + \delta\phi - \Delta$. The protocol ends when the volume fraction falls into the range $\phi \in [\phi_J + \delta\phi - \Delta, \phi_J + \delta\phi + \Delta]$.

To speed up simulations where population pressure significantly slows down growth ($P \gg P_0$), we use an adaptive time-step. In this method, we scale the time-step dt by the largest cellular growth-rate in the population γ_{min}: $dt' = dt \cdot \gamma/\gamma_{min}$. This method ensures that, even while the population is under pressure, the fastest-growing cells add the same amount of volume per time-step as they would have without feedback. Unless noted explicitly, all results in this chapter use this adaptive time-step method.

3.4.3 Calculation of mechanical properties

For each static packing, we calculate the stress tensor $\hat{\Sigma}$ via the Virial expression:

$$\hat{\Sigma}_{\alpha\beta} = \frac{1}{2L^2} \sum_{i>j} \sum_{k,l} \left(r^{\alpha}_{ik,jl} F^{\beta}_{ik,jl} + r^{\beta}_{ik,jl} F^{\alpha}_{ik,jl} \right) \tag{S3.5}$$

where $F^{\alpha}_{ik,jlj}$ is the α-component of the force $\vec{F}_{ik,jl}$ on kth lobe of particle i resulting from overlap with the lth lobe of particle j, and $r^{\alpha}_{ik,jl}$ is the α-component of the vector from the center of mass of lobe ik to the center of mass of lobe jl. The pressure is calculated from the stress tensor as $P = \frac{1}{2}(\hat{\Sigma}_{xx} + \hat{\Sigma}_{yy})$.

To calculate bulk modulus B, the simulation box is compressed by $d\phi = 10^{-8}$, and the modulus is calculated from the definition $B = \phi dP/d\phi$.

To determine shear modulus G of a cellular packing, the response to quasistatic simple shear is calculated. To that end, for a static packing at $\delta\phi = \phi - \phi_j$, each cell is subject to a small affine shear strain (along the x direction with gradient in the y direction):

$$\mathrm{x_i} \rightarrow \mathrm{x_i} + \delta\gamma_{\mathrm{xy}}\mathrm{y_i} \tag{S3.6}$$

where $\mathrm{r_i} = (\mathrm{x_i}, \mathrm{y_i})$ is the location of the center of mass of a particle i, and $\delta\gamma_{\mathrm{xy}} = \delta\mathrm{x}/\mathrm{L} = 10^{-6}$, and L is size of the system. Following the application of shear strain, the system is relaxed via energy minimization. Then, shear modulus is calculated from the definition $G = d\Sigma_{xy}/d\gamma_{xy}$.

Throughout this chapter we measure P, B, and G in units of the cell-cell modulus k.

3.4.4 Pressure scale (P_{max}) at confluency ($\phi = 1$)

Population pressure P is determined by the overlap between cells, which in turn is set the compression beyond the jamming point $\delta\phi = \phi - \phi_J$. Here, we estimate the pressure P_{max} resulting from compression of cell packings from jamming $\phi_J = 0.84$ to confluency $\phi = 1$.

By explicitly calculating the force between lobes ik and jl, $F^{\alpha}_{ik,jl} = -\partial_{r^{\alpha}_{ik}}\mathrm{V} = r^{\alpha}_{ik,jl}/r_{ik,jl} \times k\delta_{ik,jl}$, we can reduce the population pressure to $P = \frac{1}{2L^2}\sum_{i>j}\sum_{kl} kr_{ik,jl}\delta_{ik,jl}$. This can be expressed as an average over the $N_c = Nz/2$ contacts in the system, so that $P = \frac{Nz}{4L^2}\langle kr_{ik,jl}\delta_{ik,jl}\rangle$.

To estimate P, we assume that we have a population of monodisperse spherical cells with diameter σ with $z \approx z_J = 4$ and $\phi_J = 0.84$. Further assuming that cells compress purely affinely upon infinitesimal compression, equivalent to swelling cells from σ to $\sigma + d\sigma$ while keeping the box size fixed at L, and that no new contacts are made in the process allows us to simplify pressure to $P = \frac{N}{L^2}k\sigma d\sigma$. Since the volume fraction is $\phi = \frac{N\pi\sigma^2}{4L^2}$, $d\phi = \frac{N\pi\sigma}{2L^2}d\sigma$ and $\frac{N}{L^2}\sigma d\sigma = \frac{2}{\pi}d\phi$. This allows us to relate P to changes in ϕ: $P/k = \frac{2}{\pi}d\phi$.

Finally, we are able to calculated the pressure $P_{\mathrm{max}}/k = \frac{2}{\pi}0.16 \approx 0.1$ generated by compressing a cell paacking from $\phi_J = 0.84$ to $\phi = 1$. This value is consistent with our measured data in Fig. 3.1g.

3.4.5 Modified isostaticity at jamming point

In this section we describe why the "isostatic" criterion for growing budding cells differs from the naive expectation of $Z_{\text{iso}}^{\text{naive}} = 6$.

In order for a system to be mechanically-stable, it must have as many contacts in the system (N_c) as degrees of freedom (N_d). This is the naive isostatic, or Maxwell, criterion. Since budding cells have 3 degrees of freedom per cell, the system has a total of $N_d = 3N$ degrees of freedom and we would naively expect there to be be $N_c = N_d = 3N$ degrees of freedom at jamming, or $Z_{\text{iso}}^{\text{naive}} = 2N_c/N = 6$ contacts per cell. This argument breaks down, however, because not all degrees of freedom in the system are constrained. Unconstrained buds and rattlers decrease the contact number at jamming Z_J below $Z_{\text{iso}}^{\text{naive}} = 6$ because contacts are not required to constrain these degrees of freedom. The isostatic criterion, taking into account unconstrained buds and floaters, is $N_c^{\text{iso}} = 3N - 3N_r - N_u - 1$ where N_r and N_u are the number of rattlers and unconstrained buds in the system and the -1 is a finite-size correction. We can express the isostatic criterion as $Z_{\text{iso}} = 2N_c^{\text{iso}}/(N - N_r) = 6 - 2f_u - 2/(N - N_r)$ contact per (non-rattler) cell, where f_u is the fraction of (non-rattler) cells with an unconstrained bud. Fig. S3.2 shows that this isostacity criterion holds for nearly all packings analyzed. Note that in the main text we use the large-system limit $Z_{\text{iso}}\big|_{N\to\infty} = 6 - 2f_u$ and in Fig. S3.2 we take into account finite-size effect by adding $2/(N - N_r)$ to Z_J[6].

3.4.6 Hyperstaticity due to unconstrained bud growth

In this section we describe why growth under extreme feedback produces "hyperstatic" ($Z > Z_{\text{iso}}$) packings. In the case of extreme feedback ($P_0 \to 0$), only unconstrained buds grow above the jamming point and these buds cease growing once they come into contact with their neighbors. If there are $N_u = f_u N$ unconstrained buds at jamming and of these $\Delta N_u = \Delta f_u N$ have come into contact with their neighbors due to growth above jamming, then the population needs $Z_{\text{iso}} = 2(3N - N_u + \Delta N_u)/N = 6 - 2f_u + 2\Delta f_u$ contacts for mechanical stability. However, each new unconstrained bud needs 2 contacts to stabilize it, so that the contact number increases to $Z = 2(3N - N_u + 2\Delta N_u)/N = 6 - 2f_u + 4\Delta f_u$ as unconstrained buds make contact. So, as unconstrained buds make contact the system become hyperstatic with $\Delta Z' = Z - Z_{\text{iso}} = 2\Delta f_u$. In the extreme case, $\Delta Z' = 2f_u$ is determined by the number of buds that were unconstrained at jamming. Note that this deviation from isostaicity is twice as large as the deviation from the

coordination number at jamming, $\Delta Z = Z - Z_J = 4\Delta f_u$, which we show in Chapter 3.

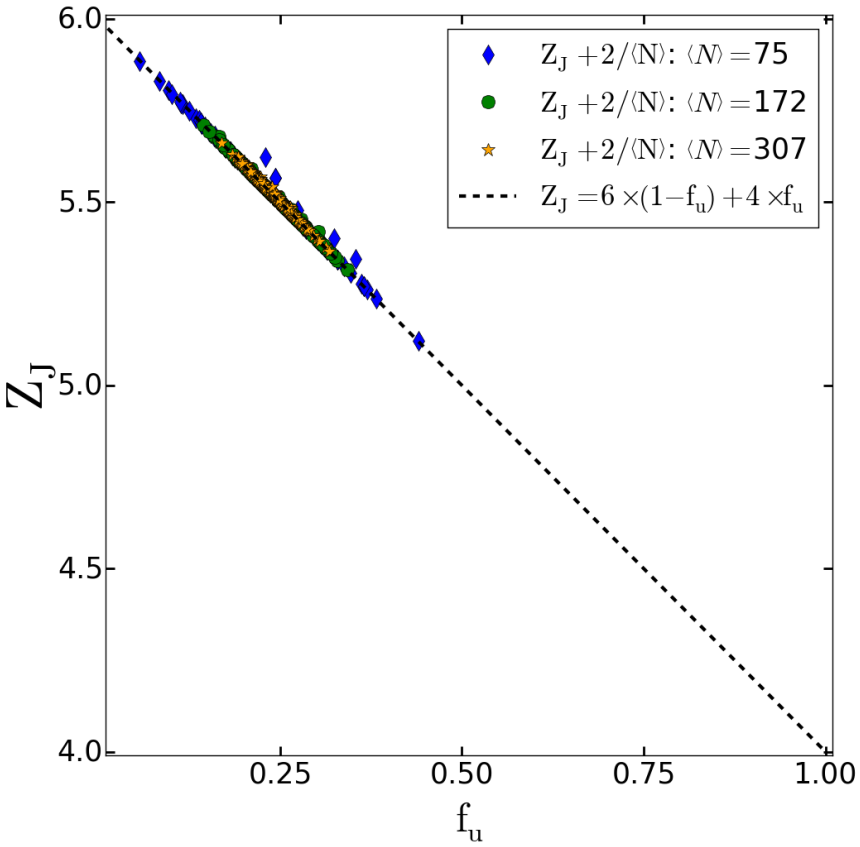

Figure S3.2: Average number of contacts Z_J as a function of a fraction of unconstrained buds f_u. Dashed-line gives the relation $Z_{iso} = 6 - 2f_u$ from constraint counting arguments. A small correction $2/\langle N \rangle$ has been added to Z_J to account finite-size effects (Section 3.4.5). All simulated packings have at least as many contacts as expected ($Z_J \geq Z_{iso}$) while the majority of packings exactly satisfy $Z_J = Z_{iso}$. Numerical data is shown for system sizes $\langle N \rangle = 75$,$\langle N \rangle = 172$ $\langle N \rangle = 307$.

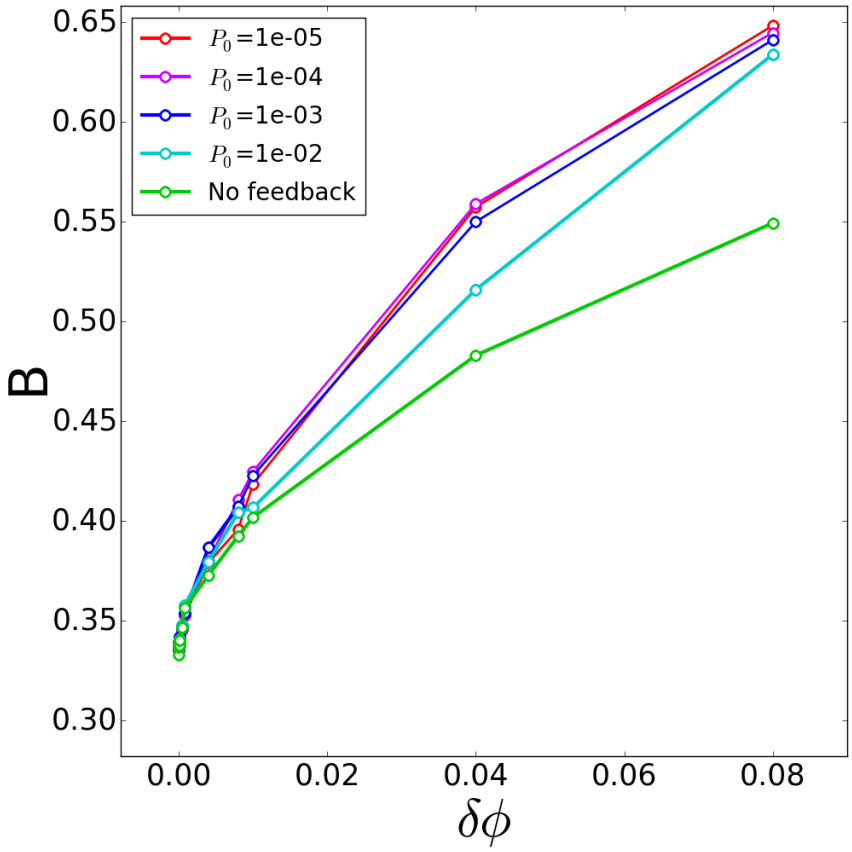

Figure S3.3: Bulk modulus as a function of volume fraction above jamming $\delta\phi = \phi - \phi_J$ for populations growing under five different feedback strengths.

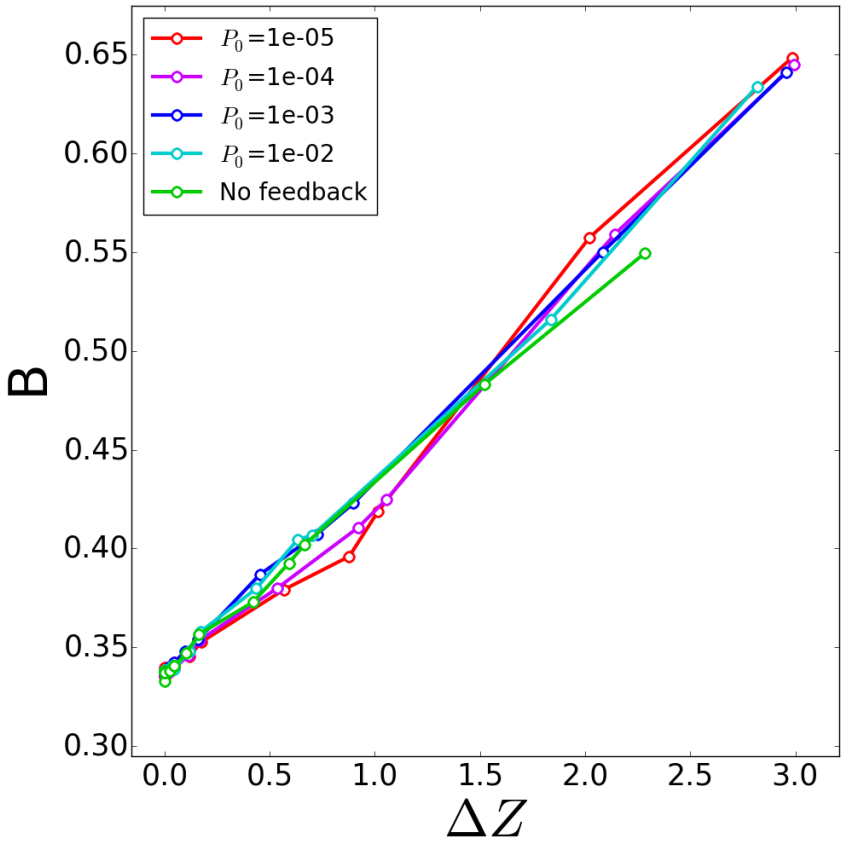

Figure S3.4: Bulk modulus as a function of number of cell-cell contacts above jamming $\Delta Z = Z - Z_J$ for populations growing under five different feedback strengths.

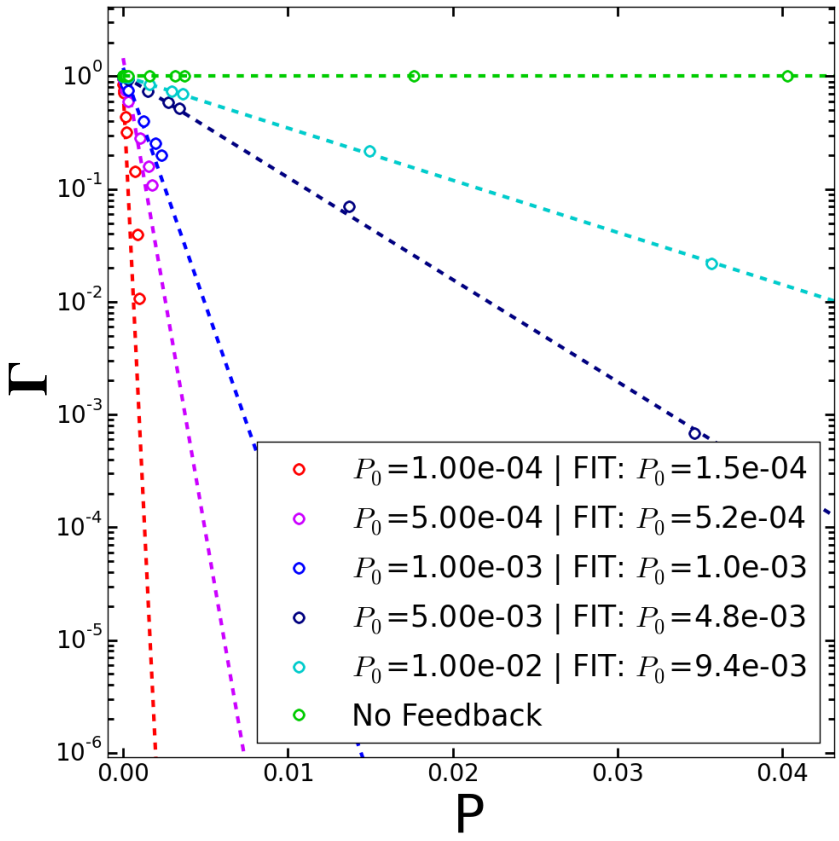

Figure S3.5: Population-averaged growth rate Γ as a function of the population averaged pressure P. Γ is calculated from individual cell growth rates γ_i as $\Gamma = 1/A \sum_i \gamma(i) A(i)$, where $A(i)$ is the area of the i^{th} cell, $\gamma(i)$ is the growth rate of the i^{th} cell (at a given time-step), and $A = \sum_i A(i)$. Population-averaged pressure is calculated form the stress tensor $\Sigma_{\alpha\beta}$ (see Section 3.4.3 for details). The results are for 6 different strengths of feedback: No feedback (green), $P_0 = 10^{-2}$(cyan), $P_0 = 5 \cdot 10^{-3}$(dark blue), $P_0 = 10^{-3}$(blue), $P_0 = 5 \cdot 10^{-4}$(purple), and $P_0 = 10^{-4}$ (red). Dashed-lines are fits to the numerical data. Fitted feedback strengths are given of the right-hand side of the legend. Simulations were done with time-steps kept constant, without the adaptive time-steps method.

References

[1] P. Gniewek. Jamming by Growth - Software. `https://github.com/pgniewko/jamming-growth`, 2018. [Online; accessed 31-August-2018].

[2] C. F. Schreck, N. Xu, and C. S. O'Hern. A comparison of jamming behavior in systems composed of dimer-and ellipse-shaped particles. *Soft Matter*, 6(13):2960–2969, 2010.

[3] M. Delarue, J. Hartung, C. Schreck, P. Gniewek, L. Hu, S. Herminghaus, and O. Hallatschek. Self-driven jamming in growing microbial populations. *Nature Physics*, 12(8): 762, 2016.

[4] W. H. Press, B. P. Flannery, S. A. Teukolsky, and W. T. Vetterling. *Numerical recipes in Fortran*. Cambridge Univ. Press, 1992.

[5] J. Olafsen. *Experimental and Computational Techniques in Soft Condensed Matter Physics*. Cambridge University Press, 2010.

[6] C. P. Goodrich, A. J. Liu, and S. R. Nagel. Finite-size scaling at the jamming transition. *Physical Revirew Letters*, 109:095704, 2012.

4
Packings of Yeast Cells

In this chapter, we study the structure of compacted packings of elastic shells as a model for the packings of confined yeast populations, Figure 4.1. Our starting point is the notion of a budding yeast cell as an elastic spherical shell. With this approximation, I can quantitatively study deformations of the budding yeast cells[1], a feature that cannot be studied with classical soft sphere models[2,3]. In Section 4.1, I present a more detailed discussion of the cell model from the elasticity theory perspective. Although there are models in literature that consider cells as deformable objects[4,5], in this chapter I lean toward a model from which the mechanics can be derived directly from the continuum mechanics theory, without any further simplifications or assumptions. In Section 4.2, I characterize disordered packings of shells starting from the jamming point at the volume fraction $\phi_j \approx 0.64$[6] up to the volume fraction $\phi \approx 1$. I compare these packings to a soft-spheres model with only two-body contact forces. To that end, I analyze the coordination number of the elastic shells, radial distribution function, and the shells' shape metrics as the system gets more and more compressed. In Section 4.3, I postulate a simple mechanism of an adaptation of the yeast cells to the compressive mechanical stress, and compare it to the experimental data presented in Figure S2.6 (Chapter 2)[1]. I also point out that one of the consequences of the model is a homogeneity of the mechanical stresses and turgor pressures as the system gets more compressed. Finally, in Summary section, I discuss directions for further research. I end this chapter with Appendix, where I provide results for the effective friction coefficient μ_{eff} between shells — the property that is not explicitly built into the model, but emerged implicitly from the contact mechanics model.

4.1 Model of a Budding Yeast Cell

I consider the mechanics and the structure of 3D packings of budding yeast cells. To get insight into the effects that stem from the deformability and granularity of the cells, I approximate *Saccharomyces cerevisiae* cells in an undeformed state as spherical objects, *cf.* Figure 4.1, Top Panel.

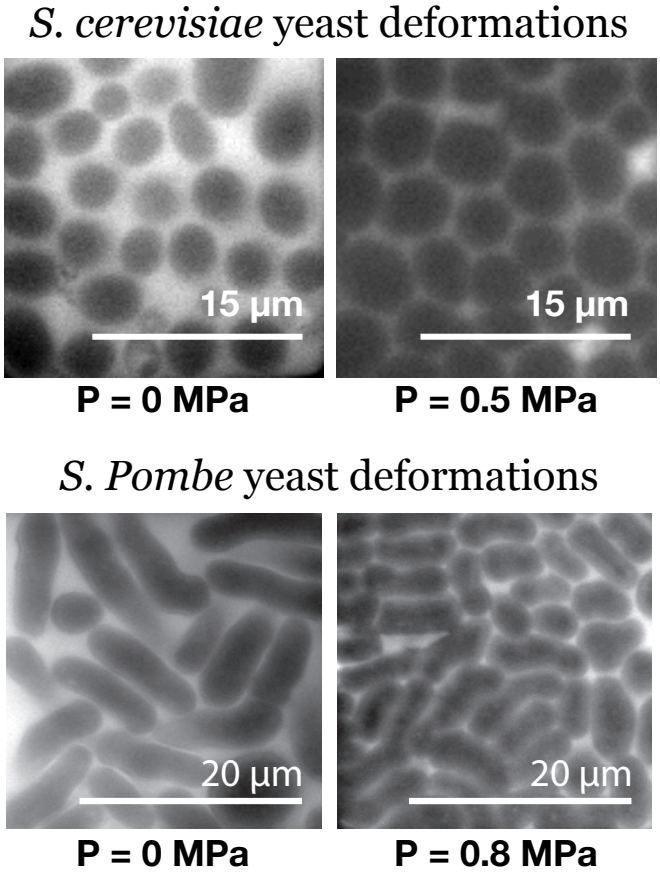

Figure 4.1: Yeast populations growing in confined space. **Top Panel**: Packings of *S. cerevisiae* yeast cells at the jamming point (further growth leads to pressure buildup) and when the bioreactor is almost completely filled[1]; **Bottom panel**: the same as in **Top Panel** but for *S. pombe* yeast (courtesy of Morgan Delarue).

The diameter of a budding yeast cell is about $D \approx 5\mu m$[7], putting the cells at the border between the microscopic and macroscopic worlds. The budding yeast cells are large enough to avoid the substantial effects of the thermal fluctuations of the environment. Thus, to model some cellular components that are crucial to the mechanics of the cells, we can use continuum mechanics theory. The content of the cell is maintained by a semipermeable membrane. The osmolarity inside the cell is higher than the outside due to the high concentration of glycerol and ions inside the cell[8]. Because of the difference in the chemical potential of water, water molecules enter the cell[8]. This results in cell swelling, and it is a mechanism responsible for maintaining the cell's shape. The wa-

ter influx stops with the change in the chemical potential of water that is due to the increase of hydrostatic pressure inside the cell balancing the chemical potential of water outside the cell. For organisms like budding yeast, this excess pressure, called *turgor*, can reach values of the order of 1 MPa, which is about three orders of magnitude higher than in mammalian cells . The lipid bilayer is not strong enough to balance the turgor of the magnitude of MPa, and it is mainly the cell wall that is responsible for the integrity and protection of the budding yeast cells. The cell wall is a structure that is basically a biopolymeric cross-linked network of polysaccharides (β-1,3- and β-1,6-glucans), chitin, and mannoproteins[9]. The thickness and elasticity of the cell wall may vary during the cell cycle[9], but its Young modulus has been found to be about $E \approx 100$ MPa, and the cell wall thickness $t \approx 0.099\mu m$, Table 4.1. The wall stiffness is larger in the chitin-rich bud-scars[10–12], but in the first-order approximation, I neglect this heterogeneity. Additionally, the resistance of the eukaryotic cell cytoskeleton to deformation has been estimated to be of the order of $\sim$ 1-4 kPa[13]. In that context, the presence of the cytoskeleton can be neglected in further considerations about yeast cells mechanics. Yeast cells dwelling in the natural environment have a tendency to strongly adhere to each other, a mechanism known as *flocculation*[14]. Flocculation is mostly caused by the expression of two proteins, flo1p and flo11p, that are attached to the outer layer of the cell wall[14]. However, most lab-strains are selected against the expression of these proteins[15]. Thus, in the model below, we neglect cell-cell adhesion.

In the model, the potential influence of the cellular nucleus on the mechanics is neglected — sometimes these effects are included in order to study yeast cells under extreme conditions, *i.e.* upon hydrostatic loads reaching up to 250 MPa[16]. Thus, it is primarily the cell wall mechanics and the turgor that determine the mechanical properties and deformbilty of the budding yeast cells. This approach was previously used to model a single budding yeast cell in order to obtain the mechanical properties of a single cell in compression experiments[17–21] and indentation experiments[22]. The computational model of a slightly pressurized elastic shell is described in Appendix B. In the next section, we analytically discuss the elastic mechanics of compressed shells, and extract the major determinants of the mechanics of the compacted packings of these shells.

Elastic and Pressure Forces

In the section below, we discuss the flattening and the geometry of an elastic, pressurized, and spherical shell pushed by a rigid wall. The main goal is to analyze stretching, bending, and volumetric energy contributions to the mechanics of a spherical shell upon compression. In the following,

Parameter Name	Symbol	Yeast strain	SI value($\pm\sigma$)	Reference
Cell wall thickness	t	S. cerevisiae Y9	99 nm	Smith *et al.*[20]
Young's modulus	E	S. cerevisiae Y9	107 ± 2.8 MPa	Smith *et al.*[20]
Turgor pressure	P	S. cerevisiae Y9	1.08 MPa	Smith *et al.*[20]
Cell diameter	$2R$	S. cerevisiae Y9	5.0 μm	Phillips *et al.*[7]
Poisson ratio	ν	S. cerevisiae	1/2	-

Table 4.1: Parameters used in Finite-Element Method (or Mesh-Spring) simulations. The cell wall is primarily a polymeric network of: β-1,3- and β-1,6-glucans, chitin molecules, and mannoproteins[9]. Hence, we assumed a Poisson ratio to be the same as for natural rubber, *i.e.* $\nu \approx 0.5$[23].

we discuss three different regimes: i) at very small loads, the deformation is small enough to be insensitive to finite thickness of a shell, hence a Hertz-like contact is developed, *i.e.* the deformation region is too small to cross the thickness of the shell; ii) at larger forces, the shell still flattens, but the disc-like deformation is larger than the thickness of the shell. The geometry and mechanics of this region involves the balance between bending, stretching, and volumetric energies; iii) finally, as the pushing force increases, the stretching energy dominates the deformation energy, and the contact develops an inverted cap where stretching and volume energies are traded for bending energies. We intend to find the conditions for the third regime to occur, when the internal pressure is non-zero, *i.e.* $P > 0$. At each of these regimes, the change in volumetric energy W_P, is proportional to the internal pressure and the volume change due to the deformation ΔV, *i.e.* $W_P = P\Delta\text{V}$. This term is the same for the first and the second regimes, thus it is not pivotal for the transition between Hertz-like and shell-like behavior. The transition between the second and the third regimes involves a symmetric inversion of the spherical cap, hence doubling the volumetric contribution in the third regime, *cf.* Figure 4.2 a-c.

We assume that the inverted cap may occur only for relatively low pressure values, where the unpressurized shell geometry is not significantly distorted. Hence, we first consider the case of the unpressurized shell and then discuss the contribution from the internal pressure.

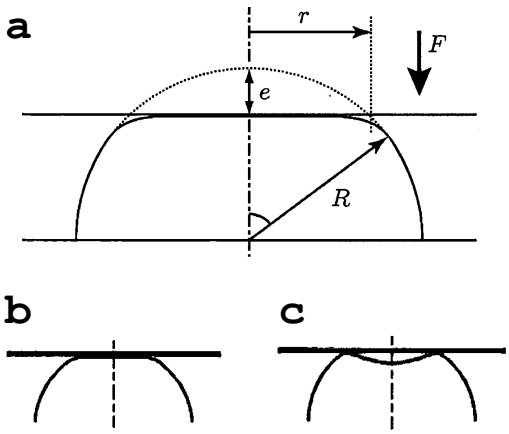

Figure 4.2: a: Geometry of the elastic spherical shell pushed with force F by a rigid wall. The initial radius of the shell is R; r is the radius of the contact disc or the ring in the case of inward buckling (Figure 4.2 c); e is a deformation of the shell from the initial geometry; **b**: Disc-like contact geometry between the wall and the shell; **c**: At certain deformations, the shells create an inward cap, and the contact region between the shell and the wall is a circular ring. Sketch adapted from Audoly & Pomeau[24].

- *Hertz-like Contact Between a Shell and a Rigid Plate*

For very small forces, the region affected by the pushing wall is of the order of the diameter size of a Hertz-like contact disc. The vertical displacement e is related to the pushing force F as

$$e \sim \left(\frac{F^2}{E^2 R}\right)^{1/3} \tag{4.1}$$

and the Hertz energy scales as $W_H \sim F\, e \sim E r^3 \left(\frac{e}{r}\right)^2$, where r is a radius of the contact disc, E is the Young's modulus, and R the size of the shell. The radius of the contact region r can be easily found from the geometry, and it is $r = \sqrt{2eR}$ (for $r, e \ll R$). In order to stay in the regime of the Hertz-like contact, the deformation zone cannot be larger than the shell's thickness t. Hence, the contact stays Hertz-like if the contact radius is less than shell's thickness $r < t \Rightarrow e < e_c = t^2/R$. Simple algebra gives us that, at this point, the magnitude of the force is $F_c \sim Et^3/R$.

• *Disc-like Contact Between a Shell and a Rigid Plate*

As the contact size grows larger than the shell thickness ($r > t$), the stretching and bending contributions need to be balanced. The bending energy density is $\mathcal{E}_b \sim Et^3\Delta\kappa^2$, where $\Delta\kappa = \kappa - \kappa_0$ is the change of the mean curvature of the shell where, for a sphere, $\kappa_0 = \frac{1}{2}\Big(1/R + 1/R\Big)$. Upon flattening of the contact region, the change of the mean curvature is $\Delta\kappa \approx -1/R$. Therefore, the bending energy density is $\mathcal{E}_b \sim Et^3(1/R)^2$, and the total bending energy is $W_b \sim Et^3(r/R)^2$ (with the same coefficient as the F.-von K. plate bending energy, *i.e.* $\frac{1}{12}(1-\nu^2)$[24]). On the other hand, the stretching energy density is $\mathcal{E}_s \sim Et(\partial u/\partial x)^2$, where $(\partial u/\partial x)$ is the general strain. We assume a straight down projection of the shell cap onto the contact disc and roughly homogeneous deformation over the contact region — so the contributions from deformations in radial and angular directions are comparable. Likewise, in the Hertz-contact problem, the radius of the disc is $r \sim \sqrt{eR}$. The material length along that flat disc has been shortened from $r' \approx R\sin^{-1}(r/R)$ in the rest state to r. Thus, $\partial u \approx r' - r = R\,(r/R + (r/R)^3/3! + ...) - r \sim r^3/R^2$, whereas $\partial x \approx r$. Therefore, our generalized strain is $(\partial u/\partial x) \sim r^2/R^2$. From this, we have the stretching energy density $\mathcal{E}_s \sim Et(r^2/R^2)^2$ and the total stretching energy $W_s \sim Et(r^4/R^4)r^2$. As the bending energy density does not depend on r, and the stretching energy density does, the deformation is dominated by bending, up to the point where $\mathcal{E}_b \approx \mathcal{E}_s$. This occurs for the disc radius of the order of $r^2 \sim tR$. Since $r^2 \sim eR$, this means that the stretching energy takes over when the shell flattening is of the order of the thickness of the shell $e \approx t$. Beyond that point, we can see that $\mathcal{E}_s$ is rapidly growing with r, and as the pushing force is larger than some critical value F_{bckl}, another equilibrium state is established.

• *Inverted Cap*

Upon further deformation, for which $e > t$, the shell develops an inverted cap, similar to the case studied by Pogorelov[24,25]. For the inverted cap there are two main components to the elastic energy: i) the energy of the mean curvature change from $+1/R$ to $-1/R$ (integrated over the surface of the cap), and ii) the elastic (bending and stretching) energy in the ridge that is in contact with the pushing wall. The first component is easy to calculate: $W_{b(cap)} \sim \mathcal{E}_b r^2 \sim Eh^3(r/R)^2$. The energy in the ridge is basically the same as in the Pogorelov's problem[25], and it reads $W_{ridge} \sim Ee^{3/2}t^{5/2}/R$[25]. The ridge energy quickly dominates bending, as early as $r \gg tR$.

This completes the analysis of the behavior of the elastic energy as the spherical shell is pushed by the rigid walls, for the internal pressure $P = 0$.

• *Internal Pressure*

In addition to the elastic energy, for the pressurized shells, we have an energy component due to volume reduction. The change in volumetric energy is $W_P = P\Delta \mathrm{V} \sim Pr^2 e \sim Pe^2 R$. For the Hertz-like and disc-like contacts, the change of the volume is the volume of the spherical cap, whereas upon the transition from the disc-like to the inverted cap geometry, the volume is twice the volume of the spherical cap with radius r, and height e. In the range of Hertz-like contact, *i.e.* $0 < e < e_c = t^2/R$, the ratio between elastic and volumetric energies scales as:

$$\frac{W_H}{W_P} \sim \frac{E}{P}\frac{r}{R} = \frac{E}{P}\frac{\sqrt{eR}}{R} = \frac{E}{P}\sqrt{\frac{e}{R}} < \frac{E}{P}\frac{t}{R} \tag{4.2}$$

We can see, that for very small deformations, $e \to 0$, the deformation is first controlled by the pressure. As the deformation approaches $e \to e' \approx R(P/E)^2$, the elastic contribution starts playing a role and dominates in the range $e \in [e', e_c]$, where $e_c = t^2/R$. Next, in the regime $t^2/R < e < t$, the elastic energy is dominated by bending. The ratio between the bending energy and the volumetric energy is:

$$\frac{W_b}{W_P} \sim \frac{Et^3(r/R)^2}{Pe^2R} = \frac{E}{P}\left(\frac{t}{R}\right)^2\left(\frac{t}{e}\right) \tag{4.3}$$

We can see that for the parameters in Table 4.1 this ratio is: $5.0 \approx (E/P)(t/R) > W_b/W_P > (E/P)(t/R)^2 \approx 0.1$. Thus, for $e \ll t$, the deformation is dominated by bending, and the volumetric term takes over as the deformation approaches $e \sim t$. At this point, the stretching energy W_s dominates the bending energy. If the deformation proceeds even further, $e > t$, and in the case of no internal pressure, the stretching energy in the deformed flat disc is traded for the elastic energy in the inverted cap, and the ring-like contact emerges between the shell and the wall, Figure 4.2 c. However, in the case of non-zero internal pressure $P > 0$, the energetic cost of this transition is increased by $W_P = P\Delta \mathrm{V}$, and the buckling does not occur for $t < e < e^*$. The condition for the stability of the flat circular disc is $W_P > W_s$, and the characteristic length-scale e^* can be

estimated from the condition $W_s \approx W_p$, from which we get:

$$e^* \approx t \left(\frac{P}{E}\right) \left(\frac{R}{t}\right)^2 \tag{4.4}$$

For the data in Table 4.1, this condition provides $e^* \approx 10t$. As we can see, for deformations in the range $e \in [t, e^*]$, the W_P term dominates the stretching energy. In this regime (*i.e.* flat contact), the total energy is $W = W_b + W_s + W_P \approx W_P$. Because $W \approx W_P$, in the range of deformations $e \in [t, e^*]$, the deformation energy scales as $W \approx W_p \sim P\Delta \mathrm{V} \sim Pe^2R \sim Pe^2$. This leads to the final approximation of the deformation force that reads: $F \sim eP$, and allows further interpretation of the experimental results in Section 4.3.

Pressurized elastic shells behave similarly upon an indentation larger than the thickness of the shell, $e \gg h$, where it has been experimentally and numerically found that the deformation force depends linearly on the deformation and the internal pressure, $F \sim eP$[22,26]. The dominance of the turgor pressure over membrane mechanics has been also used in the estimation of turgor pressure in a single plant cell[27,28], a single bacterial cell (*Magnetospirillum gryphiswaldense*)[29], and elastic properties of a filamentous fungal hyphae[30].

4.2 Characterization of the Packings Structure

The knowledge of the structure can give us a lot of information about properties of the solid material[31]. Thus, we start our investigation of the packings of elastic shells from the analysis of their structural properties. It has been proven that the densest possible packing of rigid spheres is the FCC lattice, with a coordination number Z=12, and the packing density $\phi = \pi/(3\sqrt{2}) \approx 0.74$[32,33]. FCC packing has a periodic structure with translational and rotational symmetries. These symmetries do not enter into the physics of disordered materials, because they depend on the presence of long-range order, of which disordered materials are depleted[31]. Since the disordered materials are depleted of long-range order, and only short-range order is present, it is difficult to extract any structural informations from, for example, diffraction experiments. As the structure is not periodic, we cannot just give a structure of a unit cell to give a full description of the system. Thus, we have to be content with incomplete information about the packings structure, information which typically is statistical in its nature. First, we discuss the radial distribution function (rdf) which lays down the foundation for the discussion of the power-laws of the other structural parameters. Next,

we look at the coordination number Z, as this number can give us an idea about how compacted is the structure.

To study the packings of shells, as a model for confined budding yeast cells, we start from the random close packing model (RCP). RCP was used with much success as a model for amorphous materials such as foams[34–36], emulations[37], simple liquids[38,39], and (metallic) glasses[40,41]. The density of the RCP is lower than FCC, and it is $\phi_{RCP} \approx 0.64$[6]. More compact disordered packings are generated by changing the size of the simulation box. The results presented here are for elastic shells with constant volume. The rationale and relevance of this choice is given in Section 4.3. The packings are floaters-free and generated as described in Gniewek *et al.*[42].

4.2.1 Radial Distribution Function and the Coordination Number

The utility of the radial distribution function (rdf) for structural characterization comes down to the amount of information which is extractable from the radial distribution function $\rho(r/\sigma)$, before it levels off at larger values (for the sake of readability, we assume that $\sigma = 1$). However, rdf cannot be placed in a unique correspondence with a definite structural model. At the jamming point, rdf for RCP packings has many singular properties[6,43]. In particular, it has been shown that its first peak is a δ-function at $r = 1$. The area under this δ-function is the average coordination number Z. On the high side of the function, $\rho(r)$ has a power-law decay $\rho(r) \propto (r-1)^{-\gamma}$, with the exponent $\gamma = 1/2$[44]. It is proposed that this power-law is a vestige of the configurations visited before reaching the jamming point ϕ_j[45]. Additionally, the second peak of $\rho(r)$ is split into two singular sub-peaks — one at $r = \sqrt{3}\sigma$ and the other at $r = 2\sigma$, see Figure 4.3 a.

Since the disordered materials lack a crystal order, a strict definition of the nearest-neighbor contact (necessary for example for coordination number calculations) is not possible. The average coordination number Z (also called the average *contact number*) although providing oversimplified data in comparison with a full crystal structure is the most valuable single piece of structural data. For FCC structure, the coordination number is $Z = 12$. This number can be lower, and it was shown that the minimum average number of contacts that provide mechanical rigidity is $Z_j = 6 - 4/N$[46], where N is the number of particles in a periodic box. It was also found that RCP has exactly that minimum number of required contacts[6]. This allows us to understand the structural and mechanical properties and identify relevant correlation length-scales[45,47].

As the system is compressed above the jamming point, the height of the first peak decreases as $\rho(1) \sim 1/\delta\phi$[6,44]. Additionally, new contacts are created and the average coordination number

is $Z > Z_j$. More specifically, a small affine compression of the configuration is equivalent to an increase of the particle diameter by the amount $\delta r \approx (\phi - \phi_j)/3\phi_j$. Then, the number of extra contacts $\Delta Z = Z - Z_j$ can be calculated as[45]:

$$\Delta Z \approx 4\pi \int_1^{1+\delta r} \rho(r) r^2 dr \propto \int_1^{1+\frac{1}{3}\frac{\phi-\phi_j}{\phi_j}} \rho(r) r^2 dr \propto \int_1^{1+(\phi-\phi_j)} (r-1)^{-\gamma} r^2 dr \sim (\phi-\phi_j)^{1-\gamma} \tag{4.5}$$

For $\gamma = 1/2$ we can see that this gives us a known relation $\Delta Z \sim \delta\phi^{1/2}$ [6,44,45]. In Figure 4.3 b, we can see that initially, as the packings get more compacted, the number of extra contacts ΔZ has a power-law dependence. However, the exponent that we found is $\beta \approx 0.6$ rather than the expected $\beta = 1/2$. It is not the effect of the deformabilty of the particles because the packings of soft-spheres, with only two-body Hertzian contact forces, also have the similar exponent, Figure 4.3 c. It is also likely not the finite size effect, as the same exponent value is found for a ∼50% smaller system, Figure 4.3 b. Moreover, it does not seem possible that the small effective friction, discussed in Section 4.5.1, is responsible for this deviation, as the friction does not impact the exponent γ, but rather the height of the first peak $\rho(1)$, *i.e.* the number of contacts required for mechanical stability[48,49]. Interestingly, a very similar exponent value, $\beta \approx 0.68$, was found experimentally with compressed packings of soft, frictionless, elastic shells[50,51]. This puzzling result can be explained by the fact that if the initial packings at the jamming point are floaters-free, then the exponent $\gamma \approx 0.4$ — giving us the expected value of the exponent β as $\beta = 1 - \gamma \approx 0.6$. Indeed, our simulations and the experimental protocol by Jose *el al.*[50,51] were such that the initial packings were depleted of floating particles.

For compressions $\delta\phi > 0.15$, we can see, however, a departure from the fractional power-law dependence in ΔZ — an effect that interestingly is not present for the packings of soft spheres with two-body interactions, Figure 4.3 b. Near to $\phi \approx 1$, we notice that the shapes of the contacts between the shells are polygonal, and the shells themselves resemble the *honeycomb structure*. Looking at packings at $\phi = 1$ recalls the Kelvin Problem: "What space-filling arrangement, with similar cells of equal volume, has minimal surface area"? This question is relevant here because, as discussed in the previous section, the energy of deformed shells is mostly stored in the stretched membrane. Thus, in the first order approximation, we can assume that just by minimizing the total surface, we will also approximately minimize the elastic energy of the whole system. We also expect that the answer to our problem is likely different from the Weaire–Phelan structure[52], as the

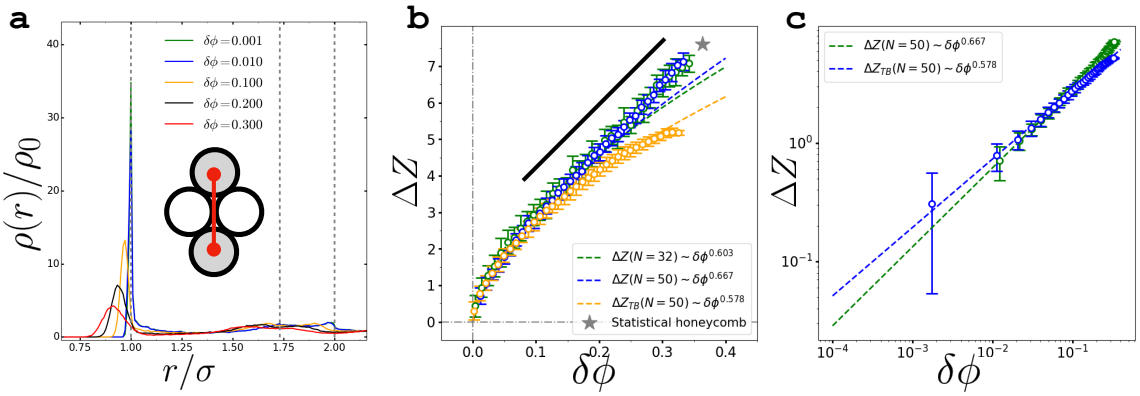

Figure 4.3: a: Normalized radial distribution function $\rho(r)/\rho_0$ for five different compressions: $\delta\phi$=[1E-3,1E-2,1E-1,2E-1,3E-1]. Vertical dashed-lines are at: 1.0, $\sqrt{3}$, and 2.0. Inset: A schematic of the packing geometry. Red bar gives the geometry corresponding to $r/\sigma = \sqrt{3}$. **b**: Excess contact number $\Delta Z = Z - Z_j$ for the packings of 32 and 50 elastic shells, and 50 soft-spheres with Hertzian contact forces. Z_j is taken from the formula $Z_j = 6 - 4/N$, where N is the number of particles in the system (see the main text). Next, the power-law dependence $\Delta Z = Z - Z_j \sim (\phi - \phi_j)^\beta$ is fitted in order to find ϕ_j and β. The exponents β are i) $\beta = 0.603 \pm 0.050$ for N=32; ii) $\beta = 0.667 \pm 0.081$ for N=50; and iii) $\beta = 0.0578 \pm 0.012$ for N=50 soft spheres. **c**: the same data as in **b**, but in log-log scale (N=32 not shown for clarity).

packings that we are studying lack any long-range order.

In the paper *Close Packing and Froth*[53], Coxeter discussed a similar question, namely if there is a division of space by identical polyhedra. There is a solution in non-Euclidean spaces, however there is no solution to this problem in Euclidean space, unless one accept the possibility of cells with facets that are polygons with exactly 5.12 edges, *i.e.* p-gons with $p = 5.12$[53]. This result however has been interpreted by Coxeter in statistical terms, defined as the structure called *Statistical Honeycomb*, which is a collection of Voronoi polyhedra generated by random array fill space[31,53]. Moreover, the average number of facets per cell in *Statistical Honeycomb* is $F = 12/(6-p) = 13.6$. The number of facets F in *Statistical Honeycomb* can be interpreted as the number of contacts Z between the compressed shells, and this number is remarkably close to one found in our simulations ($Z = 6 + \Delta Z$, Figure 4.3 b). Thus, these results suggest that for the compressed random close packings of elastic shells, deformed in order to minimize elastic energy and in the limit of $\phi = 1$, the final structure is the *Statistical Honeycomb* with $Z \approx 14$ and polygonal facets with an average of $\bar{p} \approx p = 5.12$ edges per facet.

4.2.2 Shells Deformation and Coordination Number

In order to understand the qualitative transition of the excess contact number (ΔZ) from the fractional power-law to the linear dependence, and its relation to shells deformations, Figure 4.3 b-c, the changes in the shell shapes upon compression are quantified. We extracted the shapes from the mass distribution, encoded in the gyration tensor[54], although other metric could be used as well. In our case, the gyration tensor gives the distribution of the mass of the shell around its center of mass and is defined as:

$$\mathrm{S}_{\alpha\beta} = \frac{\int d\mathrm{r}\rho(\mathrm{r})r_\alpha r_\beta}{\int d\mathrm{r}\rho(\mathrm{r})} \approx \frac{1}{2N^2}\sum_{i=1}^{N}\sum_{j=1}^{N}(r_\alpha^i - r_\alpha^j)(r_\beta^i - r_\beta^j) = \frac{1}{N}\sum_{i=1}^{N}(r_\alpha^i - r_\alpha^{cm})(r_\beta^i - r_\beta^{cm}) \quad (4.6)$$

where the r.h.s. is the approximation for the discrete mesh representation, r_{cm} is a position of the center of mass, and r_α is α^{th} component of the r vector. We can find a coordination system $(\mathcal{V}_1, \mathcal{V}_2, \mathcal{V}_3)$, where the gyration tensor is expressed as: $\mathrm{S} = \mathcal{V}\Lambda\mathcal{V}^T$, where $\mathrm{V} = [\mathcal{V}_1, \mathcal{V}_2, \mathcal{V}_3]$, and $\Lambda = \mathrm{diag}(\lambda_1^2, \lambda_2^2, \lambda_3^2)$, such that $\lambda_1^2 \geq \lambda_2^2 \geq \lambda_3^2$. The shape metrics such as asphreicity b is defined as $b = \lambda_1^2 - (\lambda_2^2 + \lambda_3^2)/2$, and the reduced aspect ration reads $\delta\varepsilon = \lambda_1/\lambda_3 - 1$. The results are presented in Figure 4.4 a. We can see that for relatively low compressions, $\delta\phi < 0.1$, the shells remain spherical and the behavior of $\Delta Z(\delta\phi)$ follows the expected fractional power-law. As the shells get more deformed in the range $\delta\phi \in [0.1, 0.2]$, we observe a coordinated change in the number of extra contacts and shape metrics. The progress of the deformation can be seen more clearly in Figure 4.4 b-e. At first, as the particles are spherical, the rotational degrees of freedom do not contribute in any way to the stability of the packings, *i.e.* they are simply zero-frequency modes[55]. As the particles get more deformed, these zero-frequency modes become mobilized into finite-frequency excitations, and they require the additional number of contacts, δZ, to provide mechanical rigidity to the packing. It was found that this additional number of contacts scales with the reduced aspect ratio as a power-law, $\delta Z \sim \sqrt{|\delta\varepsilon|}$[55]. In the inset of Figure 4.4 a, we can see that as the system is getting more compacted, the shells deform and their deformation changes as a power-law, $\delta\varepsilon \sim \delta\phi^2$. Then, the extra contacts required to immobilize the rotational degrees of freedom depends on $\delta\phi$ as $\delta Z \sim \delta\phi$. Adding this contribution on top of the scaling for the translational degrees of freedom, Equation 4.5, we obtain the relation for the total number of contacts required for the mechanical stability $\Delta Z \sim \mathrm{C}_\phi \cdot \delta\phi^\beta + \delta\mathrm{Z} = \mathrm{C}_\phi \cdot \delta\phi^\beta + \mathrm{C}_\varepsilon \cdot \delta\phi$, where $\beta \approx 0.5 - 0.6$. Depending on the exact values of the coefficients C_ϕ and C_ε, somewhere around

$\delta\phi \approx 0.1$ the contribution for deformation dominates and leads the linear dependence as found in Figure 4.3 b for $\delta\phi \gtrsim 0.15$. We conclude that it is likely that these shape changes, here quantified by $\delta\varepsilon$, are responsible for the qualitative change in the relationship between ΔZ and $\delta\phi$.

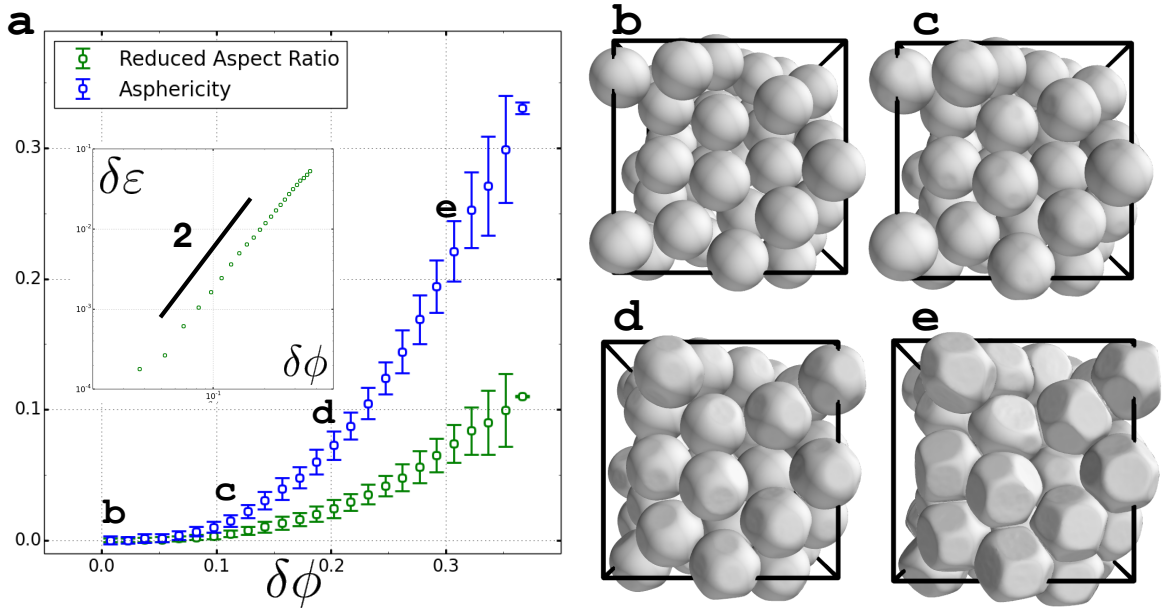

Figure 4.4: a: Average shape metrics for the packings of elastic cells as a function of the reduced volume fraction $\delta\phi = \phi - \phi_j$. Error bars give one standard deviation. For each of the shells, a gyration tensor is calculated and its three principal moments, $\lambda_1^2 \geq \lambda_2^2 \geq \lambda_3^2$, are calculated (see the main text). Asphericity is calculated as $b = \lambda_1^2 - (\lambda_2^2 + \lambda_3^2)/2$, whereas the reduced aspect ratio as $\delta\varepsilon = \lambda_1/\lambda_3 - 1$[54]. Inset: Log-log plot of the reduced aspect ratio $\delta\varepsilon$ as a function of the reduced volume fraction $\delta\phi$. The black, thick line gives the slope for the square dependence: $\delta\varepsilon \sim \delta\phi^2$. **b-e**: Examples of 50 shells (with periodic boundary conditions), at different stages of compaction. Letters (b-d) correspond to the reduced volume fractions $\delta\phi$ as in Figure 4.4 a.

4.3 A Simple Model of Turgor Adaptation

Upon severe osmotic shock, yeast cells experience a significant volume reduction. Osmotic shrinkage is completed within a few tens of seconds after the osmolarity jump, and this result in a substantial increase in protein concentration. That macromolecular density increase leads to the dramatic stalling of several signaling and cellular processes[56]. Thus, upon osmotic shock, the HOG pathway is activated to ensure water homeostasis and volume recovery[56–58]. Similarly, in yeast cells

that are exposed to significant compressive mechanical stress, the SMuSh pathway (Ste11 through Mucin/Sho1 pathway) activates the HOG pathway — which lets cells survive the challenges of compressive mechanical stress[59]. Although the molecular details of this response are yet to be elucidated, it is reasonable to hypothesize that upon large compressive forces, cells not only arrest their cell cycle to prevent further pressure buildup, but also upregulate their turgor pressure in order to prevent a volume drop. If one assumes that in compacted cellular packings, it is possible to distinguish two subpopulations of cells: i) the growing ones, and ii) the ones that are stopped in the cell cycle or are growing very slowly (due to the compressive stress or depletion of nutrients), we can approximately model the turgor adaptation in compressed cells by keeping the volumes of the elastic membranes constant and then compressing the simulation box, *cf.* Figure 4.5 a. This is still an approximation, and the adaptation of the non-growing cells would require simultaneous turgor upregulation of the growing cells — an effect that is not yet accounted in our numerical model. However, in Figure 4.5 b, we can see that if cells are considered as elastic membranes[1], the experimental data (blue dots) suggest that the population average turgor[1] ($\langle \Pi \rangle \approx P/\Theta$) increases alongside the growth-induced pressure, P. These results agree very well with the simulation data, Figure 4.5 b; both for the model with and without bending energy.

To further inspect the possible adaptation of the turgor pressure (modeled for elastic membranes as the hydrostatic pressure), we present data on how the average turgor pressure increases upon the compaction of packings, Figure 4.6 a. We can see that, close to the jamming point, the pressure increases slowly; However, it abruptly increases, by about an order of magnitude, as the packings get closer to the point of complete space-filling, $\phi \approx 1$. This behavior is paralleled by the increase of the average contact force, Figure 4.6 b. In fact, we can see that there is a roughly proportional relationship between the average turgor pressure and the average compressive force that each of the elastic shell experiences: $\langle \Pi \rangle \propto F_c^{\perp}$, Figure 4.6 c. However, as the turgor pressure increases, the differences between the shells' turgors are not growing as well, and in fact the differences stay very small, as shown by the coefficients of variation in the inset of Figure 4.6 a. The same is true for the contact forces — but the coefficient of variation for most of the packing fractions is larger and about $cv = \sigma(F_c^{\perp})/\left\langle F_c^{\perp} \right\rangle \approx 0.5$ (inset in Figure Figure 4.6 b). This is a signature of the *force-chains*, force structures responsible for the mechanical rigidity of the granular packings[61]. Closer to the jamming point, the coefficient of variation is noticeably larger and about ≈ 2.0. This is an anticipated result because, close to the jamming point, the probability distribution of the contact forces decays exponentially $P(F_c^{\perp}) \sim \exp(-F_c^{\perp})$, whereas for compacted system, it crosses over

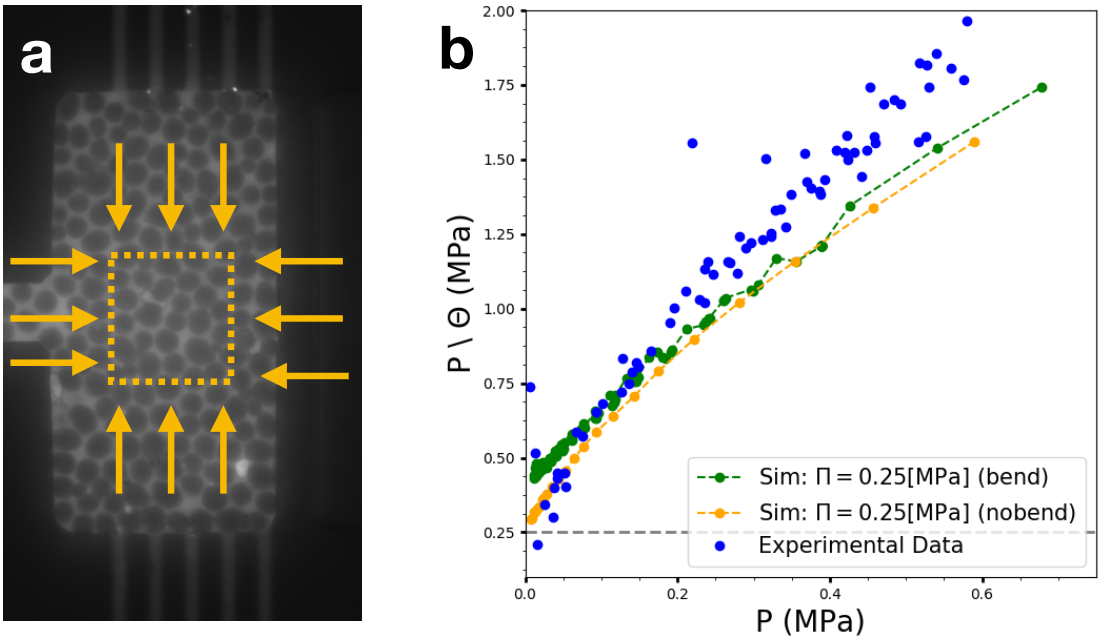

Figure 4.5: a: A schematic of cells in compacted populations of budding yeast [1] (orange, dashed-line square), pushed by the neighboring growing cells (orange arrows). The model depicts a hypothetical scenario where some cells are stalled in the cell-cycle and other are growing. See the main text for details. **b**: Average pressure exerted on the box walls P by the cells/shells over the the average surface coverage Θ given as a function of the average pressure P. Simulations are given for N=16 elastic shells, with and without bending term in the elastic energy. The shells' volumes are kept constant at their initial values. The initial turgor pressure has been set to $\Pi_0 = 0.25$MPa, as this value is close to the value commonly taken as the turgor pressure of budding yeast cells in a liquid culture [60]. The packings of the monodisperse cells are generated by compressing jammed packings by moving the walls of the simulation box — a procedure imitating compression of the cells by their neighbors, as seen in the orange dashed-line box in Figure 4.5 a. Blue dots are the experimental data from Delarue *et al.* [1].

to the Gaussian distribution, $P(F_c^{\perp}) \sim \exp(-\left[F_c^{\perp}\right]^2)$ [36,51,62]. Altogether, this result suggests that as the packings are progressively compressed, the forces and their internal pressure do not increase in variability, but rather stay roughly homogeneous.

4.4 Summary

The above results are very promising, but more analysis is required. First, the disordered packings studied here are all monodisperse, whereas microbial cells in a bioreactor are usually of different sizes, *i.e.* polydisperse[1]. Next, in order to fully confirm (or reject) the *Statistical Honeycomb* hy-

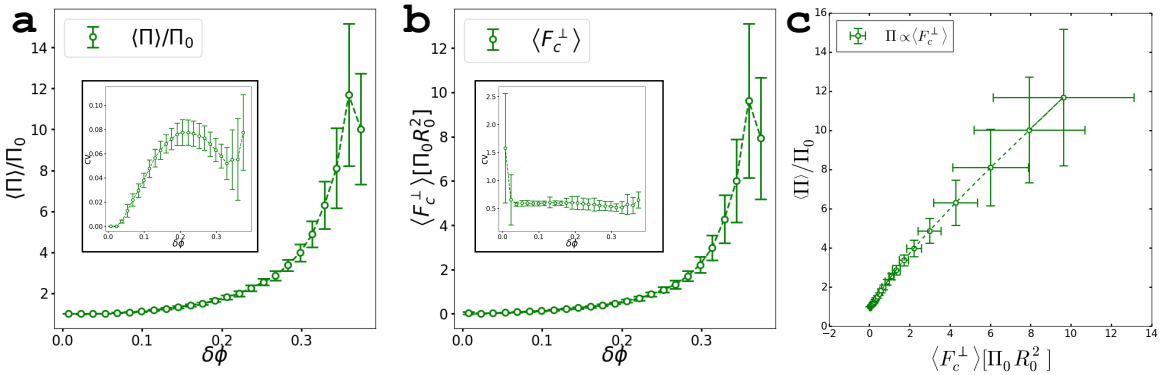

Figure 4.6: **a**: Average turgor pressure (averaged over 50 cells, and 50 independent simulations) normalized by the initial turgor pressure $\Pi_0 = 0.25$MPa, as a function of reduced volume fraction $\delta\phi = \phi - \phi_j$. Error bars give one standard deviation $\sigma(\langle\Pi\rangle)$. Inset: Coefficient of variation of the average turgor pressure as a function $\delta\phi$: $cv = \sigma(\langle\Pi\rangle)/\langle\Pi\rangle$. **b**: Average normal contact force $\mathrm{F}_c^{\perp}$ as a function of reduced volume fraction $\delta\phi$. Inset: coefficient of variation of the average contact force as a function of $\delta\phi$. **c**: Average contact force $\mathrm{F}_c^{\perp}$ as a function of the average (and normalized by $\Pi_0 = 0.25$MPa) turgor pressure.

pothesis discussed in Section 4.2, larger systems need to be analyzed (at least 100 cells/shells). This is necessary in order to make sure that the finite-size effects do not hinder measure values. Moreover, a comprehensive comparison between geometries of the Voronoi cells in the *Statistical Honeycomb* and deformed cells for $\phi \approx 1$ can provide further evidence for or against the model. Additionally, to corroborate the nature of the extra contacts due to the requirement of the stabilization of the mobilized rotational degrees of freedom, it is necessary to investigate the changes in the vibrational spectra as the system becomes more compact, and pinpoint the moment at which rotational and translational spectra overlap[55]. To that end, we can use the model presented in this chapter or a simpler one, where initially spherical particles deform into ellipsoids upon compression by the neighboring particles.

The model presented in this chapter provides a unique opportunity to study compacted packings of deformable objects in much more detail than in the previous studies. Namely, close to the jamming point, where deformations and contact forces are small, simple models such as soft-spheres are a good approximation. However, as the shells get more deformed, significant departures from the simple pictures are observed. First, the linear or Hertzian contact forces are no longer a valid description even for two-body interactions, as the inter-particle contact starts behaving like a stiffening-spring, *cf.* Appendix B.6. Second, contacts are no longer independent, as the regions im-

pacted by two different contacts start overlapping, and participants of different contacts eventually come into a mutual contact as well, *i.e.* three (and higher order)-body problem[63,64]. This problem was recently discussed for soft materials close to the jamming threshold[65]. In this case, many-body interactions are responsible for the *logarithmic term* in an asymptotic two-body interactions, yielding a relation that cannot be approximated by a power-law anymore[65]. Additionally, in strongly compacted systems, particle deformation is so significant that new contacts between particles can be created as a result of compression by the neighbors[63,66,67]. These extra contacts may in turn contribute to the higher resilience of the material[63,64,66]. These three effects are likely in charge of granular materials mechanics, although their relative contributions are still to be elucidated.

Finally, in Figure 4.5 b, the simulations are in a surprisingly good agreement with the experimental data[1], even though the computational model is very simple. However, the weakness of the model is that despite the fact that it is reasonable to assume that some subpopulation of cells do not grow upon confinement, the compression by other cell necessarily requires other cells to maintain the growth. A simple biomass production model can be implemented in both spring-mesh and Finite Element methods. Namely, the numerical algorithm increases the linear size of the triangular elements, and the amount of the biomass is defined by the relaxed sizes of these elements. This procedure is similar to the one described in Rodriguez *et al.*[68] and Vetter *et al.*[69], where the deformation tensor F is decomposed as $F = AG$, where A described a purely elastic response, and G is a diagonal tensor describing the amount of added biomass[69].

4.5 Appendix

4.5.1 Friction forces

In the budding yeast cell model presented in this chapter and Chapter 2, friction is neglected. Friction is likely playing some role in the mechanics of the cellular packings, but at such a small length-scale, it is very difficult to measure or even estimate the magnitude of it experimentally. Although the friction is not implemented explicitly in the elastic shells model, there is an effective friction between compressed shells due to the roughness of the surface. This surface roughness results from the approach used to model the contact mechanics between shells, namely placing repulsive spheres at the vertex nodes. Interestingly, covering mesh with finite repulsive particles is a common way of introduction friction between objects in computer graphics[70].

Numerical estimation of the friction coefficients

We measure the effective friction coefficient for a given packings as $\mu_{\text{eff}} = \max_{m,n}\left(|\mathrm{F}^{\perp}_{mn}|/|\mathrm{F}^{\parallel}_{mn}|\right)$, where $\mathrm{F}^{\parallel}_{mn}(\mathrm{F}^{\perp}_{mn})$ is a normal (tangential) force for a contact between cells m and n, and $\mathrm{F}_{mn} = \mathrm{F}^{\parallel}_{mn} + \mathrm{F}^{\perp}_{mn}$[71]. The contact force between two cells m and n is:

$$\begin{aligned}
\mathrm{F}_{mn} &= \int_{\partial\Omega} d\sigma \mathrm{f}_{mn} && \text{(S4.1)}\\
&= \int_{\partial\Omega} d\sigma \left[\mathrm{f}^{\perp}_{mn} + \mathrm{f}^{\parallel}_{mn}\right] && \text{(S4.2)}\\
&= \int_{\partial\Omega} d\sigma \mathrm{f}^{\perp}_{mn} + \int_{\partial\Omega} d\sigma \mathrm{f}^{\parallel}_{mn} && \text{(S4.3)}\\
&= \mathrm{F}^{\perp}_{mn} + \mathrm{F}^{\parallel}_{mn} && \text{(S4.4)}
\end{aligned}$$

It is easy to calculate the contact force, which is $\mathrm{F}_{mn} = \sum_{i\in m} \mathrm{f}_i = -\sum_{j\in n} \mathrm{f}_j$, where the sums are over vertex nodes i (or j) that belong to a cell m (or n). The contact force perpendicular to the contact surface can be calculated as:

$$\mathrm{F}^{\perp}_{mn} \approx \frac{1}{3}\sum_i \sum_{j(i)} \left(\frac{A_{j(i)}}{C_i}|\mathrm{f}_i \cdot \mathrm{n}_{j(i)}|\right)\hat{\mathrm{f}}_i \qquad \text{(S4.5)}$$

where: $j(i)$ are the indices of triangles that contain a vertex i, f_i is a force on the i^{th} vertex, $\hat{\mathrm{f}}_i = \mathrm{f}_i/\|\mathrm{f}_i\|$, $\mathrm{n}_{j(i)}$ is a normal vector of the $j(i)^{th}$ triangle, $A_{j(i)}$ is the area of the $j(i)^{th}$ triangle, and C_i is a dual area of the i^{th} vertex (Appendix A.3.1). From the above, the tangential force is easily calculated as $\mathrm{F}^{\parallel}_{mn} = \mathrm{F}_{mn} - \mathrm{F}^{\perp}_{mn}$. Numerical data below gives the effective friction coefficient as a function of the reduced volume fraction (averaged over 50 simulations).

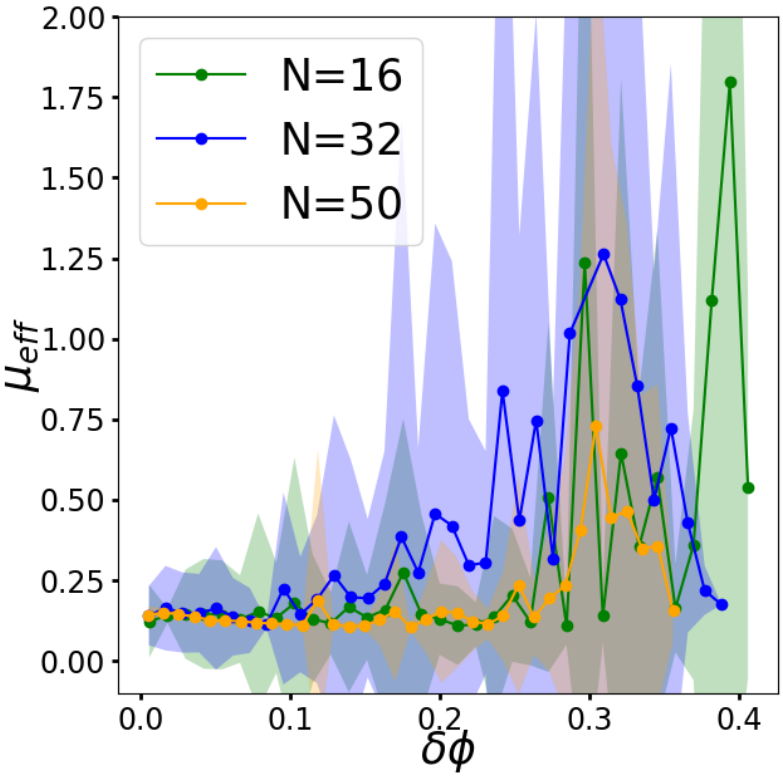

Figure S4.1: Effective friction coefficient μ_{eff} as a function of a reduced volume fraction $\delta\phi = \phi - \phi_j$. Coefficients were estimated as described in Section 4.5.1, for N=16, 32, and 50 elastic shells, with periodic boundary conditions. The averages (solid dots) are calculated over 50 independent simulations, and the envelopes give one standard deviation.

References

[1] M. Delarue, J. Hartung, C. Schreck, P. Gniewek, L. Hu, S. Herminghaus, and O. Hallatschek. Self-driven jamming in growing microbial populations. *Nature Physics*, 12(8): 762, 2016.

[2] M. Basan, J. Prost, J. J.F., and E. J. Dissipative particle dynamics simulations for biological tissues: rheology and competition. *Physical Biology*, 8:026014, 2011.

[3] D. Drasdo and S. Hoehme. Modeling the impact of granular embedding media, and pulling versus pushing cells on growing cell clones. *New Journal of Physics*, 14:055025, 2012.

[4] S. Sandersius and T. Newman. Modeling cell rheology with the subcellular element model. *Physical Biology*, 10:015002, 2008.

[5] F. Milde, G. Tauriello, H. Haberkern, and P. Koumoutsakos. Sem++: A particle model of cellular growth, signaling and migration. *Computational Particle Mechanics*, 1:211–227, 2014.

[6] C. O'Hern, L. Silbert, A. Liu, and S. Nagel. Jamming at zero temperature and zero applied stress: The epitome of disorder. *Physical Review E*, 68:011306, 2003.

[7] R. Phillips, J. Kondev, and J. Theriot. *Physical Biology of the Cell.* Garland Science, Taylor & Francis Group, 2009.

[8] M. de Maranon I, P. Marechal, and P. Gervais. Passive response of saccharomyces cerevisiae to osmotic shifts: cell volume variations depending on the physiological state. *Biochemical and Biophysical Research Communications*, 227:519–23, 1996.

[9] E. Cabib and J. Arroyo. How carbohydrates sculpt cells: chemical control of morphogenesis in the yeast cell wall. *Nature Reviews*, 11:648–655, 2013.

[10] A. Touhami, B. Nysten, and Y. Dufrene. Nanoscale mapping of the elasticity of microbial cells by atomic force microscopy. *Langmuir*, 19:4539–543, 2003.

[11] N. Blanco, M. Reidy, J. Arroyo, and C. E. Crosslinks in the cell wall of budding yeast control morphogenesis at the mother-bud neck. *Journal of Cell Science*, 125:5781–5789, 2012.

[12] R. Chaudhari, J. Stenson, T. Overton, and C. Thomas. Effect of bud scars on the mechanical properties of saccharomyces cerevisiae cell walls. *Chemical Engineering Science*, 84:188–196, 2012.

[13] P. Kollmannsberger and B. Fabry. Linear and nonlinear rheology of living cells. *Annual Review of Materials Research*, 41:75–97, 2011.

[14] L. Vachova, V. Stovicek, O. Hlavacek, O. Chernyavskiy, L. Stepanek, L. Kubinova, and P. Z. Flo11p, drug efflux pumps, and the extracellular matrix cooperate to form biofilm yeast colonies. *The Journal of Cell Biology*, 194:679–687, 2011.

[15] L. Fichtner, F. Schulze, and G. Braus. Differential flo8p-dependent regulation of flo1 and flo11 for cell-cell and cell-substrate adherence of s. cerevisiae s288c. *Molecular Microbiology*, 66:1276–1289, 2007.

[16] C. Hartmann and A. Delgado. Numerical simulation of the mechanics of a yeast cell under high hydrostatic pressure. *Journal of Biomechanics*, 37:977–87, 2004.

[17] A. Smith, K. Moxham, and A. Middelberg. On uniquely determining cell-wall material properties with the compression experiment. *Chemical Engineering Science*, 53:3913–3922, 1998.

[18] A. Smith, Z. Zhang, and C. Thomas. Wall material properties of yeast cells: Part 1. cell measurements and compression experiments. *Chemical Engineering Science*, 55:2031–2041, 2000.

[19] A. Smith, K. Moxham, and A. Middelberg. Wall material properties of yeast cells. part 2. analysis. *Chemical Engineering Science*, 55:2043–2053, 2000.

[20] A. Smith, Z. Zhang, C. Thomas, K. Moxham, and A. Middelberg. The mechanical properties of saccharomyces cerevisiae. *Proceedings of the National Academy of Sciences of the United States of America*, 97(18):9871–9874, 2000.

[21] J. Stenson, P. Hartley, C. Wang, and C. Thomas. Determining the mechanical properties of yeast cell walls. *Biotechnology Progress*, 27:505–12, 2011.

[22] D. Vella, A. Ajdari, A. Vaziri, and A. Boudaoud. The indentation of pressurized elastic shells: from polymeric capsules to yeast cells. *Journal of the Royal Society Interface*, 9:448–455, 2012.

[23] G. Greaves, A. Greer, R. Lakes, and T. Rouxel. Poisson's ratio and modern materials. *Nature Materials*, 10:823–837, 2011.

[24] B. Audoly and Y. Pomeau. *Elasticity and Geometry: From hair curls to the nonlinear response of shells*. Oxford University Press, 1st edition, 2010.

[25] D. Landau, L. Pitaevskii, A. Kosevich, and E. Lifshitz. *Theory of Elasticity*. Butterworth-Heinemann, 3rd edition, 1986.

[26] D. Vella, A. Ajdari, A. Vaziri, and A. Boudaoud. Indentation of ellipsoidal and cylindrical elastic shells. *Physical Review Letters*, 109:144302, 2012.

[27] C. Wang, L. Wang, and T. C.R. On uniquely determining cell–wall material properties with the compression experiment. *Annals of Botany*, 93:443–53, 2004.

[28] P. Durand-Smet, E. Gauquelin, N. Chastrette, A. Boudaoud, and A. Asnacios. Estimation of turgor pressure through comparison between single plant cell and pressurized shell mechanics. *Physical Biology*, 14(5):055002, 2017.

[29] M. Arnoldi, M. Fritz, E. Bauerlein, M. Radmacher, E. Sackmann, and A. Boulbitch. Bacterial turgor pressure can be measured by atomic force microscopy. *Physical Review E*, 21: 1034–44, 2000.

[30] L. Zhao, D. Schaefer, H. Xu, S. Modi, W. LaCourse, and M. Marten. Elastic properties of the cell wall of aspergillus nidulans studied with atomic force microscopy. *Biotechnology Progress*, 21:292–299, 2005.

[31] R. Zallen. *The physics of amorphous solids*. John Wiley & Sons, 1983.

[32] B. Cipra. Packing challenge mastered at last. *Nature*, 281:1267, 1998.

[33] N. Sloane. Kepler's conjecture confirmed. *Nature*, 395:435–436, 1998.

[34] D. Durian. Foam mechanics at the bubble scale. *Physical Review Letters*, 75:4780–4783, 1995.

[35] D. Durian. Bubble-scale model of foam mechanics: Melting, nonlinear behavior, and avalanches. *Physical Review E*, 55:1739–1751, 1997.

[36] G. Katgert and M. van Hecke. Jamming and geometry of two-dimensional foams. *Europhysics Letters*, 92:34002, 2010.

[37] J. Lin, I. Jorjadze, L. Pontani, M. Wyart, and J. Brujic. Evidence for marginal stability in emulsions. *Physical Review Letters*, 117:208001, 2017.

[38] J. Finney. Random packings and the structure of simple liquids. i. the geometry of random close packing. *Proceedings of the Royal Society of London*, 319:479–493, 1970.

[39] J. Finney. Random packings and the structure of simple liquids. ii. the molecular geometry of simple liquids. *Proceedings of the Royal Society of London*, 319:495–507, 1970.

[40] M. Cohen and D. Turnbull. Metastability of amorphous structures. *Nature*, 203:964, 1964.

[41] P. Chaudhari and D. Turnbull. Structure and properties of metallic glasses. *Science*, 199: 11–21, 1978.

[42] P. Gniewek and O. Hallatchek. Liquid transport through packings of elastic shells. *https://arxiv.org/abs/1807.00249*, 2018.

[43] L. A. Silbert, L.E. and S. Nagel. Structural signatures of the unjamming transition at zero temperature. *Physical Review E*, 73:041304, 2006.

[44] A. Liu, S. Nagel, W. van Saarlos, and M. Wyart. The jamming scenerio - an introduction and outlook. *https://arxiv.org/abs/1006.2365*, 2010.

[45] M. Wyart. On the rigidity of amorphous solids. *Annales de Physique*, 30:1–96, 2005.

[46] C. Goodrich and A. Liu. Finite-size scaling at the jamming transition. *Physical Review Letters*, 109:095704, 2012.

[47] A. Liu and S. Nagel. The jamming transition and the marginally jammed solid. *Annual Review of Condensed Matter Physics*, 1:347–69, 2010.

[48] L. Silbert, D. Ertas, G. Grest, T. Halsey, and D. Levine. Geometry of frictionless and frictional sphere packings. *Physical Review E*, 65:031304, 2002.

[49] L. Silbert. Jamming of frictional spheres and random loose packing. *Soft Matter*, 6:2918–2924, 2010.

[50] J. Jose, G. Blab, A. van Blaaderen, and A. Imhof. Jammed elastic shells - a 3d experimental soft frictionless granular system. *Soft Matter*, 11:1800–1813, 2015.

[51] J. Jose, A. van Blaaderen, and A. Imhof. Random three-dimensional jammed packings of elastic shells acting as force sensors. *Physical Review E*, 93:062901, 2016.

[52] D. Weaire and R. Phelan. A counter-example to kelvin's conjecture on minimal surfaces. *Philosophical Magazine Letters*, 69:107–110, 1994.

[53] H. Coxeter. Close-packing and froth. *The Illinois Journal of Mathematics*, 2:746–758, 1958.

[54] D. Theodorou and U. Suter. Shape of unperturbed linear polymers: Polypropylene. *Macromolecules*, 18(6):1206–1214, 1985.

[55] Z. Zeravcic, N. Xu, A. Liu, S. Nagel, and W. van Saarloos. Excitations of ellipsoid packings near jamming. *Europhysics Letters*, 87:26001, 2009.

[56] A. Miermont, Waharte, F., S. Hu, M. McClean, S. Bottani, S. Leon, and P. Hersen. Severe osmotic compression triggers a slowdown of intracellular signaling, which can be explained by molecular crowding. *Proceedings of the National Academy of Sciences of the United States of America*, 110:5725–5730, 2013.

[57] M. Siderius and W. Mager. Conditional response to stress in yeast. *Monatshefte fur Chemie/Chemical Monthly*, 134:1433–1444, 2003.

[58] A. Miermont, J. Uhlendorf, M. McClean, , and P. Hersen. The dynamical systems properties of the hog signaling cascade. *Journal of Signal Transduction*, 2011:930940, 2011.

[59] M. Delarue, G. Poterewicz, O. Hoxha, J. Choi, W. Yoo, J. Kayser, L. Holt, and O. Hallatschek. Scwish network is essential for survival under mechanical pressure. *Proceedings of the National Academy of Sciences of the United States of America*, 114:13465–13470, 2017.

[60] M. P. Martinez de Maranon, I. and P. Gervais. Passive response of *Saccharomyces cerevisiae* to osmotic shift: cell volume variations depending on the physiological state. *Biochemical and Biophysical Research Communications*, 227(2):519–523, 1996.

[61] M. Cates, J. Wittmer, J.-P. Bouchaud, and P. Clauidin. Jamming, force chains, and fragile matter. *Physical Review Letters*, 81:1841–1844, 1998.

[62] C. O'Hern, S. Langer, A. Liu, and S. Nagel. Random packings of frictionless particles. *Physical Review Letters*, 88:075507, 2002.

[63] B. Harthong, J.-F. Jerier, P. Doremus, D. Imbault, and F.-V. Donze. Modeling of high-density compaction of granular materials by the discrete element method. *International Journal of Solids and Structures*, 46:3357–3364, 2009.

[64] N. Brodu, J. Dijksman, and R. Behringer. Multiple-contact discrete-element model for simulating dense granular media. *Physical Review E*, 91:032201, 2015.

[65] R. Hohler and S. Cohen-Addad. Many-body interactions in soft jammed materials. *Soft Matter*, 13:1371–1383, 2017.

[66] M. Gonzalez and A. Cuitino. A nonlocal contact formulation for confined granular system. *Journal of the Mechanics and Physics of Solids*, 60:333–350, 2012.

[67] M. Gonzalez and A. Cuitino. Microstructure evolution of compressible granular systems under large deformations. *Journal of the Mechanics and Physics of Solids*, 93:44–56, 2016.

[68] E. Rodriguez, A. Hoger, and A. McCulloch. Stress-dependent finite growth in soft elastic tissues. *Journal of Biomechanics*, 27:455–467, 1994.

[69] R. Vetter, N. Stoop, T. Jenni, F. Wittel, and H. Herrmann. Subdivision shell elements with anisotropic growth. *The International Journal for Numerical Methods in Engineering (IJNME)*, 95:791–810, 2013.

[70] N. Bell, Y. , Yu, and P. Mucha. Particle-based simulation of granular materials. *Eurographics/ACM SIGGRAPH*, pages 77–86, 2005.

[71] A. Boromand, A. Signoriello, F. Ye, C. O'Hern, and M. Shattuck. Jamming of deformable polygons. *arXiv:1801.06150*, 2018.

5

Fluid Flow Through Packings of Elastic Shells

In this chapter, different from the previous chapters, ϕ stands for the sample's porosity, not the volume fraction.

5.1 Introduction

The physics of fluid flow through disordered porous media is of fundamental importance to a wide range of engineering and scientific fields including enhanced oil recovery, carbon capture and storage, contamination migration in ground-water, water transport, and nutrient transport in tissues and microbial colonies[1–5]. This has led to a substantial effort in looking for relationships between the effective physical transport properties and the structural properties of porous materials. In spite of the extensive work that has been done, a full description of liquid transport in a broad range of material parameters is elusive[6]. Experimental studies, especially in 3D systems, are limited because imaging material samples and resolving fluid flow stream lines are challenging tasks[7–9]. Numerical studies are most often tackled in 2D due to the high computational burden[10–16]. Even though a broad range of material porosities in 2D systems has been covered, a drawback of these studies is that, for disordered materials, the percolation transition coincides with the rigidity transition[17]. For 3D systems, simulations are commonly performed for an idealized model of randomly distributed inter-penetrating objects like cubes or spheres[18–21]. These systems are good prototypes to study critical phenomena, but liquid transport in complex geometries depends on boundary condition details; thus, the relevance of these models for actual materials is not clear[22]. There is also work done on fluid transport in geometries obtained from the microtomography of collected materials. However, these studies are performed using a small number of samples and at relatively high porosity[23,24].

In recent years, the interest in granular systems made of deformable and strongly compacted elastic shells and membranes increased[25–27]. This class of models is of interest not only in physics and

engineering, but also increasingly in biological research of, for example, small cell clusters[28,29], epithelial cells[30], and jammed microbial packings in confined spaces[4,31]. Henceforth, in this chapter, we focus on a model of granular materials where particles are represented as elastic spherical shells, with the volume of these shells kept constant — motivated by experimental work on confined microbial populations[4,31]. For such a model of the granular system, we then numerically study a single-phase viscous flow in Darcy's regime, *i.e.* laminar flow with a linear relation between volumetric flow and pressure gradient. We consider packings in a very broad range of porosities, from the point the packings start to be mechanically stable (jamming transition[32]) down to the porosities where the liquid transport ceases to exist (percolation transition[17]). We mainly focus on a model by Kozeny and Carman[33,34], the classical permeability-porosity framework. First, we briefly introduce the Kozeny-Carman model. Then, we present how the key features of the Kozeny-Carman model can be physically grounded in a percolation theory. Finally, we present numerical evidence on how different structural features of granular porous material contribute to the fluid transport in granular porous media.

Kozeny-Carman Model

Permeability κ measures the ability of fluids to flow through porous media and it is part of the proportionality constant in Darcy's law, the relation between fluid volumetric discharge per unit area U (in units of length/time) and a pressure gradient:

$$\mathrm{U} = -\frac{\kappa}{\eta}\nabla \mathrm{P}(\mathrm{r}) \tag{5.1}$$

where η is the dynamic viscosity of the fluid, and $\mathrm{P}(\mathrm{r})$ is the pressure at the location r. This phenomenological relation is valid at low Reynolds numbers when the flow is laminar. For small pressure gradients, we can further assume $\nabla \mathrm{P} = \Delta \mathrm{P}/\mathrm{L}$, where L is the linear size of the system.

For low Reynolds number flow in a straight and cylindrical capillary channel, we have the Poiseuille equation:

$$\mathrm{U}_{\text{capillary}} = -\beta\frac{\mathrm{R}^2}{\eta}\frac{\Delta \mathrm{P}}{\mathrm{L}} \tag{5.2}$$

where R is the radius of a capillary, β is a numerical factor that accounts for the shape of the capillary,

and L is the length of the capillary. If a capillary occupies only a fraction of the material, the liquid discharge per area unit is correspondingly lower. Assuming that the capillaries are homogeneously distributed in the material, the scaling factor is the amount of the void space in the material, called a porosity ϕ:

$$U = -\beta\phi\frac{R^2}{\eta}\frac{\Delta P}{L} \tag{5.3}$$

For capillaries that are not straight, Kozeny pointed out that due to the tortous character of the flow, the length of the equivalent channels should be $\langle\lambda\rangle \equiv \tau_H \cdot L$, where τ_H is called hydraulic tortuosity, and the fluid discharge needs to be scaled down by it[33]. Carman further reasoned that it takes τ_H times more time to discharge the same amount of fluid through porous media than it takes for straight capillaries (in a macroscopic direction of the flow). Thus, the discharge rate should additionally be τ_H-times smaller[34]. Capillaries are not limited to just the circular cross-sections. For the general shape of the capillary, the radius R is commonly replaced by a hydraulic radius R_h[35] (defined as the ratio of the cross-sectional area normal to flow to the wetted perimeter of the flow channels), but sometimes other parameters are used, for example, the critical pore radius[36].

Thus from Equation 5.3, the final relation for the capillary flow in a porous material is[34]:

$$U = -\phi\beta\frac{R_h^2}{\tau_H \cdot \eta} \cdot \frac{\Delta P}{\tau_H \cdot L} = -\frac{\beta\phi R_h^2}{\tau_H^2}\frac{1}{\eta}\nabla P \tag{5.4}$$

Comparing Equation 5.1 with Equation 5.4, a general formula for permeability reads

$$\kappa = \beta\frac{\phi R_h^2}{\tau_H^2} \tag{5.5}$$

and is called the Kozeny-Carman equation. Despite being semi-empirical, Equation 5.4 is commonly used as a simple model for the permeability in porous materials.

5.2 Methods

5.2.1 Packings of Deformable Shells

Generation of Compressed Packings

The initial packings of the shells are generated using a standard jamming, with periodic boundary conditions algorithm [32]. Starting from these jammed packings, more compacted packings are generated by changing a linear dimension of the simulation box. The changes of the box size are minute, and less than 0.4% of the size an elastic shell. After every box size change, the mechanical stresses are relaxed using the FIRE algorithm [37], see Section 5.5.1 fore more details.

Shells Mechanics

Every shell is modeled as a membrane using about 5000 triangular finite elements per shell. The ratio of a shell thickness t to the initial diameter D_o is $t/D_o = 0.02$, so bending effects can be neglected and the shell material is modeled as an isotropic St. Venant-Kirchhoff membrane [38,39]. All of the shells are slightly pressurized at the beginning of the simulation, with initial pressure P_o, and filled with an incompressible liquid. The ratio between P_o and Young's modulus E is equal to $P_o/E = 0.0025$. The force due to the shell volume-dependent pressure $P(V_{shell})$ on a vertex i is calculated as: $F(r_i) = \nabla_{r_i}\left(P(V_{shell})\cdot V_{shell}\right)$ where $V_{shell}(r_1, ..., r_{N_{vert}})$ is a function of the N_{vert} vertices in the meshwork and the volume change for the vertex i is calculated using the tetrahedral volume defined by the vertex i, its neighboring vertices in the meshwork, and the center of the mass [4,31]. Once the mechanical forces are equilibrated, the constant shell volume constraint is enforced by varying the shells' internal pressures. If the volume of a shell is not equal to the preassigned value V_o, the pressure P_{new} is adjusted to the value $P_{new} = P_{old}\left(1 + (V_o - V)/V\right)$. This inevitably drags the system out of mechanical equilibrium and the system needs to be equilibrated again. The protocol continues until the volumes of the shells reach their preassigned volumes within 0.1% of accuracy.

5.2.2 Identification of a Percolating Cluster

To identify clusters that percolate the void space between the shells, we project a packing of shells onto a 3D lattice with a lattice constant δ, see Fig. 5.1 A. Every lattice site that contains a shell's vertex is considered impermeable to the liquid, Fig. 5.1 A. The shells are represented as finite elements. Thus, for a small enough lattice constants δ, the membrane is permeable to the liquid, *i.e.* the liquid

can enter the interior of the shell. This problem can be overcome by identifying impermeable lattice sites using triangles defined by vertices rather than by vertices alone. However, the mid-surface plane is used to represent the three-dimensional shells in two-dimensional form, so even though two shells are in contact, there is a finite gap between their mid-surfaces, Fig. 5.1 B. Thus, below a certain lattice size $\delta_c \approx 0.025$, the packings are mostly permeable, and percolating clusters identified for $\delta < \delta_c$ are dubious.

Finally, we look for a percolating cluster using the connected-component labeling algorithm (implemented in the `scipy.ndimage` Python library). The cluster is said to percolate the system if it contains lattice sites on the two opposite sides of the simulation box. One of the characteristic length-scales in the system is the initial diameter of a shell, D_0. We choose to express the lattice sizes, δ, in units of D_0. In principle, we would like to generate a lattice with $\delta \to 0$ as we want to estimate a fluid flow in the continuum limit. However, due to the aforementioned limitations, the resolution of the lattices in our study is finite and varies from a coarse one to a fine one, and it is in the range [0.030, 0.080]. Finally, percolation clusters identified in this way are used for hydraulic radius and Lattice-Boltzmann calculations.

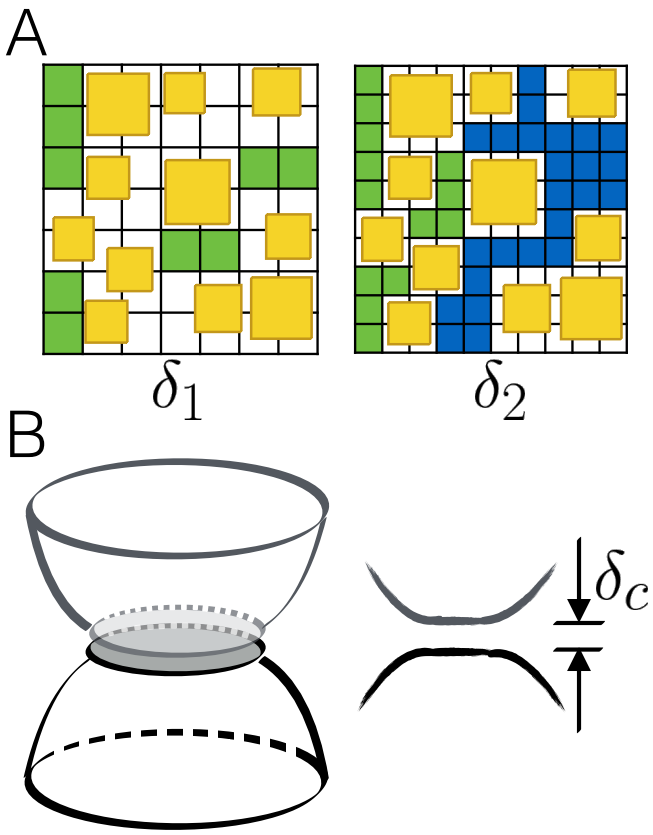

Figure 5.1: Identification of a percolating cluster: **A**. A schematic of a 2D system projected onto a lattice with two different lattice sizes. Every lattice site that contains any part of a particle (yellow shapes) is considered to be occupied and impermeable to liquid (white squares). For the lattice resolution δ_1 and a given configuration, there is no percolating cluster capable of carrying liquid through the packing, but there are some unoccupied lattice sites (green squares). For the lattice size δ_2, there is a percolating cluster (blue squares). There are also some unoccupied lattice sites (green squares) that do not belong to the percolating cluster. **B**. A sketch of two elastic shells in contact. Shells are represented by mid-surfaces, so despite the fact that they are in contact, there is a finite gap between them ($\delta_c \approx 0.025$).

5.2.3 Lattice Boltzmann Simulations

Velocity fields of the fluid flow through the packings of the shells are solved with the Lattice-Boltzmann (LB) method[40] using the D3Q19 lattice topology. This method has proven to be successful in studies of liquid flow in porous materials[10–13,15,18–21,23,24,41–45]. We use this method to obtain a solution to the Navier-Stokes equation for the flow in low Reynolds numbers limit. The LB method is using

a velocity distribution function rather than velocity and pressure fields and is numerically more stable than the Finite Element Method at the irregular boundaries that are inevitable in porous materials[40]. To ensure better numerical stability for the complex geometry of the pores, we use multiple relaxation times (MRT) to solve linearized Boltzmann equation with LB method[46].

Permeability of the packing and the flow field are resolved by setting a pressure difference ΔP between two opposite sides of the simulation box, sufficiently small to keep the flow in the incompressible and laminar regimes (Stokes flow). Every simulation is performed for periodic boundary condition (PBC) in directions perpendicular to the pressure gradient. In the direction of the pressure gradient, the system is open and the boundary conditions are set by pressure difference[23,24]. No-slip boundary condition has been applied to the solid material boundaries. It has been found[13,40] that when the channels carrying liquid become very narrow (of the order of one lattice site) LB simulations become unstable and the evaluation of the stream lines become inaccurate. To deal with this problem we use an approach proposed in[13], where every lattice site on which flow equations are solved is further refined into M^3 smaller cubic elements (refinement level: M). Strictly speaking $\tilde{\delta} = \delta/\mathrm{M}$, is a lattice size of the fluid phase, and throughout this chapter we use $\mathrm{M} = 3$ (unless stated otherwise). Due to computational limitations, LB calculations are performed for the lattice constant $\delta = 0.04$ (unless stated otherwise).

The flow fields obtained from LB simulations for each lattice site, $u(\mathrm{r})$, are further used to calculate the permeability and the tortuosity. Permeability is calculated as $\kappa = \eta \cdot \langle u(\mathrm{r}) \rangle / \nabla \mathrm{P}$, and tortuosity as $\tau_H = \frac{\langle u(\mathrm{r}) \rangle}{\langle u(\mathrm{r})_x \rangle}$, see Section 5.5.3 for the formal derivation. Permeability is given in numerical units, and conversion to physical units can be done following Latt[47]. All the LB simulations are performed with PALABOS (`http://www.palabos.org`), and the source-code is publicly available at `https://github.com/pgniewko/porous-LB`.

The simulated model of the porous material accounts for deformability and the mechanics of the shell membrane using Finite Elements method. The mechanics of the shells are resolved with $\sim 3.75 \cdot 10^5$ degrees of freedom, and some of the LB simulations required up to $\sim 10^7$ lattice points to resolve the fluid velocity field. In turn, the resolution of the calculation imposes restrictions on the largest system size that we are able to study. Finite size effects for the studied systems may result in small anisotropies in the permeability tensor[14], but recent studies show that transport in complex porous geometries can be reasonably well captured if the size of the system is roughly $\gtrsim 10$ times larger than the pore size[23,41,48,49].

5.3 Results

5.3.1 Percolation transition

In idealized systems, such as random packings of overlapping cubes or spheres (and their complementaries, where the solid material is drilled in random locations, rather than deposited[51,52]), the void space between them undergo a percolation transition[50,53–56]. Since, in the vicinity of the percolation threshold, a minute deposition of solid material can disconnect the percolating cluster and prevent further liquid transport, the abruptness of this transition is well understood. The model studied in this work differs from the aforementioned ones in that the narrow necks in the percolating cluster decays continuously upon the compaction of the material. Thus, the existence of a sharp system, size-dependent, percolation transition is not obvious. To address this aspect, following the protocol described in Section 5.2.2, percolating clusters have been identified for three system sizes (N=16, 32, and 50 elastic shells) and various lattice resolutions, Fig. 5.2 A. The results for $\delta = 0.04$ are shown in the Fig. 5.2 A and B. As the system gets larger, the transition becomes steeper, as expected in a first-order transition case[54,56,57]. The steepness of this transition depends on the system size L, and scales as $\sim L^{1/\nu}$, where ν is a critical exponent of the correlation length. In a continuum percolation model, this exponent is approximately equal $\nu \approx 0.88$[58].

Fig. 5.2 C shows that a sharp drop in fluid transport capabilities occurs for different lattice resolutions and that the percolation threshold shifts towards lower porosity values as δ decreases — an effect anticipated from the studies on idealized models[50]. The finite representation of the elastic shells in the studied does not allow for calculations in the continuum limit. It is nevertheless possible to extrapolate a percolation threshold in the continuum limit $\delta \to 0$. In Fig. 5.2 D, we estimated that for N=50, the percolation threshold in the continuum limit is $\phi_c^*(\mathrm{N} = 50) = 0.035 \pm 0.014$, which is consistent with the values obtained for other granular porous materials[50,55–57,59].

For each system size, the percolation threshold ϕ_c for a finite δ and N is expected to be related to the threshold in the continuum limit ϕ_c^* as a power-law $\phi_c(N) - \phi_c^*(N) \equiv \Delta\phi(N) \sim \delta^\beta$[50]. In Fig. 5.2 D, we estimate the lattice-size scaling exponent to be $\beta = 1.1$ for N=50, and similar values of β are found for $N = 16, 32$; *cf.* Table S5.1. The value of the exponent β is in good agreement with the prediction made by Koza *et al.*[50], where the exponent is estimated to be 1 — yielding an approximate relation for the lattice-size dependent percolation threshold that obeys: $\phi_c(N) - \phi_c^*(N) \sim \delta$. Additionally, these fits in the continuum limit are subject to a finite system

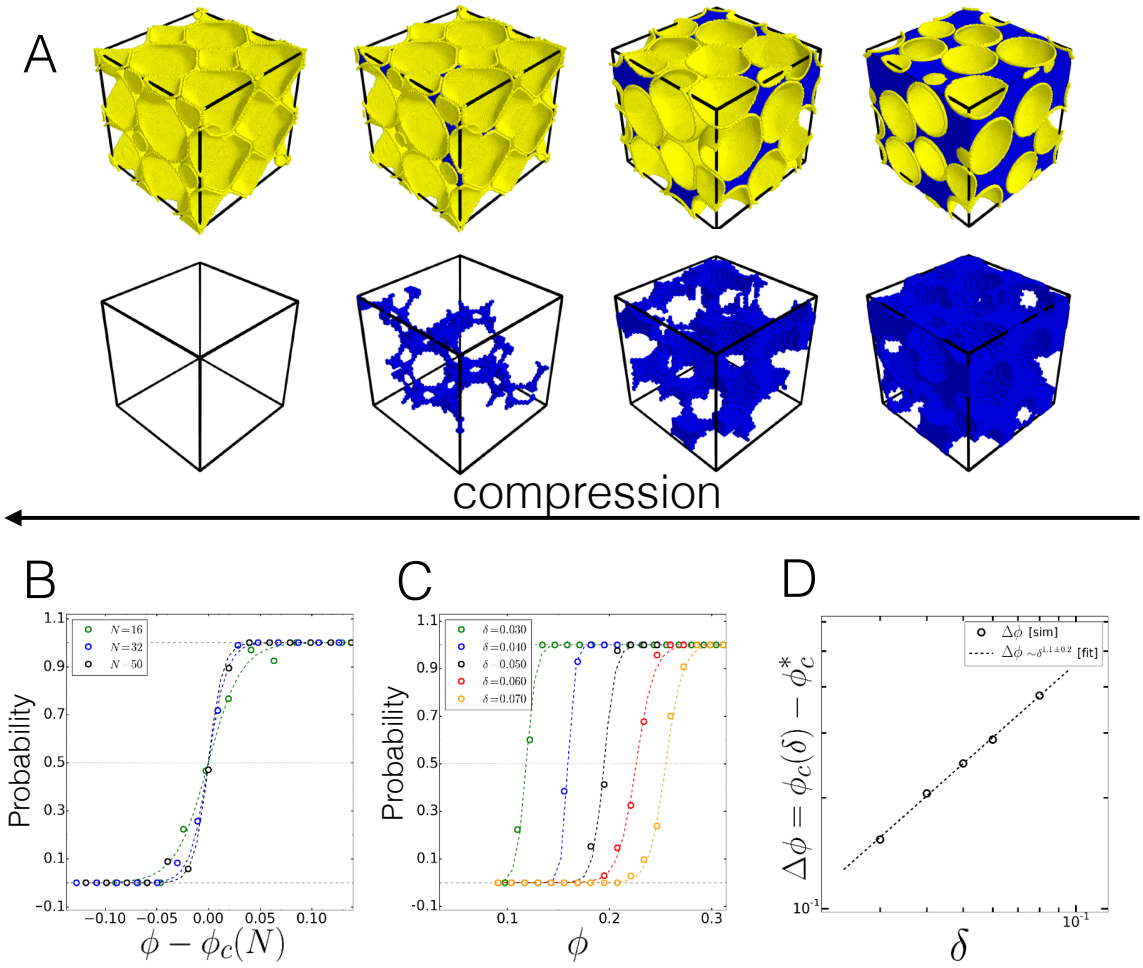

Figure 5.2: Percolation transition: **A**. Percolating clusters (in blue) and deformable shells (in yellow) as the compaction of the system progresses. For clarity, the smallest system is presented (N=16) with a lattice resolution $\delta = 0.04$. As the system is more and more compacted, the percolating cluster gets smaller and more tortuous, and eventually disappears at the critical porosity. **B**. Percolation probability for three system sizes: N=16, 32, and 50. Dashed lines are sigmoid fits to the numerical data, and binned averages are given by open dots. The lattice-size dependent percolation threshold $\phi_c(N)$ has been estimated as the porosity value for which percolation probability is equal to 0.5. The plots represent data for the lattice $\delta = 0.04$. **C**. Percolation probabilities for the system size N=50 and varying lattice sizes: $\delta = \{0.03, 0.04, 0.05, 0.06, 0.07\}$. As the resolution of the lattice increases, the percolation threshold shifts toward lower porosity values. **D**. We extrapolated the percolation threshold in the continuum limit. Dashed line is a power-law fit, where ϕ_c^* and the exponent for δ are two fitting parameters. The fitted percolation threshold in continuum limit is $\phi_c^* = 0.035 \pm 0.014$, and the exponent is equal to 1.1 ± 0.2. The relation $\Delta\phi \sim \delta^{1.1}$ agrees well with the work of Koza *et al.*[50]. Details of a fitting procedure can be found in Section 5.5.6.

size correction, that overestimates (in a first order) the thermodynamic limit by $\phi_c^*(N) = \phi_c^*(\infty) + C_I L^{-1/\nu}$, where $C_I \sim \mathcal{O}(1)$, $L \sim N^{1/d}$, and $d = 3$[55,57,60,61]. An accurate extrapolation to the thermodynamic limit requires data for systems spanning many orders of magnitude, but in Section 5.3.3 and Section 5.3.4 we show that transport properties discussed in this work do not depend on the exact value of $\phi_c^*(\infty)$, but rather on a reduced porosity $\delta\phi(\delta, N) \equiv \phi - \phi_c(\delta, N)$ — a value that can be well estimated for a given lattice size δ, and system size N[62]. Despite the fact that the universality class of the model studied in this contribution remains an open question, the numerical results clearly point to common characteristics between the model studied in this work and previously studied percolation models[50,55,56,61,62]. Thus, we use the formalism of percolation theory in the analysis of fluid flow obstruction in the vicinity of the critical porosity value ϕ_c, which in this study is $\phi_c \approx 0.15$ (unless stated otherwise).

5.3.2 Decrease of hydraulic radius R_h with the porosity

The hydraulic radius is defined as a ratio of a cross-section of a liquid carrying channel to its wetted perimeter, see Section 5.5.2 for more details. Only in relatively simple cases, such as a laminar flow inside a pipe, can the hydraulic radius be directly related to the geometry of the system. In practice, finding this value is problematic because it is difficult to accurately predict a channel's shape along the flow stream lines. The situation gets even more complicated in complex geometries where percolating channels can merge or branch out. Thus, the hydraulic radius is commonly approximated by the ratio of the volume to the wetted area of a cluster carrying the liquid[63].

Using the percolating clusters identified for the packings of elastic shells, we estimated the hydraulic radii for different lattice resolutions as a ratio of the number of lattice sites belonging to the cluster divided by the number of surface sites[41,64]. Using a geometric argument adapted from references[65,66], the hydraulic radius is predicted to vanish linearly at the limit of zero porosity, see Section 5.5.2. Results corroborating this prediction can be found in Fig. 5.3. The results indicate that the hydraulic radius decays like:

$$\mathrm{R_h} \propto \phi/(1-\phi) \tag{5.6}$$

as the porosity goes to 0. If the hydraulic radius was reaching 0 at the percolation threshold ϕ_c, this would indicate that as the porosity approaches the percolation threshold $\phi \to \phi_c$, most of the fluid flow occurs in the layer in the vicinity of the percolating cluster's bounding surface, where

the effects of viscosity are significant. Thus, the liquid transport could be controlled by a no-slip boundary condition on the cluster's surface and not necessarily the complex (tortuous) geometry of the cluster. However, the hydraulic radius vanishes independently of lattice size, and its value at the percolation threshold is finite, as one would expect from a percolation theory[67].

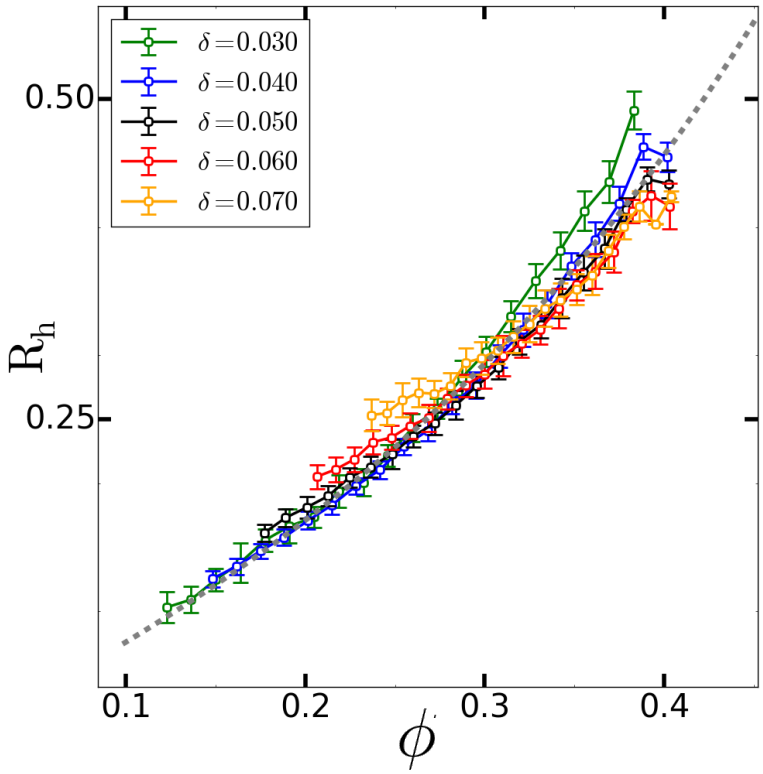

Figure 5.3: Hydraulic radius R_h: Hydraulic radius as a function of porosity ϕ for the system size N=50. For each packing, a percolating cluster has been identified and the hydraulic radius is then calculated as a ratio of the volume of the cluster and the total surface area. Error bars give one standard deviation. Dashed-lines are the fits to $\mathrm{R_h} \propto \phi/(1-\phi)$ for $\delta = 0.04$. See Section 5.5.2 for details.

5.3.3 Tortuosity divergence at the percolation threshold

Tortuosity underpins the relationship between a transport process and the underlying geometry and topology of the pores[68]. Recently it has been shown, numerically and analytically, that the tortuosity depends on material structural properties, and may vary significantly close to the perco-

lation threshold[13,15,35,69–71]. Although percolation ideas have been proposed in the context of tortuosity in 3D porous materials[72], they have not been thoroughly tested near the percolation threshold. In this contribution, we numerically show a link between the geometry of a percolating cluster and the liquid transport through porous materials with a complex geometry of pores at the percolation threshold.

Scaling arguments from Ghanbarian and co-workers[6,72,73] suggest that the tortuosity scales, in the thermodynamics limit, with the reduced porosity ($\delta\phi = \phi - \phi_c$) according to $\tau_H \sim \delta\phi^{\nu(1-\mathrm{D})}$, where ν is a critical exponent of the correlation length ($\nu \approx 0.88$ for the continuum percolation model in 3D), D is the fractal dimension of the cluster through which the liquid is transported, and $\delta\phi = \phi - \phi_c$. It was found that the fractal dimension for the most probable path through which liquid is transported is approximately $D \approx 1.43$[74–77], implying:

$$\tau_H \sim \delta\phi^{-0.38} \tag{5.7}$$

To test this dependence, we evaluated the tortuosity from the velocity field as described in the Section 5.2.3, and the results are presented in Fig. 5.4 A and Fig. 5.4 B. Close to the jamming threshold, $\delta\phi \approx 0.25$, we find that the tortuosity is $\tau_H \approx 1.4$. This result agrees very well with experimental measurements for the packings of glass beads, $\tau_H \approx \sqrt{2}$[63]. For porosities close to jamming, the numerical results for all three lattice refinements overlap (Fig. 5.4 A) and agree with the volume-averaged analytic prediction for mono-dispersed spheres[70,71] (*cf.* black line in Fig. 5.4 B). The increase of tortuosity (and its variance; inset in Fig. 5.4 A) upon approaching the percolation threshold is caused by the complex geometry of the percolating cluster rather than numerical artifacts coming from the increased resolution of the liquid phase lattice, *cf.* Fig. S5.4 in Appendix. For the porosities close to the percolation threshold, $\delta\phi \approx 0.0$, we can see that numerical simulations are consistent with the predicted divergence for the hydraulic tortuosity, Fig. 5.4 A. However, divergence of a hydraulic tortuosity as $\tau_\mathrm{H} \sim \delta\phi^{-0.38}$ is expected in the thermodynamic limit, *i.e.* $N \to \infty$. From Equation S5.17, we can see that for finite system sizes, where $C_I L^{-1/\nu} \gg \delta\phi$, the tortuosity is finite and reaches a maximum value at $\delta\phi = 0$. This maximum tortuosity scales with the system size as $\tau_H^{\max}(N|\delta\phi = 0) \sim N^{-(1-D)/d} \approx N^{0.14}$ ($D = 1.43$, $d = 3$, and recall that $N \sim L^d$; see Section 5.5.4 for details). In Fig. 5.4 B, we can see that the maximum tortuosity on the approach to the percolation threshold increases with the system size, and we expect that as larger systems are simulated, these values will approach the scaling relation $\tau_H \sim \delta\phi^{-0.38}$, denoted

by the black dashed-line in Fig. 5.4 B. In contrast to the relatively loose packings, for which lattice refinement is not crucial, lattice refinement for LB calculations is essential for the packings in the proximity of the percolation transition. This in turn sets the technical limitations on the system size that can be feasibly simulated. A potential solution to this obstacle could be an evaluation of a geometric tortuosity[63] and capitalizing on the relation between geometric and hydraulic tortuosities[78].

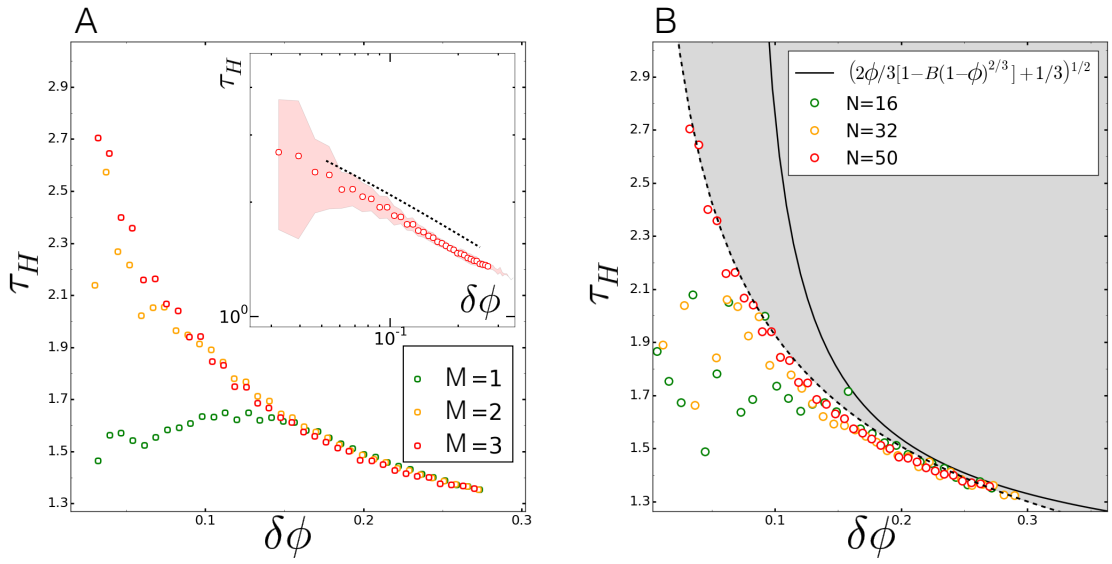

Figure 5.4: A: Hydraulic tortuoisity calculated for the system size N=50, and lattice resolution $\delta = 0.04$. The fluid flow is solved on a lattice with three sizes $\tilde{\delta} = \delta/\mathrm{M}$, where M=1,2, and 3. At higher porosities, ϕ, all three lattice refinements give similar results. Closer to the percolation threshold ($\delta\phi \lesssim 0.1$), tortuosity calculations for the liquid phase with a refinement level M=1 break down[13]. For the refinement levels M=2 and 3, the results suggest a divergence of the tortuosity at the percolation threshold ($\phi_c \approx 0.15$ for $\delta = 0.04$). Error-bars have been set to 0 for better readability. Data with error bars can be found in Fig. S5.3. Inset: Log-log plot of the same data. Red envelope gives one standard deviation. Dashed line with a slope -0.38 is given as a reference for comparison. **B**: Hydraulic tortuoisity calculated for three different system sizes: N=16, 32, 50 and the refinement level M=3. Black dashed line is an expected tortuosity dependence $\tau_H \sim \delta\phi^{-0.38}$ in the limit of $\mathrm{N} \to \infty$. The black line provides an analytic prediction from Ahmadi *et al.*[70,71] with a parameter B=1.16. Details of a fitting procedure can be found in Section 5.5.6.

5.3.4 Kozeny-Carman model of permeability

By construction of the Kozeny-Carman model, the liquid transport thorough the material is ensured down to the porosity $\phi = 0$. However this is not the case for granular porous materials. To account for this in Equation 5.3, the porosity ϕ is replaced by the reduced porosity, $\phi \to \delta\phi^\gamma = (\phi - \phi_c)^\gamma$. Exponent γ is sometimes taken *ad hoc* to be equal to $\gamma = 1$ in references[55,79,80], however there is no firm argument supporting this particular choice. Since this exponent is yet unknown, we try to estimate γ from a fit to the numerical data. Knowing γ is not crucial for highly porous materials, for which $\delta\phi \approx \phi$, but it is essential for lower porosities, where the factor $\delta\phi^\gamma$ contributes to the vanishing permeability κ at the percolation threshold, $\delta\phi \to 0$.

In Section 5.3.1, we found numerically that the percolation threshold depends on the resolution of the used lattice. Moreover, in Section 5.3.2 we found that the hydraulic radius reaches 0 at the porosity $\phi = 0$, and do not strongly depend on the lattices resolution δ. Finally, in Section 5.3.3 we found that the tortuosity of flow stream lines diverges upon the approach of the percolation threshold, consistent with the prediction $\tau_H \sim \delta\phi^{-0.38}$. Using Equations 5.5, 5.6, and 5.7, we can put together a relationship between material porosity and permeability κ that reads:

$$\kappa = C_\kappa \times \frac{\delta\phi^{\gamma+0.76}\phi^2}{(1-\phi)^2} \tag{5.8}$$

where C_κ is a constant. A fit of this model is presented in Fig. 5.5 (black dashed-line). Results are given for the lattice resolution $\delta = 0.04$, for which the tortuosity diverges and the flow ceases at porosity $\phi_c \approx 0.15$. We can see in Fig. 5.5 that Equation 5.8 captures quite accurately the change of the material permeability κ in a broad range of porosities—from the onset of the jamming up to the percolation threshold, and regardless of the model fitting method, *cf.* Fig. 5.5 and Fig. S5.5. Depending on the fitting procedure, the value of the exponent γ varies slightly, with the average (over four different fitting procedures) value $\gamma = 0.89 \pm 0.15$. This is quite close to the value used *ad hoc*, $\gamma = 1.0$. In the limit of the large porosities, *i.e.* where $\phi \gg \phi_c^*$, we can approximate $\delta\phi^\gamma \approx \phi^\gamma$, which reduces Equation 5.8 to a simpler form $\kappa \sim \phi^{3.59}/(1-\phi)^2$ (with $\gamma \approx 0.83$). Interestingly, this approximate form, with a fractional power close to 3.6, is in good agreement with recent experimental and numerical work, where this exponent has been estimated to be 3.7 (for porosities such that $\phi - \phi_c \approx \phi$)[23,24]. It is worth noting that although the above model depends on a value of ϕ_c (which also encompasses finite-size effects), it does not affect the generality of

the model because of two reasons: i) the value of the hydraulic radius is quite insensitive to the lattice size used in the calculations; ii) flow tortuosity and dilution of the capillaries is determined by a reduced porosity $\delta\phi$, thus Equation 5.8 should apply for various system and lattice sizes in the vicinity of the percolation threshold even though the exact percolation thresholds are different.

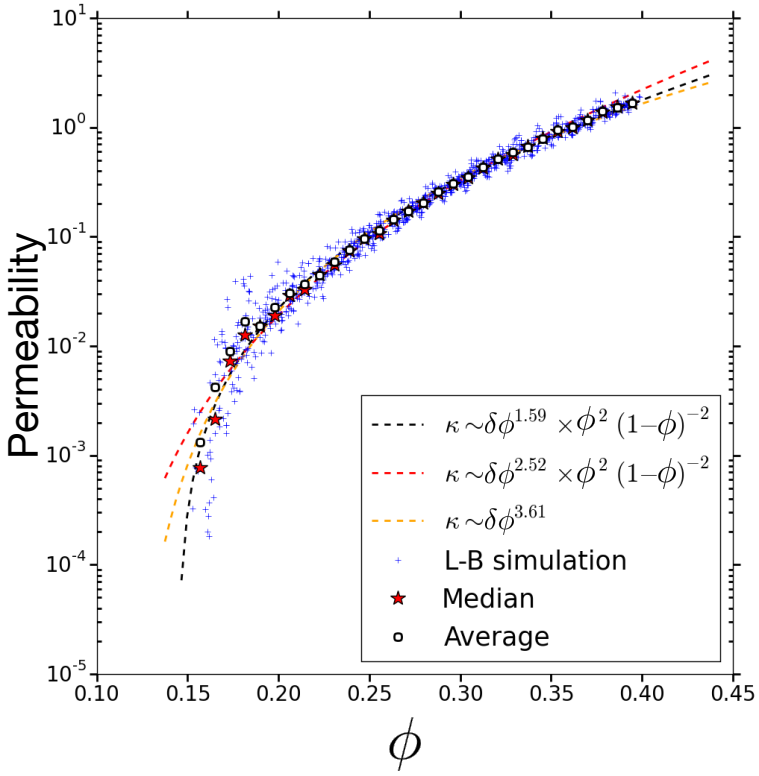

Figure 5.5: Permeability of deformable elastic shells packings in Darcy's regime: Permeability obtained from Lattice-Boltzmann simulations for the system size N=50, and lattice resolutions $\delta = 0.04$ and $\tilde{\delta} = \delta/3$ for the solid and fluid phases, respectively. Blue crosses represent permeability for individual simulations. Black open circles represent binned averages, and red stars correspond to medians. Permeability κ is given in numerical units, *i.e.* $[\kappa] = \tilde{\delta}^2$. Dashed lines correspond to three different models: i) $\mathrm{R_h} \sim \phi/(\phi - 1)$, $\tau_\mathrm{H} \sim \delta\phi^{-0.38}$, and the exponent γ being a fitting parameter; ii) $\mathrm{R_h} \sim \phi/(\phi - 1)$, $\gamma = 1.76$, and $\tau_H \sim \delta\phi^{-0.38}$; iii) power-law *ansatz*: $\kappa \sim \delta\phi^{\bar{e}}$. Fitting details can be found in Section 5.5.6.

In this work we compare Equation 5.8 to a *scaling ansatz* $\kappa \sim \delta\phi^{\bar{e}}$, a good guess for the transport properties in disordered systems and close to the critical point[62]. Halperin *et al.*[51,52] showed that there are several universality classes of porous media where the scaling $\bar{e}$ depends on the model's

details. For example, in the so called *Swiss-cheese* model $\bar{e} \approx 4.4 - 4.5$, whereas for the Inverted *Swiss-cheese* model $\bar{e} \approx 2.4 - 2.5$. The relation $\kappa \sim \delta\phi^{\bar{e}}$ fits the data in a broad range of porosities, yellow dashed-lines in Fig. 5.5 and Fig. S5.5. However, the fitted exponent values depend on the fitting procedure and vary in the range of $[2.72, 3.88]$, with an average value $\bar{e} = 3.4$. Moreover, the estimated percolation threshold (ϕ_c) differs noticeably from the estimations made in Fig. 5.2 C. Despite the fact that the power-law scalings are often very useful, it is not always clear how they relate to the connectedness of the pores and the tortuosity of the flow[62]. Additionally, in Fig. S5.5 A and Fig. S5.5 B, we compare our numerical data to the standard Kozeny-Carman model, where $\kappa \sim \phi^3/(1-\phi)^2$ [2,34,65,66,69,79,81]. Some authors extended the Karman-Cozeny model by accounting for fractal geometry of porous materials[35,69,81], but these models still assume permeability down to porosity $\phi = 0$. This classical model has been successfully applied to many porous materials[2,19,66,82,83] for which $\phi - \phi_c \approx \phi$ (*i.e.* $\phi_c \approx 0.0$). However, in this work, we study permeabilities for the system projected on a lattice for which the above approximation does not hold. Therefore, the Kozeny-Carman model performs worse, as shown by the green dashed-line in Fig. S5.5 A and B.

5.4 Discussion and Conclusions

Our results support a simple model of the fluid flow retardation in deformable granular materials, compressed from the onset of mechanical stability at the jamming point down to the percolation threshold. Porous materials is essentially described as a collection of tortuous and randomly placed capillaries, where, close to the percolation threshold, tortuosity and capillaries dilution dominate liquid transport. We have shown that upon compaction, the void space between pressurized elastic shells undergoes a sharp, system-size dependent transition. We also find that the hydraulic radius vanishes in a lattice-resolution independent manner as the porosity diminishes. Next, using Lattice-Boltzmann simulations, we have shown that tortuosity of the flow stream lines abruptly increases at the percolation threshold. In Equation 5.5, the effects of the capillaries' density and tortuosity are factorized, and this has motivated a substantial research devoted to tortuosity[63,73]. Combined with a percolation scaling theory, we were able to support the fractional dependence of tortuosity on the porosity of the sample. Our work underscores that at higher porosities, where the fluid flow is not tortuous (τ_H is mildly varying for larger ϕ), the major geometric determinant of the flow obstruction is the amount of the void space accessible to fluid — captured in the quadratic dependence

on a hydraulic radius R_h. In turn, upon the approach to the percolation threshold, the complex geometry of liquid transporting channels ultimately leads to the flow hindrance. Nonetheless, the dilution of the capillaries upon the approach to the percolation threshold, described by the γ exponent, remains elusive. We found numerically that $\gamma \approx 0.89 \pm 0.15$, which is close to the *ad hoc* value $\gamma = 1.0$[55,79], but this value does not have a firm grounding in the percolation theory. In Section 5.5.5, we present a simple argument from the percolation theory that suggests this exponent to be $\gamma = 1.76$. If tortuosity is neglected, this would explain our numerical data very well. However, when the tortuosity contribution is included, this leads to the decay of the permeability in the vicinity of the percolation threshold with the exponent close to 2.5, *i.e.* $\kappa \sim \delta\phi^{2.52}$. Despite the fact that this is very close to the Inverted *Swiss-cheese* model exponent ($\bar{e} \approx 2.4 - 2.5$), it does not reproduce the numeral data well, *cf.* Fig. 5.5 and Fig. S5.5. This intriguing result motivates further research on the capillary model in the proximity of the percolation threshold within a framework of the percolation theory. Additionally, this work, alongside the works of others[41,73,83–85], can be potentially useful in studying other transport processes like, for example, electrical conductivity of an electrolyte (as well as the electrical tortuosity τ_e — an analog of the hydraulic tortuosity τ_H in the fluid transport)[63,73,86,87].

Finally, in our work we considered only packings of identical shells. In Section 5.5.2 we can see that poly-dispersity seems to contribute only a constant factor in the relation for R_h, Equation S5.8, without changing its functional dependence on the porosity ϕ. Furthermore, in 3D packings of unequal spheres, polydispersity has only a minor impact on the percolating clusters[55,88]. Therefore Equation 5.8 may be applicable to other disordered and compacted systems made of deformable particles.

5.5 Appendix

5.5.1 Generation of jammed packings

To generate jammed packings, we randomly place particles in a cubic box with periodic boundary conditions. The initial radii of these spherical particles are set such that the initial volume fraction is about $\psi_0 = 0.01$. Next, we successively increase or decrease the radii of the particles, with every change followed by the energy minimization with FIRE algorithm[37] and velocity-verlet integrator[89]. The parameters used in the FIRE algorithm are: $dt_{FIRE} = 0.1$, $dt^{max}_{FIRE} = 1.5$, $\alpha_{FIRE} = 0.1$, $N_{min} = 5$, $f_\alpha = 0.99$, $f_{inc} = 1.1$, $f_{dec} = 0.25$. Termination condition for the FIRE algorithm is:

$\max_i |f_i| \leq 10^{-15}$.

Initially, for each inflation step, the particle's radius is increased following the rule: $r_{new} = r_{old} \cdot (1 + \epsilon_r)$, where initially, $\epsilon_r = 0.01$. The forces between particles are Hertzian: $F(R) = -\frac{4}{3}E^*\sqrt{R^*}\hat{R}h^{3/2}$, where h is an overlap between particles, $\hat{R}$ is a unit vector along R, E^* is an effective Young's modulus where $1/E^* = (1-\nu^2)/E + (1-\nu^2)/E$, R^* is an effective radius, and r being a radius of a particle. In this chapter we use $E = 1$, $\nu = 0.5$. The pressure in the simulation box is calculated as: $P = -\frac{1}{3}\sum_\alpha \sigma_{\alpha\alpha}$, where the stress tensor $\sigma_{\alpha\beta}$ is obtained from the virial formula: $\sigma_{\alpha\beta} = -\frac{1}{V}\sum_i \sum_{i>j} r_{ij}^\alpha F_{ij}^\beta$, where r_{ij}^α is α^{th} component of the vector pointing from the center of a particle j to i, and F_{ij}^β is β^{th} component of the contact force between particles i and j.

When the pressure of the packing is greater than $P > 2 \cdot P_{min} = 2 \cdot 10^{-8}$, the parameter ϵ_r is halved, and the particles' sizes are deflated according the rule: $r_{new} = r_{old} \cdot (1 - \epsilon_r)$. When the pressure drops below $P_{min} = 10^{-8}$, the ϵ_r is again halved and the particles are inflated. The process continues until the pressure P settles at the value $P_{min} < P < 2P_{min}$. If the packing contains any rattler, the configuration is rejected and a procedure is repeated. The final configuration provides positions of soft-spheres particles that are next replaced by the Finite Element representation. The packings generated using the described algorithm have been tested in terms of the number of contacts (Fig. S5.1) and the finite size effects on the volume fraction at jamming point (Fig. S5.2)[32].

5.5.2 Hydraulic radius: a geometric argument[65,66]

For a packed bed of spherical particles with a particle size distribution $n(D_p)$, the i^{th} moment of the particle size distribution is:

$$\mu_i = \int_\circ^\infty D_p^i n(D_p) dD_p \tag{S5.1}$$

If a horizontal cut is made across the packing, one obtains circular disks of the size x, projected on the sectional plane. The size distributions of these disks is:

$$f(x) = \int_\circ^\infty P(x|D_p) P(D_p) dD_p \tag{S5.2}$$

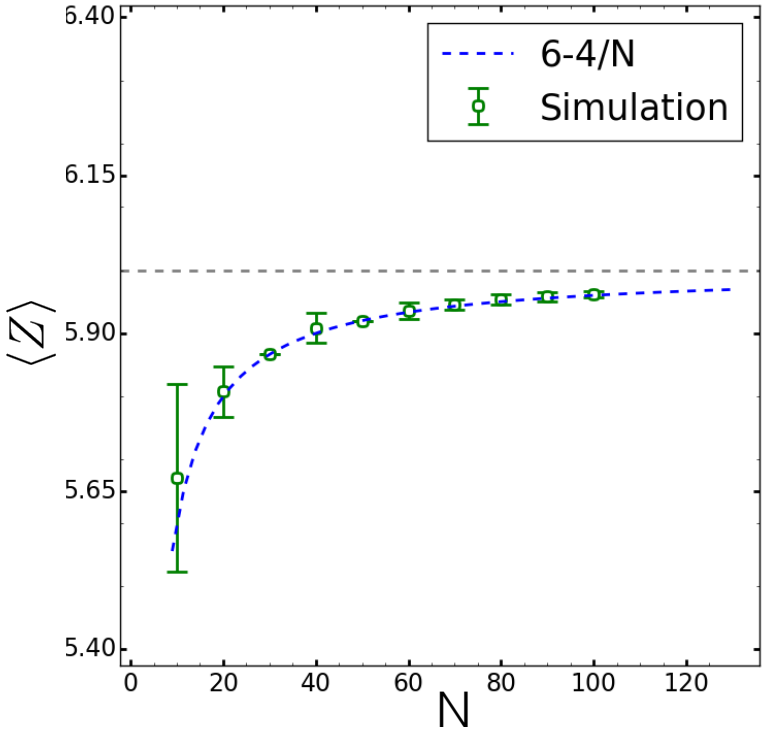

Figure S5.1: Average contact number: A mechanically stable system must have a force balance on each particle. For N spheres in d dimensions the number of constraints that has to be satisfied by the inter-particle forces is $d \times N$. In the system with periodic boundaries this number is $d \times N - d$. Additionally, there is one more degree of freedom, a volume fraction at the jamming, that has to be constrained. Thus, counting argument provides the number of constraining equations that needs to be $N_c = d \times N - d + 1$. According Maxwell's criterion, the number of inter-particle contacts, $N \langle Z \rangle / 2$, must be at least equal to the number of equations N_c. For frictionless spheres the packing at the jamming point has exactly this number of contacts: $\langle Z \rangle = 2d - 2(d-1)/N$; which for 3D average number of contact per particle is $\langle Z \rangle = 6 - 4/N$[32]. The results in Fig. S5.1 are in the range of N that is meaningful for the present study: (10,100). For each N, 100 different packings are generated. Error bars give one standard deviation.

Here $P(D_p)$ is the pdf of D_p:

$$P(D_p) = \frac{n(D_p)}{\int n(D_p) dD_p} = \frac{n(D_p)}{\mu_0} \tag{S5.3}$$

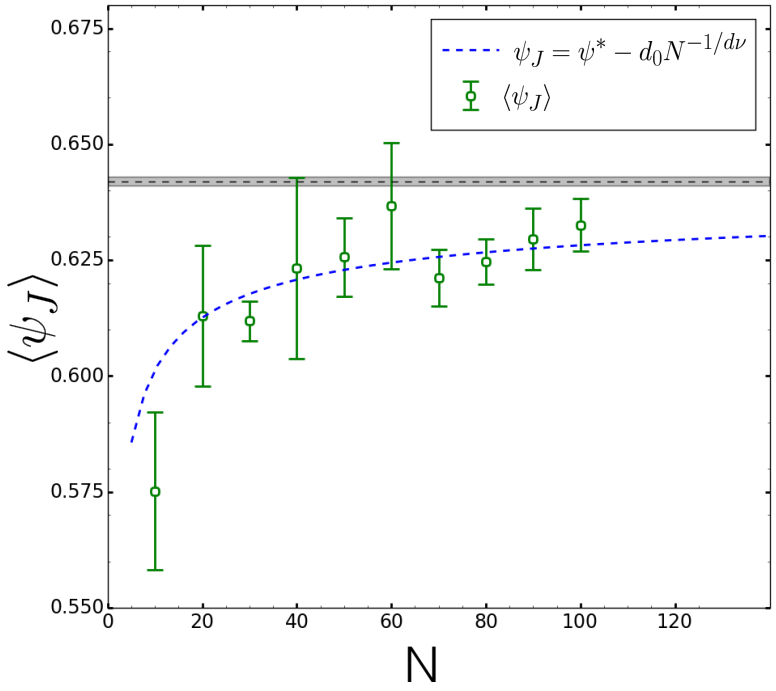

Figure S5.2: Distribution of the volume fraction at the jamming threshold ψ_J: The position of the maximum of the jamming volume fraction distribution exhibits finite-size scaling: $\psi^* - \psi_J = d_0 N^{-1/d\nu}$, where $d_0 = 0.12 \pm 0.03$, $d = 3$, $\nu = 0.71 \pm 0.08$, and $\psi^* = 0.639 \pm 0.001$ [32]. The asymptotic value is plotted as a shaded area. The green dots in the plot are the average values calculated from 100 independent simulation. Error bars give one standard deviation.

$P(x|D_p)$ is a conditional probability density function that given a sphere diameter D_p the diameter of a given disc in a plane cut ranges between x and $x + dx$. Note that disks of the same size can originate from spheres of a different size because the disc size depends on the position at which a sphere is cut.

It has been shown that a plane cut through a random spheres packing provides a distribution of disks on a plane that follows [65,66]:

$$P(x|D_p) = \frac{x}{D_p\sqrt{D_p^2 - x^2}}\left[1 - \Theta(x - D_p)\right] \tag{S5.4}$$

where $\Theta(\cdot)$ is the Heaviside function. Substituting Equation S5.4 into Equation S5.2, we get:

$$f(x) = \int_0^\infty \frac{n(D_p)}{\mu_0} \frac{x}{D_p\sqrt{D_p^2 - x^2}} \left[1 - \Theta(x - D_p)\right] dD_p \tag{S5.5}$$

Thus, for a given plane cut, the amount of the surface occupied by the disks on that plane is given as:

$$\alpha = N_\alpha \frac{\pi}{4} \int_0^\infty x^2 f(x) dx = N_\alpha \frac{\pi}{6} \frac{\mu_2}{\mu_0} \tag{S5.6}$$

where N_α is number of discs per unit cross-section area. Integrating over the whole body, we obtain the volume of the solid material: $V = \alpha L^3$, where L is a linear dimension of a body. We can see that α is proportional to the volume fraction $\phi = V/L^3$, and finally $N_\alpha \propto \phi = 1 - \phi$, where ϕ is a sample porosity. Similarly, the wetted perimeter per unit area of bed Σ can be obtained from:

$$\Sigma = N_\alpha \pi \int_0^\infty x f(x) dx = N_\alpha \frac{\pi^2}{4} \frac{\mu_1}{\mu_0} \tag{S5.7}$$

leading to $\Sigma \sim N_\alpha \propto 1 - \phi$.
Finally, the hydraulic radius R_h is:

$$R_h = \frac{1 - \alpha}{\Sigma} = \frac{2}{3\pi} \frac{\phi}{1 - \phi} \frac{\mu_2}{\mu_1} \tag{S5.8}$$

Hydraulic radius calculated from a percolation cluster is given in lattice units δ. Additionally, from Equation S5.8 we can see that μ_2 scales as $\mu_2 \propto \delta^2$, whereas μ_1 scales as $\mu_2 \propto \delta$. Thus, in Fig. 5.3 to compare hydraulic radii calculated for different lattice sizes, we scale their values by δ^{-2}.

5.5.3 Tortuosity calculation

For the fluid flow, hydraulic tortuosity τ_H is defined as:

$$\tau_H = \frac{\langle \lambda \rangle}{L} \geq 1 \tag{S5.9}$$

where $\langle \lambda \rangle$ is the mean length of the fluid particles paths and L is a linear dimension of a porous medium in the direction of a macroscopic flow. Despite this simple definition, tortuosity is not

easy to measure experimentally and computationally. In real porous media, flow streams are complicated, as the fluid fluxes continuously change their sectional area, shape, and orientation, or the flow streams branch and rejoin. It is also not clear how the average in Equation S5.9 should be calculated: over the whole volume or over the planar cross-section, and if so, what is the most proper cross-section to do this? It has been concluded that the proper hydraulic tortuosity should be calculated as an average in which streamlines are weighted with fluid fluxes[15,20,63]. Thus tortuosity can be calculated as:

$$\tau_H = \frac{\sum_i \tilde{\lambda}_i \omega_i}{\sum_i \omega_i} \tag{S5.10}$$

where i enumerates discrete streamlines, $\tilde{\lambda}_i = \lambda_i / L$, λ_i is the length of the i^{th} streamline with the weight $\omega_i = 1/t_i$, where t_i is a time in which fluid particles move along the i^{th} streamline[15]. The rationale behind ω_i factor is to weigh each streamline proportionally to the volumetric flow associated with a streamline. For the incompressible flow, t_i tells how long it takes for the particles in a given streamline to travel a distance L in a macroscopic flow direction. Thus, the average component of the velocity for that streamline, in a direction of the flow, is proportional to the weight factor $\langle v_x \rangle_i \sim \omega_i$. Extending this idea in the continuous limit, for a cross-section perpendicular to the macroscopic flow, the hydraulic tortuosity can be formulated as:

$$\tau_H = \frac{\int_A u_x(\mathrm{r}) \tilde{\lambda}(\mathrm{r}) d\sigma}{\int_A u_x(\mathrm{r}) d\sigma} \tag{S5.11}$$

where A is a cross-section perpendicular to the axis x, both integrals are taken over the surface $d\sigma \in A$, $\tilde{\lambda}(\mathrm{r})$ is the length of a streamline intersecting with the surface A at the location r (normalized by L), and $u_x(\mathrm{r})$ is the component of the velocity field at $\mathrm{r} \in A$ normal to A. Moreover, it was shown that the cut can be done not necessarily in a direction of the macroscopic flow but in principle in any direction[15]. Even though there is a freedom in the location of where the cut can be done, both integrals are still difficult to calculate numerically[13].

This numerical problem can be bypassed by noticing that[15]:

$$\tau_H = \frac{\int_A u_\perp(\mathrm{r}) \tilde{\lambda}(\mathrm{r}) d\sigma}{\int_A u_\perp(\mathrm{r}) d\sigma} = \frac{\int_V u(\mathrm{r}) d\nu}{\int_V u_x(\mathrm{r}) d\nu} \tag{S5.12}$$

and the r.h.s. can be further simplified as[15]:

$$\tau_H = \frac{\langle u \rangle}{\langle u_x \rangle} \tag{S5.13}$$

This form of tortuosity is particularly handy in numerical analysis since it requires only solving the flow field without struggling with resolving streamlines[13,20]. Some inaccuracies may occur in Equation S5.13 if the eddies exist in the flow. Although it cannot be assured that such structures do not occur in complex porous materials, the contribution from eddies to Equation S5.11 is negligible at low Reynolds numbers[15].

Finally, the velocity field is found with Lattice-Boltzmann simulations. Then, τ_H can be calculated from the values of the flow at each node in the lattice:

$$\tau_H = \frac{\sum_{\mathrm{r}} u(\mathrm{r})}{\sum_{\mathrm{r}} u_x(\mathrm{r})} \tag{S5.14}$$

where r runs over all lattice nodes[20].

5.5.4 Hydraulic tortuosity: percolation theory argument

The evolution of the void region between overlapping, randomly located spheres undergoes a percolation transition[55,56]. This transition exhibits a critical behavior and falls into a continuum percolation universality class[55,56,61]. For porous materials, a porosity ϕ acts like the percolation probability in a classical percolation theory. Above a certain porosity threshold ϕ_c, there exists a cluster that spans the whole system and facilitates fluid transport. This has been leveraged to connect tortuosity with material porosity[6,72,73]. Here we present an equivalent but simpler argument.

Percolation theory predicts that a mean distance ξ between any two sites on a cluster is given by a scaling law[58]:

$$\xi \sim |\phi - \phi_{\mathrm{c}}|^{-\nu} \tag{S5.15}$$

where ν is a critical exponent of the correlation length. The total length of a walk λ constructed on that cluster has a fractal dimension D and reads $\lambda \sim \xi^D$ [90]. At the percolation threshold, the correlation length scale ξ diverges and is the same as the system size. From the definition of a tortuosity

τ_H, we have then (close to the percolation threshold):

$$\tau_H = \frac{\lambda}{\xi} \sim \xi^{D-1} \sim |\phi - \phi_c|^{\nu(1-D)} \equiv \delta\phi^{\nu(1-D)} \tag{S5.16}$$

For a finite system, there is an additional finite-size correction that accounts for the shift of the percolation transition. Taking this into account, the scaling for τ_H reads:

$$\tau_H \sim |\phi - \phi_c + C_I \cdot L^{-1/\nu}|^{\nu(1-D)} \tag{S5.17}$$

where C_I is a constant and it is of the order of $C_I \sim \mathcal{O}(1)$.
It has been shown that the most probable traveling length of an incompressible flow on a percolating cluster falls into the same universality class as the optimal path in strongly disordered media and the shortest path in the invasion percolation with trapping[74,75] — for which the fractal dimension is $D \approx 1.43$[76,77]. Finally, taking the exponent $\nu \approx 0.88$, one gets a scaling law for tortuosity ($L \to \infty$): $\tau_H \sim |\phi - \phi_c|^{-0.38} \equiv \delta\phi^{-0.38}$. For finite systems ($N < \infty$), tortuosity reaches maximum value at $\delta\phi = 0$, which scales with the system size as $\tau_H^{\max} \sim L^{-(1-D)} = N^{-(1-D)/d} \approx N^{0.14}$, where $d = 3$ is a system dimension.

A similar scaling argument was numerically tested for 2D overlapping squares on Cartesian lattice[15], where via finite-size scaling analysis, it was shown that the tortuosity in the neighborhood of percolation transition is controlled by the fractal geometry of a percolating channel.

5.5.5 Scaling argument for the γ exponent

Taking a planar cut through the porous material, we observe n_c capillaries distributed over the area of the cut. If the material is isotropic, the direction of the cut does not matter, and we can assume that the cut is made perpendicularly to the direction of fluid transport. This plane-cut would obviously contain cross-sections of all the capillaries that are responsible for the liquid transport thorough the material in the given direction. Close to the percolation threshold, we expect to have a single capillary in the area that is proportional to ξ^2, where ξ is the correlation length. If that is the case, the expected number of capillaries penetrating thorough the material is $n_c \propto L^2/\xi^2$, where L is the linear size of the body. ξ is related to the exponent of the correlation length ($\nu \approx 0.88$) as $\xi \sim \delta\phi^{-\nu}$. Therefore, we have a power-law relation between the number of capillaries and $\delta\phi$ which reads $n_c \sim \delta\phi^{2\nu} \approx \delta\phi^{1.76}$.

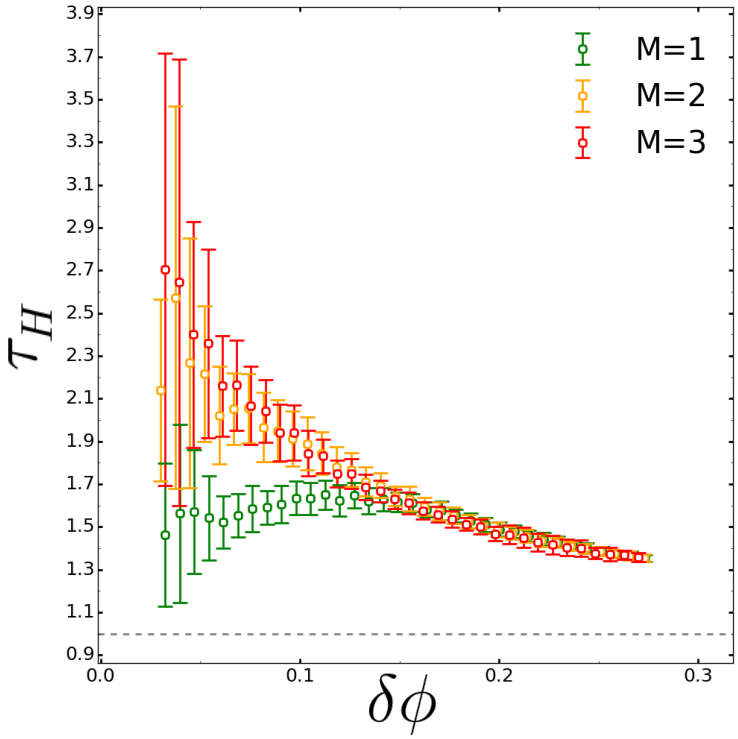

Figure S5.3: The same numerical data as in Fig. 5.4 — with error bars.

5.5.6 Parameters fitting procedure

Parameters fitting and standard deviation estimations are done with a non-linear least squares method from the `scipy` Python library.

Extrapolating percolation threshold to the continuum limit

In Fig. 5.2 D, we extrapolate a percolation threshold down to the continuum limit ϕ_c^*, *i.e.* $\delta \to 0$. To that end, we fit a sigmoid function to the percolation probability data in Fig. 5.2 C. Next, for different δ we take a porosity at which the percolation probability is equal $1/2$ as a percolation threshold. Finally, we fit a power-law dependence: $\phi_c - \phi_c^* = A \cdot \delta^\beta$. The fitting results are in Table S5.1 (row: Fig. 5.2 D). Parameters are obtained as a result of minimization of the function: Error $= \sum_i \left(\phi_{c,i}^{\text{num}} - \phi_{c,i}^{\text{fit}}\right)^2$, where $\phi_{c,i}^{\text{num}}$ is a percolation threshold estimated from the numerical

data, and $\phi_{c,i}^{\text{fit}}$ is estimated from the power-law dependence for varying ϕ_c^*, A, and β.

Fitting power-law dependences for tortuosity

We fit a power-law dependency for tortuosity data obtained from Lattice-Boltzmann simulations. The relation has a functional form $\tau_{\text{H}} = \text{C}_\tau(\phi - \phi_{\text{c}})^{-0.38}$, where there are only two fitting parameters: ϕ_c and a constant factor C_τ. Porosity ϕ is a value known from Finite Elements simulations, and the exponent -0.38 is predicted from a percolation theory, see Section 5.5.4. We perform a non-linear fit by minimizing the error function: Error $= \sum_{\text{i}} \left(\tau_{\text{i}}^{\text{num}} - \tau_{\text{i}}^{\text{fit}}\right)^2$, where the index i runs over all experimental samples, $\tau_{\text{i}}^{\text{num}}$ is a numerical tortuosity from LB simulations for the system i, whereas $\tau_{\text{i}}^{\text{fit}}$ is a fit to the power-law dependency. The results are given in the Table S5.1 (row: Fig. 5.4 B).

Parameters estimation for permeability

Fits are done for three different permeability relations: i) $\kappa = C_\kappa(\phi - \phi_c)^{\gamma+0.76}\phi^2(1-\phi)^{-2}$, ii) $\kappa = C_\kappa(\phi - \phi_c)^{2.52}\phi^2(1-\phi)^{-2}$, and iii) $\kappa = C_\kappa(\phi - \phi_c)^{\bar{e}}$. In Fig. 5.5, Fig. S5.5 A, and Fig. S5.5 B, a percolation threshold is a fitting parameter ϕ_c, whereas in Fig. S5.5 C and Fig. S5.5 D, the percolation threshold is held fixed and estimated (for N=50) from the equation $\phi(\delta) = 0.035 + 3.76 \cdot \delta^{1.1}$, where $\delta = 0.04$ and the numerical parameters are taken from Fig. 5.2 D. Fits are done for two different error functions i) Error $= \sum_{\text{i}} \left(\log \kappa_{\text{i}}^{\text{num}} - \log \kappa_{\text{i}}^{\text{fit}}\right)^2$ in Fig. 5.5 and Fig. S5.5 A and C, and ii) Error $= \sum_{\text{i}} \left(\kappa_{\text{i}}^{\text{num}} - \kappa_{\text{i}}^{\text{fit}}\right)^2$ in Fig. S5.5 B and D. $\kappa_{\text{i}}^{\text{num}}$ is a permeability value obtained from LB simulations for the i^{th} packing, whereas $\kappa_{\text{i}}^{\text{fit}}$ is a value for a given set of parameters. The results of these fits can be found in Table S5.1.

Figure	Formula	Fitting Parameters	Error Function	Parameter Values
Fig. 5.2 D	$\phi_c(\delta, N) - \phi_c^*(N) = A_N \cdot \delta^{\beta_N}$	A_N,$\phi_c^*(N)$, β_N	$\sum_i \left(\phi_{c,i}^{num} - \phi_{c,i}^{fit}\right)^2$	$A_{16} = 3.70 \pm 0.9$ $A_{32} = 3.77 \pm 0.7$ $A_{50} = 3.67 \pm 1.0$ $\phi_c^*(16) = 0.064 \pm 0.010$ $\phi_c^*(32) = 0.053 \pm 0.020$ $\phi_c^*(50) = 0.035 \pm 0.014$ $\beta_{16} = 1.2 \pm 0.2$ $\beta_{32} = 1.0 \pm 0.1$ $\beta_{50} = 1.1 \pm 0.2$
Fig. 5.4 B	$\tau_H = C_\tau \left(\phi - \phi_c\right)^{-0.38}$	C_τ,ϕ_c	$\sum_i \left(\tau_i^{num} - \tau_i^{fit}\right)^2$	$\phi_c = 0.124 \pm 0.004$
Fig. 5.5	$\kappa = C_\kappa(\phi - \phi_c)^{\gamma+0.76}\phi^2(1-\phi)^{-2}$	C_κ,ϕ_c,γ	$\sum_i \left(\log \kappa_i^{num} - \log \kappa_i^{fit}\right)^2$	$\phi_c = 0.146 \pm 0.003$ $\gamma = 0.83 \pm 0.17$
	$\kappa = C_\kappa(\phi - \phi_c)^{2.52}\phi^2(1-\phi)^{-2}$	C_κ,ϕ_c	$\sum_i \left(\log \kappa_i^{num} - \log \kappa_i^{fit}\right)^2$	$\phi_c = 0.101 \pm 0.038$
	$\kappa = C_\kappa(\phi - \phi_c)^{\bar{e}}$	C_κ,ϕ_c,$\bar{e}$	$\sum_i \left(\log \kappa_i^{num} - \log \kappa_i^{fit}\right)^2$	$\phi_c = 0.115 \pm 0.053$ $\bar{e} = 3.61 \pm 0.30$
Fig. S5.5 A	$\kappa = C_\kappa(\phi - \phi_c)^{\gamma+0.76}\phi^2(1-\phi)^{-2}$	C_κ,ϕ_c,γ	$\sum_i \left(\log \kappa_i^{num} - \log \kappa_i^{fit}\right)^2$	$\phi_c = 0.146 \pm 0.003$ $\gamma = 0.83 \pm 0.17$
	$\kappa = C_\kappa(\phi - \phi_c)^{2.52}\phi^2(1-\phi)^{-2}$	C_κ,ϕ_c	$\sum_i \left(\log \kappa_i^{num} - \log \kappa_i^{fit}\right)^2$	$\phi_c = 0.101 \pm 0.038$
	$\kappa = C_\kappa(\phi - \phi_c)^{\bar{e}}$	C_κ,ϕ_c,$\bar{e}$	$\sum_i \left(\log \kappa_i^{num} - \log \kappa_i^{fit}\right)^2$	$\phi_c = 0.115 \pm 0.053$ $\bar{e} = 3.61 \pm 0.30$
Fig. S5.5 B	$\kappa = C_\kappa(\phi - \phi_c)^{\gamma+0.76}\phi^2(1-\phi)^{-2}$	C_κ,ϕ_c,γ	$\sum_i \left(\kappa_i^{num} - \kappa_i^{fit}\right)^2$	$\phi_c = 0.150 \pm 0.002$ $\gamma = 0.86 \pm 0.14$

	$\kappa = C_\kappa(\phi - \phi_c)^{2.52}\phi^2(1-\phi)^{-2}$	C_κ,ϕ_c	$\sum_i \left(\kappa_i^{\text{num}} - \kappa_i^{\text{fit}}\right)^2$	$\phi_c = 0.060 \pm 0.066$
	$\kappa = C_\kappa(\phi - \phi_c)^{\bar{e}}$	C_κ,ϕ_c,$\bar{e}$	$\sum_i \left(\kappa_i^{\text{num}} - \kappa_i^{\text{fit}}\right)^2$	$\phi_c = 0.120 \pm 0.001$ $\bar{e} = 3.88 \pm 0.18$
Fig. S5.5 C	$\kappa = C_\kappa(\phi - \phi_c)^{\gamma+0.76}\phi^2(1-\phi)^{-2}$	C_κ,γ	$\sum_i \left(\log\kappa_i^{\text{num}} - \log\kappa_i^{\text{fit}}\right)^2$	$\phi_c(\text{fixed}) = 0.141$ $\gamma = 0.91 \pm 0.13$
	$\kappa = C_\kappa(\phi - \phi_c)^{2.52}\phi^2(1-\phi)^{-2}$	C_κ	$\sum_i \left(\log\kappa_i^{\text{num}} - \log\kappa_i^{\text{fit}}\right)^2$	$\phi_c(\text{fixed}) = 0.141$
	$\kappa = C_\kappa(\phi - \phi_c)^{\bar{e}}$	C_κ,$\bar{e}$	$\sum_i \left(\log\kappa_i^{\text{num}} - \log\kappa_i^{\text{fit}}\right)^2$	$\phi_c(\text{fixed}) = 0.141$ $\bar{e} = 2.72 \pm 0.14$
Fig. S5.5 D	$\kappa = C_\kappa(\phi - \phi_c)^{\gamma+0.76}\phi^2(1-\phi)^{-2}$	C_κ,γ	$\sum_i \left(\kappa_i^{\text{num}} - \kappa_i^{\text{fit}}\right)^2$	$\phi_c(\text{fixed}) = 0.141$ $\gamma = 0.97 \pm 0.16$
	$\kappa = C_\kappa(\phi - \phi_c)^{2.52}\phi^2(1-\phi)^{-2}$	C_κ	$\sum_i \left(\kappa_i^{\text{num}} - \kappa_i^{\text{fit}}\right)^2$	$\phi_c(\text{fixed}) = 0.141$
	$\kappa = C_\kappa(\phi - \phi_c)^{\bar{e}}$	C_κ,$\bar{e}$	$\sum_i \left(\kappa_i^{\text{num}} - \kappa_i^{\text{fit}}\right)^2$	$\phi_c(\text{fixed}) = 0.141$ $\bar{e} = 3.50 \pm 0.17$

Table S5.1: Fitting parameters for a percolation threshold in the continuum limit ϕ_c^*, tortuosity τ_H, and permeability κ that are investigated in this chapter. In Fig. S5.5 C and Fig. S5.5 D, ϕ_c is fixed, so no standard deviations are given.

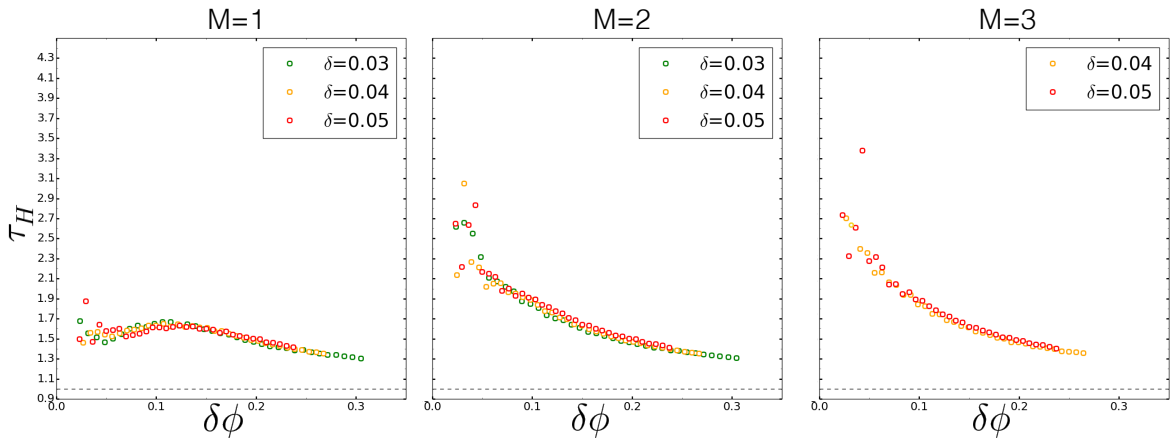

Figure S5.4: Tortuosity calculated for three different δ and different lattice refinement levels: LB simulations are performed on percolating clusters that are detected for three different lattice sizes: $\delta = [0.03, 0.04, 0.05]$, and $N = 50$. The flow fields are resolved on lattices with a size $\tilde{\delta} = \delta/\mathrm{M}$, where $\mathrm{M} = 1, 2, 3$ are lattice refinement levels[13]. Tortuosity increases as the refinement level increases, consistently with previous studies[13]. The same behavior is observed for all δ. This suggests that the abrupt increase of τ_H close to the percolation threshold is caused by the fractal geometry of the percolation cluster rather than by artifacts of the numerical methods. Each data-point is an average from about 100 simulations. τ_H is given as a function of $\delta\phi$, where lattice size dependent percolation threshold was estimated from the fits in Fig. 5.2 D, and Table S5.1: $\{\phi_c(0.03) = 0.113, \phi_c(0.04) = 0.141, \phi_c(0.05) = 0.171\}$. Error-bars are not shown for better readability.

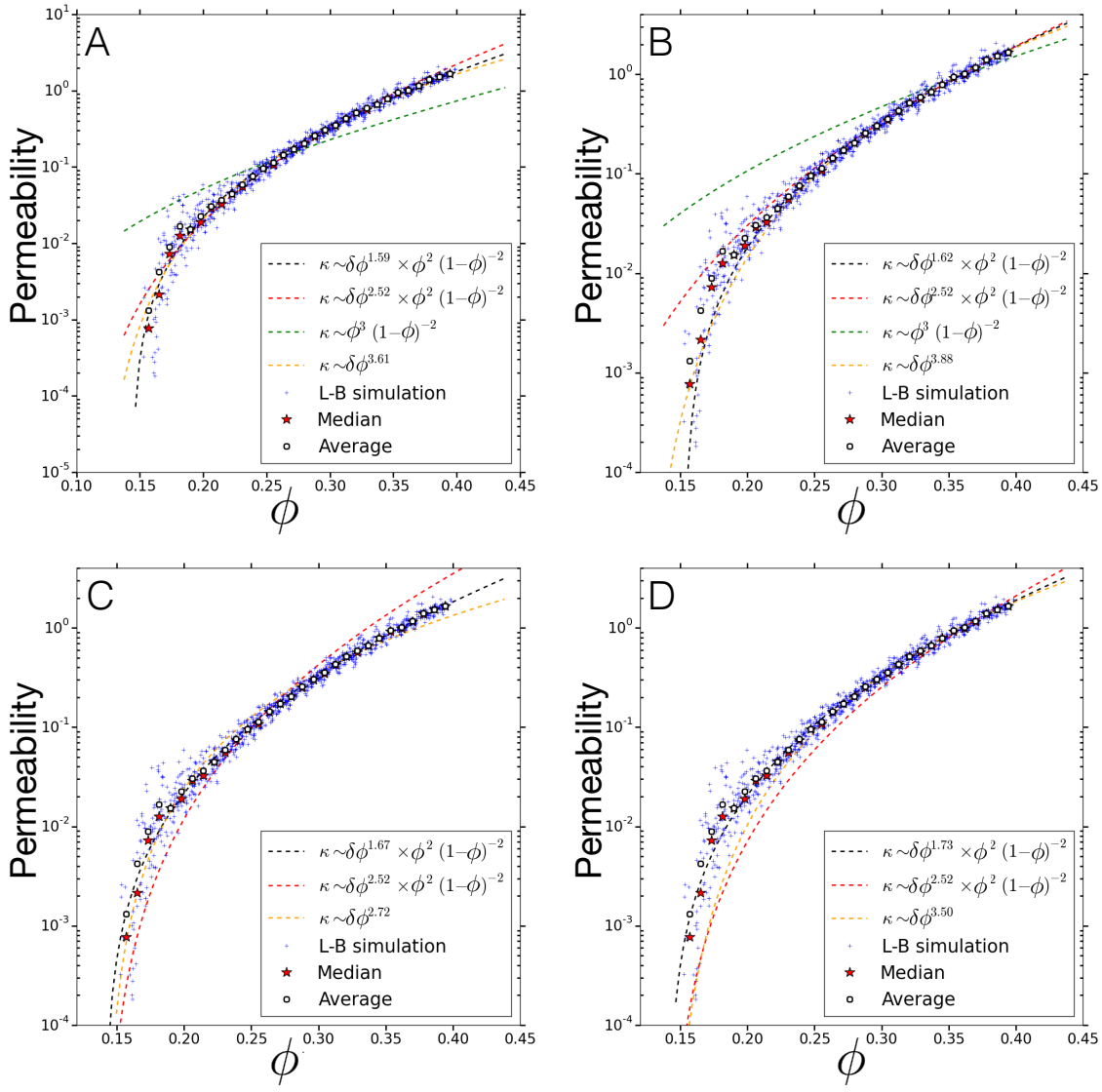

Figure S5.5: Permeability obtained from Lattice-Boltzmann simulations for the system size N=50, the lattice resolution $\delta = 0.04$, and the lattice size for the fluid phase $\tilde{\delta} = \delta/3$. Symbols are the same as in Fig. 5.5; blue crosses represent permeability for individual simulations, black open circles represent binned averages, red stars are median values, and dashed lines correspond to different models. Fitted parameters are given in Table S5.1. In Fig. S5.5 A and B, ϕ_c is a free parameter, whereas in Fig. S5.5 D, ϕ_c is fixed at $\phi_c = 0.141$ (see Section 5.5.6). Classical Kozeny-Carman model ($\kappa \sim \phi^3/(1-\phi)^2$) is given for a comparison in Fig. S5.5 A and B. Error functions used in a fitting procedure are given in Table S5.1.

References

[1] M. Sahimi. Flow phenomena in rocks: from continuum models to fractals, percolation, cellular automata, and simulated annealing. *Reviews of Modern Physics*, 65:1393–1534, 1993.

[2] J. Bear and A. H.-D. Cheng. *Modeling Groundwater Flow and Contamination Transport*. Springer, 2010.

[3] M. Sahimi. *Flow and Transport in Porous Media and Fractured Rock: From Classical Methods to Modern Approaches, 2nd Edition*. Wiley-VCH Verlag GmbH & Co. KGaA, 2011.

[4] M. Delarue, J. Hartung, C. Schreck, P. Gniewek, L. Hu, S. Herminghaus, and O. Hallatschek. Self-driven jamming in growing microbial populations. *Nature Physics*, 12(8): 762, 2016.

[5] R. Hornung, A. Grunberger, C. Westerwalbesloh, D. Kohlheyer, G. Gompper, and J. Elgeti. Quantitative modelling of nutrient-limited growth of bacterial colonies in microfluidic cultivation. *Journal of the Royal Society Interface*, 15:20170713, 2018.

[6] A. Hunt and M. Sahimi. Flow, transport, and reaction in porous media: Percolation scaling, critical-path analysis, and effective medium approximation. *Reviews of Geophysics*, 55:993–1078, 2017.

[7] J.-F. Gaillard, C. Chen, S. Stonedahl, B. Lau, D. Keane, and A. Packman. Imaging of colloidal deposits in granular porous media by x-ray difference micro-tomography. *Geophysical Research Letters*, 34:L18404, 2007.

[8] D. Gostovic, J. Smith, D. Kundinger, K. Jones, and E. Wachsman. Three-dimensional reconstruction of porous lscf cathodes. *Electrochemical and Solid-State Letters*, 10:B214–B217, 2007.

[9] P. Tahmasebi, M. Sahimi, and J. Andrade. Image-based modeling of granular porous media. *Geophysical Research Letters*, 44:4738–4746, 2017.

[10] A. Cancelliere, C. Chang, E. Foti, D. H. Rothman, and S. Succi. The permeability of a random medium: comparison of simulation with theory. *Physics of Fluids A: Fluid Dynamics*, 2(12):2085–2088, 1990.

[11] A. Koponen, M. Kataja, and J. Timonen. Tortuous flow in porous media. *Physical Review E*, 54(1):406, 1996.

[12] A. Koponen, M. Kataja, and J. Timonen. Permeability and effective porosity of porous media. *Physical Review E*, 56(3):3319, 1997.

[13] M. Matyka, A. Khalili, and Z. Koza. Tortuosity-porosity relation in porous media flow. *Physical Review E*, 78(2):026306, 2008.

[14] Z. Koza, M. Matyka, and A. Khalili. Finite-size anisotropy in statistical uniform porous media. *Physical Review E*, 79:066306, 2009.

[15] A. Duda, Z. Koza, and M. Matyka. Hydraulic tortuosity in arbitrary porous media flow. *Physical Review E*, 84(3):036319, 2011.

[16] C. Scholz, F. Wirner, J. Gotz, U. Rude, G. Schroder-Turk, K. Mecke, and C. Bechinger. Permeability of porous materials determined from the euler characteristic. *Physical Review Letters*, 109:264504, 2012.

[17] R. Zallen. *The physics of amorphous solids*. John Wiley & Sons, 1983.

[18] R. S. Maier, D. Kroll, Y. Kutsovsky, H. Davis, and R. S. Bernard. Simulation of flow through bead packs using the lattice boltzmann method. *Physics of Fluids*, 10(1):60–74, 1998.

[19] M. L. Stewart, A. L. Ward, and D. R. Rector. A study of pore geometry effects on anisotropy in hydraulic permeability using the lattice-boltzmann method. *Advances in Water Resources*, 29(9):1328–1340, 2006.

[20] M. Matyka and Z. Koza. How to calculate tortuosity easily? In *AIP Conference Proceedings 4*, pages 17–22. AIP, 2012.

[21] S. Bakhshian and M. Sahimi. Computer simulation of the effect of deformation on the morphology and flow properties of porous media. *Physical Review E*, 94(4):042903, 2016.

[22] P. Lehmann, M. Berchtold, B. Ahrenholz, T. J., A. Kaestner, M. Krafczyk, H. Fluhler, and H. Kunsch. Impact of geometrical properties on permeability and fluid phase distribution in porous media. *Advances in Water Resources*, 31:1188–1204, 2008.

[23] C. Chen, A. I. Packman, and J.-F. Gaillard. Pore-scale analysis of permeability reduction resulting from colloid deposition. *Geophysical Research Letters*, 35(7):L07404, 2008.

[24] C. Chen, B. L. Lau, J.-F. Gaillard, and A. I. Packman. Temporal evolution of pore geometry, fluid flow, and solute transport resulting from colloid deposition. *Water Resources Research*, 45(6), 2009.

[25] J. Jose, G. Blab, A. van Blaaderen, and A. Imhof. Jammed elastic shells - a 3d experimental soft frictionless granular system. *Soft Matter*, 11:1800–1813, 2015.

[26] J. Jose, A. van Blaaderen, and A. Imhof. Random three-dimensional jammed packings of elastic shells acting as force sensors. *Physical Review E*, 93:062901, 2016.

[27] A. Boromand, A. Signoriello, F. Ye, C. O'Hern, and M. Shattuck. Jamming of deformable polygons. *arXiv:1801.06150*, 2018.

[28] S. Sandersius and T. Newman. Modeling cell rheology with the subcellular element model. *Physical Biology*, 10:015002, 2008.

[29] F. Milde, G. Tauriello, H. Haberkern, and P. Koumoutsakos. Sem++: A particle model of cellular growth, signaling and migration. *Computational Particle Mechanics*, 1:211–227, 2014.

[30] Y. Jamali, M. Azimi, and M. Mofrad. A sub-cellular viscoelastic model for cell population mechanics. *PLoS ONE*, 5:e12097, 2010.

[31] P. Gniewek. *Mechanics of Confined Microbial Populations*. PhD thesis, University of California, Berkeley, 2018.

[32] C. S. O'Hern, L. E. Silbert, A. J. Liu, and S. R. Nagel. Jamming at zero temperature and zero applied stress: The epitome of disorder. *Physical Review E*, 68(1):011306, 2003.

[33] J. Kozeny. Uber kapillare leitung des wassers im boden. *Sitzungsber Akad. Wiss. Wien.*, 136: 271–306, 1927.

[34] P. C. Carman. Fluid flow through granular beds. *Transactions-Institution of Chemical Engineers*, 15:150–166, 1937.

[35] A. Costa. Permeability-porosity relationship: A reexamination of the kozeny-carman equation based on a fractal pore-space geometry assumption. *Geophysical Research Letters*, 33(2), 2006.

[36] N. Nishiyama and T. Yokoyama. Permeability of porous media: Role of the critical pore size. *Journal of Geophysical Research: Solid Earth*, 122:6955–6971, 2017.

[37] E. Bitzek, P. Koskinen, F. Gähler, M. Moseler, and P. Gumbsch. Structural relaxation made simple. *Physical Review Letters*, 97(17):170201, 2006.

[38] H. Delingette. Triangular springs for modeling nonlinear membranes. *IEEE transactions on visualization and computer graphics*, 14(2):329–341, 2008.

[39] H. Delingette. Biquadratic and quadratic springs for modeling st venant kirchhoff materials. *Biomedical Simulation*, pages 40–48, 2008.

[40] S. Succi. *The lattice Boltzmann equation: for fluid dynamics and beyond*. Oxford University Press, 2001.

[41] C. Arns, M. Knackstedt, and N. Martys. Cross-property correlations and permeability estimation in sandstone. *Physical Review E*, 72:046304, 2005.

[42] C. Pan, L.-S. Luo, and C. T. Miller. An evaluation of lattice boltzmann schemes for porous medium flow simulation. *Computers & Fluids*, 35:898–909, 2006.

[43] C. Jin, P. A. Langston, G. E. Pavlovskaya, M. R. Hall, and S. P. Rigby. Statistics of highly heterogeneous flow fields confined to three-dimensional random porous media. *Physical Review E*, 93(1):013122, 2016.

[44] S. Singh, F. Jiang, and T. Tsuji. Impact of the kinetic boundary condition on porous media flow in the lattice boltzmann formulation. *Physical Review E*, 96(1):013303, 2017.

[45] L. Amarsid, J.-Y. Delenne, P. Mutabaruka, Y. Monerie, F. Perales, and F. Radjai. Viscoinertial regime of immersed granular flows. *Physical Review E*, 96(1):012901, 2017.

[46] K. N. Premnath and J. Abraham. Three-dimensional multi-relaxation time (mrt) lattice-boltzmann models for multiphase flow. *Journal of Computational Physics*, 224:539–559, 2007.

[47] J. Latt. *Choice of units in lattice Boltzmann simulations*, 2008.

[48] R. Jager, M. Mendoza, and H. Herrmann. Mechanism behind erosive bursts in porous media. *Physical Review Letters*, 119:124501, 2017.

[49] R. Jager, M. Mendoza, and H. Herrmann. Channelization in porous media driven by erosion and deposition. *Physical Review E*, 95:013110, 2017.

[50] Z. Koza, G. Kondrat, and K. Suszczyński. Percolation of overlapping squares or cubes on a lattice. *Journal of Statistical Mechanics: Theory and Experiment*, 2014(11):P11005, 2014.

[51] B. Halperin, S. Feng, and P. Sen. Differences between lattice and continuum percolation transport exponents. *Physical Review Letters*, 54:2391–2394, 1985.

[52] S. Feng, B. Halperin, and P. Sen. Transport properties of continuum systems near the percolation threshold. *Physical Review B*, 35:197–214, 1987.

[53] A. R. Kerstein. Equivalence of the void percolation problem for overlapping spheres and a network problem. *Journal of Physics A: Mathematical and General*, 16(13):3071, 1983.

[54] W. Elam, A. Kerstein, and J. J. Rehr. Critical properties of the void percolation problem for spheres. *Physical Review Letters*, 52:1516–1519, 1984.

[55] S. Van der Marck. Network approach to void percolation in a pack of unequal spheres. *Physical Review Letters*, 77(9):1785, 1996.

[56] D. Priour Jr. Percolation through voids around overlapping spheres: a dynamically based finite-size scaling analysis. *Physical Review E*, 89(1):012148, 2014.

[57] J. Liu and K. Regenauer-Lieb. Application of percolation theory to microtomography of structured media: Percolation threshold, critical exponents, and upscaling. *Physical Review E*, 83:016106, 2011.

[58] D. Stauffer and A. Aharony. *Introduction to Percolation Theory*. Oxford University Press, New York, 1994.

[59] B. Ghanbarian and C. Berg. Formation factor in bentheimer and fontainebleau sandstones: Theory compared with pore-scale numerical simulations. *Advances in Water Resources*, 107: 139 – 146, 2017.

[60] B. Lorenz, I. Orgzall, and H.-O. Heuer. Universality and cluster structures in continuum models of percolation with two different radius distributions. *Journal of Physics A: Mathematical and General*, 26(18):4711, 1993.

[61] M. Rintoul and S. Torquato. Precise determination of the critical threshold and exponents in a three-dimensional continuum percolation model. *Journal of Physics A: Mathematical and General*, 30(16):L585, 1997.

[62] N. S. Martys, S. Torquato, and D. Bentz. Universal scaling of fluid permeability for sphere packings. *Physical Review E*, 50(1):403, 1994.

[63] M. B. Clennell. Tortuosity: a guide through the maze. *Geological Society, London, Special Publications*, 122(1):299–344, 1997.

[64] C. Arns, M. Knackstedt, W. Pinczewski, and K. Mecke. Euler-poincare characteristics of classes of disordered media. *Physical Review E*, 63:031112, 2001.

[65] K. Ng. A model for flow regime transitions in concurrent down-flow trickle-bed reactors. *AIChE Journal*, 32(1):115–122, 1986.

[66] M. J. MacDonald, C.-F. Chu, P. P. Guilloit, and K. M. Ng. A generalized blake-kozeny equation for multisized spherical particles. *AIChE Journal*, 37(10):1583–1588, 1991.

[67] P. Leath and G. Reich. Scaling form for percolation cluster size and perimeters. *Journal of Physics C: Solid State Physics*, 11:4017–4035, 1978.

[68] B. Yu and P. Cheng. A fractal permeability model for bi-dispersed porous media. *International Journal of Heat and Mass Transfer*, 45:2983–2993, 2002.

[69] P. Xu and B. Yu. Developing a new form of permeability and kozeny–carman constant for homogeneous porous media by means of fractal geometry. *Advances in Water Resources*, 31 (1):74–81, 2008.

[70] M. M. Ahmadi, S. Mohammadi, and A. N. Hayati. Analytical derivation of tortuosity and permeability of monosized spheres: A volume averaging approach. *Physical Review E*, 83: 026312, 2011.

[71] M. M. Ahmadi, S. Mohammadi, and A. N. Hayati. How particle shape affects the flow through granular materials. *Physical Review E*, 85:036310, 2012.

[72] B. Ghanbarian, A. G. Hunt, M. Sahimi, R. P. Ewing, and T. E. Skinner. Percolation theory generates a physically based description of tortuosity in saturated and unsaturated porous media. *Soil Science Society of America Journal*, 77(6):1920–1929, 2013.

[73] B. Ghanbarian, A. G. Hunt, R. P. Ewing, and M. Sahimi. Tortuosity in porous media: a critical review. *Soil Science Society of America Journal*, 77(5):1461–1477, 2013.

[74] Y. Lee, J. S. Andrade Jr, S. V. Buldyrev, N. V. Dokholyan, S. Havlin, P. R. King, G. Paul, and H. E. Stanley. Traveling time and traveling length in critical percolation clusters. *Physical Review E*, 60(3):3425, 1999.

[75] A. Sheppard, M. Knackstedt, W. Pinczewski, and M. Sahimi. Invasion percolation: new algorithms and universality classes. *Journal of Physics A: Mathematical and General*, 32: L521–L529, 1999.

[76] M. Porto, S. Havlin, S. Schwarzer, and A. Bunde. Optimal path in strong disorder and shortest path in invasion percolation with trapping. *Physical Review Letters*, 79(21):4060, 1997.

[77] M. Cieplak, A. Maritan, and J. R. Banavar. Invasion percolation and eden growth: Geometry and universality. *Physical Review Letters*, 76(20):3754, 1996.

[78] W. Sobieski, M. Matyka, J. Golembiewski, and S. Lipinski. The path tracking method as an alternative for tortuosity determination in granular beds. *Granular Matter*, 20:1–14, 2018.

[79] G. Mavko and A. Nur. The effect of a percolation threshold in the kozeny-carman relation. *Geophysics*, 62(5):1480–1482, 1997.

[80] C. Berg. Permeability description by characteristic length, tortuosity, constriction and porosity. *Transport in Porous Media*, 103:381–400, 2014.

[81] B. Yu. Analysis of flow in fractal porous media. *Applied Mechanics Reviews*, 61:050801, 2008.

[82] R. McGregor. The effect of rate of flow on rate of dyeing ii–the mechanism of fluid flow through textiles and its significance in dyeing. *Journal of the Society of Dyers and Colourists*, 81:429–438, 1965.

[83] C. Berg and R. Held. Fundamental transport property relations in porous media incorporating detailed pore structure description. *Transport in Porous Media*, 112:467–487, 2016.

[84] S. W. Coleman and J. C. Vassilicos. Transport properties of saturated and unsaturated porous fractal materials. *Physical Review Letters*, 100:035504, Jan 2008.

[85] C. F. Berg. Re-examining archie's law: Conductance description by tortuosity and constriction. *Physical Review E*, 86:046314, Oct 2012.

[86] G. E. Archie et al. The electrical resistivity log as an aid in determining some reservoir characteristics. *Transactions of the AIME*, 146(01):54–62, 1942.

[87] P.-Z. Wong. Conductivity, permeability, and electrokinetics. In P. zen Wong, editor, *Methods in the Physics of Porous Media*, volume 35 of *Experimental Methods in the Physical Sciences*, pages 119 – 159. Academic Press, 1999.

[88] M. Rintoul. Precise determination of the void percolation threshold for two distributions of overlapping spheres. *Physical Review E*, 62:68–72, 2000.

[89] M. P. Allen and D. J. Tildesley. *Computer simulation of liquids*. Oxford university press, 1989.

[90] S. Havlin and D. Ben-Avraham. Diffusion in disordered media. *Advances in Physics*, 36: 695–798, 1987.

6
Conclusions

The central theme of this thesis is the notion that microbial populations, on the scale of hundreds of cells, can be described as a granular material rather than a continuum. This proposal was extensively corroborated in Chapter 2. In the aforementioned chapter, combining microfluidics experiments, individual based simulations, and image analysis methods, we revealed that the structure of confined microbial populations is disordered, that the population dynamics is intermittent, and that contact forces are heterogeneous. We also found that these confined populations can generate and strive under very large pressures that can reach even the magnitude of 1 MPa. In Chapter 3, we show that the feedback of mechanical stress on the growth rate controls the mechanical properties of budding yeast population in a non-trivial way. Aiming at further understanding of the structure of extremely compacted microbial populations, I developed a model that treats cells as separate entities, but also captures the deformation of these cells with great accuracy. Armed with this numerical model, in Chapter 4, I uncovered the structural consequences of cells deformability and how these deformation may give rise to the unexpected emergence of rotational degrees of freedom that need to be constrained. Finally, in Chapter 5, capitalizing on the idea of treating a microbial population as a living granular material, I studied fluid transport through the packings of compressed elastic shells — our proxy model of a compacted microbial population. The notion of these packings as a granular porous material, combined with percolation theory, provided us with a description of the flow obstruction near the percolation threshold.

Appendix A
Unstructured Mesh Generation on a Sphere

A.1 Mesh Generation

Mesh generation is the first step in a wide range of applications from scientific computing to computer graphics. A mesh is a set of nodes and a topology of links between these points. These nodes and links determine where and how the model is solved.

The simplest approach to mesh generation is generating a structured mesh such as the Cartesian grid. In this approach, the nodes are located at the intersection of perpendicular lines and the mesh elements are rectangular. This kind of mesh is extremely simple and quick to generate. However, applicability of this mesh is also limited to the simplest geometries, and the mesh generation method requires modifications for curved boundaries — so-called a body-fitted mesh generation[1]. This is still essentially the Cartesian grid, but mesh elements are shaped to fit the boundaries. This procedure gets increasingly difficult as the complexity of the boundary increases and it is not guaranteed that such a procedure exists for all boundaries. Alternatively, an unstructured mesh can be generated. One of the advantages of the unstructured mesh is that nodes can be set on the boundary surface, allowing for the greater accuracy required in numerical calculations. Another advantage is flexibility in terms of boundaries to which this algorithm can be applied, and the number of nodes that represent the mesh. There is some substantial work done towards mesh generation, and some numerical packages are publicly available, for example: `DistMesh`[2], and `Triangle`[3].

A.2 Sphere Triangulation Algorithms

A.2.1 Iterative Algorithms

Iterative triangulation of a sphere is a mesh generation method where the algorithm starts with a predefined triangulation (called in this chapter *a triangulation level 1*), and then a higher resolution mesh is generated in an iterative manner. The iterative process replaces every triangle belonging to

the mesh by a set of triangles obtained by a subdivision of the original ones and projecting it back onto the sphere. Examples of a triangle subdivision process are depicted in Figure A.1. `Simple` subdivision splits a triangle into two triangles (*bisection*), where the longest side is divided into two pieces of the same length, and the middle point is connected to the node on the opposite side of the triangle, Figure A.1 a. For `Simple` triangulation, the starting triangulation is a cube with a topology as in Figure A.2 a.1. `Platonic` triangulation uses any Platonic figure as a starting point, for example, an octahedron or an icosahedron, *cf.* Figure A.2 b.1 and c.1[4,5]. Every equilateral triangle is subdivided into four new triangles (*quadrisection*), and the new nodes are projected back onto the sphere, Figure A.1 b.

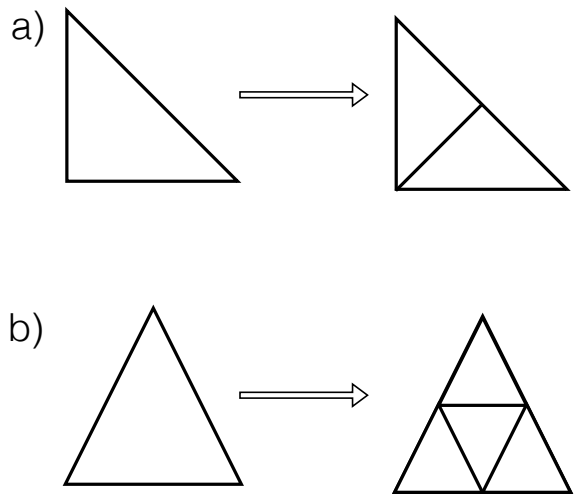

Figure A.1: Subdivision of a triangle: a) Bisection in the `Simple` algorithm. b) Quadrisection of an equilateral triangle used in the `Platonic` triangulation algorithm.

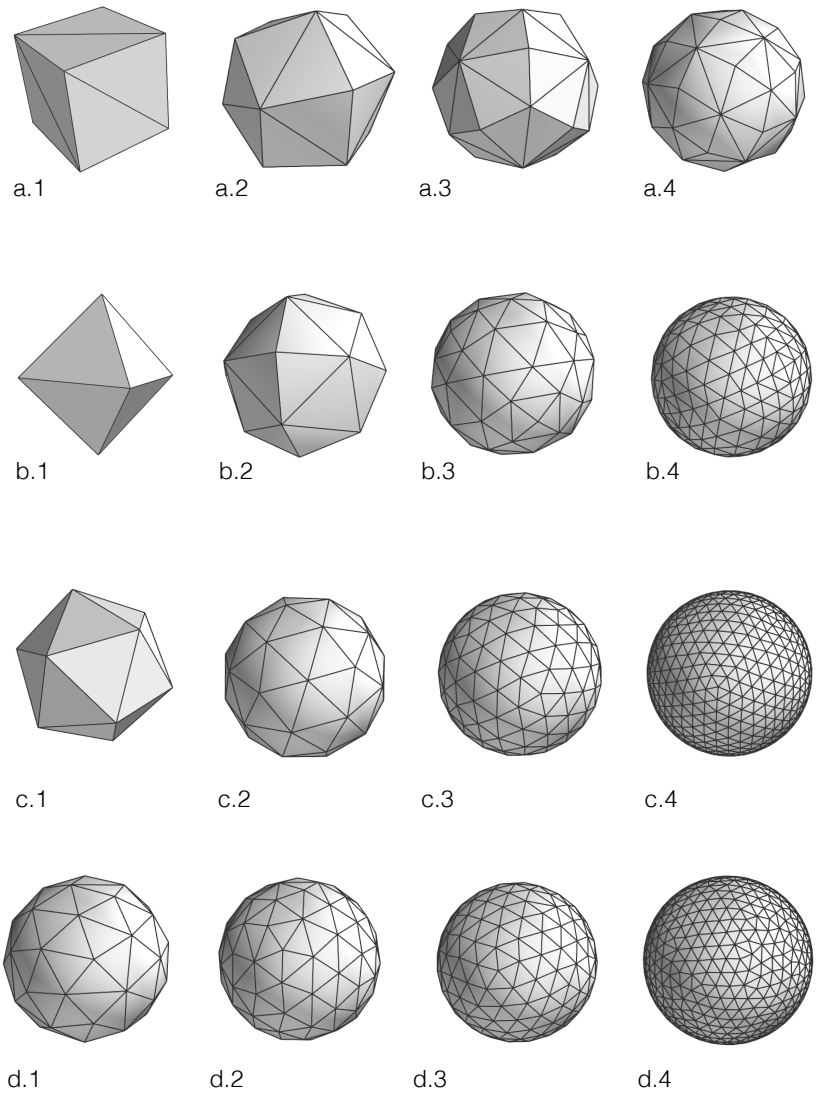

Figure A.2: (a) `Simple` triangulation: Subdivision of a triangular element is presented in Figure A.1 a. (b) `Icosahedron` Triangulation, and (c) `Octahedron` triangulation: The method of the triangular element Quadrisection of a triangular element is presented in Figure A.1 b. (d) `Stochastic` triangulation: Mesh is generated as described in Section A.2.2. Four different mesh sizes are shown: N=51 (d.1), N=100 (d.2), N=204 (d.3), N=625 (d.4).

A.2.2 rndmesh - Monte Carlo mesh generation algorithm

Iterative algorithms that generate a mesh by subdividing triangles are simple and computationally very efficient. However, the main disadvantage of these algorithms is that they cannot generate a mesh with an arbitrary number of nodes. In other words, iterative algorithms are restricted to the specific number of vertex nodes resulting from a subdivision procedure.

In many mechanics calculations, it is crucial to have control over a density of nodes on the sphere surface and to be able to simulate an object of arbitrary size. To that end, we developed a Monte Carlo algorithm that is an extension of the algorithm proposed in Paulose *et al.*[6]. The algorithm takes two parameters *i)* the radius R of a sphere to triangulate, *ii)* and the number of vertex nodes in a mesh N, and it returns a set of points that are distributed on the surface of that sphere. The fictitious size of each vertex r_v is chosen such that for a given N, nodes cover the whole sphere uniformly, *i.e.* $N\pi r_v^2 = 4\pi R^2$. First, these nodes are randomly distributed on a sphere. Then, for such a configuration, Simulated Annealing Monte Carlo (SAMC) simulation[7] is performed as follow: the simulation starts at the temperature $T_{max} = 1000$ [en.u.] and the system is cooled down to the temperature $T_{min} = 0.1$ [en.u], where [en.u.] stands for the energy unit. The cooling process is performed in $n_{anneals} = 200$ steps. At the i^{th} step, the temperature is decreased exponentially: $T_i = T_{max} \cdot \exp[-\Delta T \cdot (i-1)]$, where $\Delta T = \log(T_{max}/T_{min})/(n_{anneals} - 1)$. Each annealing step consists of $n_{mc} = 100$ Monte Carlo steps. A single Monte Carlo step consists of N attempts of displacement of a randomly selected node. A new configuration is accepted using the Metropolis criterion[8]. For the Metropolis criterion, the energy difference is evaluated using a repulsive part of the Lenard-Jones-8 potential with the parameter $\epsilon = 1.0$ [en.u.]. The potential has a cut-off at $r_c = 3 \times \sigma = 3 \times 2 \times r_v$. As the interactions are short-ranged, the computational complexity of the simulation is $\mathcal{O}(N)$. At the temperature T_{min}, the topology of the mesh is generated for the final configuration using Delaunay triangulation of points on a sphere — Algorithm 772 from a STRIPACK library[9]. The *pseudo-code* of the Monte Carlo procedure (except Algorithm 772) is given in Algorithm Boxes 1, 2, and 3.

Algorithm 1 Simulated Annealing Procedure

```
procedure SimMC(x)                                              ▷ x given
    T_max, T_min, n_anneals, n_mc, r_v                          ▷ Parameters
    ΔT ← log(T_max/T_min)/(n_anneals − 1)
    for i ← 1, n_anneals do
        T_i ← T_max × exp[−ΔT(i − 1)]
        for j ← 1, n_mc do
            x ← MCSTEP(x, T_i, r_v)
    {triangle}_i ← Algorithm772(x)                              ▷ Triangulate sphere
```

Algorithm 2 Single Monte Carlo Step

```
procedure MCSTEP(x,T,r_v)
    N ← len(x)                                                  ▷ Parameters
    for i ← 1, N do
        dx ← Uniform[−0.5r_v, 0.5r_v]
        x̃ ← Project(x, dx)                                      ▷ Project onto sphere
        x ← Metropolis(x, x̃, T, r_v)
```

Algorithm 3 Metropolis Criterion

```
procedure Metropolis(x, x̃, T, r_v)
    E_1 ← E(x, r_v)                                             ▷ Calculate energy
    E_2 ← E(x̃, r_v)                                             ▷ Calculate energy
    ΔE = E_2 − E_1
    p ← Uniform[0, 1]                                           ▷ Get a (pseudo) random number
    if p < min(exp[−ΔE/T], 1) then
        return x̃
    else
        return x
```

A.3 Mesh quality metrics

In engineering and computer graphics, the quality of the mesh is of crucial importance. Equilateral triangles of roughly the same size are desirable when solving PDEs with the Finite Element Method[10]. It is also desirable to avoid elements that are not very proportional, *i.e.* when one of the element's dimension is much larger than the other. Below, we provide definitions of some of the quality metrics used in mesh quality evaluation.

A.3.1 Triangle geometry metrics

Dual area of the i^{th} vertex node in the mesh is defined as:

$$C_i = \frac{1}{3} \sum_{t \in \{T\}_i} A_t \tag{A.1}$$

Here t denotes a single triangular element, $\{T\}_i$ denotes a set of triangular elements that contain the node i, and A_t is the area of the triangle t.

The dual area metric of the vertex is basically a normalized area of the surface that is associated with the given point.

Dual ratio area is defined as:

$$q_A = \frac{\min\limits_i C_i}{\max\limits_i C_i} \tag{A.2}$$

where: $\min\limits_i$ and $\max\limits_i$ refer to the maximum and minimum over the whole set of nodes in the mesh, and describes the spread in the areas that are associated with vertex nodes in the mesh. The smaller the dual ratio, the better. Angular departure from $\pi/3$ (the value for equilateral triangle) is quantified as:

$$q_\theta = \frac{\min\limits_T (\min\limits_{k=1,2,3} \theta_k)}{\pi/3} \tag{A.3}$$

q_θ and q_A are important in particular, because the maximum allowed time used in hyperbolic PDEs solvers (like for advection equation) is controlled by q_A and q_θ[11] — with larger q_A, the time step Δt can be longer. Contrary to q_A, q_θ controls Δt in an inverse manner, meaning that the lower the q_θ,

the larger the integration time-step.

The last parameter is a relation between the size of circles that are inscribed (r_{in}) and described (r_{out}) on a triangular element:

$$q = \min_i 2\frac{r_{in}}{r_{out}} = \min_i \frac{(b+c-a)(c+a-b)(a+b-c)}{abc} \tag{A.4}$$

where a, b, and c are lengths of triangle sides, and index i runs over all triangular elements. Other metrics could include distributions of the above statistics, but a more comprehensive analysis is left out for further investigations.

A.3.2 Bounding volume calculations

Two different approaches to calculate a volume contained by a spherical mesh are presented.

Volume Calculation — Tetrahedral elements

For any non-concave object with non-zero volume, its center of the mass is contained in the interior of the body. If that is the case, the volume calculation is relatively simple. Namely, the volume is calculated as a sum of tetrahedrons build on top of each triangular element in the mesh and the center of the mass as the fourth vertex. This method, although restricted to convex objects, gives an easy way to calculate volume change upon displacement of a single vertex.

Volume Calculation — Divergence Theorem

There is a more general way of calculating the volume of an arbitrary, closed, and non-intersecting object. This method is based on the Divergence Theorem.

$$\int_\Omega \mathrm{d}\nu \, (\nabla \cdot \mathrm{F}) = \int_{\partial\Omega} \mathrm{dS} \, (\mathrm{F} \cdot \mathrm{n}) \tag{A.5}$$

where F is any vector field, and n is the pointing vector of the surface element. Taking an arbitrary vector field $\mathrm{F} = (\mathrm{x}, 0, 0) \equiv \bar{\mathrm{x}}$, we have $\nabla \cdot \mathrm{F} = 1$. Thus the left hand side of the divergence theorem reads: $\int_\Omega \mathrm{d}\nu = \int_{\partial\Omega} \mathrm{dS} \, (\bar{\mathrm{x}} \cdot \mathrm{n}) = \mathrm{V}$. Then the numerical formula to calculate the volume

of a triangulated surface is:

$$V = \int_{\partial\Omega} dS\,(\bar{x}\cdot n) \approx \sum_i n_x^i s_i \tag{A.6}$$

where n_x^i is x-component of a normal vector of the i^{th} triangular element, and s_i is the area of the i^{th} triangular element. This approach is used, for example, in medical physics[12].

A.3.3 Curvature estimation for the mesh

A mesh is often generated for continuum mechanics calculations in engineering and computer graphics. One of the energy component of interest is the bending energy. This requires an estimation of the local radius of curvature. Many techniques are developed for that purpose, but for simplicity and performance purposes, the most popular method is based on the angle between two neighboring triangular elements, θ. θ is the angle between normal vectors $\hat{n}_1$ and $\hat{n}_2$ of two triangular elements that share an edge, and it is calculated from "The Law of Cosine": $\hat{n}_1 \cdot \hat{n}_2 = |\hat{n}_1| + |\hat{n}_2| - 2|\hat{n}_1||\hat{n}_2|\cos(\theta)$, Figure A.3. Having estimated θ, the radius of curvature R_{est} can be estimated as ($R_{est}^{-1} = 1/R_{ext}$):

$$R_{est}^{-1} = 2\sin(\theta/2)/h \tag{A.7}$$

where $h = (h_1 + h_2)/2$, and h_1 and h_2 are altitudes of the triangles projected on a common edge, $\hat{e}$.

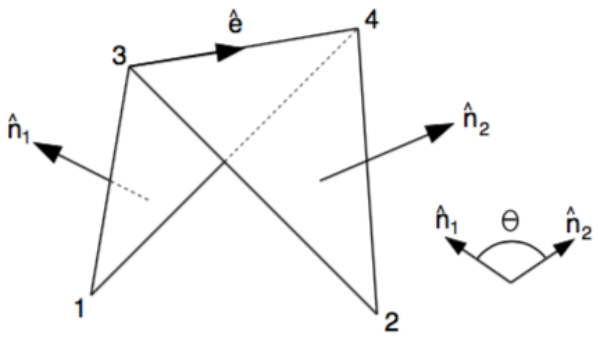

Figure A.3: Mesh geometry: Two triangles are sharing edge $\hat{e}$. The angle between two elements is defined for two normals $\hat{n}_1$ and $\hat{n}_2$. Sketch from Bridson *et al.*[13].

A.4 Results

A.4.1 A sphere approximated by a mesh

A sphere is an idealized object. Triangulation approximates this object as a collection of flat triangular facets, but this representation is subject to inaccuracies. These inaccuracies are crucial when comparing to analytic solutions. The results of this approximation (for `Simple` algorithm) are presented in Figure A.4. We can see that it takes a relatively large number of points, on the order of thousands rather than hundreds, to accurately approximate both the surface and the volume of a sphere. However, for simple iterative algorithms, the number of vertex nodes grows very quickly, and this may become a limitation if higher accuracy is needed.

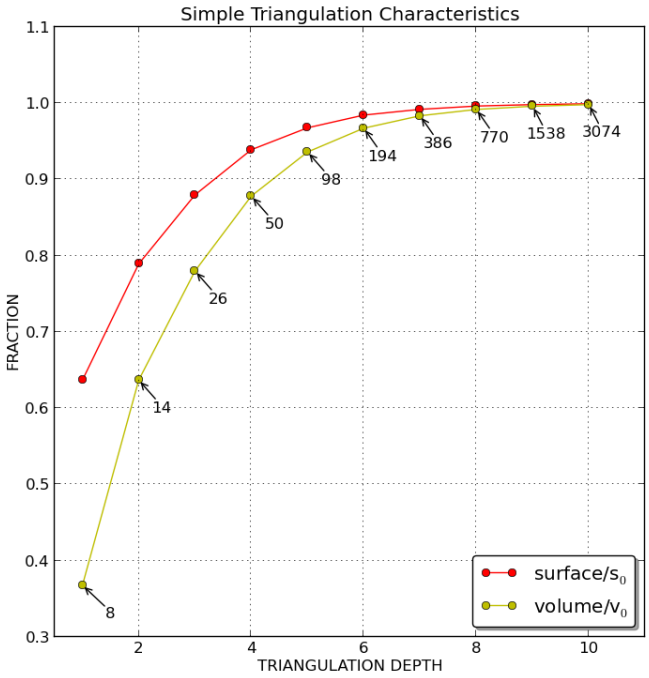

Figure A.4: Sphere approximated by a mesh: A relative surface area and a sphere volume, calculated for the first 10 triangulation levels for the `Simple` algorithm (*cf.* Figure A.2 a). Arrows give the number of nodes in a mesh. In this Figure, `TRIANGULATION DEPTH` is used in the same sense as the `triangulation level.`

A.4.2 Mesh quality

The algorithm that produces equilateral triangles is desired when solving PDEs with Finite Element Method. The upper bound for the maximum error depends only on the smallest angle in the mesh, and if all angles are close to 60^o, a good numerical stability is achieved. The metric that captures this behavior is q_θ, with $q_\theta = 1$ if all triangles are equilateral. It can be seen from Tables A.1, A.3, and A.4, that `Simple`, `Icosahedron`, and `Octahedron` triangulations provide meshes with quite good q_θ in the entire range of different mesh resolutions. This is not the case for `Tetrahedron` triangulation, where q_θ quickly drops to about 0.5, Table A.2. Although values of q_θ for `Simple` and `Tehtrahedron` algorithms are not that different, we can see that the q_A metric decreases to less than 0.1 for `Tetrahedron` triangulation, whereas it stays about 0.5 for `Simple` triangulation. The rule of thumb is that if all triangles in the mesh have $q \geq 0.5$, the mesh is considered high quality[2]. This is the case for all iterative algorithms except `Tetrahedron` triangulation. We can also see that `Icosahedron` triangulation is much better in terms of all the metrics than any other iterative algorithm, Table A.3.

For relatively small meshes ($N < 500$) and low $T_{end} < 1.0$, the quality of random meshes (`rndmesh`) is better than for `Simple`, `Tetrahedron` and `Octahedron` triangulations, Table A.5. Although the same is true for larger meshes, the quality is sightly worse, Table A.5. The reason for that can be two-fold: first, as the system size increases, the energy landscape becomes more complex. In such a case, the quality of the mesh boils down to the sampling efficiency. Secondly, q-metrics are defined for min and max functions; they take only extreme values under a consideration. As the system grows larger, the fluctuation magnitudes increase, making it more likely to find a low quality triangular element. From Table A.6, we can see that the choice of the final temperature T_{end} is also crucial for the quality of generated meshes. As the temperature is lowered in the SAMC algorithm, the glass transition occurs at around the temperature $T_g \approx 1.3-1.4$[14,15], and high quality meshes can be extracted from the configurations obtained for $T < T_g$. Finally, we can see, that in terms of q_A-metric, while larger random meshes ($N \approx 2500$) are comparable to the ones from `Icosahedron` triangulation, the metrics q_θ and q for `rndmesh` are noticeably worse. Nevertheless, quality of the random meshes is still good enough for reliable engineering and graphics calculations.

A.4.3 Curvature estimation accuracy

Local curvature estimation is essential for mechanics calculations on curved surfaces. The accuracy of this estimation depends on the geometry of a mesh and is one of the quality metrics. To benchmark different algorithms, for a given sphere with a known radius R_o, we generate meshes with different resolutions. Next, for each pair of triangles that share an edge, we estimate a radius of curvature R_{est}, as described in Section A.3.3. The results are in Figure A.5. We can see that for coarser meshes, where the angles between triangles are larger, the estimations are very accurate. This changes for finer meshes (as the local geometry is more planar), and the estimates are subject to much larger errors. For the `Icosahedron` method, the errors are relatively low. However, the `Simple` triangulation method has much lager inaccuracies — up to 5-fold overestimation of the radius of curvature.

A.4.4 Computational time performance

In SAMC calculations, there are only short-ranged, non-bonded interactions between individual particles. For computational efficiency, identification of neighbor particles is handled with the linked-cells list method[16] — implemented in the `nbody` library available at `https://github.com/pgniewko/nblists`. The computational cost of the simulation is $\mathcal{O}(N)$, where N is the number of vertex nodes on a sphere. In Figure A.6, results are shown for the computational cost as a function of system size, the number of Monte Carlo steps, and the number of temperature anneals. We can clearly see that the scaling with the system size is pretty linear $\mathcal{O}(N)$ — as expected for the linked-cells method.

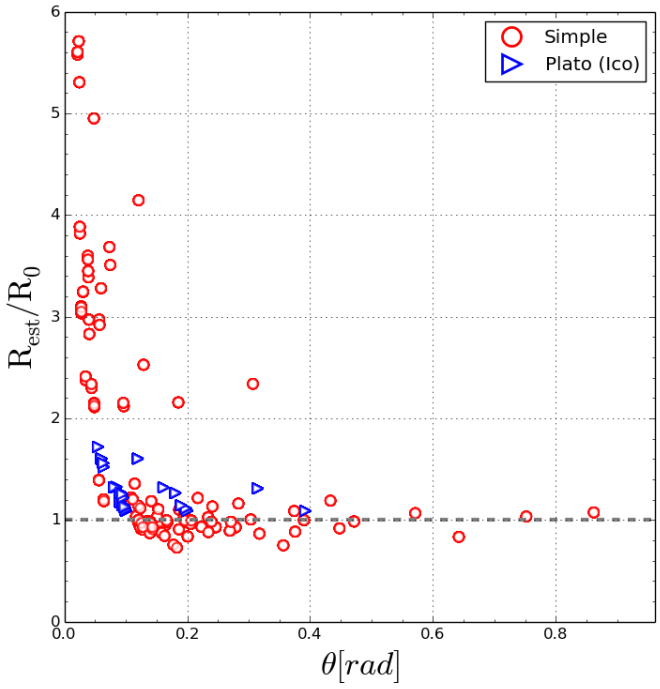

Figure A.5: Curvature estimation for two different triangulation techniques and different triangulation levels. θ can be calculated for a pair of two triangles sharing an edge. R_o is given, and R_{est} is estimated as described in Section A.3.3.

A.5 Conclusions and Further Directions

Further work will include more comprehensive quality tests of the random meshes (for example, distribution of the q-metrics). The `rndmesh` library implements a method that creates roughly uniform meshes on a sphere. However in some applications, the heterogeneities in a mesh may be desired. To that end, `rndmesh` can be further extended by introducing a one-body, position-dependent potential.

Finally, the `rndmesh` library can be used in solving The Thomson Problem — an arrangement of identical charges on the surface of a sphere. Mathematically, the task is a search for the global minimum of the energy function $E = \sum_{i \neq j} r_{ij}^{-1}$, where $r_{ij} = \sqrt{(x_i - x_j)^2 + (y_i - y_j)^2 + (z_i - z_j)^2}$, and subject to the constraint $x_i^2 + y_i^2 + z_i^2 = 1$. The Thomson Problem can be generalized to

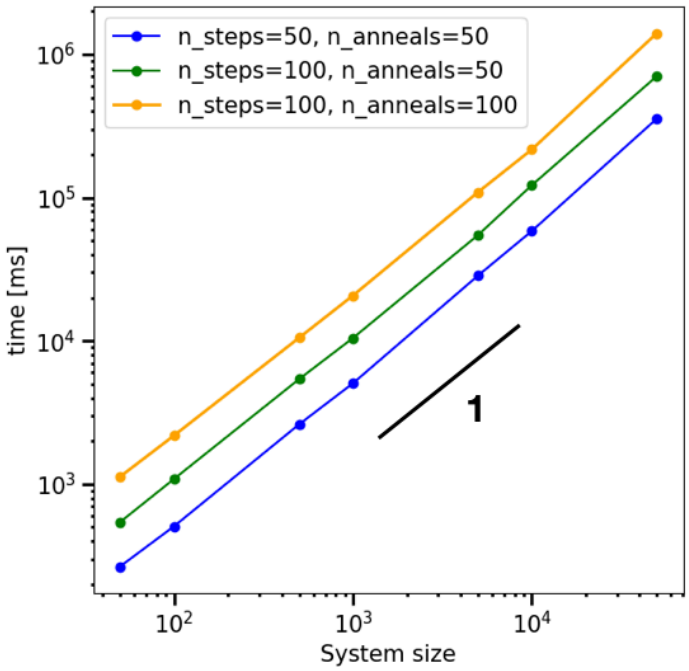

Figure A.6: Scaling of the computational cost of triangulation as a function of the system size, number of MC steps, and number of temperature anneals. Simulations were performed on a single 1.8 GHz Intel Core i5 CPU, with 8GB of RAM.

the repulsive potential of the form $x^{-\alpha}$ (Riesz α-kernels). The solution to the problem has many applications in physics, chemistry, and biology, but the general solution is still unknown[17].

References

[1] C. Helzel, M. Berger, and R. LeVeque. A high-resolution rotated grid method for conservation laws with embedded geometries. *SIAM Journal on Scientific Computing*, 26(3): 785–809, 2005.

[2] P.-O. Persson and G. Strang. A simple mesh generator in matlab. *SIAM Review*, 46(2): 329–345, 2004.

[3] J. Shewchuk. Triangle: Engineering a 2d quality mesh generator and delaunay triangulator. In *Applied computational geometry towards geometric engineering*, pages 203–222. Springer, 1996.

[4] R. Heikes and D. Randall. Numerical integration of the shallow-water equations on a twisted icosahedral grid. part i: Basic design and results of tests. *Monthly Weather Review*, 123(6):1862–1880, 1995.

[5] R. Heikes and D. Randall. Numerical integration of the shallow-water equations on a twisted icosahedral grid. part ii. a detailed description of the grid and an analysis of numerical accuracy. *Monthly Weather Review*, 123(6):1881–1887, 1995.

[6] J. Paulose, G. Vilegenthart, G. Gompper, and D. Nelson. Fluctuating shells under pressure. *Proceedings of the National Academy of Sciences of the United States of America*, 109(48): 19551–19556, 2012.

[7] S. Kirkpatrick, C. Gelatt, and M. Vecchi. Optimization by simulated annealing. *Science*, 220(4598):671–680, 1983.

[8] N. Metropolis, A. Rosenbluth, M. Rosenbluth, A. Teller, and E. Teller. Equation of state calculations by fast computing machines. *Journal of Chemical Physics*, 21(6):1087–1092, 1953.

[9] R. Renka. Algorithm 772: Stripack: Delaunay triangulation and voronoi diagram on the surface of a sphere. *ACM Transactions on Mathematical Software (TOMS)*, 23(3):416–434, 1997.

[10] K.-J. Bathe. *Finite Element Procedures*. Klaus-Jurgen Bathe, 2nd edition, 2014.

[11] R. Abgrall and M. Mezine. Construction of second order accurate monotone and stable residual distribution schemes for unsteady flow problems. *Journal of Computational Physics*, 188(1):16–55, 2003.

[12] S. Hughes, T. D'Arcy, D. Maxwell, J. Saunders, C. Ruff, W. Chiu, and S. R.J. Application of a new discreet form of gauss' theorem for measuring volume. *Physics in Medicine and Biology*, 41:1809–21, 1996.

[13] R. Bridson, S. Marino, and R. Fedkiw. Simulation of clothing with folds and wrinkles. *Eurographics/SIGGRAPH*, 2003.

[14] R. Guerra, C. Kelleher, A. Hollingsworth, and P. Chaikin. Freezing on a sphere. *Nature*, 554:346–350, 2018.

[15] J.-P. Vest, G. Tarjus, and P. Viot. Glassy dynamics of dense particle assemblies on a spherical substrate. *Journal of Chemical Physics*, 148:164501, 2018.

[16] M. Allen and D. Tildesley. *Computer simulation of liquids*. Oxford university press, 1989.

[17] D. Mehta, J. Chen, D. Chen, H. Kusumaatmaja, and D. Wales. Kinetic transition networks for the thomson problem and smale's 7th problem. *Physical Review Letters*, 117:028301, 2016.

Level	# Nodes	# Triangles	q_A	q_θ	q
1	8	12	0.667	0.750	0.828
2	14	24	0.667	0.852	0.935
3	26	48	0.500	0.681	0.869
4	50	96	0.493	0.627	0.729
5	98	192	0.487	0.582	0.748
6	194	384	0.483	0.568	0.646
7	386	768	0.480	0.556	0.711
8	770	1536	0.477	0.553	0.624

Table A.1: `Simple Triangulation`: Geometric quality metrics for different triangulation levels. For the definitions of the metrics q_A, q_θ, and q, please refer to the main text.

Level	# Nodes	# Triangles	q_A	q_θ	q
1	4	4	1	1	1
2	10	16	0.367	0.662	0.710
3	34	64	0.218	0.545	0.537
4	130	256	0.116	0.512	0.482
5	514	1024	0.087	0.503	0.469
6	2050	4096	0.079	0.501	0.465
7	8194	16384	0.077	0.500	0.464
8	32770	65536	0.076	0.500	0.464

Table A.2: `Tetrahedron Triangulation`: Geometric quality metrics for different triangulation levels. For the definitions of the metrics q_A, q_θ, and q, please refer to the main text.

Level	# Nodes	# Triangles	q_A	q_θ	q
1	12	20	1	1	1
2	42	80	0.784	0.926	0.989
3	162	320	0.740	0.907	0.973
4	642	1280	0.667	0.902	0.970
5	2562	5120	0.648	0.900	0.969
6	10242	20480	0.642	0.900	0.969
7	40962	81920	0.641	0.900	0.969
8	163842	327680	0.640	0.900	0.969

Table A.3: `Icosahedron Triangulation`: Geometric quality metrics for different triangulation levels. For the definitions of the metrics q_A, q_θ, and q, please refer to the main text.

Level	# Nodes	# Triangles	q_A	q_θ	q
1	6	8	1	1	1
2	18	32	0.572	0.820	0.906
3	66	128	0.474	0.768	0.850
4	258	512	0.361	0.755	0.834
5	1026	2048	0.328	0.751	0.830
6	4098	8192	0.320	0.750	0.8289
7	16386	32768	0.317	0.750	0.829
8	65538	131072	0.317	0.750	0.828

Table A.4: `Octahedron Triangulation`: Geometric quality metrics for different triangulation levels. For the definitions of the metrics q_A, q_θ, and q, please refer to the main text.

r_v	# Nodes	# Triangles	q_A	q_θ	q
0.45	123	242	0.661	0.729	0.829
0.4	156	308	0.635	0.668	0.731
0.35	204	404	0.624	0.651	0.719
0.3	277	550	0.615	0.633	0.690
0.25	400	796	0.614	0.624	0.671
0.2	625	1246	0.580	0.605	0.644
0.15	1111	2218	0.588	0.617	0.671
0.1	2500	4996	0.596	0.623	0.681

Table A.5: Geometric quality metrics for Monte Carlo mesh generation algorithms. The simulation starts at T=1000 [en.u.], and anneals the system down to T=0.1 [en.u.]. The size of the sphere is kept constant, $R = 2$, whereas the size of the vertex nodes is decreased, r_v.

Temperature	# Nodes	# Triangles	q_A	q_θ	q
0.1	2500	4996	0.595	0.619	0.657
1	2500	4996	0.566	0.607	0.663
10	2500	4996	0.381	0.514	0.583
50	2500	4996	0.218	0.387	0.410
100	2500	4996	0.182	0.349	0.333
250	2500	4996	0.135	0.304	0.329
500	2500	4996	0.110	0.242	0.227
750	2500	4996	0.085	0.251	0.224

Table A.6: Geometric quality metrics for Monte Carlo mesh generation algorithms. The number of vertex nodes is kept constant at N=2500 and $r_v = 0.1[a.u.]$. The simulation procedure is described in Section A.2.2. The simulations start at the temperature T=1000 and stops at the temperature T=Temperature [en.u.].

Appendix B
Mechanics and Simulations of Elastic Shells

B.1 Linear Elasticity Theory

B.1.1 Foundations

A basic assumption in the linear elasticity theory is that stress is a linear function of the strain:

$$\sigma_{ij} = C_{ijkl}\varepsilon_{kl} \tag{B.1}$$

where σ_{ij} is the stress tensor, ε_{kl} is the strain tensor, and C_{ijkl} the 4^{th}-order stiffness tensor. In 3D, stress and strain tensors can both have 9 elements, implying that the stiffness tensor can have $9 \cdot 9 = 81$ independent elements. However, stress and strain tensors are symmetric, which reduces their number of independent elements to 6, and as a result, the number of C_{ijkl} independent elements cannot be greater than 36. Additionally, we have:

$$\sigma_{ij} = \frac{\partial W}{\partial \varepsilon_{ij}} \Rightarrow C_{ijkl} = \frac{\partial^2 W}{\partial \varepsilon_{ij}\varepsilon_{kl}} \tag{B.2}$$

where W is a density energy function. Since the order of differentiation is arbitrary, we can see that $C_{ijkl} = C_{klij}$, which further reduces the number of possible independent elements in C_{ijkl} to 21. Further reduction of the independent elements occurs for isotropic materials. If we consider an isotropic material, then the elements of C_{ijkl} must be independent of the coordinate system. They can be independent only if they transform in the same way as δ_{ij} tensor (Kronecker delta). There are only two possible combinations that fulfill this requirement: $\delta_{ij}\delta_{kl}$ and $\delta_{ik}\delta_{jl} + \delta_{il}\delta_{jk}$. Thus, for isotropic materials, there can be only two independent parameters (λ and μ):

$$C_{ijkl} = \lambda\left(\delta_{ij}\delta_{kl}\right) + \mu\left(\delta_{ik}\delta_{jl} + \delta_{il}\delta_{jk}\right) \tag{B.3}$$

where λ and μ are called Lamé coefficients, which are measured in units of pressure (μ has a special name: *shear modulus*).

Similarly, for isotropic materials, the stress tensor must be related to the strain tensor in a way independent of the coordination system. One such possibility is $\sigma_{ij} = \text{const} \cdot \varepsilon_{ij}$. However, there is also the possibility of the unit tensor δ_{ij} multiplied by a scalar that is a function of ε. The only scalar function such as that, is $\sum \varepsilon_{ii}$. Thus, the stress tensor can be expressed in a general form (for isotropic materials) :

$$\sigma_{ij} = 2\mu\epsilon_{ij} + \lambda\epsilon_{kk}\delta_{ij} \tag{B.4}$$

B.1.2 Shear and bulk moduli

The shear modulus μ describes the material's resistance to the volume-preserving deformation (simple shear), and it is independent of dimension d. Contrary to the shear modulus, the bulk modulus (K_B) accounts for the resistance to the volumetric compression as:

$$K_B = -\frac{P}{\mathrm{V}/\mathrm{V}_0} \tag{B.5}$$

where V_0 and V are the material's volumes before and after application of the pressure P. For isotropic materials, the stress tensor corresponding to the uniform compression is $\sigma_{\alpha\beta} = -P\delta_{\alpha\beta}$, and the pressure P can be easily expressed as $\sigma_{\alpha\alpha} = -P \cdot d$. Moreover, the trace of the strain tensor is $\varepsilon_v \equiv \varepsilon_{\alpha\alpha} \approx \mathrm{V}/\mathrm{V}_0$ (exact in the limit $\varepsilon_{\alpha\alpha} \to 0$). Because the trace of σ_{ij} is $\sigma_{\alpha\alpha} = (2\mu + d\lambda)\varepsilon_{\alpha\alpha}$, the bulk modulus depends (through Equation B.4) on a material dimensionality through Equation B.4. In 2D the bulk modulus is[1]:

$$K_B = \frac{\sigma_{\alpha\alpha}}{d\varepsilon_{\alpha\alpha}} = \lambda + \frac{2}{d}\mu = \lambda + \mu \tag{B.6}$$

B.2 Elastic description of shell mechanics

An elastic shell resists both stretching and out-of-plane deformations. For a thin shell, these two contributions can be factorized, and the total energy can be represented as a sum of these two contributions:

$$W = W_s + W_b \tag{B.7}$$

where W_s and W_b stand for in-plane stretching and out-of-plane bending energies, respectively.

In the elasticity theory of thin plates, a deformation is represented by an in-plane displacement vector field $\mathrm{u} = (u_1(\mathrm{r}), u_2(\mathrm{r}))$ and an out-of-plane deflection field $f(\mathrm{r})$. Displacement defined this way maps the point $(x_1, x_2, 0)$ in the mid-plane reference state to $(x_1 + u_1, x_2 + u_2, f)$. The strain tensor, for the displacement fields $u(\cdot)$ and $f(\cdot)$, is then defined as:

$$\varepsilon_{ij} = \frac{1}{2}\Big(\partial_i u_j + \partial_j u_i + \partial_i u_k \partial_j u_k + \partial_i f \partial_j f\Big) \tag{B.8}$$

where the indices run over 1 and 2, and the displacement fields are evaluated along the mid-surface. For small displacements, the quadratic terms in u_k can be neglected, but we must keep the term quadratic in deflection f since there is no lower order in f.

Having the strain tensor defined by Equation B.8, we can get the stretching energy W_s by integrating out the z-direction in Equation B.1 (assuming a constant thickness of the plate t). In terms of the two Lamé coefficients μ and λ and the the strain tensor ε_{ij}, the stretching energy is:

$$W_s = \frac{1}{2} Y \int_\Omega \mathrm{dS}\, \left(2\mu\varepsilon_{\mathrm{ij}}^2 + \lambda\varepsilon_{\mathrm{kk}}^2\right) \tag{B.9}$$

The integral is over the area of the reference state. The Lamé coefficients are related to the other familiar material parameters, such as the *modulus of stiffness* $Y = E \cdot t$, and the Poisson ratio ν by relations:

$$E = \frac{4\mu(\mu + \lambda)}{2\mu + \lambda} \tag{B.10}$$

$$\nu = \frac{\lambda}{2\mu + \lambda} \tag{B.11}$$

The Poisson coefficient ν measures a tendency of the material to shrink in a direction perpendicular to the stretching stress (or expand upon applied compression).

Similarly to W_s, assuming no shear in a direction perpendicular to the mid-surface, the bending energy for the isotropic shell is defined as:

$$W_b = \frac{1}{2}\kappa \int_\Omega \mathrm{dS}\, \left[(\nabla^2 f)^2 - 2(1-\nu)\det(\partial_i \partial_j f)\right] \tag{B.12}$$

where $\kappa = Et^3/12(1-\nu^2)$ is called the *bending rigidity*. Twice the mean curvature H ($H =$

$1/R_1 + 1/R_2$) and Gaussian curvature K ($K = 1/R_1R_2$, where R_1 and R_2 are the canonical radii of curvature) can be expressed in terms of f as:

$$H = \nabla \cdot \left(\frac{\nabla f}{\sqrt{1 + |\nabla f|^2}} \right) \tag{B.13}$$

$$K = \frac{\det(\partial_i \partial_j f)}{(1 + |\nabla f|^2)^2} \tag{B.14}$$

For small $|\nabla f|$, $H \approx \nabla^2 f$ and $K \approx \det(\partial_i \partial_j f)$. Thus for small deflections, the bending energy can be approximated as:

$$W_b \approx \int_\Omega \mathrm{dS} \left(\frac{1}{2}\kappa H^2 - \kappa_G K \right) \tag{B.15}$$

where $\kappa_G = Et^3/12(1+\nu)$ is called the *Gaussian rigidity*. From the Gauss-Bonnet theorem of compact surfaces, the second term is a topological invariant $\int dSK = 2\pi\chi(X)$, where $\chi(S)$ is called the Euler-Poincaré characteristic of the surface. For surfaces that are topologically equivalent to spheres, $\chi = 2$. Since we do not consider any topological transformations, and we study only homogeneous shells, this term is constant and can be dropped out from further calculations of the bending energy and forces. If the material is heterogeneous or the material's thickness varies, then the Gaussian rigidity terms needs to be included in Equation B.15[2–4].

B.2.1 Contributions from stretching and bending

Considering the simplest case of a homogeneous plate or a shell, two parameters determine the behavior of the body: $Y = Et$, and $\kappa = Et^3/12(1-\nu^2)$. As a result, the thickness of the shell strongly affects its elastic behavior. In particular, for very thin plates and shells, the cubic dependence of κ on t ($\kappa \propto t^3$) determines that bending is highly favorable over stretching. This behavior is demonstrated by the ease of bending a piece of paper compared to stretching it[5,6]. Flat elastic plates can exhibit pure bending with no associated in-plane stretching. This is not always true for shells that have non-zero curvature in their undeformed state. The underlying curvature mediates a linear coupling between out-of-plane displacements and in-plane strains, *i.e.* any transverse deformation ω introduces a strain of the order of ω/R_0, where R_0 is the radius of curvature in the relaxed state[6]. This coupling causes the localization of the normal deformation within a narrow width in the spherical shell[5]. Deformation of maximum depth ω, localized over a length l,

leads to the curvature change $\propto \omega/l^2$ and strain $\propto \omega/R_0$. This corresponds to the energy densities per unit area $W_s(l,\omega) \propto Y\omega^2/R_0^2$, and $W_b(l,\omega) \propto \kappa\omega^2/l^4$ [6]. Minimizing the sum of energies $W_s + W_b$, with respect to l, gives a typical length-scale of a deformation localization:

$$l^* = \left(\frac{\kappa R_0^2}{Y}\right)^{1/4} \equiv \frac{R_0}{\gamma^{1/4}} \tag{B.16}$$

where we introduced a dimensionless Föppl-von Kármán number[3]:

$$\gamma \equiv \frac{Y R_0^2}{\kappa} \approx 10\left(\frac{R}{h}\right)^2 \tag{B.17}$$

The Föppl-von Kármán number quantifies the relative importance of stretching to bending deformations for spherical shells. A shell is considered thin when $\gamma \gtrsim 1000$, *i.e.* when $h \lesssim 0.1R_0$ [5].

B.2.2 Elastic Stretching Energy

General Overview of Spring-Mesh Models

The elastic stretching energy W_s can be approximated by the energy of elastic harmonic springs with bonds between the nodes[7]:

$$W_s = \sum_{\langle i,j\rangle} k_{ij}\left(|r_{ij}| - |r_{ij}^\circ|\right)^2 \tag{B.18}$$

where $|r_{ij}|$ and $|r_{ij}^\circ|$ are the lengths of the deformed and initial states of the bond connecting points i and j. This form, irrespective of the relation between a spring constant k_{ij} and Y, reproduces the stretching energy component of the elastic energy in the continuum limit for materials with only $\nu = 1/3$ (2D), see Section B.2.2. Having potential energy calculated, the forces between two nodes connected by a spring can be calculated as:

$$F_{ij} = -F_{ji} = k_{ij}\left(r_j - r_i\right)\left(1 - \frac{|r_{ij}^\circ|}{|r_{ij}|}\right) \tag{B.19}$$

Seung and Nelson's Model

Seung and Nelson considered a 2D triangular lattice with unit spacing[7]. Lattice deformation maps a point r_i into the new location r'_i. The streching energy W_s is defined as:

$$W_s = \frac{1}{2}\mathrm{k}\sum_{\langle i,j\rangle}\left(|\mathrm{r}'_i - \mathrm{r}'_j| - 1\right)^2 = \frac{1}{2}\mathrm{k}\sum_a U_a \tag{B.20}$$

where k is a stiffness constant (same for all of the springs), the sum runs over all pairs of connected nodes $\langle a, b\rangle$, and U_a is a sum over nearest neighbors b of a node a: $U_a = \frac{1}{2}\sum_b \left(|\mathrm{r}'_a - \mathrm{r}'_b| - 1\right)^2$. Using the metric tensor, it is shown that[7]:

$$U_a = \frac{3}{8}\left(2\varepsilon_{ij}^2 + \varepsilon_{kk}^2\right) \tag{B.21}$$

Thus, in the limit of infinitesimally small edge lengths (continuum limit), the stretching energy is approximated as:

$$W_s = \frac{1}{2}\mathrm{k}\sum_a U_a \approx \frac{1}{\sqrt{3}}\mathrm{k}\int_\Omega \mathrm{d}S U(\mathrm{r}) = \frac{\sqrt{3}}{8}\mathrm{k}\int_\Omega \mathrm{d}S(2\varepsilon_{ij}^2 + \varepsilon_{kk}^2) \tag{B.22}$$

Comparing the above with Equation B.9, we get the Lamé coefficients: $\lambda = \mu = \frac{\sqrt{3}}{4}\mathrm{k}$, from which in 2D we obtain the Poisson ratio $\nu = \frac{1}{3}$ (in 3D we get $\nu = \frac{1}{4}$, known as the Cauchy value), and the *modulus of stiffness* $Y = \frac{2}{\sqrt{3}}\mathrm{k}$. At this point, it is important to note that the spring stiffness k is a free parameter and can be adjusted to match material property Y, whereas the Poisson ratio is fixed and equal to $\nu = 1/3$ for all membranes simulated with this method. This stems from the fact that U_a is a central force potential, *i.e.*, the total energy can be expressed as $W_s = \frac{1}{2}\mathrm{k}\sum_{i\neq j} U_a\left(\|\mathrm{r}_{ij}\|\right)$, where F is a deformation tensor, $\mathrm{r}_{ij} = \mathrm{r}_j - \mathrm{r}_i$ is the distance between two nodes i and j, and $U_a(\cdot)$ is a given potential.

Kot, Nagahash & Szymczak's Model

Kot *et al.*[8,9] took the idea of Seung and Nelson a step further[7] and extended it to the cases of disordered meshes. Homogeneous and isotropic medium can be characterized by two independent parameters. As we already pointed out, for all models with central forces (including spring meshes),

the Poisson ratio is fixed at $\nu = 1/3$. Thus, we need one more elastic parameter to complete the description of the material. The simplest quantity to calculate is the bulk modulus K_B. The matrix form of Hooke's Law (Equation B.4) is:

$$\begin{pmatrix} \sigma_{11} \\ \sigma_{22} \\ \sigma_{33} \\ \sigma_{23} \\ \sigma_{13} \\ \sigma_{12} \end{pmatrix} = \begin{pmatrix} 2\mu+\lambda & \lambda & \lambda & 0 & 0 & 0 \\ \lambda & 2\mu+\lambda & \lambda & 0 & 0 & 0 \\ \lambda & \lambda & 2\mu+\lambda & 0 & 0 & 0 \\ 0 & 0 & 0 & \mu & 0 & 0 \\ 0 & 0 & 0 & 0 & \mu & 0 \\ 0 & 0 & 0 & 0 & 0 & \mu \end{pmatrix} \begin{pmatrix} \epsilon_{11} \\ \varepsilon_{22} \\ \varepsilon_{33} \\ 2\varepsilon_{23} \\ 2\varepsilon_{13} \\ 2\varepsilon_{12} \end{pmatrix}$$

For a membrane, we can assume that: $\sigma_{i3} = \varepsilon_{i3} = 0$, and the above matrix equation reduces to:

$$\begin{pmatrix} \sigma_{11} \\ \sigma_{22} \\ \sigma_{12} \end{pmatrix} = \begin{pmatrix} 2\mu+\lambda & \lambda & 0 \\ \lambda & 2\mu+\lambda & 0 \\ 0 & 0 & \mu \end{pmatrix} \begin{pmatrix} \varepsilon_{11} \\ \varepsilon_{22} \\ 2\varepsilon_{12} \end{pmatrix}$$

For a 2D system, mechanical parameters such as bulk modulus K_B (planar modulus in 2D), Poisson's ratio ν, and Young's modulus E for 2D system are related to Lamé coefficients as:

$$K_B = \lambda + \mu \ , \ \nu = \frac{\lambda}{\lambda + 2\mu} \ , \ E = \frac{4\mu(\lambda+\mu)}{\lambda+2\mu} \tag{B.23}$$

We can also easily check that $E = 2K_B(1-\nu)$. Upon an isotropic compression, the strain tensor is $\varepsilon_{ij} = \delta_{ij}\varepsilon$ where $\varepsilon < 0$, and the energy density is:

$$\Delta \mathrm{e} = \frac{1}{2}\sigma : \varepsilon_{ij} = \frac{1}{2}\varepsilon^2 \cdot 2 \cdot (2\lambda + 2\mu) = 2K_B\epsilon^2 = \frac{E}{1-\nu}\varepsilon^2 \tag{B.24}$$

If we assume that all the spring constants are the same (*i.e.* $\mathrm{k_i} = \mathrm{k}$) and that all the springs are

compressed uniformly (*i.e.* $\varepsilon_i = \varepsilon \Rightarrow l_i = L_i(1+\varepsilon)$) we have:

$$\Delta e = \frac{1}{V}\sum_i \frac{1}{2} k_i L_i^2 \varepsilon_i^2 = \frac{1}{2t \cdot A_0}\varepsilon^2 k \sum_i L_i^2 \tag{B.25}$$

where L_i is the relaxed length of the spring, A_0 the area of the membrane before the compression, and t is the membrane's thickness (which does not change upon compression).
Finally, we get a relation for a spring constant:

$$k = \frac{2Y}{1-\nu}\frac{A_0}{\sum_i L_i^2} \tag{B.26}$$

Since $\nu = 1/3$, the spring constant for unstructured meshes is $k = 3YA_0/\sum_i L_i^2$[10]. If we consider a hexagonal lattice, made of N identical equilateral triangles with edges of length $L_i = \alpha$, then $A_0 = \sqrt{3}N\alpha^2/4$, whereas $\sum_i L_i^2 = 3/2N\alpha^2$. Substituting it into Equation B.26, we obtain $k = \sqrt{3}Y/2$, identical to Nelson *et al.*[7,11].

Van Gelder's Model

The model developed by Allen Van Gelder is another version of the spring-mesh model for the simulation of isotropic elastic materials[12]. Since the spring-mesh models cannot match the Finite Element Method exactly, the idea behind Van Gelder's model is to parametrize every spring in the mesh in such a way that the mechanics of every triangular elements matches, as closely as possible, the deformation of an isotropic elastic material[12]. That said, the model is limited to the case where external forces are uniformly distributed along each edge in the mesh and deformations are linear. For a triangle as in Figure B.1 A (for a small deformation), a spring constant for edge c reads[12]:

$$k_c(T) = \left(\frac{Y}{1+\nu}\right)\frac{A_T}{|c|^2} + \left(\frac{Y\nu}{1-\nu^2}\right)\frac{|a|^2+|b|^2-|c|^2}{8A_T} \tag{B.27}$$

where $Y = Et$; E is Young's modulus; t is material thickness; A_T is the area of the triangle T that contains the edge c; $|a|$,$|b|$, and $|c|$ are the lengths of the edge; and ν is the Poisson ratio.

It is important to note that although ν appears to be a free parameter, in fact it is not. For the spring-mesh, the Poisson ratio is $\nu = 1/3$ (Section B.2.2), contrary to the value $\nu = 0$ used in a paper by van Gelder[12].

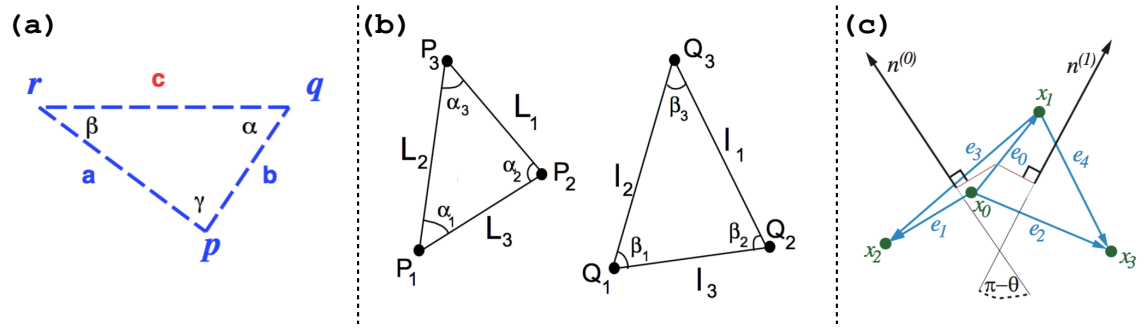

Figure B.1: (a): An undeformed triangular element with the area A_T. Sketch from Van Gelder[12] **(b)** Rest triangle T_P (on the left), with vertex nodes positions P_i, edge lengths L_i, and rest angles α_i, is deformed into a triangle T_Q (on the right) with vertex nodes positions Q_i, edge lengths l_i, and rest angles β_i. Sketch from Delingette[13,14] **(c)**: Geometry of a *bending hinge*. Two triangles sharing an edge e_0, between nodes x_0, and x_1. $\pi - \theta$ is an angle between normals $n^{(0)}$, and $n^{(1)}$ of the triangular elements T_0 and T_1, and θ is the angle between two triangular elements. $\alpha_1 = \angle(\hat{e}_0, \hat{e}_1)$, $\alpha_2 = \angle(\hat{e}_0, \hat{e}_2)$, $\alpha_3 = \angle(-\hat{e}_0, \hat{e}_3)$, $\alpha_4 = \angle(-\hat{e}_0, \hat{e}_4)$. Sketch from Wardetzky *et al.*[15].

If the edge is a boundary edge, then Equation B.27 applies directly. However, if the edge is shared by two triangles, T_1 and T_2 (the edge c is in the bulk of the material), then the spring stiffness is a sum of the contributions from these two triangles: $k_c = k_c(T_1) + k_c(T_2)$[12].

Delingette's Biquadratic Springs

As discussed in previous sections, spring-mesh models cannot reproduce completely elastic materials mechanics, and they perform especially poorly for disordered meshes[12]. The disadvantages of the spring-mesh models have been improved upon by Delingette[13,14], with the model called Triangular Biquadratic Springs Model. The model is equivalent to the Finite Elements Method, but it is expressed in a much simpler form. The advantage of the model is that it is easy to implement, yet still gets the correct continuum mechanics description for non-linear finite deformations. To capture the behavior for different values of Poisson ratio, the model requires angular springs that resist changes in the element's angles. The model considers a compact domain $\Omega \subset \mathbb{R}^2$ that is deformed into another domain $\Phi(\Omega)$. A material point $X \in \Omega$ is moved to a new position $\Phi(X) \in \Phi(\Omega)$, where $\Phi(X)$ is the deformation function. The right Cauchy-Green deformation tensor C is defined as $C = \nabla\Phi^T \nabla\Phi$, and the Green-Lagrange strain tensor $\mathcal{E}$ is defined as $\mathcal{E} = 1/2(C - I)$. The Green-Lagrange strain tensor is invariant to translation and rotation, thus is appropriate for

large-displacement description. The membrane is assumed to be an isotropic St. Venant Kirchhoff membrane (a linear relationship between the stress and strain), for which the energy density is defined as:

$$W_s(\mathrm{X}) = \frac{\lambda}{2}(\mathrm{tr}\mathcal{E})^2 + \mu \mathrm{tr}(\mathcal{E}^2) \tag{B.28}$$

where λ and μ are the Lamé coefficients. The total stretching energy is then:

$$W_s = \int_\Omega \mathrm{dS} W(\mathrm{X}) = \int_\Omega \mathrm{dS} \left(\frac{\lambda}{2}(\mathrm{tr}\mathcal{E})^2 + \frac{\mu}{2}\mathrm{tr}(\mathcal{E}^2) \right) \tag{B.29}$$

This is is the simplest hyperelastic material model, where the linear elastic material model is extended to the nonlinear regime. The surface is discretized into a set of linear triangular elements $\{\mathrm{T}\}_\mathrm{i} \in \Omega_h$ (due to this assumption, we get closed-form stiffness matrices). This surface discretization leads to a formula for the stretching energy of a triangle T_P deforming into a triangle T_Q (Figure B.1 B) which is:

$$W_s(\mathrm{T}_P) = \sum_{i=1}^{3} \frac{k_i^{\mathrm{T}_P}}{4} \left(l_i^2 - L_i^2\right)^2 + \sum_{i \neq j} \frac{c_k^{\mathrm{T}_P}}{2} \left(l_i^2 - L_i^2\right)\left(l_j^2 - L_j^2\right) \tag{B.30}$$

The model is called Triangular Biquadratic Springs since the first term can be interpreted as the energy of three tensile biquadratic springs that prevent edges from stretching, and the second term can be seen as three angular biquadratic springs that prevent any changes of the element's angles ($c_k^{\mathrm{T_P}}$ controlling the change of the angles around nodes $\mathrm{Q_i}$ and $\mathrm{Q_j}$). Applying Rayleigh-Ritz analysis to Equation B.30, the force acting on vertex i due to the triangular element deformation is:

$$\mathrm{F}_i^{\mathrm{T}_P} = \sum_{j \neq j} k_k^{\mathrm{T}_P} \Delta^2 l_k (\mathrm{Q_j} - \mathrm{Q_i}) + \sum_{j \neq i} (c_j^{\mathrm{T}_P} \Delta^2 l_i + c_i^{\mathrm{T}_P} \Delta^2 l_j) \left(\mathrm{Q_j} - \mathrm{Q_i}\right) \tag{B.31}$$

where:

$$k_i^{\mathrm{T}_P} = \frac{Y(2\cot^2\alpha_i + 1 - \nu)}{16(1-\nu^2)A_P} \tag{B.32}$$

$$c_k^{\mathrm{T}_P} = \frac{Y(2\cot\alpha_i \cot\alpha_j + \nu - 1)}{16(1-\nu^2)A_P} \tag{B.33}$$

$$\Delta^2 l_i = \left(l_i^2 - L_i^2\right) \tag{B.34}$$

where A_P is the area of a triangle T_P, and α_i are defined in Figure B.1 b.

The energy required to deform the whole triangulated surface Ω_h is simply the sum of the energies for each triangle $\mathrm{T}_P \in \Omega_h$. Thus, if an edge is shared by two triangles T_1 and T_2, the total stiffness of the edge is $k_\mathrm{T} = k^{\mathrm{T}_1} + k^{\mathrm{T}_2}$. The tensile stiffness is always positive, while the angular stiffness may be zero or even negative. For a triangular lattice with $\alpha = \pi/3$ and $\nu = 1/3$ the angular stiffness is zero and the model reduces to the standard spring-mesh model. Biquadratic springs were successfully applied in biomechanics research[16].

B.2.3 Elastic Bending Energy

The bending energy W_b requires an estimation of the surface curvature. There are two common ways of handling this task.

Bending Springs Energy

The most popular, and conceptually the simplest approach, is an introduction of a fictitious spring that controls the angle between two triangles that share an edge, see Figure B.1 C. Similarly to the discrete version of the stretching energy (Equation B.20), the discrete version of the bending energy reads (for a flat surface):

$$W_b = \frac{1}{2}\tilde{\kappa} \sum_{\langle\alpha,\beta\rangle} |\mathrm{n}_\alpha - \mathrm{n}_\beta|^2 = \tilde{\kappa} \sum_{\langle\alpha,\beta\rangle} (1 - \mathrm{n}_\alpha \cdot \mathrm{n}_\beta) \tag{B.35}$$

where the sum runs over all pairs of triangles $\langle\alpha, \beta\rangle$ that share a common edge, n_α and n_β are normals of triangular elements, and $\tilde{\kappa}$ is a renormalized bending constant. A relation between the bending rigidity κ and the microscopic parameter $\tilde{\kappa}$ is most easily derived by comparing the bending energy of a triangular lattice folded into a shape of a cylinder. This can be easily done and yields[7]:

$$\kappa = \frac{\sqrt{3}}{2}\tilde{\kappa} \tag{B.36}$$

where $\kappa = Et^3/12(1-\nu^2)$. Such a renormalization, however, depends on the shape into which we fit, and repeating the calculation for a sphere gives $\kappa = \frac{1}{\sqrt{3}}\tilde{\kappa}$[17,18]. For its simplicity, this approach

is very popular in the physics community for elastic shells simulations[7,11,18–20]. It has to be pointed out that in the process of renormalizing the constant $\tilde{\kappa}$, the integration in Equation B.35 runs over the whole area of triangle, rather than just over $1/3$ part of it. Because of that, it is important to keep in mind that in the computer graphics community, where a similar approach is used, the renormalization of that constant differs by a constant factor due to an improper integration over a surface[15].

This approach can be extended by parameterizing the bending stiffness for each bending spring. From the trigonometry we have:

$$(1 - \mathrm{n}_\alpha \cdot \mathrm{n}_\beta) = 1 - \cos(\pi - \theta) = 1 + \cos(\theta) \tag{B.37}$$

Then, the bending stiffness can be parametrized for each bending hinge, κ_i as:

$$W_b = \sum_i \kappa_i (1 + \cos(\theta_i)) = \kappa \sum_i \frac{3|\mathrm{e}_0^2|}{A_i} \left(2 \cos\left(\frac{\theta_i}{2}\right)\right)^2 \tag{B.38}$$

where $\kappa_i = 3|\mathrm{e}_0^2|\kappa/A_i$, A_i is a combined area of two triangles meeting at the edge $\mathrm{e_i}$, and θ_i is e_i's dihedral angle, *cf.* Figure B.1 c. This is a mathematical form for the bending energy used in the computer graphics community[15,21–23]. This form also partially deals with the problem of unstructured meshes, where the bending stiffness is a property that depends on the local geometry of the triangular mesh. Equation B.38 applies to the plate that is flat at equilibrium. If the initial metric of the membrane is curved, then the equation has the form:

$$W_b = \sum_i \kappa_i (1 + \cos(\theta_i - \theta_0)) \tag{B.39}$$

Finally, for the dynamics simulations, forces can be calculated for each vertex $i = 0, 1, 2, 3$ meeting at the hinge j (denoted as e_0 in Figure B.1 c) as:

$$\mathrm{F}_i = -\nabla_{\mathrm{x}_i} W_j = -\frac{3|\mathrm{e_j}|^2}{A_j} \sin\left(\theta_j - \theta_j^0\right) \nabla_{\mathrm{x}_i} \theta \tag{B.40}$$

A gradient $\nabla_{\mathrm{x}}\theta$ can be calculated for the every vertex in the pair of triangles[15] and using the notation

as in Figure B.1 c, these derivatives are:

$$\nabla_{\mathrm{x}_0}\theta = -\frac{1}{|\mathrm{e_j}|}\left[\cot(\alpha_3)\mathrm{n}^{(0)} + \cot(\alpha_4)\mathrm{n}^{(1)}\right] \tag{B.41}$$

$$\nabla_{\mathrm{x}_1}\theta = -\frac{1}{|\mathrm{e_j}|}\left[\cot(\alpha_1)\mathrm{n}^{(0)} + \cot(\alpha_2)\mathrm{n}^{(1)}\right] \tag{B.42}$$

$$\nabla_{\mathrm{x}_2}\theta = \frac{1}{|\mathrm{e_j}|}\left[\cot(\alpha_1) + \cot(\alpha_3)\right]\mathrm{n}^{(0)} = \frac{|\mathrm{e_j}|}{2A(\mathrm{T}_0^{\mathrm{j}})}\mathrm{n}^{(0)} \tag{B.43}$$

$$\nabla_{\mathrm{x}_3}\theta = \frac{1}{|\mathrm{e_j}|}\left[\cot(\alpha_2) + \cot(\alpha_4)\right]\mathrm{n}^{(1)} = \frac{|\mathrm{e_j}|}{2A(\mathrm{T}_1^{\mathrm{j}})}\mathrm{n}^{(1)} \tag{B.44}$$

where $A(\mathrm{T}_0^{\mathrm{j}})$ and $A(\mathrm{T}_1^{\mathrm{j}})$ are the areas of the triangles in the pair j; $\mathrm{n}^{(0)}$ and $\mathrm{n}^{(1)}$ are the normal vectors defining these triangles; and $|\mathrm{e_j}|$ is a shared edge in the hinge j (denoted as e_0 in Figure B.1 c). For the definitions of the angles $\alpha_{[1,2,3,4]}$ see Figure B.1 (c).

Bending Energy From Surface Discretization Operator

It has been noticed that renormalization of the bending stiffness done as in[7] is not the most suitable for disordered meshes[24]. The computer graphics community deals with it by relating bending stiffness of the hinge between two triangular elements to the geometry of these triangles $\kappa_i = \kappa\frac{3|\mathrm{e}_i^2|}{A(\mathrm{T}_0)+A(\mathrm{T}_1)}$, *cf.* Equation B.38. In the physics community, it is the bending energy rather than the bending forces that is evaluated at the mesh nodes. This approach is not implemented in the `elasticshells` software, but we describe it for the completeness of the discussion. In this approach, the curvature tensor is constructed from the mean curvature H and Gaussian curvature (trace $H \approx \nabla^2 f$, and determinant $K \approx \det(\partial_i\partial_j f)$, respectively). An approximation for the mean curvature associated with the i^{th} vertex node is[24]:

$$H_i = \frac{1}{\sigma_i}\mathrm{n_i}\cdot\left[\sum_{j(i)}\frac{\sigma_{ij}}{r_{ij}}\left(\mathrm{R}_i - \mathrm{R}_j\right)\right] \tag{B.45}$$

where $\sigma_{ij} = r_{ij}\left[\cot(\theta_k) + \cot(\theta_{k'})\right]/2$ is a length of a bond in the dual mesh connecting the centers of the two triangles $\{i,j,k\}$ and $\{i,j,k'\}$ that share an edge e_{i-j}, with the length r_{ij}, and

angles θ_k and $\theta_{k'}$ calculated at the nodes k and k'; n_i is the surface unit vector normal at the i^{th} node (the average of the normal of the faces surrounding the node i); R_i and R_j are Cartesian coordinates of the vertices i and j; $\sigma_i = \sum_{j(i)} \sigma_{ij} r_{ij}/4$ is the area of the dual cell of the node i (the polygon of bonds surrounding vertex i), and $j(i)$ is a set of nodes neighboring the i^{th} node. Using the Gauss-Bonnet theorem for Voronoi regions, the Gaussian curvature at the i^{th} node is[17]:

$$K_i = \frac{1}{\sigma_i}\left(2\pi - \sum_{k(i)} \alpha_k\right) \tag{B.46}$$

where α_k is an angle subtended by triangle k at the vertex i, and the sum runs over all facets that contain the i^{th} node. The discretized version of the bending energy for a metric with a curvature R_0 (for simplicity, we assume it is the same for all the nodes) is the sum over all contributions from the nodes in a mesh:

$$W_b = \frac{Et^3}{24(1-\nu^2)} \sum_i \sigma_i \left[\left(H_i - \frac{2}{R_0}\right) - 2(1-\nu)\left(K_i - \frac{H_i}{R_0} + \frac{1}{R_0^2}\right)\right] \tag{B.47}$$

For the uniform shell, the Gaussian curvature energy is an invariant and the term $\propto K_i$ can be ignored. However, if the shells are not homogeneous, then the Gaussian curvature is not an invariant and needs to be considered as well[25]. This approach has been very successful in the mechanics of elastic shells[16,19,24,26–28], and it was especially instrumental for materials with varying properties on a shell's surface[2–4]. In these cases, for each node we replace $R_0 \to R_0(i)$ and, if necessary, the thickness $t \to t(i)$ as well[2].

B.2.4 Pressure Force I

The spherical membranes that we study can be pressurized. The internal pressure prevents the membrane from collapse due to the outer pressure and helps to keep its spherical shape. For further discussion we indicate the difference between the internal pressure p_2 and outer pressure p_1 as $\Pi \equiv \Delta p = p_2 - p_1 > 0$.

For the triangulated surface, the simplest way to calculate the pressure force F_p acting on the i^{th} triangular element is simply: $\mathrm{F}_p = \Pi \hat{\mathrm{n}}_i \mathrm{dS_i}$, where $\hat{\mathrm{n}}_i$ is a normal vector pointing outside-out, and

$\mathrm{dS_i}$ is the area of the i^{th} triangular element. This method is conceptually very simple and useful in computer graphics, where we deal with objects having complex geometry. This method, however, requires calculation of the normal vector and deciding how to distribute the pressure force among all the vertices belonging to the triangular element. For simple shapes such as spheres, there is an alternative approach that we present next.

Pressure Force II

The contribution to the total energy from the internal pressure is:

$$W_{\Pi} = \int_0^{\tilde{\mathrm{V}}} dW = \int_0^{\tilde{\mathrm{V}}} \mathrm{dV}\,(\Pi \cdot \mathrm{V}) \tag{B.48}$$

The change of the energy due to the volumetric change is:

$$dW_{\Pi} = \mathrm{V d}\Pi + \Pi \mathrm{dV} \tag{B.49}$$

If the pressure inside the object is assumed to be constant, the above equation reduces to a simpler form: $dW_{\Pi} = \Pi \mathrm{dV}$, and the total energy is simply: $W_{\Pi} = \Pi \mathrm{V}$. The force acting on the vertex i in a mesh due to pressure is:

$$\mathrm{F}_p(\mathrm{x}_i) = -\frac{\partial}{\partial \mathrm{x}_i} W = -\frac{\partial}{\partial \mathrm{x}_i} \Pi \mathrm{V} \tag{B.50}$$

Again, if the pressure is constant, then the force is simply:

$$\mathrm{F}_p(\mathrm{x}_i) = -\Pi \frac{\partial}{\partial \mathrm{x}_i} \mathrm{V} \tag{B.51}$$

If the pressure inside the membrane is not constant, the situation requires a bit more elaboration. The simplest case is a membrane filled with an ideal gas. For an ideal gas, the pressure and the volume of the gas are related as $\Pi \mathrm{V} = \mathrm{nRT}$, where n is the amount of gas, R is the gas constant, and T is temperature. In further derivations, we denote $\tilde{\mathrm{N}} = \mathrm{nRT}$. The membrane is a closed system, and the volumetric change is isothermal, thus we can write $\Pi_1 \mathrm{V}_1 = \Pi_2 \mathrm{V}_2$. Furthermore, we assume that the membrane may have some excluded volume V_e. For such a case, the pressure

energy reads:

$$W_{\Pi}(\mathrm{V}) = \int_{\mathrm{V}_e}^{\mathrm{V}} \mathrm{dV}' \Pi(\mathrm{V}') = \int_{\mathrm{V}_e}^{\mathrm{V}} \mathrm{dV}' \left(\frac{\tilde{\mathrm{N}}}{\mathrm{V}'} \right) = \tilde{\mathrm{N}} \ln \left(\frac{\mathrm{V}}{\mathrm{V}_e} \right) \tag{B.52}$$

and the force is:

$$\mathrm{F}_p(\mathrm{x}_i) = -\frac{\partial}{\partial \mathrm{x}_i} W_{\Pi}(\mathrm{V}) = -\frac{\tilde{\mathrm{N}}}{\mathrm{V}} \frac{\partial}{\partial \mathrm{x}_i} \mathrm{V} = -\Pi(\mathrm{V}) \frac{\partial}{\partial \mathrm{x}_i} \mathrm{V} \tag{B.53}$$

where $\Pi(\mathrm{V}) = \frac{\mathrm{nRT}}{\mathrm{V}-\mathrm{V}_e}$. In Section B.2.4, we show how to evaluate a derivative $\partial \mathrm{V}/\partial \mathrm{x}_i$ for the volume calculated as a sum of tetrahedrons build on the triangular mesh and the center of the mass of the spherical membrane.

Volume derivative calculations

To calculate the force acting on a node due to the internal pressure, we pick a point inside a shell (it can be, for example, the center of mass) and split the shell into a set of tetrahedrons. A tetrahedron is defined by four points: $A = (A_x, A_y, A_z)$, $B = (B_x, B_y, B_z)$, $C = (C_x, C_y, C_z)$, $D = (D_x, D_y, D_z)$. Let us assume that the point D is a position of the center of mass. The total volume is equal to the sum of all tetrahedrons: $\mathrm{V} = \sum_i \mathrm{V}_i$, Appendix A.3.2. Thus, the problem of the pressure forces reduces to the calculation of a tetrahedron's volume derivative.

The volume of the tetrahedron is then given by:

$$\mathrm{V} = |(A - D) \cdot ((B - D) \times (C - D))|/6 \tag{B.54}$$

For three points a, b, and c, the derivative of a scalar triple product in a direction x is:

$$\partial_x \left[a \cdot (b \times c) \right] = \partial_x a \cdot (b \times c) + a \cdot \partial_x (b \times c) \tag{B.55}$$

If b and c are fixed points, and only a can change, then:

$$\partial_x \left[a \cdot (b \times c) \right] = (\partial_x a) \cdot (b \times c) \tag{B.56}$$

Thus, for fixed points B, C, and D, we have, in the x direction, of the point A:

$$\partial_A \mathrm{V} = \partial_A (A - D) \cdot [(B - D) \times (C - D)] /6 \tag{B.57}$$
$$= (B - D) \times (C - D)/6 \tag{B.58}$$

For the point A, the derivatives in y and z directions can be calculated analogically. For the vectors B and C, we use the same method, leveraging the cyclic formula (for brevity we take $D = 0$):

$$A \cdot (B \times C) = C \cdot (A \times B) = B \cdot (C \times A) \tag{B.59}$$

Finally, to calculate the total volume derivative, we need to add up all of the volume changes from tetrahedrons that meet at the given vertex node.

Constant volume algorithm

The `elasticshells` package also implements a constant-volume model. The constant volume is controlled by varying shells' internal hydrostatic pressures. If the volume of the shell is not equal to the preassigned value $\mathrm{V_o}$, the pressure Π_{new} is adjusted to the value $\Pi_{\text{new}} = \Pi_{\text{old}} \left(1 + (\mathrm{V}_0 - \mathrm{V}) /\mathrm{V}\right)$. This inevitably drags the system out of mechanical equilibrium and the system needs to be equilibrated, see Section B.4. The protocol continues until the volumes of the shells reach their preassigned volumes within 0.1% of accuracy.

B.2.5 Membrane contact mechanics

The penetration of two shells is prevented by the repulsive interaction between vertex nodes belonging to different shells. The radius of the repulsive vertex R_v is usually assumed to be equal to the thickness of the shell t. The vertex nodes cover the surface densely enough, so each triangular element is completely covered by its three vertices. The repulsive force between non-bonded nodes is modeled by the Hertizian repulsive force:

$$\mathrm{F(R)} = -\frac{4}{3} h^{3/2} E^* \sqrt{R^*} \hat{\mathrm{R}} \tag{B.60}$$

where R^* is defined as $R^{*-1} = R_i^{-1} + R_j^{-1}$, the effective Young modulus $\frac{1}{E^*} = \frac{1-\nu_i^2}{E_\mathrm{i}} + \frac{1-\nu_j^2}{E_\mathrm{j}}$, h is the overlap between two vertices $h = R_i + R_j - |\mathrm{R}|$, and $\hat{\mathrm{R}}$ is a unit vector along $\mathrm{R} = \mathrm{R}_i - \mathrm{R}_j$. In all of our simulations, we assumed $E_i = E_j = E$, $\nu_i = \nu_j = \nu$, and $R_i = R_j = R_v$, thus we have have $E^* = E/2(1-\nu^2)$, and $R^* = 1/2R_v$. For the contact mechanics with rigid walls, we use the same Equation B.60, however, with $R^* = R_v$, and the effective Young modulus calculated for the new set of parameters ν_wall and E_{wall}.

B.2.6 Handling Non-bonded interactions

The most expensive part of the simulation is the calculation of the interactions between non-bonded vertex nodes. The most straightforward implementation of the `time-driven` algorithm (see Section B.3), has the cost of the computation that scales as $\mathcal{O}(\mathrm{N}^2)$, see Figure B.2 A. This was slightly mitigated by Loup Verlet, who developed a data structure called `Verlet-list`[29,30]. In the `Verlet-list` approach, we set up the sphere of the size $R = R_c + R_s$, were R_c is the interactions' cut-off distance and R_s is the thickness of the "skin", Figure B.2 B. Next, all the particles within distance R are assigned to the list of potential particles being in contacts, *i.e.* `Verlet-list`. Next, at each time-step, only particles that belong to the particle's `Verlet-list` are considered for forces calculations. This list must be recalculated from time to time so particles that get into the R range $[0, R]$ are included and the ones that left are excluded from the list. The number of time-steps between `Verlet-list` updates (or equivalently R) is chosen based on particles velocity, density, *etc.* For example, if dr_max is the maximum distance that any particle can travel during one time-step Δt, and if we want to use `Verlet-list` for n time-steps before recalculation, than the radius of Verlet-list must be $R = R_c + n\mathrm{dr}_\mathrm{max}$. Despite the fact that the computational costs for the already constructed Verlet-lists is $\mathcal{O}(\mathrm{N})$, updating these lists dominates the computational cost, and for larger systems it still scales as $\mathcal{O}(\mathrm{N}^2)$. This cost can be reduced by applying `linked cells-list` data structure which has cost $\mathcal{O}(\mathrm{N})$[30], Figure B.2 C. The idea of `linked-cell lists` is to split the system into a collection of cells of a size comparable to the iterations' cutoff $\mathrm{L} \sim R_c$. Then, at each time step, particles are assigned to the cells and only particles belonging to the neighbor cells are considered. In the `elasticshells` software, we use the `nblists` package to handle non-bonded interactions (`https://github.com/pgniewko/nblists`). This method can be further optimized by usage of different data-structures such as `octrees`. However the gain is relatively small, reaching 50% better computational performance in expense of substantial programming work[31].

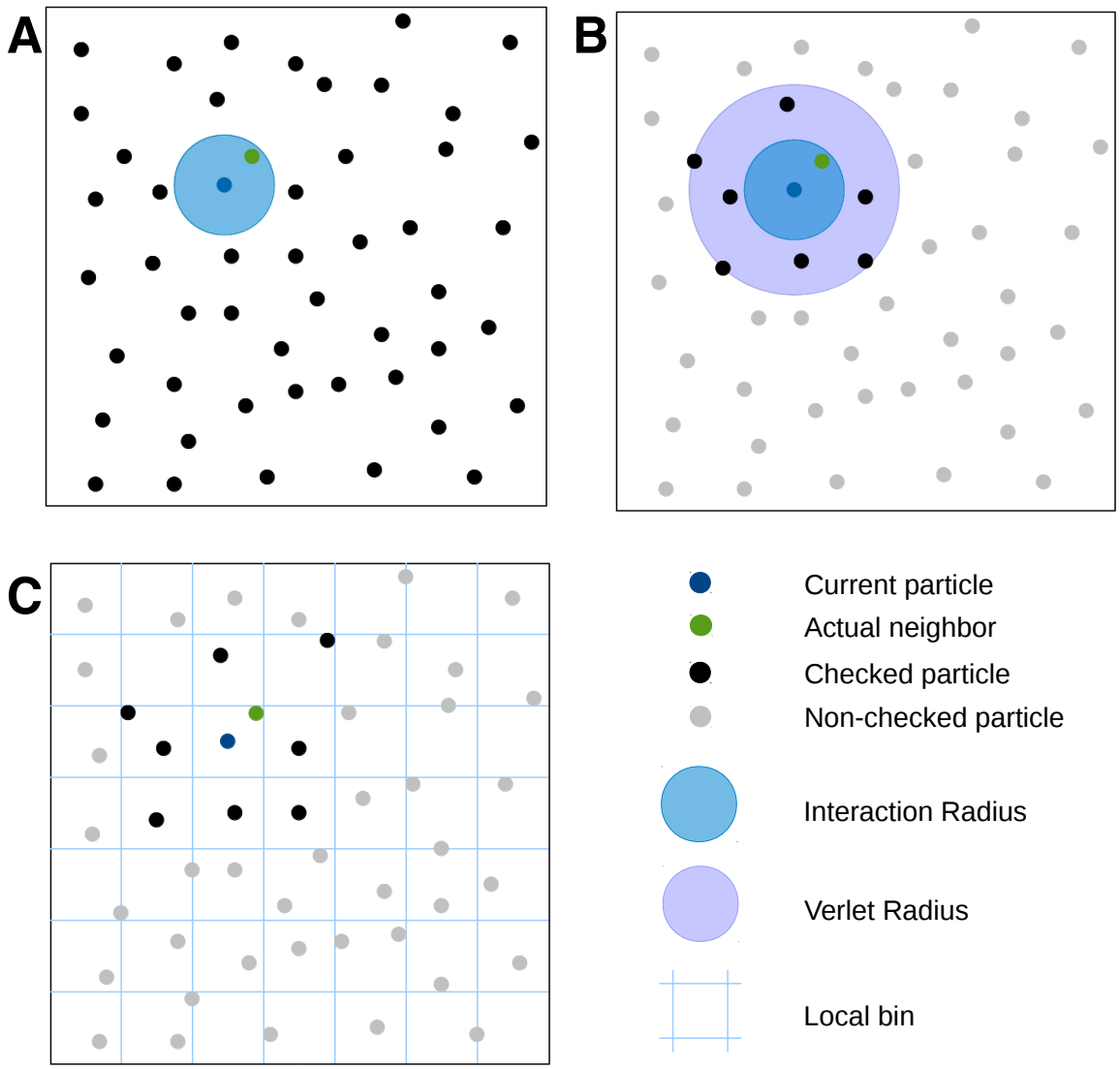

Figure B.2: Contacts detection between non-bonded particles. The most computationally demanding step in forces evaluation is identifying overlaps between non-bonded vertex nodes. In the simplest and least efficient approach, for the particle i with a finite interaction radius R_v, we need to check the separations between all of the N particles in the system. Thus the cost of the evaluation of the contact forces for all of the nodes is $\mathcal{O}(\mathrm{N}^2)$, **A**. If the interactions between nodes are only short-ranged, the cost can be slightly mitigating by constructing a `Verlet-list` with a radius larger than R_v and containing just the most likely nodes in contact, **B**. This reduces only a pre-factor in the naïve method, and the computational cost is sill $\mathcal{O}(\mathrm{N}^2)$. Much more efficient is the method where the system is divided into a set of boxes with a linear size larger than R_v. To find all of the contacts for our target node (a blue dot) we just need to check neighboring cells, **C**. This approach reduces the computational costs to $\mathcal{O}(\mathrm{N})$.

B.3 Elastic Shells Simulations

The simulations are performed in a continuous space, *i.e.* there is no fixed Euclidean grid on which we solve the mechanics of the model. The model is force-based, for which *time* has a straightforward definition. Stochasticity in the dynamics is neglected. The model is intended to simulate macroscopic systems, for which the inertia effect can be neglected — the Reynolds numbers are very small, such that the friction dominates the momentum[10,32,33]. Dropping the acceleration term in the equations of motion leads to a system of coupled first order equations applied to every node in elastic shells:

$$\mathrm{f}_d(\dot{\mathrm{x}}) - \nabla_{\mathrm{x}} W_{\mathrm{tot}} = \mathrm{f}_b \tag{B.61}$$

where the first term on the left hand side is a dumping of motion — most commonly given as $\mu\dot{\mathrm{x}}$, where μ is a friction coefficient; in our simulations, we fixed $\mu = 1$; the second term represents the internal forces due to deformation of the bodies (stretching and bending forces, Equations B.31 and B.40) or interaction between two shells in contact, Equation B.60. The right-hand side term f_b represents all of the external forces applied to the body, for example, by the simulation box upon compression, *cf.* Figure B.3.

B.3.1 Simulation scheme

Initial shells packing are generated following Gniewek *et al.*[34]. The simulation starts from a dilute packing ($\phi < 0.1$). In the next step, a linear dimension of the box is changed in small steps, Figure B.3. If the periodic boundary condition is used, the shells get compressed by the neighbor shells due to the increased density of the shells in the box. If the rigid wall boundary conditions are applied, the shells are swept by the box walls towards the center of the box, and they get compressed by the other shells and the box walls. After each change in the box size, the resulting forces are equilibrated by the energy minimization algorithm, see Section B.4. The box dimension is changed in relatively small steps not exceeding the linear size of a single vertex in the shells' mesh. During the simulation, the mesh connectivity is held fixed, *i.e.* the membranes are modeled as a solid material.

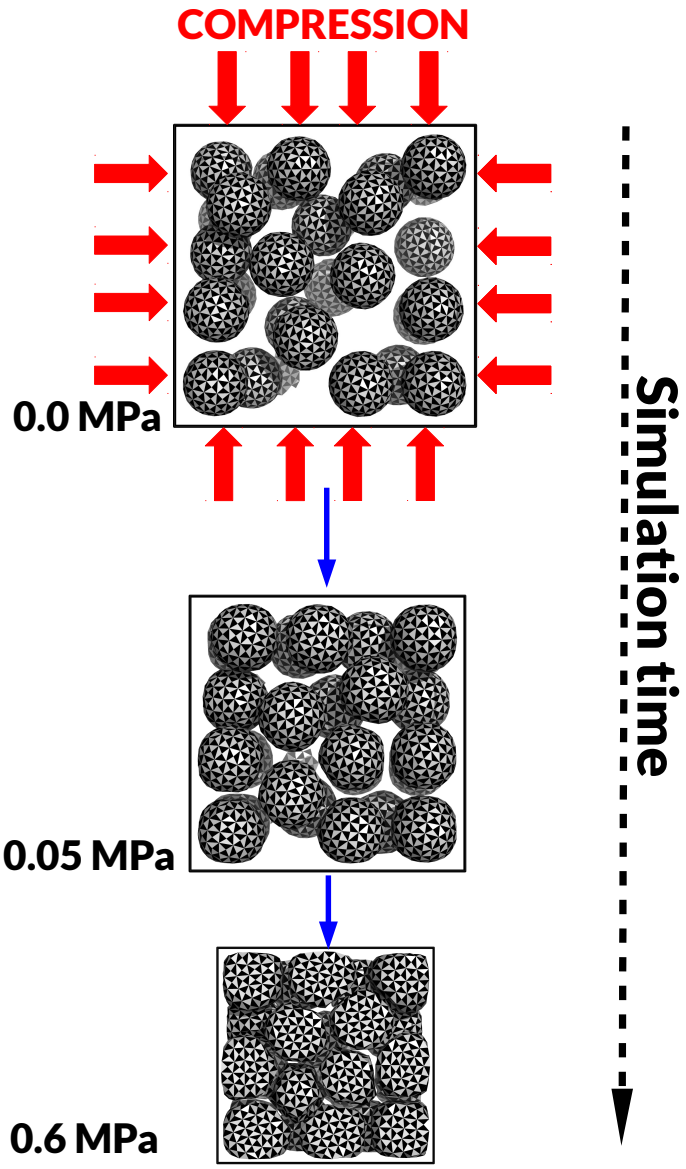

Figure B.3: Spring-mesh simulations scheme: Mono-disperse shells are randomly distributed in a rigid box. The initial concentration is low so the cells do not touch one another. The simulation box is progressively compressed, hence increasing the packing fraction, and lead to the pressure buildup. Sketch from Delarue *et al.*[10].

B.4 Energy Minimization Algorithms

We minimize the energy by solving equations of motion for a given model, until all of the forces are equilibrated. This procedure finds only a local energy minimum, but this is desired, as it does not require any complicated excluded volume energy and works very well for our purposes.

B.4.1 Integration schemes

Equation B.61 is a 1st order differential equation (ODE), so widely used integrators such as Velocity-Verlet or Leapfrog cannot be used[30]. Below, we present algorithms that can be used to solve Equation B.61. These numerical algorithms belong to the broad family of Runge-Kutta methods (R-K)[35]. The Runge-Kutta method is conventionally called "being of the s^{th} order" if its error is $\mathcal{O}(\delta t^{s+1})$. R-K numerical integrators take the general form of:

$$y_{n+1} = y_n + h \sum_{i=1}^{s} b_i k_i \tag{B.62}$$

where k^{th} coefficients are defined as:

$$k_i = f\left(t_n + c_i h, y_n + h \sum_{j=1}^{s-1} a_{ij} k_j\right) \tag{B.63}$$

All these methods can be classified using the *Butcher tableau* $\left(\begin{array}{c|c} C & A \\ \hline & B \end{array}\right)$:

$$\begin{array}{c|cccc} c_1 & a_{11} & a_{12} & \dots & a_{1s} \\ c_2 & a_{21} & a_{22} & \dots & a_{2s} \\ \vdots & \vdots & \vdots & \ddots & \vdots \\ c_s & a_{s1} & a_{s2} & \dots & a_{ss} \\ \hline & b_1 & b_2 & \dots & b_s \end{array} \tag{B.64}$$

Below, we start with description of the simplest case called the Euler-method, and later on we discuss higher order methods.

Explicit and Implicit Euler

The over dumped dynamics is modeled with a set of the 1st order ODEs:

$$\dot{x} = f(x) \tag{B.65}$$

The change over time can be approximated by the difference of two consecutive states:

$$\frac{\partial \mathrm{x}}{\partial t} \approx \frac{x_{n+1} - x_n}{h} = f(x) \tag{B.66}$$

We need to decide at what point we evaluate the function $f(x)$. The most obvious choice is to evaluate $f(x)$ at x_n. This leads to a scheme called *Forward Euler*:

$$x_{n+1} + x_n + h \cdot f(x_n) \tag{B.67}$$

This scheme assumes forces to be constant throughout the entire time-step. This approach overshoots the exact solution, making an error grow relatively quickly, and making the scheme numerally unstable. However, it is attractive because it can be evaluated directly using known $f(x_n)$, and we do not have to solve a linear system of equations. An alternative is to evaluate the function $f(x)$ at x_{n+1} which leads to this system of equations:

$$x_{n+1} - h \cdot f(x_{n+1}) = x_n \tag{B.68}$$

Denoting $\Delta x = x_{n+1} - x_n$, the function f can be expanded in the Taylor's series:

$$f(x_n + \Delta x) \approx f(x_n) + f'(x_n)\Delta x \tag{B.69}$$

leading to:

$$\Delta x = h\left(f(x_n) + f'(x_n)\Delta x\right) \tag{B.70}$$

This can be rewritten as:

$$\left(\frac{1}{h}\mathrm{I} - f'(x_n)\right)\Delta x = f(x_n) \tag{B.71}$$

and finally, a solution to the time-step can be found as:

$$\Delta x = \left(\frac{1}{h}\mathrm{I} - f'(x_n)\right)^{-1} f(x_n) \tag{B.72}$$

This scheme is called *Backward Euler*, and it is more numerically stable than *Forward Euler*, making it very popular in the computer graphics[36]. However, the method requires more work, although the computational cost pays back, because the time step h can be increased, usually, by an order of magnitude in comparison to *Forward Euler*.

For the *Forward-Euler* (first order) method with a time step δt, the error is $\mathcal{O}(\delta t^2)$, and the *Butcher table* is:

$$\begin{array}{c|c} 0 & 0 \\ \hline & 1 \end{array} \tag{B.73}$$

However, this method is not recommended for practical use[35]. The *Butcher table* for *Backward Euler* is:

$$\begin{array}{c|c} 1 & 1 \\ \hline & 1 \end{array} \tag{B.74}$$

Second-order Runge-Kutta methods

The explicit (*i.e.* A matrix being lower triangular), generic, second-order method is given by the table:

$$\begin{array}{c|cc} 0 & 0 & 0 \\ x & x & 0 \\ \hline & 1-\frac{1}{2x} & \frac{1}{2x} \end{array} \tag{B.75}$$

where for $x = 1/2$ we obtain the explicit midpoint method:

$$\begin{array}{c|cc} 0 & 0 & 0 \\ 1/2 & 1/2 & 0 \\ \hline & 0 & 1 \end{array} \tag{B.76}$$

However, this linearly stable Runge-Kutta time discretization can generate oscillations around the energy minima. The other second order R-K method is referred to us as Heun's method ($x = 1$)

and it can be written using the *Butcher table* as:

$$\begin{array}{c|cc} 0 & 0 & 0 \\ 1 & 1 & 0 \\ \hline & 1/2 & 1/2 \end{array} \tag{B.77}$$

Despite the fact that for each time-step we have to evaluate forces twice, we can increase the time step δt by at least one order of magnitude, and as a result, get better efficiency and numerical stability than for simpler methods. Although stochasticity is neglected in our simulations, Heun's method can be easily extended to stochastic differential equations[37].

Fast Inertial Relaxation Engine: FIRE

The FIRE method is a general optimization framework where a point in a phase-space is attributed with a fictitious mass. The trajectory of that point is solved with a variant of MD simulation, and the energy excess is properly removed to provide a fast convergence. Specifically, the system obeys the following equation of motion:

$$\dot{\mathrm{v}}(t) = \frac{\mathrm{F}(t)}{m} - \gamma(t)|\mathrm{v}(t)| \left[\hat{\mathrm{v}}(t)\hat{\mathrm{F}(t)}\right] \tag{B.78}$$

where m is the fictitious mass, $\mathrm{v}(t) = \dot{\mathrm{x}}$ is the velocity, $\mathrm{F}(t) = -\nabla W(\mathrm{x})$ is the force, and $\hat{\cdot}$ (hat) denotes a unit vector. If the power is positive, such as $P(t) = \mathrm{F}(t) \cdot \mathrm{v}(t)$, the particle accelerates in a direction that is steeper than the current direction of motion via the function $\gamma(t)$. If the power $P(t)$ is negative, then all the particles in the system stops, *i.e.* the velocity vector is set to zero, $\mathrm{v}(t) = 0$.

Algorithm 4 Energy Relaxation with FIRE algorithm[38]. MD $(\cdot)$ is your favorite MD integrator.

procedure INTEGRATOR(x, Δt) ▷ Full simulation
  α_{start}, Δt_{max}, f_α, f_{inc}, f_{dec}, N_{min} ▷ Parameters
  it $\leftarrow 1$, cut $\leftarrow 1$
  $\alpha \leftarrow \alpha_{\text{start}}$
  $v \leftarrow 0$
  $F \leftarrow \text{FORCES}(x)$ ▷ Calculate Forces
  while $\max_i(F_i) \geq F_{\text{min}}$ do
    $x, F, v \leftarrow \text{MD}\,(x, v, \Delta t)$ ▷ MD integrator
    $P \leftarrow v \cdot F$
    $v \leftarrow (1-\alpha)v + \alpha\hat{F}|v|$ ▷ $\alpha = \gamma(t)\Delta t$
    if $P > 0$ & $(\text{it} - \text{cut}) > N_{\text{min}}$ then
      $\Delta t \leftarrow \min\,(\Delta t \cdot f_{\text{inc}}, \Delta t_{\text{max}})$
      $\alpha \leftarrow \alpha \cdot f_\alpha$
    else if $P \leq 0$ then
      $v \leftarrow 0$
      cut $\leftarrow$ it
      $\Delta t \leftarrow \Delta t \cdot f_{\text{dec}}$
      $\alpha \leftarrow \alpha_{\text{start}}$
    it $\leftarrow$ it $+ 1$

In our simulations, we use FIRE with the Velocity-Verlet integrator[30]. The other parameters used in FIRE algorithm are: $\Delta t = 0.1$, $\Delta t_{\text{max}} = 1.5$, $\alpha_{\text{start}} = 0.1$, $N_{\text{min}} = 5$, $f_\alpha = 0.99$, $f_{\text{inc}} = 1.1$, $f_{\text{dec}} = 0.25$. The termination condition for the FIRE algorithm is $\max_i |F_i| \leq 10^{-15}$.

The optimizer is easy to understand and implement, and found in some applications in physics[39]. The method has proven to be comparable in many cases to state-of-the art optimizers such as L-BFGS[38,40]. Despite the fact that methods like L-BFGS[41] gain their superiority by having additional curvature information[40], they cannot be applied to every problem.

Other methods

Next, we describe methods that were also tested but are not included in the final release of the `elasticshells` software. These methods, although efficient for some problems, have not proven its superiority to the FIRE or Heun's methods. We discuss them for completeness.

Gear predictor-corrector

This method offers great flexibility and good numerical stability because a corrector step amounts to a feedback mechanism that can dampen instabilities that might be introduced by the prediction step, see Appendix E in Allen & Tildesley[30].

Although the Gear corrector-predictor (c-p) is not more stable than Runge-Kutta integrators (roughly the same dt can be used) it requires one more (50%) force evaluation than R-K. In our simulations, the 3rd order Gear c-p integrator was implemented because it saves memory space and gives the same errors for largest possible values of dt; see Allen & Tildesley[30] and also f.02 code in the Allen & Tildesley[30] codes library.

With the corrector predictor method, it is possible to iterate over correction-prediction steps. However, there is little gain in it because each iteration requires a forces evaluation. Thus one may better run simulations with a shorter time step and only one iteration. Moreover, even if we iterate a c-p algorithm with a shorter time step, we still do not get the exact trajectory. This is why we gain more accuracy by going to a shorter time step rather than by iterating to convergence at a larger value of dt.

Conjugate gradients

The details of the method are complex and we do not intend to repeat it here since there are many good resources on-line[42]. The source code for the method is provided in resources such as "Numerical Recipes in C++"[35] and is also freely available in the GNU Scientific Library[43]. The `elasticshells` method did not find a broader use because, for strongly compressed systems, the optimizer was crossing the energy barrier caused by the excluded volume of the membrane, and the membranes ended up intersecting.

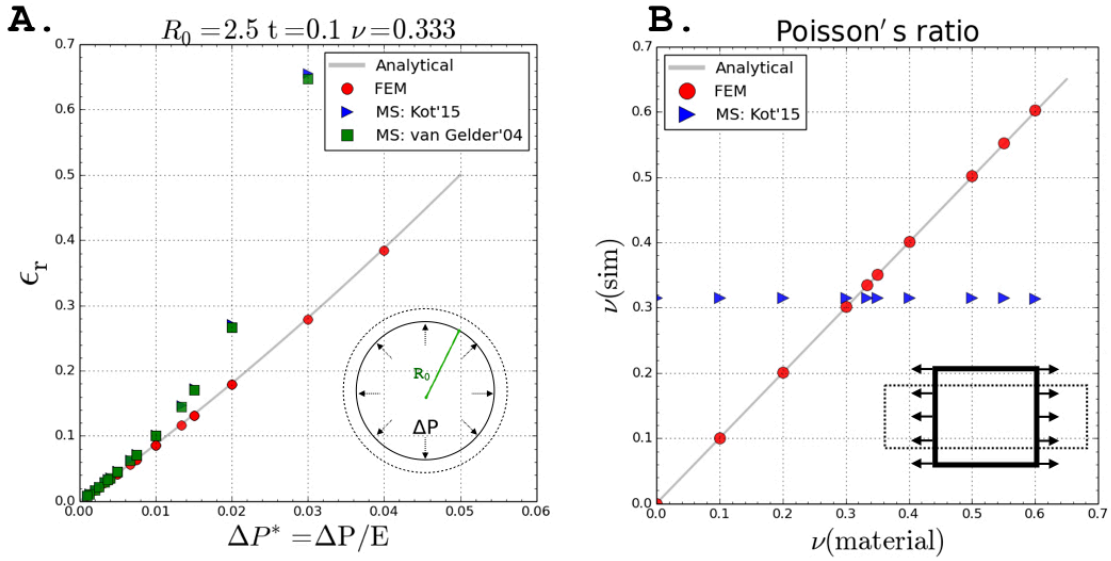

Figure B.4: A: A pressurized elastic membrane with $R_0 = 2.5$ m, $t = 0.1$ m, $E = 25$ MPa, $\nu = 1/3$. The mesh is generated with the `Icosahedral` triangulation algorithm (Appendix A.2.1), and triangulation level=4 (Appendix A.2.1). The energy minimum is found with Heun's integrator, and a time step $\mathrm{dt} = 0.00025$s. The radial strain ϵ_r is given as a function of a reduced pressure $\Delta P^* = \Delta P/E$. **Inset**: Initially relaxed spherical membrane (black line) is pressurized with an internal pressure ΔP, and settles into a mechanically stable state (dotted line). **B**: A square membrane with linear size $\mathrm{L} = 2.28$ m, with the number of vertex nodes in a hexagonal lattice about $N \approx 2200$, elastic material $E = 25$ MPa, $\mathrm{t} = 0.1$ m. Energy minimum is found with Heun's integrator, and a time-step $\mathrm{dt} = 0.00025$ s. **Inset**: Initially relaxed square membrane (black line) is axially stretched (black arrows) with a small force that results in a small strain ($\varepsilon \ll 1$), and settles into a mechanically stable state (dotted line).

B.5 Simple Benchmarking Tests

B.5.1 A pressurized spherical membrane

We consider large deformations of a pressurized, spherical membrane. In this numerical experiment we compare spring-mesh models, with two ways of setting spring constants[8,12], and Finite-Element Method (FEM)[13,14]. The energy density is formulated in terms of the finite Green strain tensor $\mathcal{E}$. The potential energy of the membrane, in terms of the Green strain tensor $\mathcal{E}$, is:

$$W_s = \frac{Et}{2(1-\nu^2)}\left[\mathcal{E}_{11}^2 + \mathcal{E}_{22}^2 + 2\nu\mathcal{E}_{11}\mathcal{E}_{22}\right] \tag{B.79}$$

For the inflated spherical membrane, due to the symmetry of the problem, $\mathcal{E}_{11} = \mathcal{E}_{22} = \frac{1}{2}(\lambda^2 - 1)$, where λ is a stretch of the membrane. The energy density in terms of λ, Et, and ν is:

$$W_s = \frac{Et}{4(1-\nu)}\left(\lambda^2 - 1\right)^2 \tag{B.80}$$

The internal pressure ΔP that balances the stretch λ is:

$$\Delta P = \frac{\partial W_s}{\partial R} = \frac{Et}{R_0(1-\nu)}\left(\lambda^3 - \lambda\right) \tag{B.81}$$

where the radius of the inflated sphere is $R = \lambda R_0$. Since $\lambda = 1 + \varepsilon_r$, where ε_r is an engineering strain, we have:

$$\varepsilon_r + \frac{3}{2}\varepsilon_r^2 + \frac{1}{2}\varepsilon_r^3 = \frac{\Delta P R_0}{2Et}(1-\nu) \tag{B.82}$$

This solution reproduces a known solution $\varepsilon_r = \Delta P R_0(1-\nu)/2Et$ in the infinitesimal strain limit $\varepsilon_r \to 0$[44]. In numerical simulations, we estimate a membrane stretch from the volume as $\lambda = 1 + \varepsilon_r = \sqrt[3]{V/V_0}$. To compare with the analytical solution, we numerically solve Equation B.82 for ε_r. In Figure B.4 A, we plot a radial strain ϵ_r as a function of the pressure difference ΔP. We keep the membrane properties constant, whereas we change the value of the internal pressure. We choose the Poisson ratio $\nu = 1/3$ to make the benchmark fair for spring-mesh models. In Figure B.4 A, we can see that for small radial strains ϵ_r, all three approaches reproduce similar analytical results. However, for strains larger than 1%, we can see a noticeable deviation for spring-mesh models, whereas FEM reproduces large strains mechanics very close to the analytical solution. Small inaccuracies for FEM may be the result of the residual errors in the volume evaluation, Appendix A.4.1.

B.5.2 Poisson ratio

One of the problems with simple spring-mesh models is that they cannot simulate a material accurately with a Poisson ratio different than $\nu = 1/3$. Upon force being applied uniaxially (in direction 1), the strain in that direction is ε_1, whereas it shrinks in a transverse direction ε_2. The Poisson's ratio is defined as:

$$\nu = -\frac{\varepsilon_1}{\varepsilon_2} \tag{B.83}$$

To estimate numerically the value of ν in spring-mesh and FEM, we perform a numerical experiment in which a square membrane is uniaxially stretched with a force F (sufficiently small to keep the strains small) homogeneously, and distributed along both edges in 1-direction, *i.e.* all components of the stress tensor are zero except σ_{11}, see Figure B.4 B. Upon application of the load, the square membrane has dimension $L \times L$ stretching into a rectangular shape of dimension $L_1 \times L_2$. The axial strain is then estimated as $\varepsilon_1 = (L_1 - L)/L$, and $\varepsilon_2 = (L_2 - L)/L$. In Figure B.4 B, we plot the values estimated numerically $\nu(\text{sim})$ for the corresponding $\nu(\text{material})$. For spring-mesh, we assigned spring constants with Equation B.26. Although Poisson's ratio is formally a parameter in Equation B.26, it should have no effect on the mechanics of the membrane except for the incorrect resultant *stiffness modulus* $Y = Et$. As expected, the spring-mesh model, regardless of the preassigned value of the Poisson ratio, always gives values very close to $\nu \approx 1/3$ due to the reasons detailed in Section B.2.2. Contrary to this, FEM reproduces the preassigned Poisson ratio values pretty closely, *cf.* Figure B.4 B. (red dots).

B.5.3 Circular Plates: Small deflections

In the previous sections, the tests do not take into account the bending energy. In the next three tests, we show how a circular plate, clamped on the edge, bends due to concentrated and uniform loads. We test only FEM with and without a bending term. For the first two tests, we stay in a regime of a small deflations and compare radial deflections to the analytic solutions. In the third test, we exert large uniform loads on a clamped circular plate and compare the maximum deflection at the center of the place to the approximate analytic solution.

Concentrated Load at the Center

We consider a circular plate with a clamped edge, for which the boundary conditions are at $r = R_0$, $w = 0$ and $dw/dr = 0$, where w is a normal deflection. The load is applied at the center with a magnitude P_o, Figure B.5. For this setup, a deflection as a function of a distance to the center R is[44]:

$$w(R) = \frac{P_0}{16\pi D}\left(2r^2 \ln\left(\frac{R}{R_0}\right) + R_0^2 - R^2\right) \tag{B.84}$$

where $D = Et^3/12(1-\nu^2)$, and R_0 is a radius of the plate. The maximum deflection (in a regime of small loads), is at the loading point, and has magnitude:

$$w_{\max} = \frac{P_0 R_0^2}{16\pi D} \tag{B.85}$$

Results are presented in Figure B.5. As we can see, FEM simulations without a bending term develops a cusp at $R = 0$. This is expected as the bending term is missing, and a development of high curvatures does not cost any energy, but it relaxes in-plane stress. We can also see an abrupt displacement at $R/R_0 \to 1$. This solutions is strongly disfavored by bending; however, in the case of the missing bending term, this is allowed and only counteracted by stretching energy. When bending is included, the simulation results are reproducing analytical results very accurately — within a maximum relative error below 10%.

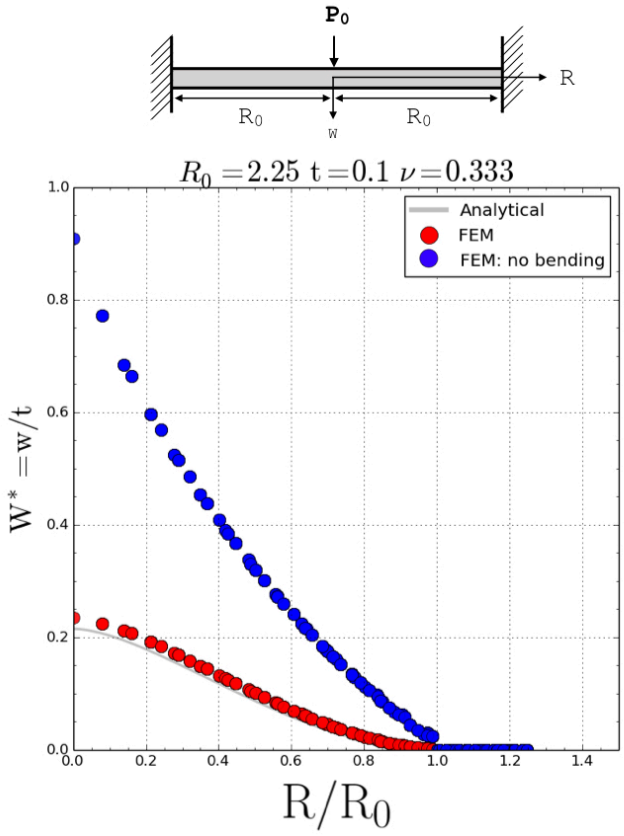

Figure B.5: Concentrated load of a clamped circular plate: A concentrated load with a magnitude $P = 5 \cdot 10^3$ N is applied to a circular plate with a radius $R_0 = 2.25$ m, thickness $t = 0.1$ m, Young's modulus $E = 25$ MPa, Poisson ratio $\nu = 1/3$, and the number of nodes in a hexagonal lattice is $N \approx 1200$. Triangular elements have a linear dimension $a \approx 0.3$ m. The energy minimum is found with Heun's integrator and a time step $\mathrm{dt} = 0.0005$ s.

Uniformly Loaded Circular Plate

The same circular plate as in Section B.5.3, with the clamped edge and the boundary conditions $r = R_0$, $w = 0$, and $dw/dr = 0$ is considered, *cf.* Figure B.6. However this time, the load P_0 is applied uniformly and perpendicularly to the surface across the whole plate. Displacement as a function of distance from the plate's center reads[44]:

$$w(R) = \frac{P_0}{64D}\left(R_0^2 - R^2\right)^2 \tag{B.86}$$

The maximum deflection in the regime of small loads is:

$$w_{\max} = \frac{P_0 R_0^4}{64D} \tag{B.87}$$

Results are presented in Figure B.6. We can notice a behavior that is similar to the case of a concentrated load at $R/R_0 \to 1$. Contrary to the previous case, the membrane solution to the uniform load does not create a cusp at $R \to 0$, but it overestimates a deflection by more than 300%. When bending is included, the relative error is significantly reduced, and at $R = 0$, is only about 10%.

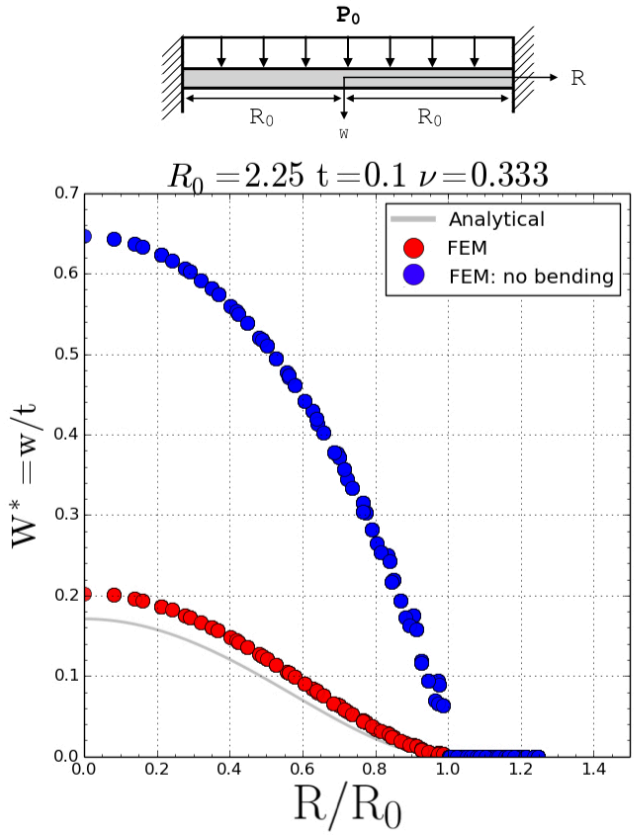

Figure B.6: Uniform load of a clamped circular plate: Uniformly distributed load with a total magnitude $P = 1 \cdot 10^3$ N is applied to a circular plate with a radius $R_0 = 2.25$ m, thickness $t = 0.1$ m, Young's modulus $E = 25$ MPa, Poisson ratio $\nu = 1/3$, and the number of nodes in a hexagonal lattice $N \approx 1200$. Triangular elements have a linear dimension $a \approx 0.3$ m. The energy minimum is found with Heun's integrator and a time step $\mathrm{dt} = 0.0005$ s.

B.5.4 Large Deflection of a Clamped Circular Plate

For small deformations ($w/t \ll 1.0$), a deflection is controlled mainly by a bending term, whereas for larger deflections, the stretching energy term dominates. For large deflections, the linear solution given by Equation B.86 does not apply, and the analytic solution does not exist. However, approximate solutions are given in an implicit form. One of the most commonly used solutions is[44]:

$$P_0 = \frac{64D}{R^3}\left(\frac{w_{\max}}{R_0}\right) + \left(\frac{8}{3}\right)\left(\frac{E}{1-\nu}\right)\left(\frac{t}{R_0}\right)\left(\frac{w_{\max}}{R_0}\right)^3 \tag{B.88}$$

The alternative form of Equation B.88 is:

$$\frac{12}{64(1-\nu^2)}\left(\frac{P}{E}\right)\left(\frac{R_0}{t}\right)^4 = \frac{w_{\max}}{t}\left[1 + \frac{1+\nu}{2}\left(\frac{w_{\max}}{t}\right)^2\right] \tag{B.89}$$

The first and second term on the right-hand side represent stretching and bending solutions, respectively[44]. This formula has been used to find $w_{\max}$ numerically as a function of dimensionless pressure $P^* = PR^4/Et^4$. The results are presented in Figure B.7. In order to plot $w_{\max}/t$ as a function of $P^* = (P/E)(R_0/t)^4$, we numerically solve Equation B.89 for $w_{\max}$ using the `Scipy` Python library. It is clear that for very small pressures P^*, the deflection is mostly controlled by the bending term and the solution is $w_{\max} = \frac{P_0 R_0^4}{64D}$, where $D = Et^3/12(1-\nu^2)$. The linear theory solution is satisfactory (*i.e.* less than 10% of the relative error) for $w_{\max} < t/2$[44]. For the value of reduced pressure $P^* < 10$, the FEM, without a bending energy component, deviates significantly from the analytical solution. However, upon large loads, the model with only the stretching term provides a quite accurate solution, *cf.* Figure B.7.

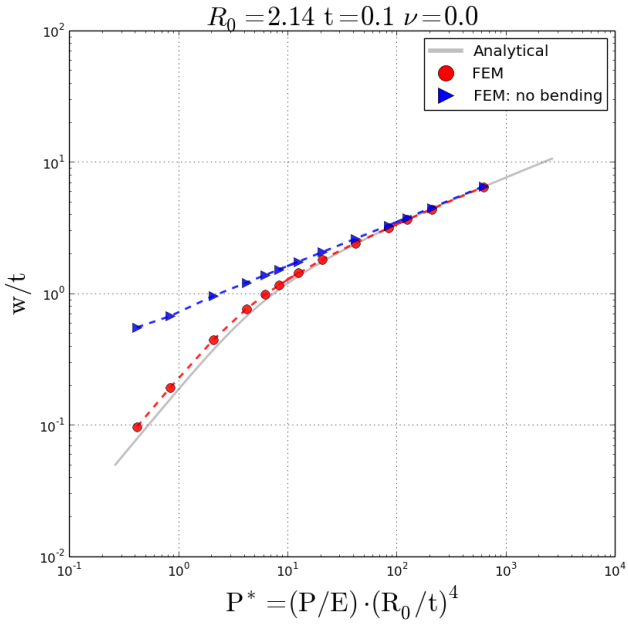

Figure B.7: Clamped plate deflection: Large deformation of a circular, clamped plate. Parameters of the plate are $E = 25$ MPa, $\nu = 0.0$, thickness $t = 0.1$ m, and $R_0 = 2.14$ m. FE model was solved on a hexagonal lattice containing $N \approx 1000$ vertex nodes and a linear size of a triangular element $a \approx 0.2$ m. The local energy minimum was found with Heun's integrator and time step $\mathrm{dt} = 0.0005$ s. Red data points represent full FEM model with stretching and bending energies, whereas blue data-points correspond to the model with only the stretching energy.

B.6 Contact Problem of an Inflated Spherical Nonlinear Membrane: Compression calculations

Next, we test FEM against the solutions of the contact problem for a large deformation of an inflated, non-linear, and spherical membrane between two rigid plates[45], Figure B.8. The solution to the contact problem is expressed in the form of three first-order ODEs for the region where the spherical membrane is not in the contact with the rigid plates. The constraint introduced by the rigid plate on the part of the membrane that is in contact with the plate reduces the number of governing equations to two ODEs. The spherical membrane is filled with an incompressible liquid, thus the volume of the membrane upon compression is kept constant, Section B.2.4. The solution gives a load-deflection relation for the inflated membrane under compression.

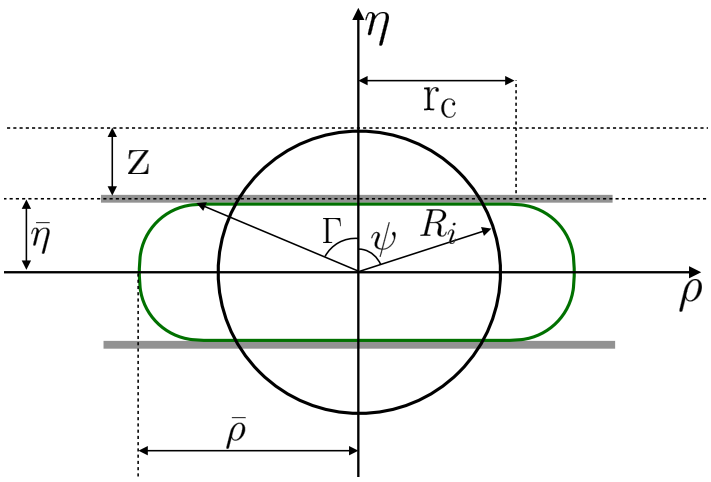

Figure B.8: Geometry of the contact problem of an inflated spherical membrane between two rigid plates: ψ is an angular position of a point on a membrane from the vertical axis of symmetry prior to compression, Γ is an angle of a point on the edge of the contact region between the compression surface and the shell, ρ and η are the horizontal and vertical coordinates, $\bar{\eta}$ is the distance between the compression surface and the equatorial plane, $\bar{\rho}$ is the laterally extended radius of the deformed membrane, z is the half-distance that the membrane has been compressed to, R_i is the radius of the inflated membrane, and r_c is the radius of the contact area.

B.6.1 Model

A sketch of the model is in Figure B.8. A membrane model is formulated as follow:

1. Deformed and undeformed profiles of a membrane and compressive loads are axisymmetric.
2. Before deformation, the elastic membrane is composed of an incompressible, homogeneous, and isotropic material with constant thickness.
3. The membrane's thickness is small in comparison to a linear dimension of the spherical membrane; therefore the bending effects can be neglected.
4. There is no friction between the membrane and the compressing plates.

A spherical membrane with thickness t and radius R_0 is inflated by the initial internal pressure P_0. Then two large parallel and rigid plates (with the inflated membrane in between them) are pressed into contact with the spherical membrane. Due to the symmetry of the problem, only the upper half of the membrane is considered. The problem setup is depicted in Figure B.8, together with

the coordination system used in further model development. For the deformation presented in Figure B.8, we define two principal stretch ratios in the meridian and circumferential directions, respectively[45]:

$$\lambda_1 = \varepsilon_1 + 1 = \frac{1}{R_0}\sqrt{\rho'^2 + \eta'^2} \tag{B.90}$$

$$\lambda_2 = \varepsilon_2 + 1 = \frac{\rho}{R_0 \sin(\psi)} \tag{B.91}$$

where derivatives in Equation B.90 are calculated in respect to ψ; R_0 is the initial radius of the uninflated membrane; and ρ and η are cylindrical coordinates, see Figure B.8 for details. Neglecting bending and shear effects, the energy function is defined as:

$$W_s = \frac{Et}{8(1-\nu^2)} \int_0^{\pi/2} d\psi \left[(\lambda_1^2 - 1)^2 + (\lambda_2^2 - 1)^2 + 2\nu(\lambda_1^2 - 1)(\lambda_2^2 - 1)\right] \tag{B.92}$$

It is worth noting that the above form is identical to the St. Venant-Kirchhoff material, given by Equation B.28. The full sets of ODEs describing the problem is derived for contact and non-contact regions as in the paper by Yang *et al.*[45].

B.6.2 Contact region

Due to the constraint imposed by the plate, there are only two ODEs, and they read:

$$\frac{d\lambda_1}{d\psi} = -\frac{\lambda_1}{\lambda_2 \sin\psi}\left(\frac{f_1}{f_3}\right) - \left(\frac{\lambda_1 - \lambda_2\cos\psi}{\sin\psi}\right)\left(\frac{f_2}{f_1}\right) \tag{B.93}$$

$$\frac{d\lambda_2}{d\psi} = -\frac{\lambda_1 - \lambda_2\cos\psi}{\sin\psi} \tag{B.94}$$

where f_1, f_2, f_3 are functions of principal tensions T_1 and T_2 and are defined in the next section.

B.6.3 Non-contact region

There are three ODEs governing the mechanics of the membrane in a non-contact region:

$$\frac{d\lambda_1}{d\psi} = \left(\frac{\delta\cos\psi - \omega\sin\psi}{\sin^2\psi}\right)\left(\frac{f_2}{f_1}\right) - \left(\frac{\omega}{\delta}\right)\left(\frac{f_3}{f_1}\right) \tag{B.95}$$

where $\delta = \lambda_2 \sin\psi$. The second equation reads:

$$\frac{d\delta}{d\psi} = \omega \tag{B.96}$$

The above is equivalent to the differential equation for λ_2:

$$\frac{d\lambda_2}{d\psi} = \left(\frac{\omega \sin\psi - \delta\cos\psi}{\sin^2\psi}\right) \tag{B.97}$$

The last equation relates the hydrostatic pressure inside the membrane to the parameter ω; that is:

$$\frac{d\omega}{d\psi} = \frac{d\lambda_1}{d\psi}\frac{\omega}{\lambda_1} + \frac{\lambda_1^2 - \omega^2}{\delta}\left(\frac{T_1}{T_2}\right) - PR_0\frac{\lambda_1\sqrt{\lambda_1^2 - \omega^2}}{T_1} \tag{B.98}$$

Finally, we define tensions T_1, T_2 in the meridian and circumferential directions, as well as three auxiliary functions f_1, f_2, and f_3:

$$T_1 = \frac{1}{\lambda_2}\frac{\partial W_s}{\partial \lambda_1} = \frac{Et}{2(1-\nu^2)} \cdot \frac{\lambda_2}{\lambda_1}\Big[\nu\lambda_2^2 + \lambda_1^2 - (1+\nu)\Big] \tag{B.99}$$

$$T_2 = \frac{1}{\lambda_1}\frac{\partial W_s}{\partial \lambda_2} = \frac{Et}{2(1-\nu^2)} \cdot \frac{\lambda_1}{\lambda_2}\Big[\nu\lambda_1^2 + \lambda_2^2 - (1+\nu)\Big] \tag{B.100}$$

$$f_1 = \frac{\partial T_1}{\partial \lambda_1} = \frac{Et}{2(1-\nu^2)}\frac{1}{\lambda_2}\Big[\lambda_1^2 + \nu\lambda_2^2 - (1+\nu)\Big] \tag{B.101}$$

$$f_2 = \frac{\partial T_1}{\partial \lambda_2} = \frac{Et}{2(1-\nu^2)}\frac{\lambda_1}{\lambda_2^2}\Big[\nu\lambda_2^2 - \lambda_1^2 + (1+\nu)\Big] \tag{B.102}$$

$$f_3 = T_1 - T_2 \tag{B.103}$$

B.6.4 Boundary conditions

Boundary conditions for this problem are:

1. At $\psi = 0$, stretches λ_1 and λ_2 are the same: $\lambda_1 = \lambda_2 = \lambda_0$. λ_0 is an unknown parameter, to be found numerically.

2. At $\psi = \Gamma$, *i.e.* at the boundary between contact and non-contact regions, the meridian stretches are the same: $\lambda_1^c = \lambda_1^{nc}$. Γ is an unknown parameter to be found numerically. Additionally, $\lambda_2 = \frac{\delta}{\sin\Gamma}$. In practice we start solving ODEs from $\psi = 0$ to $\psi = \Gamma$, and then we switch to another set of ODEs with initial values given by the above boundary conditions.

3. At $\psi = \Gamma$, we have $\eta' = 0$, and $\delta' = \lambda_1$

4. At $\psi = \frac{\pi}{2}$, we must have $\delta' = 0$, meaning $\omega = 0$.

The model also requires us to specify material parameters $Y = Et$, R_0, and λ_s. The initial stretch ratio λ_s can be, however, estimated pretty accurately from the non-linear inflated membrane model based on Equation B.82, where $\lambda_s = 1 + \varepsilon_r$. Note that specifying ν is not required, as it can be implicitly inferred from the knowledge of $Y = Et$, R_0, and λ_s.

B.6.5 ODEs solving algorithm

To solve two sets of ODEs, *i.e.* Equations B.93, B.94, B.95, B.96, and B.98, researchers usually start with prescribing a compression level $\bar{\eta}$. Then Γ and λ_0 are guessed. Next, ODEs are solved for the contact region. After that, the hydrostatic pressure P is guessed, and then the ODEs are solved for the non-contact region. Once the equations are solved, the boundary condition at $\psi = \pi/2$ is checked. If the check fails, then a new λ_0 is guessed again, and procedure is repeated. If the condition at $\psi = \pi/2$ is satisfied, then the constant volume condition is checked. If this check fails, then the new contact angle Γ is guessed and the whole procedure is repeated. Finally, when the constant volume condition is satisfied, the solution is found[45–48]. The volume used for the constant-volume condition check is evaluated as:

$$\mathrm{V} = 2\pi \int_0^{\bar{\eta}} \rho^2 d\eta \tag{B.104}$$

where $\rho = R_0\delta$[47]. For any boundary point, η can be found from the equation:

$$\frac{d\eta}{d\psi} = -R_0\Big[\lambda_1^2 - \left(\frac{d\delta}{d\psi}\right)^2\Big]^{1/2} \tag{B.105}$$

It can be seen, that for each given $\bar{\eta}$, we are looking for a set of parameters: $\{\Gamma, \lambda_0, P\}$. Finding a solution numerically is a non-trivial task because the equations that we need to solve are highly non-linear, sensitive to slight changes in parameters, and numerically unstable. Thus, in order to find a solution to the above equations for any arbitrary compression η, we took a different approach. Namely, we used Particle Swarm Optimization (PSO)[49], Section B.6.6.

B.6.6 Particle Swarm Optimization

PSO[49] is an algorithm that uses a set of particles that are moving according to the laws of mechanics in a multi-dimensional space. Contrary to the physical systems, the energy function that represents the state of each particle can be an arbitrary function of the particle's variables. The algorithm intends to search for the global scoring function minimum by a means of the "swarm wisdom". Namely, every particle has a memory and stores the information about the coordinates with the best position that it has visited so far. In each time step, the particle moves ballistically through the space; however, every particle is also attracted to its best found solution. Additionally, the particles are also following the "leader", *i.e.* they are attracted to the best solution found by the whole swarm. The parameters used in the simulations are:

1. Particle velocity scaling factor $\omega_{PSO} = 0.5$
2. Scaling factor to search away from the particle's best known position $\phi_p = 0.5$
3. Scaling factor to search away from the swarm's best known position $\phi_g = 0.5$
4. Number of particles $N = 2500$
5. Maximum number of iterations $N_{\text{iter}} = 10^4$
6. Scoring function: $\text{score}(\Gamma, \lambda_0, P) = |(\mathrm{V} - \mathrm{V}_0)/\mathrm{V}_0| + |\omega|$, where volume V is evaluated from Equation B.104 and ω is taken from the integration of ODEs at $\psi = \pi/2$.

Thus, at each time-step, the set of ODEs is solved for the every particle (defined as a set of three parameters $\{\Gamma, \lambda_0, P\}_i$ where i is the particle's index), then the volume and ω are used to score the solution, and finally the simulation proceeds for N_{iter} steps. Upon the termination of the simulation, the solution is taken as the point with the lowest value of the scoring function that was found during the simulation. Once the PSO simulations are done, we obtain for every preassigned $\bar{\eta}$ a set

of parameters $\{\Gamma, \lambda_0, P\}$. The pressure under the contact region is evenly distributed and is equal to the pressure inside the membrane. Thus, the force exerted by the membrane on a plate equals:

$$\mathrm{F} = P \times A_c = \pi P r_c^2 = P\pi(R_0\lambda_2)^2 \sin^2(\Gamma) \tag{B.106}$$

The above calculation is then repeated for each value of $\bar{\eta}$. The simulations were executed with the help of the Python library `pyswarm`.

B.6.7 Calculation results

The results comparing Finite Elements calculations to the analytic solution are presented in Figure B.9. The parameters used in the numerical calculations are: $P/E = 0.0025$, $t/R_0 = 0.04$, and $\nu = 0.5$. We can see that FEM and the analytic results agree very well. In Figure B.9 b, we can see that for deformations up to $\hat{X} \approx 0.2$, the force-deformation relation follows closely the Hertzian contact-force dependence $\hat{\mathrm{F}} \sim \hat{X}^{3/2}$. For larger compressions, the force increases much faster than given by the Hertz contact model and deviates for about an order of magnitude from the expectation — the membrane, in terms of the order parameter $\hat{X}$, can be treated as a stiffening Hertzian spring. We can see that despite the nonlinear behavior of the model, FEM can accurately reproduce the force-deformation relation.

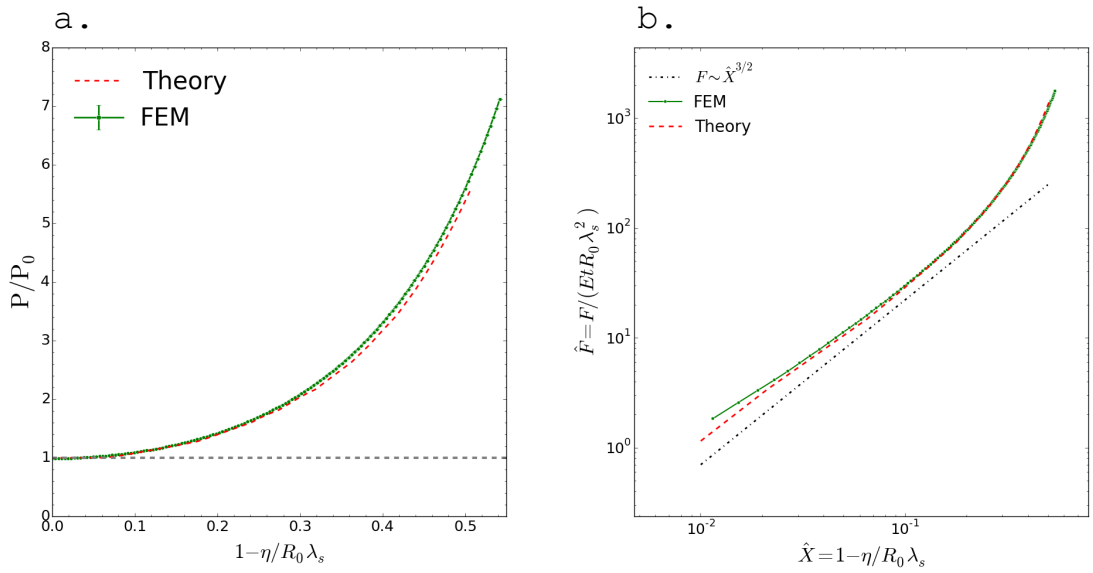

Figure B.9: A comparison of the results from FEM calculations and a semi-analytic solution (Section B.6.1): Material properties used in calculations are $P/E = 0.0025, t/R_0 = 0.04, \nu = 0.5$. (**a**): Normalized hydrostatic pressure $P^* = P/P_0$ vs a membrane deformation $\hat{X}$. (**b**): Normalized force $\hat{\mathrm{F}}$ vs a membrane deformation. Symbols are the same as in Figure B.8. Total force exerted by the membrane in FE simulations are summed up from all the vertex nodes in contact with the simulation box walls.

B.7 Buckling of an Elastic Shell

Under an increase of external pressure, an idealized shell stays spherical until the pressure reaches the critical pressure value. At this pressure, called buckling pressure p_c, a very small increment in the external pressure triggers a shell collapse that significantly reduces the shell's volume. Such a deformation happens at the pressure[50]:

$$p_c = 4\sqrt{\kappa Y}/R_0^2 \tag{B.107}$$

where $\kappa = Et^3/12(1-\nu^2)$, $Y = Et$, and R_0 is the initial radius of curvature. The buckling transition occurs at p_c as the idealized homogeneous sphere releases in-plane compression energy (*i.e.* stretching energy with $\lambda < 1$) at the cost of the bending energy in the form of an oscillatory transverse deflection[3,50]. This instability would not exist without coupling between in-plane stress (resulting from external pressure) and bending stress (due to normal deflection)[3,50]. Any defects or

heterogeneities in the shell lowers the buckling pressure due to the emergence of short-wavelength deflections[50], which are related in a non-trivial way to the defects in the structure[3]. In this test case, we generate meshes with `rndmesh` library, with different final temperatures, and with the same starting temperature $T_{start} = 1000$ [en.u], Appendix A.2.2. High temperatures introduce a larger number of defects in the mesh and generate broader distributions in terms of plain angles and linear dimensions of the triangular elements, Figure B.10. Each simulation is performed for spring-mesh models with the spring constant given by the Seung and Nelson model[7] and the bending energy as described in the Section B.2.2. Starting from the relaxed sphere, with the external pressure $P = 0$, the pressure is increased in small steps, $dP = 0.0025 p_c$, with the shell's volume and asphericity monitored alongside. Buckling is identified as a sudden drop in the shell's volume (the same results are obtained when a sudden jump of the shell's asphericity is used as a buckling criteria). In Figure B.10, we can see results for different FvK numbers: $\gamma = [1k, 5k, 10k, 50k]$, Equation B.17. We can see that for meshes generated at lower final temperatures, the mesh's topologies are quite uniform with a relatively low amount of defects. For these meshes, the structure's resistance to compressive stress is maximal for a given γ. Comparing buckling pressures p/p_c, we can see that the shells with lower FvK numbers are closer to the analytic prediction. Lower γ corresponds to thicker shells, meaning that thick shells are more resistant to the defects in the structure than thin ones. We can also see that for all γ, the structural resistance deteriorates as the mesh contains more and more defects and becomes more irregular. These irregularities in a node's location give rise to the set of functions describing the distributions of these heterogeneities, called *imperfection* modes[50]. These *imperfection* modes couple to *buckling* modes, weakening the structure and leading to the structural collapse at pressures much lower than the critical buckling pressure p_c.

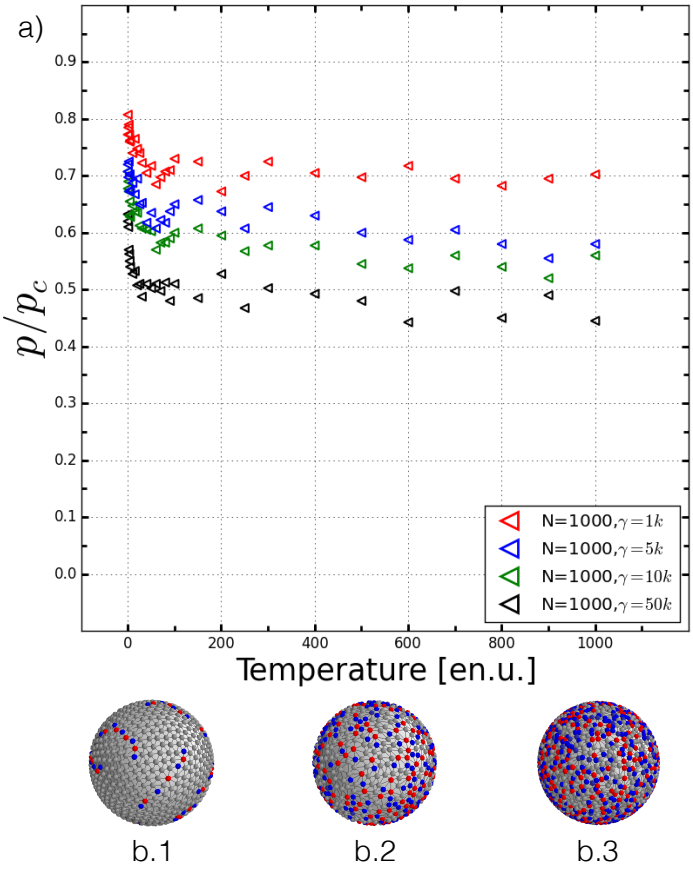

Figure B.10: Buckling pressure: (**a**): Buckling pressure calculated for meshes with varying amount of disorder; four different FvK numbers γ are tested. Calculation is based on Paulose *et al.*[3]. Temperature gives the final equilibration temperature in the `rndmesh` algorithm, Appendix A.2.2. (**b**): Three meshes used in a buckling pressure calculation. The number of vertex nodes in each mesh is $N = 1000$. Gray dots depict the vertex nodes with the number of links equal to 6; blue dots depict the vertex nodes with the number of neighbors less than 6; red dots depict the vertex nodes with the number of neighbors more than 6. Three examples for the temperatures $\mathrm{T} = 0.1$ (b.1), $\mathrm{T} = 50$ (b.2), $\mathrm{T} = 200$ (b.3) are shown.

References

[1] W. Ellenbroek, M. van Hecke, and W. van Saarloos. Jammed frictionless disks: Connecting local and global response. *Physical Review E*, 80:061307, 2009.

[2] S. Datta, S.-H. Kim, A. A. Paulose, J., D. Nelson, and D. Weitz. Delayed buckling and guided folding of inhomogenous capsules. *Physical Review Letters*, 109:134302, 2012.

[3] J. Paulose and D. Nelson. Buckling pathways in spherical shells with soft spots. *Soft Matter*, 9:8227–8245, 2013.

[4] C. Funkhouser, R. Sknepnek, T. Shimi, G. A.E., and O. d. l. C. M. Goldman, R.D. Mechanical model of blebbing in nuclera lamin meshworks. *Proceedings of the National Academy of Sciences of the United States of America*, 110:3248–3253, 2013.

[5] L. Landau and E. Lifshitz. *Theory of Elasticity*. Butterworth-Heinemann, Boston, 3rd edition, 1896.

[6] B. Audoly and Y. Pomeau. *Elasticity and Geometry: From hair curls to the nonlinear response of shells*. Oxford University Press, 1st edition, 2010.

[7] H. Seung and D. Nelson. Defects in flexible membranes with crystalline order. *Physical Review A*, 38:1005, 1998.

[8] M. Kot, H. Nagahashi, and P. Szymczak. Elastic moduli of simple mass spring models. *The Visual Computer*, 31:1339–1350, 2015.

[9] M. Kot and H. Nagahashi. Mass spring models with adjustable poisson's ratio. *The Visual Computer*, 33:283–291, 2017.

[10] M. Delarue, J. Hartung, C. Schreck, P. Gniewek, L. Hu, S. Herminghaus, and O. Hallatschek. Self-driven jamming in growing microbial populations. *Nature Physics*, 12(8): 762, 2016.

[11] J. Lidmar, L. Mirny, and D. Nelson. Virus shapes and buckling transitions in spherical shells. *Physical Review E*, 68:051910, 2003.

[12] A. Van Gelder. Approximate simulation of elastic membranes by triangulated spring meshes. *Journal of Graphics Tools*, 3:21–41, 1998.

[13] H. Delingette. Biquadratic and quadratic springs for modeling st venant kirchhoff materials. *Biomedical Simulation*, pages 40–48, 2008.

[14] H. Delingette. Triangular springs for modeling nonlinear membranes. *IEEE Transactions on Visualization and Computer Graphics*, 14:329–41, 2008.

[15] M. Wardetzky, M. Bergou, Z. D. Harmon, D., and E. Grinspun. Discrete quadratic curvature energies. *Computer Aided Geometric Design*, 24:499–518, 2007.

[16] E. Atilgan, V. Magidson, A. Khodjakov, and F. Chang. Morphogenesis of the fission yeast cell through cell wall expansion. *Current Biology*, 17:2150–7, 2015.

[17] D. Nelson, T. Piran, and S. Weinberg. *Statistical Mechanics of Membranes and Surfaces*. World Scientific, River Edge, NJ, second edition, 2004.

[18] G. Vernizzi, R. Sknepnek, and M. de la Cruz. Platonic and archimedean geometries in multicomponent elastic membranes. *Proceedings of the National Academy of Sciences of the United States of America*, 108:4292–4296, 2011.

[19] E. Yong, D. Nelson, and L. Mahadevan. Elastic platonic shells. *Physical Review Letters*, 111: 177801, 2013.

[20] D. Wan, M. Bowick, and R. Sknepnek. Effects of scars on icosahedral crystalline shell stability under external pressure. *Physical Review E*, 91:033205, 2015.

[21] R. Tamstorf and E. Grinspun. Discrete bending forces and their jacobians. *Graphical Models*, 75:362–370, 2013.

[22] A. Garg, E. Grinspun, M. Wardetzky, and D. Zorin. Cubic shells. *Eurographics/ ACM SIGGRAPH*, pages 91–98, 2007.

[23] R. Bridson and F. R. Marino, S. Simulation of clothing with folds and wrinkles. *Eurographics/ SIGGRAPH*, pages 28–36, 2003.

[24] G. Gompper and D. Kroll. Random surface discretizations and the renormalization of the bending rigidity. *Journal de Physique I*, 6:1305–1320, 1996.

[25] F. Julicher and R. Lipowsky. Domain-induced budding of vesicles. *Physical Review Letters*, 70:2964, 1993.

[26] E. Atilgan and S. Sun. Shape transitions in lipid membranes. *Journal of Chemical Physics*, 126:095102, 2007.

[27] O. Manyuhina, J. Hetzel, and F. A. Katsnelson, M.I. Non-spherical shapes of capsules within a fourth-order curvature model. *The European Physical Journal E*, 32:223–228, 2010.

[28] J. Paulose, G. Vilegenthart, G. Gompper, and D. Nelson. Fluctuating shells under pressure. *Proceedings of the National Academy of Sciences of the United States of America*, 109(48): 19551–19556, 2012.

[29] L. Verlet. Computer experiments on classical fluids. *Physical Reviews*, 159:98–103, 1967.

[30] M. P. Allen and D. J. Tildesley. *Computer simulation of liquids*. Oxford university press, 1989.

[31] R. Chowdhury, D. Beglov, M. Moghadasi, I. Paschalidis, P. Vakili, S. Vajda, C. Bajaj, and D. Kozakov. Efficient maintenance and update of nonbonded lists in macromolecular simulations. *Journal of Chemical Theory and Computation*, 10:4449–4454, 2014.

[32] G. Odell, G. Oster, P. Alberch, and B. Burnside. The mechanical basis of morphogenesis: I. epithelial folding and invagination. *Developmental Biology*, 85:446–462, 1981.

[33] P. Van Liedekerke, A. Buttenschon, and D. D. Drasdo. *Numerical Methods and Advanced Simulation in Biomechanics and Biological Processes*. Elsevier Ltd., 2018.

[34] P. Gniewek and O. Hallatschek. Liquid transport through packings of elastic shells. *https://arxiv.org/pdf/1807.00249.pdf*, 2018.

[35] W. H. Press, S. A. Teukolsky, W. T. Vetterling, and B. P. Flannery. *Numerical Recipes in C++*. Cambridge, 2002.

[36] A. Nealen, M. Muller, R. Keiser, E. Boxerman, and M. Carlson. Physically based deformable models in computer graphics. *Computer Graphics*, 25:809–836, 2006.

[37] G. E. Crooks. *Excursions in statistical dynamics*. University of California, Berkeley, 1999.

[38] E. Bitzek, P. Koskinen, F. Gahler, M. Moseler, and P. Gumbsch. Structural relaxation made simple. *Physical Review Letters*, 97:170201, 2006.

[39] C. Goodrich, A. Liu, and S. Nagel. Solids between the mechanical extremes of order and disorder. *Nature Physics*, 10:578–581, 2014.

[40] D. Sheppard, R. Terrell, and G. Henkelman. Optimization methods for finding minimum energy paths. *Journal of Chemical Physics*, 128:134106, 2008.

[41] J. Nocedal. Updating quasi-newton matrices with limited storage. *Mathematics of Computation*, 35:773–782, 1980.

[42] J. Shewchuk. An introduction to the conjugate gradient method without the agonizing pain. 1:1, 1994.

[43] B. Gough. *GNU Scientific Library Reference Manual, 3rd Edition*. Network Theory Ltd., 2009.

[44] A. C. Ugural. *Stress in beams, plates, and shells, 3rd Edition*. CRC Press, Taylor & Francis Group, 2009".

[45] W.-H. Yang and W. Feng. On the contact problem of an inflated spherical nonlinear membrane. *Journal of Applied Mechanics*, 40:209–214, 1973.

[46] K. Liu, D. Williams, and B. Briscoe. Compressive deformation of a single microcapsule. *Physical Review E*, 54:6673–6680, 1996.

[47] C. Wang, L. Wang, and C. Thomas. Modelling the mechanical properties of single suspension-cultured tomato cells. *Annals of Botany*, 93:443–453, 2004.

[48] J. Stenson, C. Thomas, and P. Hartley. Modelling the mechanical properties of yeast cells. *Chemical Engineering Science*, 64:1892–1903, 2009.

[49] J. Kennedy and R. Eberhart. Particle swarm optimization. *Proceedings of IEEE International Conference on Neural Networks*, pages 1942–1948, 1995.

[50] J. Hutchinson. Imperfection sensitivity of externally pressurized spherical shells. *Journal of Applied Mechanics*, 43:49–55, 1967.